Electronic and electrocatalytic properties of nickel oxide thin films and interfacing on silicon for water splitting devices

Raphaël Poulain

Thesis submitted in the frame of the european joint-PhD program EJD-FunMAT, for the degree of Doctor in Engineering and Technology of the Université Catholique de Louvain and the degree of Doctor Rerum Naturalium of the Technische Universität Darmstadt.

Date of the oral defense: 07/02/2020.

Supervisors:
Pr. Joris Proost
Pr. Andreas Klein

President of the Jury:
Pr. Laurent Delannay

Members of the Jury:
Pr. Ulrike Kramm
Pr. Denis Flandre
Pr. Karsten Albe
Pr. Thierry Toupance
Pr. Marian Chatenet

April 6, 2020

TECHNISCHE UNIVERSITÄT DARMSTADT

UCLouvain

EJD FunMAT
Marie Skłodowska Curie Actions

Original title:

Electronic and electrocatalytic properties of nickel oxide thin films and interfacing on silicon for water splitting devices.

Alternative titles:

Elektronische und elektrokatalytische Eigenschaften dünner Nickeloxid Schichten und deren Grenzflächeneigenschaften zu Silizium für Bauteile zur Wasserspaltung.

Propriétés électroniques et électrocatalytiques de film minces d'oxyde de nickel et interfaçage sur silicium pour des applications de craquage de l'eau.

Approved dissertation of Raphaël Poulain by:

1. Prof. Dr. Joris Proost
2. Prof. Dr. Andreas Klein

Date of submission: 07/10/19
Oral examination: 07/02/20

URN: urn:nbn:de:tuda-tuprints-114757
URL: https://tuprints.ulb.tu-darmstadt.de/id/eprint/11475

Technische Universität Darmstadt
Published in 2020 by TUprints
http://tuprints.ulb.tu-darmstadt.de
tuprints@ulb.tu-darmstadt.de

Acknowledgements

I would like to warmly thank Professor Andreas Klein who provided valuable help all along this thesis and undoubtedly enabled to carry this work to a positive end. In addition, I would like to thank Professor Joris Proost for his welcome and his support in UCL.

I want also to cite and to thank the people who provided technical support at UCL and TU-Darmstadt without who this thesis could not be what it is, along with on the UCL side, Frédéric Van Wonterghem for the XRD, Ronny Santoro and Nadine Deprez for the ICP, Marc Sinnaeve and Alban Maton for designing and machining specific pieces for my experiments, Pierre Eloy for the XPS, Cécile d'Haes for the AFM, Sabine Bebelman for the Raman, Delphin Magnin for the GIXRD, and Ester Tooten, Christian Renaux, Sebastien Faniel and Miloud Zitout for managing the WinFAB platform, and along with on the TU-Darmstadt side, Christian Dietz for the AFM, Joachim Brötz for the XRD, Kerstin Lakus-Wollny for the consumables. I want to thank the electronic structure of materials group and the surface science group for caring about the vacuum systems, the conductivity lab and the electrochemical setups. In addition, I want to thank especially Gunnar Lumbeek and Nicolas Gauquelin for their TEM/EELS measurements at the University of Antwerp, for their avaibility and their kind interaction. Eventually, I want to acknowledge Henri Savolainen, Jonas Hunka and Sirong Yang for their work at TU-Darmstadt as bachelor or master students which enabled to bring interesting insights to this thesis.

I would like to give a special mention to the professors in both university who facilitated my work, provided scientific input or gave support during this thesis with at UCL are Pr. Alain Jonas, Pr. Thomas Pardoen, Pr. Denis Flandre and Pr. Hosni Idrissi and, at TU-Darmstadt are Pr. Wolfram Jaegermann, Pr. Ulrike Kramm, Pr. Bernard Kaiser and Pr. Thomas Mayer.

I want to thank the administrative body at the UCL in the name of Catherine Bauwens and Rania Sakkal, the administrative body at TU-Darmstadt in the name of Marga Lang and Leslie Frotscher and the administrative board of the EJD-FunMAT project in the name of Pr. Thierry Toupance, Pr. Bernhard Zeimetz, Marianne Delmas and Audrey Sidobre.

Also, I want to thank the professors in my Jury who took their time to participate in the evaluation of my work: Pr. Ulrike Kramm, Pr. Denis Flandre, Pr. Karsten Albe, Pr. Marian Chatenet, Pr. Thierry Toupance and Pr. Laurent Delannay.

Finally, I cannot forget the help of the numerous people I had the luck to meet, along with those who particularly helped me during my university transitions, who provided tips regarding this thesis or the persons with whom I could hold scientific discussions.

Abstract

The thesis entitled "Electronic and electrocatalytic properties of nickel oxide thin films and interfacing on silicon for water splitting devices" deals with the implementation of nickel oxide (NiO) at the anode of a photo-water splitting device for the oxygen evolution reaction (OER). The thesis can be tackled through three main parts. The first part consists in studying the surface electronic properties of NiO and its electrical behaviour, the second part deals with the catalytic properties of NiO towards adsorbates and the OER, finally in a third part, the Si/SiO_2 interface has been studied as well as the deposition of NiO on top for assembling a functional photo-anode.

Regarding *the first part*, the surface properties of nickel oxide thin films have been investigated by in-situ X-ray photoelectron spectroscopy (XPS) and ultra-violet photoelectron spectroscopy (UPS). It has been found that, according to the condition of preparation, which defines the concentration of doping in the nickel oxide thin film, the Fermi level can be varied from 1.1 eV to 0.6 eV while the workfunction can be varied from 4.5 eV to 5.2 eV. Eventually, a charge compensation mechanism of the defects is proposed.

In collaboration with the EMAT department (Electron microscopy for Materials science) of the university of Antwerp, thin films prepared at room temperature have been studied by high resolution transmission microscopy and by high resolution electron energy loss spectroscopy. The study concluded the presence of a secondary oxygen-rich phase accumulating at the grain boundaries, which is unstable above 200 °C. This phase would be responsible for the high electrical conductivity reported for room temperature nickel oxide thin films. The instability of the secondary phase would be the origin of the electrical ageing process observed for such nickel oxide thin films.

Then, in the *second part*, oriented nickel oxide thin films have been prepared at high temperature along the (100), (110) and the (111) direction and were subsequently fundamentally studied for in-depth understanding of the nickel oxide/electrolyte interface. The nickel oxide/electrolyte interface has been studied in-situ by XPS/UPS by exposing oriented surfaces to water in vacuum and also by carrying out electrochemical measurements in an electrolyte. In vacuum, it has been found that water adsorbs in a bi-layer fashion. The first layer in contact with the surface contains hydroxides and protons (originating from the water dissociation reaction), while the second layer contains undissociated water molecules. Supported by the electrochemical study on oriented surfaces in an electrolyte, it has been assumed that the (100) oriented nickel oxide thin film offers an equal number of adsorption sites for protons and hydroxides. On the contrary, the (110) and the (111) oriented thin films would offer primarily adsorption sites for hydroxides.

Eventually, the electrochemical study of nickel oxide oriented thin films towards the oxygen evolution reaction shows that the (110) oriented thin film is the most active electrode followed by the (111) oriented thin film and then the (100) surface. The

results suggest that a non-negligible nickel hydroxide layer grows on top of the nickel oxide surface during the oxygen evolution reaction and that the nickel hydroxide layer would sustain the electrochemical reaction. The interpretation of the results lead to the assumption that the (110) oriented nickel oxide thin film would stabilize the nickel hydroxide in a form, which is catalytically more active towards the oxygen evolution reaction than the nickel hydroxide growing on top of the (100) and the (111) oriented nickel oxide thin films. The nickel hydroxide growing on top of the (100) oriented surface might be less homogeneous and thinner than the nickel hydroxide growing on top of the (111) oriented thin film. However, the optimization of the catalytic properties of a nickel oxide based catalyst would be much more affected by the temperature of preparation. Thus, as a rule of thumb, it can be retained that, whatsoever the dominant orientation, best electrochemical performances are attained when nickel oxide thin films are prepared at room temperature and at relatively high oxygen concentration during sputtering.

Finally in the *third part*, to interface nickel oxide by cathodic magnetron sputtering on silicon/silicon dioxide, it has been demonstrated that nickel oxide has to be prepared in such a way that it avoids the implantation of oxygen in the silicon dioxide, as for reactive sputtering depositions. A specific method to deposit nickel oxide by sputtering, referred to as metal layer oxidation (MLO), has been proposed and is basically split into two steps. The first step consists in the deposition of a metallic layer by sputtering in argon (oxygen free atmosphere), whereas the second step consists in oxidizing the metallic layer in an oxygen rich atmosphere while the cathode is off. The MLO method enables the elimination of the bombardment of the silicon dioxide by negatively charged oxygen ions when the sputtering is realized in the presence of oxygen in the chamber.

Then, the silicon/silicon dioxide interface has been studied in the aim to realize a metal-insulator-semiconductor tunnelling junction with nickel oxide. The study of the silicon/silicon dioxide interface shows that the interface contains donor state, located in the top 2 nm of the silicon in the vicinity of Si/SiO_2 interface, which is responsible for the pinning of the Fermi energy in silicon, especially when platinum is interfaced. When nickel oxide is deposited, by the MLO method, it is proposed that the donor state is ionized in totality. In consequence the band-deviation with nickel oxide when prepared by MLO is larger than with platinum. Moreover, the ionization of the donor state can lead to the formation of an intense electric field throughout the Si/SiO_2 interface in the 100-500 MV/m range.

At the end of the thesis, photo-anode structures based on silicon and nickel oxide have been fabricated by MLO and tested in a photo-water splitting cell. Although the devices provided positive response to light excitation, the experiments might suggest that the transfer of the charges from the silicon towards the catalytic site and the catalytic layer itself have to be improved. These last barriers should be taken into account in future works to achieve the realization of an efficient water-splitting device.

Auszug

Die Dissertation mit dem Titel "Elektronische und elektrokatalytische Eigenschaften dünner Nickeloxid Schichten und deren Grenzflächeneigenschaften zu Silizium für Bauteile zur Wasserspaltung" befasst sich mit der Implementierung von Nickeloxid (NiO) an der Photoanode eines Bauteils zur Wasserspaltung mit Bezug auf die Sauerstoffentwicklungsreaktion. Die Arbeit ist in drei Teile gegliedert. Der erste Teilt befasst sich mit der Untersuchung der elektrischen Volumeneigenschaften und der elektronischen Oberflächeneigenschaften von NiO. Der zweite Teil behandelt die katalytischen Eigenschaften von NiO gegenüber Adsorbaten und der Sauerstoffentwicklungsreaktion. Im dritten Teil werden die Eigenschaften der Si/SiO2 Grenzfläche charakterisiert und eine Photoanode durch Abscheidung einer NiO Schicht realisiert.

Im ersten Teil wurden die Oberflächeneigenschaften von dünnen Nickeloxid Schichten durch in-situ Röntgen-Photoelektronenspektroskopie (XPS) und Ultraviolett-Photoelektronenspektroskopie (UPS) untersucht. Es wurde gezeigt, dass durch die Wahl der Abscheideparameter, welche die Dotierkonzentration des Nickeloxids bestimmt, das Fermi-Niveauzwischen 0,6 eV und 1,1 eV und die Austrittsarbeit zwischen 4,5 eV und 5,2 eV variiert werden können. Hier wird ein Ladungskompensationsmechanismus durch Defekte vorgeschlagen.

In Zusammenarbeit mit der Abteilung EMAT (Elektronenmikroskopie für Materialwissenschaften) der Universität Antwerpen wurden bei Raumtemperatur hergestellte dünne Schichten mittels hochauflösender Transmissionselektronenmikroskopie und hochauflösender Elektronenenergieverlustspektroskopie untersucht. Die Ergebnisse der beiden Methoden deuten auf eine sauerstoffreiche Zweitphase an den Korngrenzen hin, welche oberhalb von 200 °C instabil ist. Diese Zweitphase könnte für die hohe elektrische Leitfähigkeit verantwortlich sein, die für dünne Nickeloxidschichten bei Raumtemperatur gemessen wird. Die Instabilität der Zweitphase könnte der Ursprung des elektrischen Alterungsprozesses sein, der für dünne Nickeloxid Schichten beobachtet wurde.

Im zweiten Teil wurden in (100)-, (110)- und (111)-Richtung orientierte Nickeloxid Schichten bei hoher Temperatur abgeschieden. Anschließend wurden die grundlegenden Eigenschaften der Nickeloxid/Elektrolyt Grenzfläche untersucht. Die orientierten Nickeloxid-Schichten wurden im Vakuum mit Wasser in Kontakt gebracht und anschließend durch in-situ XPS/UPS Messungen charakterisiert. Des Weiteren wurden elektrochemische Messungen in Kontakt mit einem Elektrolyten durchgeführt. Die Experimente in Vakuum deuten auf eine zweilagige Adsorption des Wassers hin. Die erste Lage besteht aus Hydroxiden und Protonen (welche durch die Autoprotolyse des Wassers entstehen), während die zweite Lage aus nicht-dissoziierten Wassermolekülen besteht. In Kombination mit den elektrochemischen Messungen im Elektrolyten wird angenommen, dass das in (100)-Richtung orientiere Nickeloxid eine gleiche Anzahl an Adsorptionsplätzen für Protonen und Hydroxide aufweist. Im Gegensatz hierzu würden die in (110)- und (111)-Richtung orientierten

Schichten primär Adsorptionsstellen für Hydroxide bieten.

Die elektrochemische Untersuchung von orientierten Nickeloxid Schichten in Bezug auf die Sauerstoffentwicklungsreaktion zeigten weiterhin, dass die (110)-orientierte Oberfläche die aktivste Elektrode ist, gefolgt von der (111)- und der (100)-orientierten Oberfläche. Die Ergebnisse legen nahe, dass eine nicht zu vernachlässigende Nickelhydroxidschicht während der Sauerstoffentwicklungsreaktion auf der Nickeloxidoberfläche wächst und dass diese Schicht die elektrochemische Reaktion aufrechterhält. Die Interpretation der Ergebnisse führt zu der Annahme, dass die in (110) orientierte Nickeloxid-Schicht das Nickelhydroxid in einer Form stabilisiert, die gegenüber der Sauerstoffentwicklungsreaktion katalytisch aktiver ist als das Nickelhydroxid, welches auf (100)- bzw. (111)-orientierten Nickeloxid aufgewachsen ist. Das Nickelhydroxid, das auf der (100)-orientierten Oberfläche wächst, ist möglicherweise weniger homogen und dünner als das Nickelhydroxid, das auf der (111)-orientierten Schicht wächst. Die Optimierung der katalytischen Eigenschaften eines Katalysators auf Nickeloxidbasis wird jedoch wahrscheinlich viel stärker von der Herstellungstemperatur beeinflusst. Als Faustregel kann daher beibehalten werden, dass unabhängig von der dominanten Orientierung die besten elektrochemischen Leistungen erzielt werden, wenn Nickeloxid Schichten bei Raumtemperatur und bei relativ hoher Sauerstoffkonzentration während der Kathodenzerstäubung hergestellt werden.

Im dritten und letzten Teil wurde Nickeloxid durch Kathodenzerstäubung auf oberflächenoxidierte Silizium Substrate abgeschieden. Es wurde gezeigt, dass Nickeloxid so abgeschieden werden muss, dass die Implantation von Sauerstoff in das Siliziumdioxid vermieden wird. Es wurde ein spezielles Verfahren zur Abscheidung von Nickeloxid durch Kathodenzerstäubung vorgeschlagen, das als metal-layer-oxidation (MLO) bezeichnet wird.Dieses ist im Wesentlichen in zwei Schritte unterteilt: Im ersten Schritt wird eine Metallschicht durch Kathodenzerstäubung in Argon (sauerstofffreie Atmosphäre) abgeschieden; Der zweite Schritt besteht darin, die Metallschicht in einer sauerstoffreichen Atmosphäre ohne Plasma zu oxidieren. Das MLO-Verfahren ermöglicht die Herstellung von Nickeloxid Schichten ohne Beschuss des Siliziumdioxids mit negativ geladenen Sauerstoffionen.

Anschließend wurde die Silizium/Siliziumdioxid Grenzfläche untersucht, mit dem Ziel einen Metall-Isolator-Halbleiter-Tunnelübergang mit Nickeloxid zu realisieren. Die Untersuchung Grenzfläche zeigte, dass die Grenzfläche einen Donator Zustand enthält, der sich in den oberen 2 nm des Siliziums in der Nähe der Si/SiO2 Grenzfläche befindet. Dieser ist für die Fixierung der Fermi Energie im Silizium verantwortlich, insbesondere wenn eine Grenzfläche mit Platin gebildet wird. Es wird in dieser Arbeit vorgeschlagen, dass der Donator Zustand vollständig ionisiert wird, wenn Nickeloxid nach dem MLO-Verfahren abgeschieden wird. Infolgedessen ist die Bandverbiegung mit Nickeloxid bei der Herstellung durch MLO größer als bei Platin. Darüber hinaus kann die Ionisierung des Donator Zustands zur Bildung eines intensiven elektrischen Feldes über die gesamte Si/SiO2 Grenzfläche im Bereich von 100- 500 MV/m führen.

Am Ende der Arbeit wurden Photoanoden auf Basis von Silizium und Nickeloxid (abgeschieden mit dem MLO-Verfahren) hergestellt und in einer Photokatalysezelle zur Wasserspaltung getestet. Obwohl der Aufbau eine positive Reaktion auf Lichtanregung zeigte, deuten die Experimente darauf hin, dass der Ladungsübertrag vom Silizium zur katalytischen Seite und zur katalytischen Schicht verbessert werden muss. Diese letzten Hindernisse sollten in zukünftigen Arbeiten berücksichtigt werden, um die Realisierung eines effizienten Bauteils zur Wasserspaltung zu erreichen.

Résumé

La thèse intitulée "Propriétés électroniques et électrocatalytiques de film minces d'oxyde de nickel et interfaçage sur silicium pour des applications de craquage de l'eau" porte sur l'utilisation de l'oxyde de nickel (NiO) à l'anode d'une cellule photo-électrochimique pour la réaction d'évolution de l'oxygène. La thèse se structure en trois grandes parties où sont étudiés: premièrement, les propriétés de surface et électriques des films minces de NiO, deuxièmement les propriétés catalytiques du NiO et troisièmement l'interface silicium/dioxyde de silicium (Si/SiO_2) ainsi que l'interfaçage du NiO sur la structure Si/SiO_2.

Pour la première partie, les propriétés de surface de films minces de NiO ont été étudiées in-situ par spectrométrie photoélectronique X (XPS) et ultra-violet (UPS). Il est montré que les défauts peuvent être incorporés dans le film mince notamment à basse température et haute concentration en oxygène durant le dépôt. Selon la quantité de défauts introduit, le niveau de Fermi peut être varié de 1.1 eV à 0.6 eV et dans le même temps, la fonction de travail de 4.5 eV à 5.2 eV. Un mécanisme de compensation électronique des défauts a été proposé.

En collaboration avec le département EMAT (Electron microscopy for Materials science) de l'Université d'Anvers, des films minces préparés à température ambiante ont été analysés par microscopie à transmission électronique haute résolution et spectroscopie par perte d'énergie d'électron haute résolution. L'étude a permis de mettre en évidence la présence d'une phase riche en oxygène, jusqu'ici inconnue, instable avec la température, s'accumulant aux joints de grain. Cette phase secondaire serait responsable de la haute conductivité électrique des films minces préparés à tempe rature ambiante. L'instabilité de la phase secondaire pourrait être la cause de la dégradation avec le temps de la conductivité électrique des films minces préparés à température ambiante.

Ensuite, *pour la deuxième partie*, pour l'étude des propriétés catalytiques de NiO, des films minces orientés selon les directions 100, (110) et (111) ont été préparés à haute température et puis ont été utilisés pour l'étude de l'interface oxyde de nickel/électrolyte. Les réactions d'adsorption de l'eau dans le vide des surfaces orientées ont été étudiées in-situ par XPS/UPS et aussi ont été étudiées dans un électrolyte. Les expériences d'adsorption dans le vide in-situ montrent que l'eau s'adsorbe en bi-couche, dont la première couche, en contact avec la surface du NiO, est dissociée en protons et en hydroxydes alors que la seconde est non dissociée. Supporté par une étude des réactions d'adsorption dans l'électrolyte, l'interprétation des résultats a amené à penser que les films minces orientés (100) offrent des sites d'adsorption en quantité égale pour les produits de dissociation de l'eau. Au contraire, les films minces orientés (110) et (111) pourraient ne proposer que des sites d'adsorption pour les hydroxydes.

L'étude électrochimique des films minces orientés pour la réaction de l'évolution de l'oxygène montre que la surface orientée (110) est la plus active, suivie par la surface orientée (111) puis par la surface 100. Durant la réaction d'évolution de

l'eau, une couche d'hydroxyde de nickel se forme sur la surface des films minces. La couche d'hydroxyde de nickel serait le support des réactions électrochimiques. L'analyse détaillée des résultats laisse à penser que le film orienté (110) stabiliserait l'hydroxyde de nickel dans une forme qui serait catalytiquement plus active que l'hydroxyde de nickel qui se forme sur les surface orientées (100) et 111. L'orientation (100) serait notamment moins propice pour la formation d'un hydroxyde de nickel homogène. Cependant pour autant que l'orientation joue un rôle sur l'optimisation des performances pour la catalyse du craquage de l'eau, les meilleurs résultats sont obtenus pour les films minces ayant une grande quantité de défauts, tel que produit à température ambiante et avec un haut taux d'oxygène dans la chambre de dépôt.

Enfin *pour la troisième partie*, l'interface Si/SiO_2 a été étudiée dans le but de réaliser des jonctions à effet tunnel métal-isolant-semiconducteur avec le NiO. L'étude de l'interface Si/SiO_2 à montré que l'interface contient des donneurs d'électrons, localisé dans le deux premiers nm du silicium à proximité de l'interface Si/SiO_2 responsable du blocage du niveau de Fermi en deçà des attentes quand le platinum est interfacé au cause d'une ionization partiel des doneurs. Au contraire quand l'oxyde de nickel est déposé par oxydation de couche métallique (OCM), l'ionisation des doneurs est total. En conséquence la déviation des bandes dans le silicium est plus important quand l'Oxyde de nickel est déposé par OCM qu'avec le platinium. De plus, l'ionisation des donneurs présents à l'interface Si/SiO_2 impliquerait la formation d'un champ électrique extrêmement important, de l'ordre de 100-500 MV/m. Ces défauts à l'interface peuvent venir limiter les performances de la photo-anode s'ils ne sont pas pris en considération.

Pour interfacer le NiO par pulvérisation cathodique sur les surfaces Si/SiO_2, il a été démontré que le NiO doit être déposé de sorte à éviter l'implantation d'oxygène interstitiel dans l'oxyde de silicium, comme c'est le cas si la pulvérisation réactive est adoptée. La méthode proposée pour déposer correctement le NiO par sputtering, appelée oxydation de couche métallique (OCM), se déroule en deux étapes. La première consiste à déposer une fine couche métallique de nickel par pulvérisation cathodique avec l'argon comme atmosphère. La seconde étape permet de convertir la fine couche métallique en NiO en simplement exposant à l'oxygène la couche de nickel. Lors de la seconde étape la cathode est éteinte. La méthode permet d'éliminer le bombardement de la surface d'oxyde de silicium par les ions d'oxygène négativement chargés si la pulvérisation cathodique est réalisée dans une atmosphère contenant de l'oxygène.

Pour conclure les travaux, des structures de photo-anode basées sur l'utilisation de silicium et de NiO pour la réaction de l'évolution de l'eau ont été fabriquées par OCM. Bien que la réponse des photo-anodes à une excitation lumineuse est satisfaisante, les expériences montrent que le transfert des charges du silicium vers les sites catalytiques, ainsi que la couche catalytiques, doivent être améliorées. Ces dernières barrières doivent être prises en compte afin d'obtenir une structure photo-électrochimique capable de convertir efficacement l'énergie lumineuse en énergie chimique.

This thesis has been realized between the Université Catholique de Louvain (UCL) in Belgium and the Technische Universität Darmstadt (TU-Darmstadt) in Germany in the frame of the FunMAT project on functional materials (European EJD-ITN, grant 641640).

La thèse a été réalisée entre l'Université Catholique de Louvain (UCL) en Belgique et la Technische Universität Darmstadt (TU-Darmstadt) en Allemagne dans le cadre du projet FunMAT sur les matériaux fonctionnels (European EJD-ITN, bourse 641640).

Contents

CHAPTER 1

Introduction

1.1 General context

Currently, mankind is subjected to an increasing need for an access to cheap and abundant energy. However, the actual energy scheme highly dominated by carbon resources cannot provide on a long term a safe future on geopolitical and environmental aspects. In 2018, the volume of CO_2 emission reached a historic record of 33.1 Gt[1], mostly driven by USA and emerging countries [1]. The part of renewable energy in the world energy mix, which are mostly based on solar and wind energies, increases at fast pace but traditional fossil energies (Oil, Coal and Natural gas) still dominate largely the energy landscape. The International Energy Agency forecasts that the share of renewable energies will represent 12.4 % in 2023 in the global energy demand[2]. It can be seen as a success, considering that 20 years ago renewable energies were practically not existing. Nevertheless, it remains marginal and a long road has to be realized before achieving the ideal goal to live in a carbon-free society.

Main drawbacks of renewable energies are that they cannot compete economically, mostly because of the use of expensive materials for their fabrication and also because renewable energy productions are often unpredictable assets, which cannot be driven by consumer needs. At some level, e.g: when the quantity of electricity injected on the grid is too high, renewable energies can even become a threat to security, particularly for isolated electrical grids. Thus, energy storage capacities become critical to accompany the development of the renewable energies, especially to store the production excess.

Often seen as the energy of the future, hydrogen can be used as chemical compound for energy storage. It has a great potential, as it has a theoretical energy density of 33.3 kWh/kg against 12.2 kWh/kg for gasoline[3] and as it could be easily produced from water by water-splitting reactions. The hydrogen chemical energy can be exploited in various fields (chemistry, heating, steel production...)[4] or can be converted back to electrical energy via the use of fuel cells[5].

Therefore, with regard to the environmental concerns, it could be smart

[1] The equivalent of 100 000 km^3 of air burned by human activities
[2] https://www.iea.org/topics/renewables/
[3] https://www.energy.gov/eere/fuelcells/hydrogen-storage
[4] https://www.iea.org/topics/hydrogen/
[5] https://en.wikipedia.org/wiki/Fuel_cell

and urgent to imagine and design new devices based on abundant materials for renewable energy production, which have the possibility to facilitate hydrogen-based energy storage.

In this context, solar water-splitting devices could have a strong position in providing the possibility to produce hydrogen directly from solar energy. A solar water-splitting device uses the energy of light to sustain electrochemical water-splitting reactions. Electrical charges produced in the photo-active material are directly used for the production of hydrogen from water. Overall, the solar water-splitting concept can be roughly compared to a 2-in-1 integration of a solar cell and an electrolyzer. Being original, the concept has brought considerable attention at lab scale over the last couple of years. An abundant literature is available dealing with this topic [2–8]. The realization of a solar water-splitting device has been the backbone of this thesis and pushed scientific investigations on several issues, which will be treated all along this manuscript.

1.2 FunMAT project and role of each institution

The current work was aiming at bringing scientific insights into the understanding of the interfacing of transition metal oxide (TMO) and transparent conductive oxide (TCO) onto silicon and to design an adequate solar water-splitting structure based on silicon (Si) and nickel oxide (NiO). The project was shared between two groups located in Europe, which are the institute for materials and process engineering (IMAP)[6] of the Université Catholique de Louvain (UCL/Belgium) and the electronic structure of materials (ESM) [7] group of the Technische Universität Darmstadt (TU-Darmstadt/Germany). Complementarity in the equipment proposed for research has been found between the two universities, for instance Si/SiO_2 samples were prepared in UCL and then studied in TU-Darmstadt.

The UCL provided an access to the Wallonia Infrastructure for Nano FABrication (Winfab) platform. The platform is a 1000 m^2 cleanroom class ISO 3[8] with more than 50 equipments dedicated to research on micro-electronic and related nano-technologies. A chemical cleaning bench, a furnace for silicon dioxide (SiO_2) growth in controlled atmosphere on silicon, a furnace for phosphor diffusion and a sputtering system equipped with in-situ stress sensors for thin films fabrication were used. Electrochemical characterizations of the deposited NiO thin films was also carried out.

At TU-Darmstadt, the work was mainly focused on the characterization of

[6] https://uclouvain.be/en/research-institutes/immc/imap

[7] https://www.mawi.tu-darmstadt.de/esm/esm_1/electronic_structure_of_materials/index.en.jsp

[8] https://en.wikipedia.org/wiki/Cleanroom

surfaces of sputtered thin films and on interface experiments at the DArmstadt Integrated SYstem for MATerials Research (DAISY-MAT) [9]. In addition, a wide set of experiments, as for in-situ electrical measurements, conductivity temperature dependence measurements [10, 11], optical measurements and electrochemical characterization have been realized.

Even though it was not included in the initial plan, a collaboration with the Electron Microscopy for Materials Science (EMAT) group of the University of Antwerp has been initiated to investigate the structure of sputtered NiO thin films by high resolution transmission electron microscopy (HR-TEM) and high resolution electron energy loss spectroscopy (HR-EELS). This work enabled to bring insight into the crystallographic structure and chemical composition of the NiO thin films sputtered at room temperature.

1.3 The solar water-splitting concept

Basically, solar water-splitting devices are composed of a photo-active material (e.g.: silicon, Cu(In,Ga)Se_2, GaAs), which convert sunlight into electrical energy and a catalyst (e.g.: Pt, RuO, IrO_2, NiO...), which converts the electrical energy into chemical one. In the following parts, a short introduction of the physics ruling a solar water-splitting device is made. However, for deeper and concise informations, the reader is referred to Chapter 2.

1.3.1 Conversion of the energy of sun into electrical energy

In the photo-active materials, the photon energy $h\nu$ is transferred to an electron e^-, which reaches an excited state for which the energy of the electron is higher than in the ground state. If the energy of the excited electron is above the energy of the band gap E_g of the photo-active material, the excited electron can *jump* to the upper energy band (the conduction band) leaving behind an unoccupied state (the hole) in the valence band (Figure 1.1, left). Charge neutrality of the material is preserved but negative and positive charges are not located at the same energy level. Thus, electron/hole pairs arising from photo excitation may recombine in the photoactive material, especially in the presence of defective states as depicted in the right schematic of Figure 1.1. For instance, an abrupt crystallographic termination of the photo-active material can leave behind dangling bonds, which are non-compensated covalent bonds because of missing bonding partners. These dangling bonds can produce a large amount of defect states, which might trap charges and could promote recombination of the electron/hole pairs. On the contrary, if the charges are separated before they recombine inside the photoactive material, it is possible to use the energy of the electron/hole pair for something specific as to supply energy to an electronic device. Therefore, to attain good device performances, it is crucial to reduce electron/hole pair recombination and to separate spatially the electric charges.

Charge separation of electron/hole pairs is realized under the presence of an electric field, which can be obtained by bending the bands at the photo-active surface (Figure 1.1). For instance, upward (downward) band bending at the photo-active interface would attract positive (negative) charges at the interface. Thus, electron/hole pairs can be separated spatially before they recombine and charges accumulating at the photo-active surface can be transferred to an electrode. The electric field at the interface of the photo-active material can be formed by local doping (e.g.: p/n junction) or by the contact of two materials having different workfunctions (e.g.: Schottky junction).

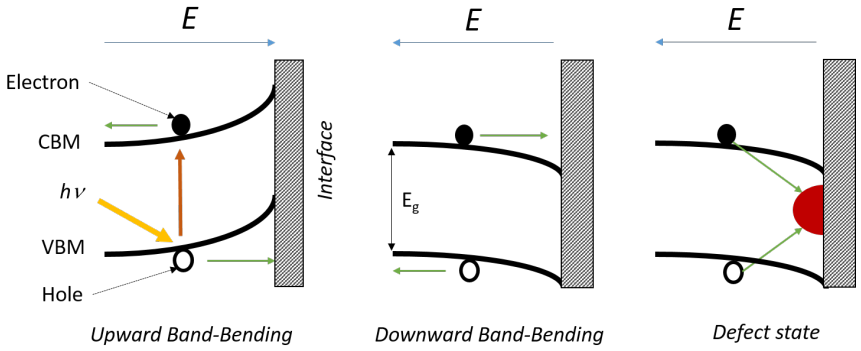

Figure 1.1: Principle of a photo-active material. The separation of the electron-hole pair, resulting from light excitation ($h\nu$), can be obtained under the presence of an electric field (E) near the photo-active interface. CBM and VBM stand for Conduction Band Minimum and Valence Band Maximum, respectively. E_g represents the band gap of the material.

1.3.2 The water-splitting reaction

Once the electron/hole pairs are separated, the energy of the photon can be transferred to sustain electrochemical water-splitting reactions at a specific catalytic site. The production of hydrogen and oxygen happen at the cathode and the anode of the device, respectively. The water-splitting reactions can be decomposed into three steps. First, in alkaline media (pH=14) the adsorption dissociation reaction leads to the formation of hydrogen adsorbate and hydroxide on the cathode side following Volmer reaction [12]:

$$H_2O + e^- + * \rightarrow H_{ads} + OH^- \tag{1.1}$$

Where the star $*$ represents a free adsorbing site for the protons. Second, the adsorbed protons H_{ads} on the cathode are converted to hydrogen gas H_2 either following the Heyrovsky or the Tafel mechanism [12]:

$$H_{ads} + H_2O + e^- \rightarrow H_2 + OH^- + *, \quad \text{(Heyrovsky)} \tag{1.2}$$

$$2\,H_{ads} \rightarrow H_2 + 2*, \quad \text{(Tafel)} \tag{1.3}$$

These two first steps lead to the so-called Hydrogen Evolution Reaction (HER). Then in a third step, after that the hydroxide ions OH^- have diffused from the cathode to the anode, they are transformed to oxygen, following the Oxygen Evolution Reaction (OER):

$$2\,OH^- \rightarrow (1/2)\,O_2 + H_2O + 2\,e^- \tag{1.4}$$

While oxygen may be released to air, hydrogen can be conveniently stored by different means [13] and can be used when requested later. The HER is triggered for potential lower than 0 V vs NHE and the OER for potential above 1.23 V vs NHE. Therefore, the minimum potential to apply between the cathode and the anode of the cell for the water-splitting reaction is 1.23 V.

1.3.3 Studied photo water-splitting device

A wide variety of photo water-splitting structures have been proposed and studied. They can be found in the form of nano-powders or flat surfaces (also called photo electrochemical cell). Generally, the latter can be a tandem cell or can be build upon one or a multiple buried junction(s) and, if necessary, the cell can be biased with an external power supply (Figure 1.2) [7, 14–18]. The illumination can be realized through the solution or from air. Additionally, a large number of possibilities are offered by the materials, which can be chosen as catalyst (e.g.: Pt, RuO_2, IrO_2, Ni-based catalyst, CoO_x, FeO_x) or by the materials for the photo-active layer(s) (e.g.: Si, GaAs, CIGS, $BiVO_4$, Fe_2O_3...). The number of possibilities being wide, a classification to tackle photo water-splitting structures has been proposed through a taxonomy approach by Lewis *et al.* [19].

Photo-electrochemical cell devices with a buried Schottky junction structure designed for the anodic reaction (OER) have been explored in this work. For buried junctions, charge separation and energy conversion are not realized at the same interface and two interfaces compose the photo water-splitting device: 1) a solid-solid interface where electric charge separation occurs and 2) a solid/liquid interface where electrical energy is converted into chemical one with the help of a catalyst. Such configuration enables to study and optimize separately each interface beforehand. The integration of the two interfaces in one device would then lead to the photo water-splitting device.

In this thesis, n-type silicon has been adopted as photo-active material because it is commercially available and also because this is a widely used material for solar energy conversion into electrical energy. Then, NiO has been selected as primary material for both the solid-solid interface and the solid-liquid interface. Indeed, large workfunction value for NiO has been reported [20], which would create large upward band bending (hole accumulation at the surface) on n-type silicon, and also because of the good catalytic properties towards the Oxygen Evolution Reaction (OER) of Ni-based catalysts. Thus, realization, study and optimization of the n-Si/NiO

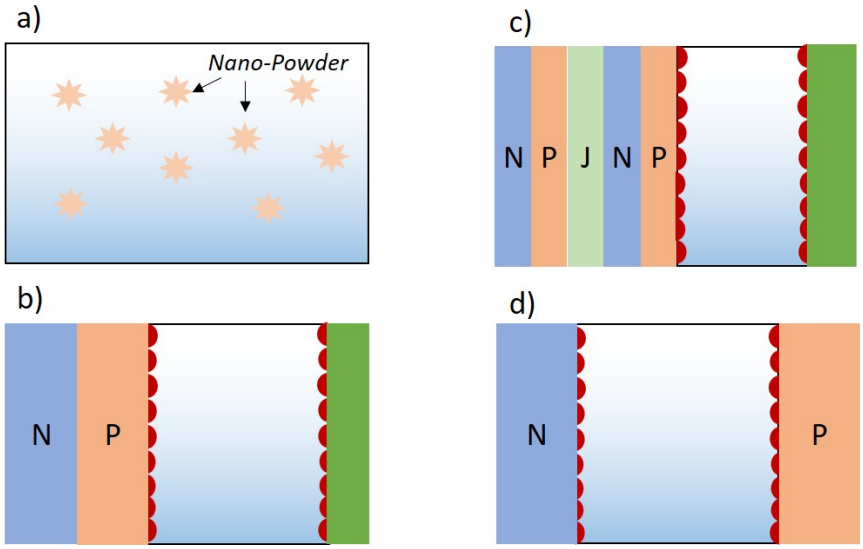

Figure 1.2: Schemes of different photo water-splitting structures. a) nano-powder in solution, b) Photo-electrochemical cell (PEC) structure with a single pn junction, while c) is a pn multi-junction and d) a tandem cell where both electrodes are photo-active. The red layers on both electrodes represent the catalytic layer, the green part a metallic layer. The cells b) and c) would be preferably illuminated from the left but this could be done from the right trough the electrolyte as well.

interface on the first hand and of the NiO/electrolyte interface on the second hand have been carried out separately. Eventually, the two interfaces, once integrated, would form a n-Si/NiO/electrolyte photo water-splitting structure as described in Figure 1.3.

The theoretical maximum output voltage is defined by the silicon band gap which is 1.1 eV [21]. It means that it would, at best, provide a maximum output voltage of 1.1 V, whereas the minimum voltage threshold to conduct water-splitting reaction is 1.23 V [15]. Therefore, the adopted design needs an additional voltage to drive the electrochemical reactions as it cannot be completely autonomous (Figure 1.3). Nevertheless, the design has raised several challenging scientific issues, for which answers would hopefully pave the way to the improvement of sustainable devices for producing clean energy.

1.4 Generality about Nickel Oxide

Nickel Oxide (NiO) is a transition metal oxide (TMO), which can be produced from the oxidation of nickel with oxygen:

$$\mathrm{Ni} + (1/2)\mathrm{O}_2 \rightarrow \mathrm{NiO} \tag{1.5}$$

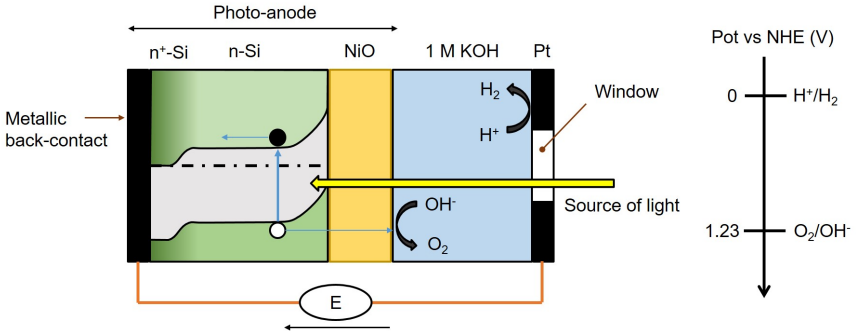

Figure 1.3: Simplified representation of the photo-water splitting structure which motivated this thesis. The cell is represented during working condition under light excitation.

NiO is affordable,[9] robust, stable in alkaline media, and has a melting point of 1955 °C. Its crystallographic structure adopts a compact rock-salt-like structure with a lattice parameter of 4.17 Å. Its density is 6.67 g/cm^3.[10]

As mentioned previously, the choice of NiO as intermediate layer between the photo-absorbing layer and the electrolyte comes from several requirements. Firstly, because of its p-type properties[11] and its large workfunction, NiO could offer adequate band bending if interfaced with n-type silicon, while it can produce a hole selective layer for the transfer of charges from silicon. Therefore, additionally to be studied for creating a rectifying p-n junction with, for instance, n-type ZnO [22] or silicon [20, 23], NiO has been explored as hole transport layer in dye sensitized solar cells [24] in silicon based MIS structure [23, 25], in organic solar cells [26–28], LEDs [29] and perovskite solar cells [30]. Secondly, NiO is stable in strong alkaline solution, where it has been used as protective coating of pn-junctions [31] and also because Ni-based catalyst have been proven to perform well towards the OER. They currently challenge the traditional and expensive, rare earth materials as catalyst for the OER, in particular when impurities are added, for instance iron in nickel hydroxide [32–35].

Additionally, NiO can be used in versatile applications: electrochromic layers [36], gas sensors [37], resistive switching layers for memory applications [38–42], thermoelectric elements [43], electrode materials for Li-based batteries [44], in pseudo-capacitive applications [45–47] and anti-ferromagnetic layers [48].

[9] Metallic nickel is cheap (∼13 US$/kg, LME, 05/04/2019) and large stock are available (∼30 years of production)

[10] `https://en.wikipedia.org/wiki/Nickel(II)_oxide`

[11] one of the rare metal oxide material having a p-type electronic conductivity as for Ag_2O, Co_3O_4 and Cu_2O

It can be seen that NiO can be implemented in numerous fields of applied science. The research carried out during this thesis on NiO properties can hopefully help other fields of research in the understanding of this material.

1.5 Summary

To summarize, the goal of this work is to study a photo-anode based on silicon and NiO to be integrated in water splitting structure for the oxygen evolution reaction. In-depth study of the Si/NiO and the NiO/electrolyte interfaces have been carried out in order to determine bottleneck issues and the leverage of optimization for creating a functional device. In addition, the bulk and the surface properties of nickel oxide have been fundamentally investigated.

First, the electronic charge compensation of defects in NiO thin films according to the preparation, basically the temperature and the oxygen concentration during the thin film growth, have been proposed in Chapter 4, these results are complemented with the Chapter 5 which unveils the origin of the high conductivity of NiO thin films prepared at room temperature, where it is shown that an oxygen-rich secondary phase accumulate at the grain boundaries which can provide conductive paths. The Chapter 6 demonstrates that this oxygen-rich secondary phase is unstable with temperature and over time. This instability can be the underlying mechanism of the electrical ageing in RT-NiO thin films reported in literature

Second, in the aim to bring valuable insights on the NiO/electrolyte interface for further optimization, the growth of (100), (110) and (111) oriented NiO thin films have been attempted. For doing this, as presented in Chapter 7, the relationship between the conditions of deposition and the NiO thin film crystallographic structure deposited on oriented platinum have been explored. Then, the most oriented NiO thin films have been subsequently studied towards water adsorption reaction in vacuum and adsorption reaction in an electrolyte as detailed in the Chapter 8. To continue further the study of the oriented thin films properties toward the electrochemical reactions, in the Chapter 9 oriented thin films have been characterized toward the oxygen evolution reaction. In complement, the systematic characterisation of nano-crystalline non-oriented NiO thin films towards the oxygen evolution reaction have been performed and is presented in Chapter 10.

Third, in order to create a proper Si/NiO solid-state junction, as detailed in Chapter 11, thermal growth of a tunnelling silicon dioxide layer on top of silicon has been optimized and passivation of the prepared Si/SiO_2 samples is proposed by surface exposure to an hydrogen plasma source in atomic mode . The idea being to reduce defect density between the silicon and the nickel oxide in forming a passivated $Si/SiO_2/NiO$ junction. Then in Chapter 11, in-situ XPS measurements have been performed on the Si/SiO_2 structure to determine the potential profile along this interface during the built-up of the space-charge layer in the silicon. This is complemented by the Chapter 13

where electrical characterization of differently prepared $Si/SiO_2/Pt$ junctions are realized. Finally a method to deposit nickel oxide by sputtering on top of the Si/SiO_2 interface which suppress the Fermi level pinning is detailed in the Chapter 14.

CHAPTER 2

Fundamentals

Summary

Along this thesis, Si/NiO and NiO/electrolyte junctions have been studied for being implemented in a photo electrochemical cell. Thus, it is of primary importance to understand the physics ruling these two junctions and what are the important NiO properties, which would tune the quality of the interfaces, and so that would define the performances of the final device.

Therefore, this chapter aims at detailing the theoretical background necessary to interpret the experimental results. It is basically divided into four parts: in a first part, the surface properties of materials will be introduced. This will be followed by a second part about the nickel oxide properties discussed. The third part will deal with the background associated to solid states junction and, finally, in a fourth part, the background associated to solid-liquid interfaces will be presented.

2.1 Surface properties of materials

Inorganic materials can be defined by their Fermi level and their workfunction. For instance, these two features can be used to estimate band alignments of solid-state junctions (see Part 2.3). The Fermi level is associated to the surface and bulk properties of the material, while the workfunction is related to the surface properties of the material only.

2.1.1 Fermi distribution and Fermi level

The electronic structure of a single atom can be described as an ensemble of discrete energy levels, which are filled by electrons according to certain rules: Pauli Exclusion Principles, Hund's rules... As sketched in Figure 2.1, the energy level of one atom has to be filled from the lowest to the highest energy level by electrons. Theoretically, there is an infinite number of energy levels, whereas there is only a finite number of electrons. Therefore, above a certain point, at the outer electronic shell, the energy levels are empty. Electrons at the lowest energy level are close to the nucleus of the atom and have strong interaction with it. On the contrary, electrons from the outer shell have lower interaction with the nucleus. Photon, thermal, or electrical energy can be transmitted to the electrons at any energy level. If one electron is excited enough and find a free energy level, it can jump from one energy level to another. The electrons can be even ejected from the atom (ionized state). For instance, this principle is the basis of X-Ray photoelectron spectroscopy where an intense X-ray energy (1486.6 eV in DAISY-MAT) is used to eject electrons from the inner shell to vacuum (see section 3.3.1).

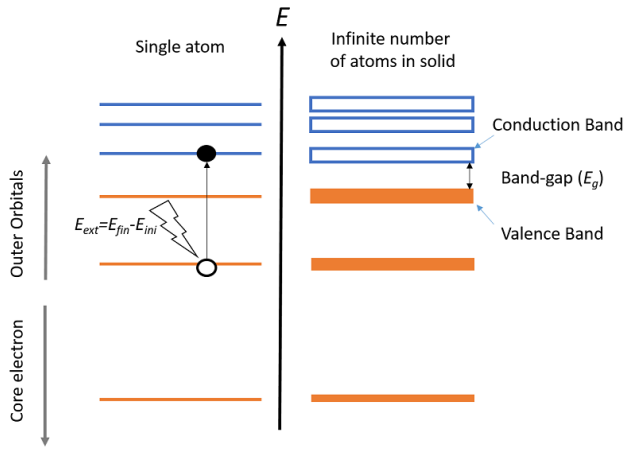

Figure 2.1: Schematic representation of electronic orbitals in the case of a single atom and an infinite number of atoms in a solid.

The electronic structure of a solid can be described by energy bands arising

from the broadening of the discrete energy levels in a single atom. The broadening is due to the orbital overlap of neighbouring atoms in a solid. Thus, discrete energy levels become bands, where the lowest energy bands are filled by electrons as for a single atom. The last band filled by electrons is called the valence band, while the first empty band is called the conduction band. Conduction band and valence band are separated by the forbidden energy gap or band gap (E_g), which corresponds to the minimum energy required to transfer an electron between a filled band and an empty band (Figure 2.1).

The probability of an electron to occupy an energy level is described by the Fermi distribution function [21]:

$$f(E) = \frac{1}{1 + e^{(E-E_F)/k_B T}} \tag{2.1}$$

where E is the energy level of the state, E_F is the Fermi energy (or Fermi level), k_B the Boltzmann constant and T the temperature. If T→0 K, the Fermi function equates to a step function where for states with $E < E_F$ the probability to be occupied by an electron is 1 and for states $E > E_F$, the probability to be occupied by an electron is 0. Therefore, a material with an energy gap at the Fermi level is not conductive. Indeed, charges need free energy levels to be displaced within a band. If all states are already occupied by charges, no charges can move.

However, equation 2.1 shows that the Fermi function broadens with temperature. Thus, at room temperature, the probability to see unoccupied states under the Fermi level and occupied states above increases. Therefore, the probability to obtain partially occupied bands, which can participate in charge transportation, increases (Figure 2.2).

The Fermi level position (E_F) to the valence band maximum is a practical value to estimate the properties of one material. For instance, if the Fermi level lies inside a valence band, little energy is required for the electron to reach an unoccupied state. Such a material has metallic behaviour. If the Fermi level is instead in the middle of the band gap the material is said to be a semiconductor or an insulator depending on the magnitude of the band gap E_g.

2.1.2 Fermi level and minority charge carrier density

In semiconductor materials, a relationship between the density of electrons (n) located in the conduction band and the Fermi level (E_F) is [21]:

$$n = N_c \exp\left(-\frac{E_{cb} - E_F}{k_B T}\right) \tag{2.2}$$

and the holes located in the valence band (p) and the Fermi level (E_F) is:

$$p = N_v \exp\left(-\frac{E_F - E_{vb}}{k_B T}\right) \tag{2.3}$$

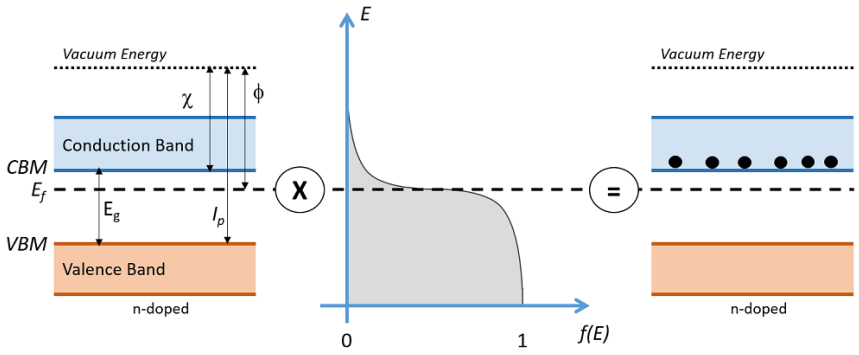

Figure 2.2: General band structure of a semiconductor (left), Fermi distribution in the semiconductor for T> 0 K (middle) and resulting position of free charge carrier (right). The case is taken for a n-type semiconductor of band gap E_g. Work function ϕ, electron affinity χ and ionization potential I_p are also represented.

where N_c and N_v are the effective density of states in the conduction band and the valence band, respectively. E_{cb} and E_{vb} stand for the absolute energy levels of the conduction band minimum and the valence band maximum, respectively. According to equations 2.2 and 2.3, it can be seen that the charge carrier densities in the conduction and the valence band can be tuned according to the Fermi level position in the band gap of the semiconductor. Consequently, the Fermi level position can be an indication of the quantity of the *dominant* charge carrier. For instance, a Fermi level close to the valence band would favour unoccupied states in the valence band and would promote hole transportation (p-type conductivity). Reciprocally, a Fermi energy close to the conduction band promotes occupied states (electrons) in the conduction band and gives rise to electron transportation (n-type conductivity) (see example in Figure 2.2).

Finally, the conductivity σ is the sum of the product of the charge carrier densities (n and p) and their mobilities (μ_e and μ_h) [21]:

$$\sigma = q\,n\mu_e + q\,p\mu_h \tag{2.4}$$

With q the elementary electric charge (the absolute value of the charge of one electron).

2.1.3 Workfunction, Electron Affinity and Ionization Potential

The workfunction ϕ is the activation energy required to thermally remove an electron interacting with the surface of the material as expressed by the Richardson's law:

$$J = A\,T^2\,exp(-\frac{\phi}{k_B\,T}) \tag{2.5}$$

with A the Richardson constant of the material and J the current arising from the thermal electron emission from the surface material to the vacuum. For such electron, the interaction with the surface material is only of electrostatic nature. Therefore, the workfunction is the energy between the Fermi level and the vacuum energy (Figure 2.2). The workfunction can be altered by the presence of surface dipoles (a pair of positive and negative charges distant of few atomic units) or it can be modified by changing the Fermi energy of the material (e.g: by doping) [49].

Other quantities related to the workfunction are the electron affinity and the ionization potential. This is for the former, the distance between the bottom of the conduction band minimum (CBM)and the vacuum energy ($\chi = E_{vac} - E_{cb}$), and for the latter this is the distance between the valence band maximum (VBM) and the vacuum energy ($I_p = E_{vac} - E_{vb}$) [49] (Figure 2.2, left).

2.2 NiO properties

2.2.1 Crystallographic structure and surface termination

nickel oxide adopts a cubic rocksalt crystallographic structure (Figure 2.3, left) with a lattice constant of 4.17 Å. Interplane distances along the (100), (110) and (111) (hkl) coordinate system are 2.08 Å, 1.47 Å and 1.20 Å, respectively. NiO is an anti-ferromagnetic material along the (111) planes (super exchange coupling) [48], for which the Néel temperature is 523 K [50].

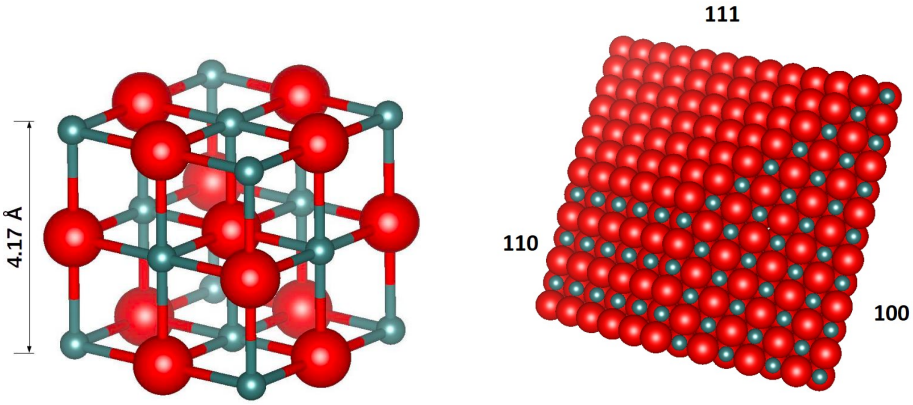

Figure 2.3: Crystallographic representation of cubic NiO structure (left) and surface representation of the 100, (110) and oxygen terminated (111) facets (right). Oxygen atoms are in red and nickel atoms in grey. On the left picture balls are proportional to ionic radius but not on the right picture. The (111) facet is oxygen terminated on the right picture.

Calculated XRD pattern with the software VESTA[1] reveals three peaks, which can be distinctively assigned to the (111), (200) and (220) crystal orientations at 37.32, 43.38 and 63.02°, respectively (Figure 2.4). The XRD PDF cards of NiO provides slightly different values than those calculated with VESTA (Table 2.1). It highlights the uncertainty on the lattice constant of NiO. According to the XRD patterns obtained with VESTA, the (200) peak is the most intense among all and the intensity of the (111) and (220) planes account for 65% and 48% of the (200) one, respectively. Peaks at higher diffraction angles than the (220) peak are found to be weak. Therefore, XRD measurements realized on NiO thin films were constrained to the 20 to 80 ° diffraction angles range.

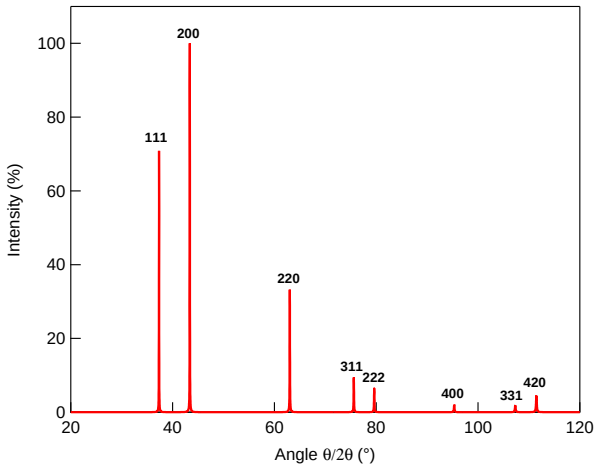

Figure 2.4: Calculated XRD pattern (VESTA) of the NiO crystal.

Growing scientific interest emerges on the properties of oriented NiO surfaces. Nickel oxide crystals can be truncated in three type of facets: the (100), (110) and the (111) (Figure 2.3, right). The (111) facet is the least populated surface with 0.13 atoms/Å^2. The (100) and the (110) facets have 0.23 and 0.16 atoms/Å^2, respectively. The calculated surface energy is the lowest for the (100) facet. Because of the alternating arrangement of charged Ni and O planes along the (111) direction, unreconstructed (111) surfaces are electrostaticaly unstable [51, 52]. In contrast, the (100) and (110) surfaces are non-polar, meaning the electric charge with underlying planes is neutral, while the (111) orientation is polar [52]. The NiO crystallographic properties are summarized in Table 2.1.

The higher surface energy of (110) and (111) facets over the (100) surface could lead to geometrical (100) faceting [53–56]. The (111) surface could be also stabilized by p(2 x 2) octopolar reconstruction [52, 57–59] or by chemical

[1]Visualization for Electronic and Structural Analysis, `http://jp-minerals.org/vesta/`

Table 2.1: Orientation dependent properties summary of nickel oxide. PDF card 47-1049 and 65-2901 have been chosen arbitrarily. The XRD diffraction angles are given for the (200), (220) and (111) in the (hkl) coordinate orientation. Interplanar distances are given as being the shortest distance between two plans. The surface energy of the (111) orientation is given for an unreconstructed surface.

(hkl)-facet	(200)-(100)	(220)-(110)	(111)-(111)
Diffraction angle (VESTA)	43.38 °	63.02 °	37.32 °
Diffraction angle (PDF 47-1049)	43.276 °	63.879 °	37.249 °
Diffraction angle (PDF 65-2901)	43.096 °	63.586 °	37.093 °
Interplane Distance (Å)	2.08	1.47	1.2
Surface atomic density (Å/cm^2)	0.23	0.16	0.13
Surface energy (J/m^2) [51]	1.15	2.77	∞

bonding with e.g. hydroxide [60, 61], or possibly by the presence of nickel vacancies in the film [62]. Contrary to the (100) orientation, hydroxyl groups spontaneously form on the (111) oriented surface when exposed to water [63]. Also, it has been reported that edges or corners between the (111) plan and the (111) reconstructed surface into (100) trigonal facets facilitate water dissociation [64].

The (100) facet is the most stable surface with the lowest surface energy for which the electronic structure is supposed to not differ substantially from bulk NiO. It has been demonstrated (theoretically studied) that a perfect NiO (100) surface is not reactive or very little to oxygen compounds (O^-, O_2^-, O and O_2) [65], CO, H_2 [65] water [63] or methane [66]. The explanation relies on the fact that the lowest excited states are far above the ground state and so would be chemically inaccessible [67]. Thus, water does not interact with lattice oxygen [68]. However, NiO (100) surfaces become reactive if defects are introduced at the surface [63, 65–67]. Also, with NiO (100) single crystal surfaces water co-adsorbs with oxygen near a defective site to form a stable hydroxide (OH^-) [68, 69].

NiO (110) is the least studied surface orientation. The calculated surface energy suggests that it is less stable than the (100) orientation (Table 2.1). Experimentally, the oriented thin film adopts a (100) faceting when prepared at 900 °C [55]. Theoretical works highlighted that NiO (110) orientation might be the most reactive facet towards methane [66], and nano-particles with exposed (110) orientation provide a robust material for energy storage application [44].

2.2.2 Valence band maximum and workfunction

Little is known about NiO surface properties, in particular concerning the NiO workfunction and Fermi level position to the valence band. Nevertheless,

the few articles providing information would suggest that NiO is a high workfunction (5-6 eV) transition metal oxide [20] with a Fermi level position located around 0.4 to 0.8 eV above the valence band [20, 70]. In reality, NiO surface properties depend a lot on the sample preparation and, as it will be seen in Chapter 4, the workfunction and the Fermi level position can be tuned from 5.2 to 4.5 eV and from 1.1 to 0.6 eV, respectively.

2.2.3 Band structure and doping

Electronic structure

The atomic number of nickel is 28, and so the electronic structure is $[Ar]4s^2 3d^8$, with the $3d^8$ orbital being lower in energy than the $4s^2$ orbital. Thus, the oxidation reaction $Ni^0 \rightarrow Ni^{2+} + 2\,e^-$ would see the two electrons from the 4s orbital to be removed away from the nickel electronic shell. Eventually, the Ni^{2+} atoms adopt the $[Ar]3d^8$ electronic configuration.

The electronic configuration of the oxygen atom, with 8 electrons, is $[He]2s^2 2p^4$. An oxygen atom needs two electrons to completely fill the 2p orbital and adopt the electronic configuration of neon: $[He]2s^2 2p^6$.

Therefore, the nickel oxide valence band would be a mixture of Ni $3d^8$ and O $2p^6$ electrons and, according to the literature, the Ni $3d^8$ states are positioned above the O $2p^6$ energy band [70]. The NiO conduction band is seemingly more complicated to tackle. At a first glance, following rules which determine the electron configuration: the conduction band of NiO would be made of the Ni 4s and Ni 4p orbital, but the Ni 3d orbital could also intervene as it can accept up to 10 electrons.

Combining XPS and Bremsstrahlung Isochromat Spectroscopy (BIS) measurements, which can measure the density of states above the Fermi level (E_F), on highly stoichiometric and clean (100) single crystal surfaces, Sawatzky *et al.* [71] identified the Ni4s and the Ni4p energy bands and non excitonic optical transitions between the O 2p energy level and the Ni 4s and Ni 4p bands. In comparing their results with theoretical work, they assigned the Ni $3d^8$ and the Ni $3d^9$ energy levels as forming the maximum of the valence band and the minimum of the conduction band of the NiO, respectively. [2]

Thus, the edge of the valence band is formed by the Ni $3d^8$ band. It would imply that, if the valence band is not totally filled, the NiO would have a metallic behaviour. However, experimentally, the conductivity of pure NiO, meaning without defects or impurities, can be as low as to 10^{13} Ω cm [50] and 10^7 Ω cm at 1 kHz [73]. It turns out instead that pure NiO provides an excellent insulator material. This contradiction has been tentatively explained by the Mott-Hubbard theory asserting that a strong d-d Coulombic repulsion between the Ni $3d^8$ and Ni $3d^9$ would occur [74], forbidding the electrons from

[2] Contrary to the work of Adlers *et al.* [72] where it was assumed this was the Ni 4s energy level forming the bottom of the conduction band.

the Ni $3d^8$ energy band (the top of the valence band) to access at low energy cost the conduction band. Nevertheless, this approach might be unaccurate and/or uncomplete as it will be detailed in the next paragraph.

Charge transfer properties

Zaanen, Sawatzky and Allen [75] evidenced that materials having strong d-d electronic correlation can behave metallic as for NiS. They assumed that the conductivity might be also related to the anion electronegativity and proposed a theory to more completely describe transition-metal compounds. As described in Figure 2.5, in this theory, assuming a charge, which is excited from the $3d^8$ band to, e.g., the $3d^9$ band, two factors are introduced: a correlation factor U (also referred to as Mott-Hubbard gap) related to the energy for the overall reaction required in order that charges are compensated by nickel atoms ($2\,d^n+U \rightarrow d^{n-1}+d^{n+1}$), and a charge-transfer factor Δ, related to the energy if the missing charge in the Ni $3d^8$ orbital is compensated by electrons from the O $2p^6$ energy band ($d^n+L+\Delta \rightarrow d^{n+1}+L^{-1}$, with L the ligand) [75, 76]. Then, it can be said that, if $U< \Delta$, the material is likely a Mott-Hubbard material because electronic transition occurs between nickel d-d bands ($(2\,Ni^{II})\,2O^{-II} \rightarrow Ni^{I}Ni^{III}\,2O^{-II}$) and $E_{gap} \propto U$. On the contrary, if $U> \Delta$, the semiconductor is of charge transfer type ($Ni^{II}O^{II} \rightarrow Ni^{III}O^{-I}$) and $E_{gap} \propto \Delta$ [75, 77]. An intermediate case where $U\sim \Delta$ can be considered and NiO might be part of it [75], though it is widely accepted that NiO is in the charge transfer category [70, 74, 78]. This is supported by STM measurements on the (100) surface where the charge on an atom is primarily distributed over the closest neighbouring atoms, e.g., potential alteration on one nickel atom is distributed over closest oxygen atoms and not on other nickel atoms [79].

Moreover photo-absorption measurements, realized by Powell and Spicer [80], show an absorption edge starting at 3.1 eV and attaining a maximum around 4 to 4.3 eV. Several absorption fringes are visible for photon energies of 4.3, 4.9, 6.1, 7.2 and 8.5 eV. This might be a clue that, during optical transition, the Ni $3d^7$ state remains in its ground state and the hole left in the $3d^8$ orbitals (state denoted Ni $3d^8Z^{-1}$) is stabilized by the ligand L (the oxygen in NiO), for which the charge is reduced by 1 (state denoted Ni $3d^8L^{-1}$), see Figure 2.5.

It is worth mentioning that a band description, where the electronic structure is represented by a continuum of states, is not appropriate to describe charge transfer insulators (Figure 2.5). Also, according to the theory developed by Zaanen *et al.*, for charge-transfer materials, it is expected that the closer the O 2p band to the cationic 3d band the higher the conductivity (the lower the charge-transfer coefficient Δ).

XPS spectra

Because of its charge-transfer nature, nickel oxide exhibits complicated XPS spectra in the valence region and in the Ni 2p region. Most of the peaks are

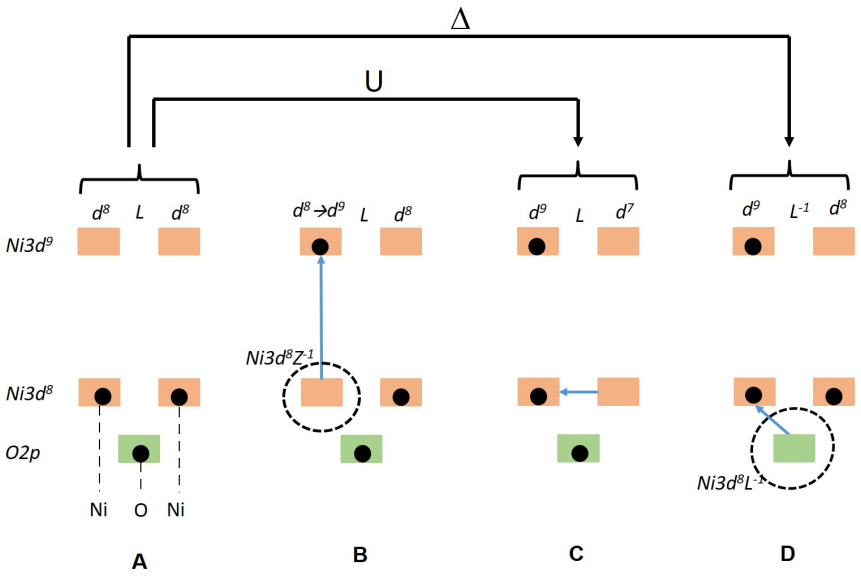

Figure 2.5: Charge compensation mechanism description in NiO crystal in the case NiO would be a Mott-Hubbard insulator (coefficient U) or a charge-transfer insulator (coefficient Δ). The ground state is described by the case A. When an electron is removed from the Ni 3d^8 orbital (case B), it can be compensated by a charge from another Ni 3d^8 orbital (Mott-Hubbard insulator, case C) or from the ligand, in other words, the oxygen O2p^6 orbital (Charge-transfer insulator, case D). The d^{8}L^{-1} state refers to the position of a hole in the ligand valence band after compensation of the hole in the Ni 3d^8 orbital, which can be also denoted as Ni 3d^{8}Z^{-1}.

the result of final state effects. It took several decades to clarify the origin of the different peaks. In the 80's Zaanen *et al.* [75] were the first to introduce a charge transfer coefficient (Δ) to the Mott insulator to take into account charge transition between the O 2p and the Ni 3d energy levels and, for a long time, the valence band edge was defined as originating from Ni 3d^{8}L^{-1} state. In 2008, Taguchi *et al.* proposed that the first transition is instead originating directly from the ejection of an electron from the Ni 3d^8 orbital (but not having an O 2p character). The lone hole in the Ni 3d^8 orbital after the electron transition can be denoted Ni 3d^{8}Z^{-1} (Figure 2.5). In the meantime, the Ni 3d^7 remains in its ground state and is located between 6-10 eV under the Fermi level. The O 2p energy band is rather wide and is shown to be located between 3 and 9 eV under the Fermi level [70, 71]. Eventually, this model could account for most effects and the Ni 3d^{8}L has been found to be actually at higher binding energy compound to the Ni 3d^{8}Z energy level, which forms the edge of the valence band (Figure 2.6).

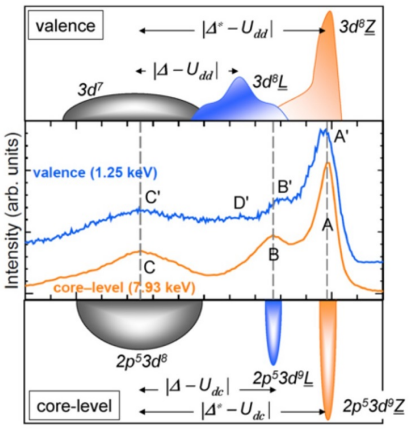

Figure 2.6: Calculated energy states position, under X-ray photoemission, in the valence band (top) and the Ni 2p region (bottom). The simulations match relatively well with the experimental results obtained on NiO exposed to a X-ray of 1.25 keV (middle). Taken from Taguchi et al. [81].

Doping in NiO and charge compensation

nickel oxide can be doped intrinsically by nickel vacancies (V''_{Ni}) [82, 83] or by extrinsic impurities as e.g. Na [43] and Li [84], which substitute for nickel and provide negative defects (e.g.: Li'_{Ni}). NiO doping leads to the creation of negative charges, which need to be compensated by positive charges for charge neutrality (holes, Ni^{3+} or O^-) [83].

Several articles report the O 2p character of holes in doped NiO [74, 84, 85]. This is rather counter-intuitive, as, at first sight, it could be thought that holes would prefer to be located at the edge of the valence band maximum, which is defined by the Ni $3d^8$ states.

It should be mentioned that X-Ray Absorption in V''_{Ni} or Li'_{Ni} doped NiO evidences the presence of an extra electronic state at 529 eV, which is not observed in pure *"defect-free"* NiO samples (Figure 2.7). The presence of this feature would be a fingerprint of larger hole densities [86] as higher conductivities are attained in Li doped NiO and intrinsically V''_{Ni} doped NiO when prepared at room temperature [83, 84, 86–88] (Figure 2.7). The nature of the hole associated to this specific feature at 529 eV has lead to a controversy. Whereas Kuiper *et al.* assigned it as having O 2p character, it was assigned to Ni 3d and by extension to the presence of Ni^{3+} by others authors [83, 87, 88] (Figure 2.7). However, the opponents of the formation of Ni^{3+} in NiO can assert that the energy required for ionizing Ni^{2+} to Ni^{3+} would be too large as the d^7 state is ∼9 eV below the Fermi energy and so is hardly accessible [70]. Also, dopants in an ordered NiO structure would be in an octahedral position surrounded primarily by oxygen atoms. The charge transfer nature of NiO

would favour the interaction between the dopant substituting to a cationic site and the closest oxygen neighbour as it could be suggested by STM measurements on the (100) surface [79]. Therefore, the charge compensation of the negative charge could be realized through the distribution of a positive charge over the oxygen atoms surrounding the defect position in the lattice. In such a case, it would mean the feature observed by X-Ray Absorption is related to a hole having primarily O 2p character.

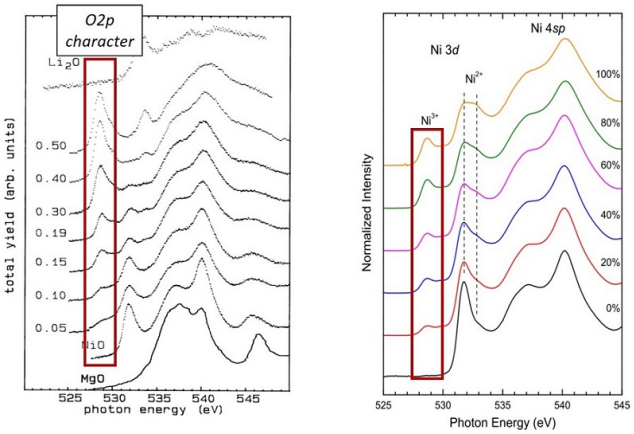

Figure 2.7: XAS measurements of the O-K edge for Li doped NiO reported by Kuiper et al. [84] (left), for NiO thin films prepared at room temperature reported by Mossanek et al. [87] (right). The former assign the feature highlighted by the red box to holes having O 2p character while the latter to the formation of Ni^{3+}. The intensity of the feature increases with both the Li doping concentration (left) and the oxygen concentration (right).

Charge compensation in NiO is not very clear in the literature. In this work, a more detailed discussion about defect compensation mechanism in NiO is available in chapter 4.

2.2.4 Optical properties

Introduction

Optically, a wide band gap value (3.6 – 4 eV) has been reported for NiO. However, two cases must be addressed: optical properties of pure NiO on the one hand and doped NiO either with extrinsic defects (Li, Na) on the other hand. The case of the intrinsic doping by nickel vacancies (V''_{Ni}) is discussed in Section 4.3.6.

Pure NiO

The optical band gap of NiO thin films prepared at high temperature (> 200 ° C) varies between 3.5 and 3.9 eV [89–91]. No reliable data has been found

about the transmittance value. In most cases transmittance is not corrected according to the thin film thickness, but value in the 70-100 % can be roughly estimated.

Photoluminescence experiments using lasers emitting in the UV wavelengths evidence a near band edge excitonic emission at 3.25 eV [92]. This excitonic transition might originate from transitions between the Ni $3d^8$ orbital (the edge of the valence band) to a sharp band under the conduction band [92]. Also an absorbing feature, which is not an excitonic state is found at 3.5 eV [92]. Excitonic transitions might be more prominent for recrystallized NiO and it could be assumed that such transitions can be associated to low defective NiO material [93]

Finally, according to the information provided above and in Section 2.2.3, a schematic of the band structure of NiO prepared at high temperature has been proposed in Figure 2.8 (left).

Li doped NiO

Lithium doped NiO prepared at high temperature display a decrease of the transmission with doping, while two features at 1.1 and 2.2 eV, respectively labeled α and β, emerge in the optical band gap [86]. The α and β features have been assigned to electronic transitions between electrons from the Ni $3d^8$ and the O $2p^6$ band to an energy level where holes are present (Figure 2.8, right). The energy level of holes is localized in the middle of the NiO energy gap [86]. The α and β transitions would be responsible for the darkening of highly doped NiO thin films.

2.2.5 Electrical properties

Introduction

Pure NiO resistivity, meaning without defects or impurities, can reach up to 10^{13} Ω cm [50] and 10^7 Ω cm at 1 kHz [73]. Conduction is characterized by a thermally activated mobility (small-polaron hopping) [73, 86] where charges are trapped in a well of 1.9 eV [73]. Hole transport by small polaron hopping might involve that the increase of conductivity in NiO, when doped, is not only due to an increase in charge carrier concentration but also to an increase in the mobility by lowering the activation energy over the barrier [73].

Another way for tackling the issue would be to imagine a charge in the NiO structure. This one is bound to travel alternatively from cationic to anionic sites. So a hole would be *transferred* between the O $2p^6$ and the Ni $3d^8$ electronic states [74]. This representation is formalised through the Correlated Barrier Height (CBH) model.

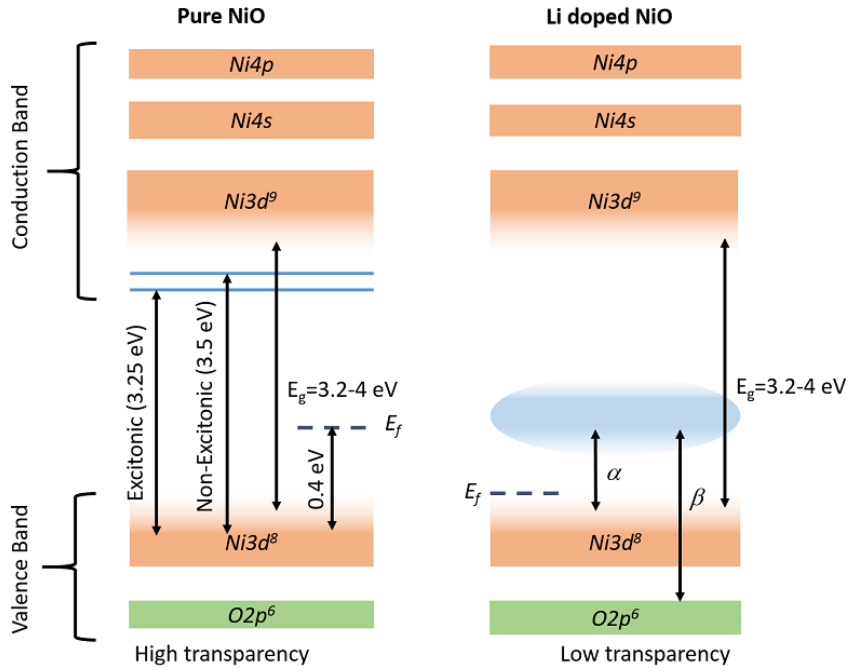

Figure 2.8: Nickel oxide band structure according to optical measurements found in the literature for pure NiO and Lithium doped NiO [70, 71, 86, 89–92, 94–96]. The Fermi level position in pure NiO has been taken from Hüfner [70].

Small polaron hopping, the CBH model

As explained before, the mobile charges in NiO (holes) are transferred continuously from $O\,2p^6$ to $Ni\,3d^8$ bands during electrical displacement. Therefore, the charges have to overcome a potential barrier and this can be done with the help of thermal energy in the form of a phonon. The addition of the energy of the phonon to the charges (hole) produce what is called a polaron. Thermal excitation can be provided from crystal vibrations. Thus, polaron induce a crystallographic distortion over its neighbouring atoms. The conductivity (σ) for a thermally activated small polaron hopping in a n-type material is given by [97, 98]:

$$\sigma(T) = e\, n\, \mu(T) \tag{2.6}$$

with e the absolute charge of an electron, n the electron density and $\mu(T)$ the temperature dependant charge carrier mobility. It means the increase in conductivity with temperature does not arise from an increase of charge carrier concentration but rather from an increase of the mobility. Temperature activation of the mobility follow an Arrhenius law and equation 2.6 can be

explicitly written as being [97]:

$$\sigma(T) = \frac{\sigma_0}{T} \exp\left(-\frac{E_A}{k_B T}\right) \tag{2.7}$$

Where σ_0 is a temperature-independent pre-factor and the activation energy E_A is basically the required energy for the charge carrier to overcome the barrier between two energy wells (Figure 2.9). The activation energy for polaron hopping can be decomposed into two terms: the polaron binding energy E_p and the transfer integral J, which is the resonant energy of the charge when it jumpse from one energy well to another [97, 99]. The relationship between E_a, E_p and J being:

$$E_a = \frac{1}{2}E_p - J \tag{2.8}$$

Therefore, the conductivity in NiO is not necessarily related to the Fermi level position in the energy gap of nickel Oxide.

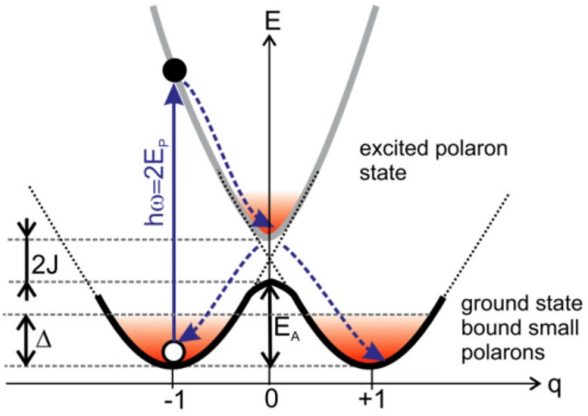

Figure 2.9: Schematic description of the polaron hopping mechanism. A polaron in the ground state is trapped in an energy well (position -1 and +1). If thermal energy is brought (phonon, energy E_p), the charge reaches an excited state and can be transfered to another energy well (transfer integral J). Taken from Mildner et al. [97].

Finally, assuming that the charge carrier density is constant over the temperature range, the activation energy for small polaron hopping can be determined as being:

$$E_A = -k_B \frac{d\ln(\sigma T)}{d(1/T)} \tag{2.9}$$

2.3 Solid state junction

During this thesis, Schottky contacts have been studied primarily by in-situ XPS and also were characterized electrically. Basically, the Schottky contacts

were obtained by depositing a contact material (Pt, NiO) onto differently prepared Si/SiO_2 surfaces. The Schottky junctions are relatively easy to fabricate and could find application in solar cells or in rectifying junctions.

2.3.1 Principles

In the absence of an external electric field, when two materials are contacted, the Fermi energies of the two materials have to align (the electron electrochemical potential is the same everywhere). But, because of the difference in workfunction of each materials, the electrons are attracted to, and would be appealed to flow to the material having the highest workfunction. However, the electrons can not flow indefinitely without electron compensation on the depleting side (e.g.: with a source of electron such as a generator) or a change in the material structure (e.g.: O^- migration, electrochemical reaction).

Thus, in solid-state Schottky junctions, an electric field opposing the flow of charges arises in the semiconductor. For instance, if the workfunction of the semiconductor is higher than that of the metal, electrons migrate from the metal to the semiconductor. Then, the semiconductor becomes negatively charged near the surface and electronic bands are bend downward (accumulation mode in Figure 2.10). Inversely, if the workfunction of the metal is higher than that of the semiconductor, electrons from the semiconductor flow to the metal. Positive charges remain at the semiconductor interface and electronic bands in the semiconductor are bend upwards (depletion mode in Figure 2.10). The accumulation/depletion of charges in the semiconductor leads to the formation of an electric field E, which can be obtained by solving the Poisson equation [21]. In a first assessment, the barrier height of n-type semiconductor can be assumed to follow electron affinity rule [100]:

$$\phi_b = \phi_m - \chi_{sc} \tag{2.10}$$

The mechanism leading to a Schottky junction might be simple, but the interface between the two materials is often accompanied by trapped charges, arising from the imperfect crystallographic structure at the transition. In reality, the contact between a semiconductor and a metal gives rarely the desired junction.

2.3.2 The Fermi level pinning

It has been observed experimentally that the band alignment at a semiconductor/metal junction is not absolutely driven by the workfunction difference of the two materials. Instead, the energy bands often stick to a fixed position, called Fermi level pinning. This is particularly strong for covalent III-V and the elemental semiconductors (Si, GaAs, CdTe, InP). Such a Fermi level pinning is not necessarily found in II-VI chalcogenides and oxide semiconductors [100, 101].

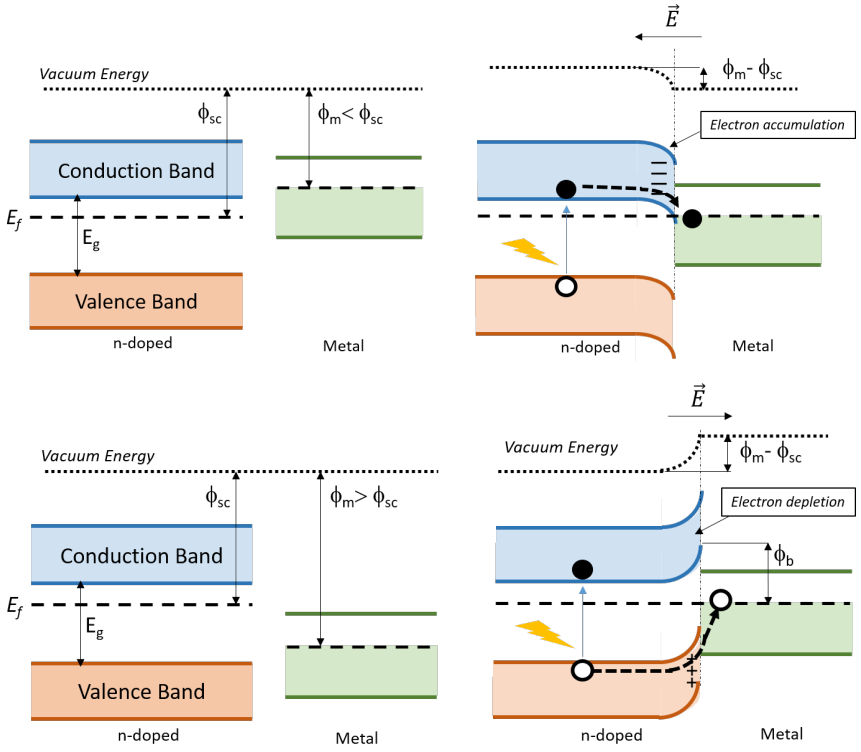

Figure 2.10: Top: Schottky contact leading to the accumulation of negative charges near a n-doped silicon surface. As the semiconductor workfunction is higher than the metal one, negative charges are attracted and move to the semiconductor. Negative charges accumulate in the n-doped silicon. Bottom: Schottky contact leading to the depletion of negative charge near a n-doped silicon surface. As the metal workfunction is higher than the semiconductor one, negative charges are attracted and move to the metal. A positive charge is left behind in the n-doped silicon. In both cases, under illumination, charge separation is generated by the electric field created in the silicon.

The Fermi level pinning arises from the ionization of defects, which can be either donors or acceptors and which have a certain dispersion in the band gap of the semiconductor. The ionization of the defects occur at a certain energy level referred as the charge neutrality level (CNL). At a Schottky contact, the defects are generally found at the semiconductor/metal transition where they can be created because of non-compensated bonds (also called dangling bond) or chemical reactions at the transition.

In the presence of defects at the interface, the effective barrier height in the semi-conductor (ϕ_b) can be estimated as being a combination of the electron affinity rule (Equation 2.10) and the energy position of the charge

neutrality level (ϕ_0) [100] :

$$\phi_b = S = (\phi_m - \chi) + (1 - S)\,(E_g - \phi_0) \tag{2.11}$$

with E_g the band gap of the semiconductor. S is *an index of interface behaviour* and can be referred to as a pinning factor as it accounts for the degree of pinning to the charge neutrality energy level (ϕ_0) of the barrier height (ϕ_b). For instance if S=0, then the semiconductor is totally pinned by interface states ($\phi_b = E_g - \phi_0$), whereas for S=1 the barrier height ϕ_b at the interface is driven by the workfunction difference between the semiconductor and the metal as $\phi_b = \phi_m - \chi$ as for equation 2.10. The factor S has been empirically determined for intrinsic interface states as being [100]:

$$S \approx \frac{1}{1 + 0.1(\varepsilon_\infty - 1)^2} \tag{2.12}$$

Quantitative considerations show that a surface state density as low as $\sim 10^{12}$ cm^{-2} is sufficient to result in Fermi level pinning on standard photo-active materials (Si, GaAs) [101]. Lower interface trapped defect density is necessary to reduce the Fermi level pinning in the silicon side. To do so, a thin insulating layer can be added between the semiconductor and the metal.

2.3.3 The metal-insulator-semiconductor Schottky junction

Si/SiO_2 based structure

In order to reduce defect states at solid-state Schottky junctions, a thin insulating layer can be inserted between the semiconductor and the metal. The consequence would be a Fermi level depinning [102]. This concept has been successfully implemented in metal insulator semiconductor (MIS) structures for complementary metal oxide semiconductor (CMOS) based applications and for solar cell applications. The insulator layer is, in general, a wide band gap material (SiO_2), or a high-permittivity oxide (e.g.: HfO_2, ZrO_2) [103]. In silicon based devices, silicon dioxide is the most used insulator layer as it can be easily grown thermally and it provides an excellent low interface defect density particularly after hydrogen passivation [104–106]. In the next parts will be introduced an overview of the literature about the intrinsic defects which can be found in an amorphous silicon dioxide, in hydrogenated silicon and at the Si/SiO_2 interface. It should be mentioned that, in this thesis, the bulk semiconductor, being a silicon single crystal, is supposed to be a defect free structure.

Defects in a-SiO_2

Thermal SiO_2 grown on silicon is amorphous [107] and different defects can develop in it.

Oxygen vacancies are the most abundant defects in SiO_2 [108]. a-SiO_2

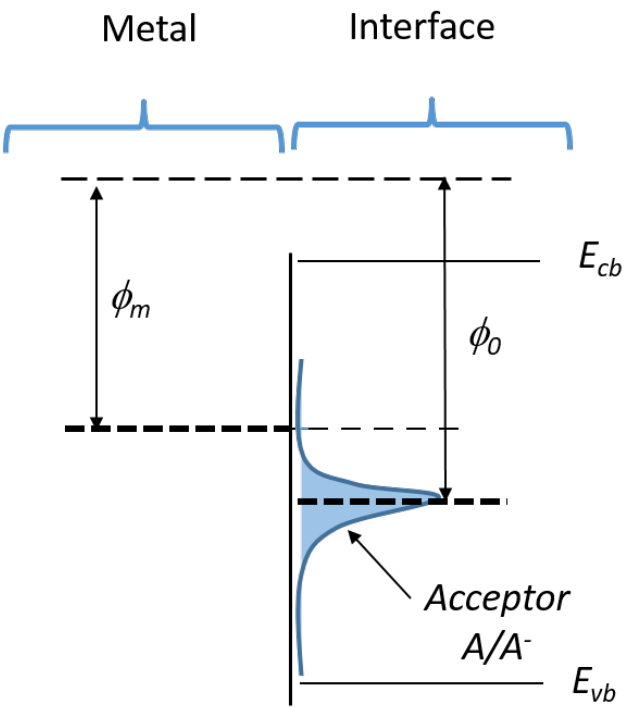

Figure 2.11: Sketch of a defective metal/semiconductor interface. A low workfunction metal interact with energy states located in the semiconductor band gap (defined by E_{vb} and E_{cb}). The filling of the acceptor state (A) leads to the formation of a net negative trapped states. If the density of defects is high, then the barrier height (ϕ_b) in the semiconductor is determined by the charge neutrality level (ϕ_0) where the transition A/A^- occurs. Otherwise the barrier height (ϕ_b) will be a combination of the metal workfunction (ϕ_m) and the charge neutrality level of the interface states (ϕ_0) as in equation 2.11. Ideally, in the absence of defects, the barrier height (ϕ_b) is defined by the metal workfunction (ϕ_m).

crystallographic structure would be stabilized in its neutral state by bridging bonds between the silicon atoms (Si-Si). DFT work has shown that, if a hole is added to the network, the bridging silicon bond can lead to the formation of E_γ and E_δ centers (Figure 2.12). For the former, the addition of holes would create a dipole in the lattice material, when the latter are stabilized by a non-localized electron (lone electron) shared between the two silicon atoms [108].

Also, when exposed to air, or during the SiO_2 growth process, *interstitial oxygen* can be found in the amorphous structure [109] and it can adopt two configurations [109–111]:

- the peroxy linkage (POL) position where the interstitial oxygen is found

between a silicon atom and an another oxygen atom:

$$\equiv Si - O - O_i - Si \equiv \tag{2.13}$$

- the oxygen bridging bonded (OBB) position where the interstitial oxygen is bonded onto another oxygen atom only:

$$\equiv Si - \overset{\overset{O_i}{|}}{O} - Si \equiv \tag{2.14}$$

Chen *et al.* [111] reported in their DFT calculations that such configurations can bring numerous energy levels for trapped states. Interestingly, the OBB defect has the particularity to convert into a Peroxy Radical (POR) defect structure where the bond between ≡Si-O is broken when exposed to irradiation (X-Ray) [111]. In the POR structure, the silicon atom would be bonded by three covalent pairs only to the silicon dioxide structure.

Defects in silicon

Intertistial hydrogen in silicon can produce a donor (H^0/H^+) or an acceptor (H^-/H^0) state. The acceptor state (H^-/H) and the donor state (H/H^+) are, respectively, situated 0.62 eV and 0.16 eV below the conduction band of silicon [112]. However, an hydrogenated silicon material in the case of an silicon dioxide overlayer might require extreme condition to be obtained as atomic hydrogen (H^0) would react spontaneously to produce charged states (H^+ or H^-), which would have a lower diffusivity [106]. For instance, hydrogenation of silicon can be promoted at very high temperature (900-1300 °C) where the sample is subsequently quenched to room temperature to be studied. *Interstitial hydrogen* in silicon can be also obtained at room temperature with specific experimental apparatus which has been named "hole-stimulated dissociation of phosphorus-hydrogen (PH) complex" [112], which is to say that it is not necessarily straightforward to implant such defects in silicon. Therefore, although possible, the formation of *interstitial hydrogen* site in silicon has been considered as unlikely in this thesis as the exposition of the Si/SiO_2 surface to the hydrogen plasma was made at 350 °C (see details in Section 3.2.4).

Defects at the Si/SiO_2 transition

In the late 90's, research endeavoured at understanding the chemical and electronic structure of the Si/SiO_2 transition with the aim to prepare the path for the upcoming aggressive downscaling of the SiO_2 thickness layer for electronic purposes. It has been found at this time that, contrary to the mainstream comprehension, when thermally grown at elevated temperature (< 950 °C) [107] the Si/SiO_2 transition is abrupt and is only few atomic layers thick (about 1-2 ML) [116]. The transition has an astonishingly low defect density with less than one defect for 10^4 interface atoms [107]. Also, no specific strain would result from the transition from a well ordered silicon

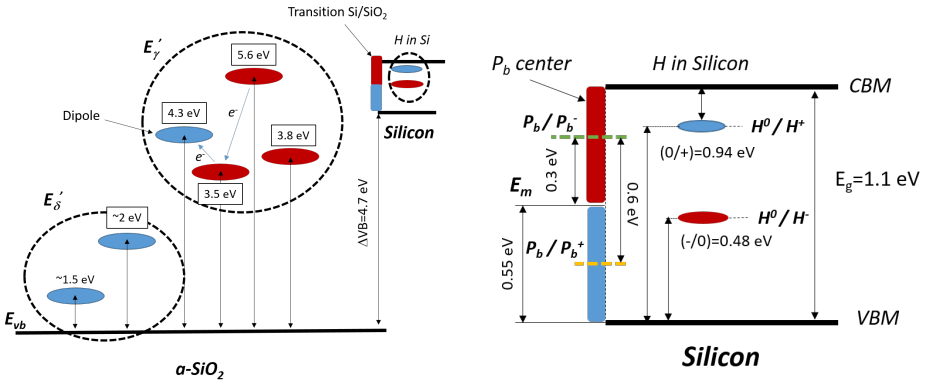

Figure 2.12: Left: Defect position at a-Si/SiO_2 interface, the plot emphasize the defects in the amorphous silicon for oxygen vacancies. Right: insight on defective states at the Si/SiO_2 transition (P_b centers) and, although very unlikely in the condition adopted along this thesis, the case of interstitial hydrogen in the silicon. In red are acceptor levels while blue are donor levels. The green and orange dotted line are imaginary Fermi positions either it is in the upper half or the lower half of the band gap, respectively. The schematic is drawn according to the literature [106, 108, 112–115]. The energy levels of interstitial oxygen are not provided in the literature.

crystallographic structure to an amorphous SiO_2 layer [107, 116]. The defects located at the interface are defined as being a trivalent silicon atom bonded to three underlying silicon atoms [114, 115] and is labelled P_b center [114]. The P_b center properties can depend on the silicon crystal termination as different P_b centers were found on (111) or (100) oriented silicon surface [115]. P_b centers are amphoteric. In the lower half of the band-gap the P_b center is donor-like ($P_b \rightarrow e^- + P_b^+$) while if the Fermi level is in the upper half of the silicon band-gap, the P_b center is an acceptor ($P_b + e^- \rightarrow P_b^-$). Such defect pins the barrier height 0.5 eV above the Fermi level for as-prepared Si/SiO_2 and UHV-transferred samples [117]. The P_b center can be removed to a certain extent by hydrogen passivation [117]. The density (D_{it}) of P_b interface states has been electrically determined to be in the 10^{10} to 10^{12} $cm^{-2}eV^{-1}$ range [114].

Hydrogen passivation

Surface passivation of the Si/SiO_2 interface can be obtained with:

- the so-called *Alneal* process. First, atomic hydrogen is produced by the reaction of alumina, evaporated on the silicon dioxide, and adsorbed water molecules on the surface and, secondly, the sample is annealed for 20 mins at 400 °C to activate the passivation [104, 118]

- the forming gas annealing (FGA) process where the sample is annealed in a reducing atmosphere (H_2:N_2 mixture) at 400 °C in a furnace [119, 120].

- atomic hydrogen generated by a plasma source where hydrogen is used as gas [121–124]. For such process, although this is not very clear, higher temperatures might be benefical to passivate the sample surface. Charge carrier life-time has been reported to be 500 μs on passivated Si/SiO_2 surface by atomic hydrogen [122].

Addition of an another dielectric layer on the SiO_2 surface

To increase interface quality, it has been reported that the addition of a second dielectric layer, as e.g. Al_2O_3, on top of the Si/SiO_2 structure can be advantageous [120, 125–127]. For instance, the addition of an alumina (Al_2O_3) layer on top of SiO_2 seems to provide substantial improvement in the interface states density, built-in voltage (Fermi level depining) and charge carrier life-time [120, 125–127]. However, the stoichiometry and the structure at the Si/SiO_2 interface should not be drastically modified by the addition of a dielectric layer on top. The defect states in SiO_2 should also still exist and not vanish when alumina is deposited on top as it can be simply summarized.

The literature on bi-layer dielectric interface would suggest that a dipole arises at the SiO_2/Al_2O_3 interface [128–130]. An interface dipole can be defined by two parameters: the distance between the two charged layers and the amount of charges Q of one pole [130]:

$$\mu = Q\,d \tag{2.15}$$

At the SiO_2/Al_2O_3 interface, the dipole vector $\vec{\mu}$ is represented pointing outside the SiO_2 layer, with the negative pole in the silicon dioxide and the positive pole in alumina as a result of oxygen migration from the alumina to the silicon dioxide layer [131]. The direction of the dipole can arise from chemical consideration as for the oxygen areal densities [128], dopant electro-negativity or ionic radius of the species involved at the interface [130].

Electrical interaction of defects with the surrounding

Electrically it has been reported that two types of defects can affect the performance of the device, especially when transient currents are used. For instance, for the Si/SiO_2 interface, the defects are:

- *Interface trapped charges* Q_{it}, which are found at the transition between the silicon and the silicon dioxide and can be positively or negatively charged. They are in electrical interaction with the silicon [132] and can be charged or discharged according to the interface potential. Most of the interface trapped charges can be suppressed by surface passivation with atomic hydrogen [132]. These interface trapped charges might be associated to the so-called P_b center detailed in Section 2.3.3.

- *Fixed oxide charges* Q_f are located near the Si/SiO_2 transition and are positively charged. Contrary to *interface trapped charges*, they are not interacting electrically with the silicon. The contribution of Q_f are likely minor for very thin dielectric layers [132], in particular a potential drop of

1 mV through a 2.5 nm dielectric layer would require up to 10^{16} charges per cm^3 and their density might be substantially reduced by hydrogen plasma passivation and large annealing temperature ($\sim$ 1000 °C) [132]. The fixed oxide charges might be related, to a certain extent, to the defects produced in bulk silicon dioxide layer as detailed in Section 2.3.3.

For the structure studied in this thesis, only interface trapped charges (Q_{it}) are considered to have a significant impact on the performance of the devices.

2.3.4 The electrical behaviour of Schottky junctions

Basically, the electrical behaviour of the Schottky junctions are governed by the ther-mionic emission of electric charges over the barrier height ϕ_b in the silicon side (Figure 2.10). Two cases can be distinguished in the following part: the theory for a Metal-Semiconductor (MS) Schottky junction and the theory when a thin insulating (dielectric) layer is inserted as for Metal-Insulator-Semiconductor (MIS) Schottky junctions. In this thesis, the electrical characterization of the junctions was performed, on the one hand, by current-voltage measurements (direct current) and, on the other hand, by capacitance-voltage measurements using impedance spectroscopy (transient current) in order to extract information about the junction properties (ϕ_b, Defects). Deeper insights about the transient current measurements for MIS Schottky junctions are detailed in Chapter 11 as this case needs to be detailed and compared to the experimental results.

IV curves

For an ideal Schottky junction, the charge flow is controlled by the thermionic emission of charge carriers over the barrier height ϕ_b formed on the semiconductor side. Charges are flowing from the semiconductor to the metal ($j_{SC\rightarrow M}$), while a reverse current is opposing it ($j_{M\rightarrow SC}$). In thermodynamic equilibrium both currents annihilate, but in the presence of a bias voltage (V_g), it is possible to favour one against the other. Thus, the current-voltage relationship in a MS Schottky contact can be written as being [21]:

$$j_{total} = j_{SC\rightarrow M} - j_{M\rightarrow SC} = j_0 \left(e^{\frac{qV_g}{\eta k_B T}} - 1 \right) = A^* T^2 e^{-\frac{\phi_b}{k_B T}} \left(e^{\frac{qV_g}{\eta k_B T}} - 1 \right) \tag{2.16}$$

With A^* being the effective Richardson constant taken approximatly as 120 $\frac{A}{cm^2 K^2} . \frac{m^*}{m_e}$ with $\frac{m^*}{m_e} \sim 1$ in silicon. ϕ_b is the barrier height defined by $\phi_b = qV_{bi} + (E_{cb} - E_F)$ where V_{bi} is the built-in voltage. η is the ideality factor of the diode. For a defect free MS Schottky junction, the current is driven by diffusion of charge carriers and the ideality factor is η=1. When the charge carrier transport is controlled by recombination-generation at the interface, the diode ideality becomes η=2. Eventually, if both currents are encountered, η takes a value between 1 and 2, which is often the case practically [21, 133].

The barrier height ϕ_b can be derived from the value of the current j_0 measured either in reverse bias or by extrapolating in the forward potential,

the IV curve on logarithmic scale to the Y-axis (Figure 2.13). The value of j_0 being theoretically equal to:

$$j_0 = A^* T^2 e^{-\frac{\phi_b}{k_B T}} \tag{2.17}$$

the barrier height at the interface can be derived as:

$$\phi_b = -k_B T \ln\left(\frac{j_0}{A^* T^2}\right) \tag{2.18}$$

Typical IV curves are displayed in Figure 2.13, where j_0 is provided for different built-in voltage V_{bi} and diode ideality factor for n-type silicon, where the conduction band E_{cb} is about 0.2 above the Fermi level.

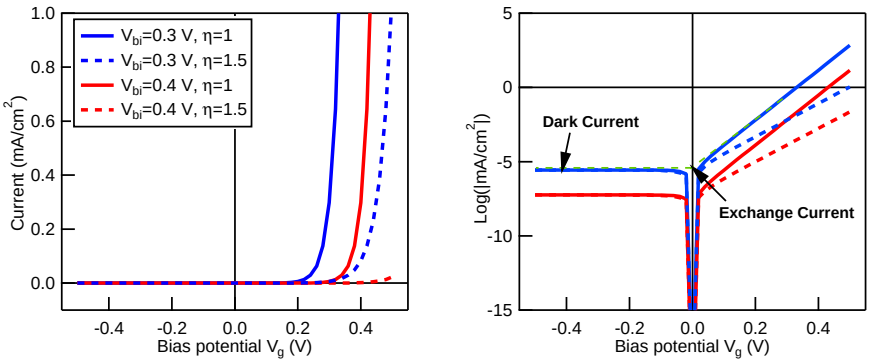

Figure 2.13: Theoretical IV curves: linear (left) and logarithmic (right) plot. The plots are realized for junctions having a built-in voltage of 0.3 and 0.4 V, and a conduction band position to the Fermi level of 0.2 eV. It can be seen that the deviation (η=1.5) from a perfect diode (η=1) leads to a slower increase of the current with increasing bias potential V_g.

The equations introduced above are valid only for a metal/semiconductor Schottky junctions. To take into account the tunnelling dielectric layer as for the MIS structures studied along this thesis, a tunnelling probability (τ_n) has to be introduced in equation 2.16. According to Hanselaer *et al.* [134], in the absence of light photo-excitation, the equation for MIS Schottky junctions is:

$$j_n = \frac{A^* \tau_n T^2}{1 + \frac{\nu_R}{\nu_D}} e^{-\frac{\phi_B}{k_B T}} \left(e^{\frac{q V_g}{\eta k_B T}} - 1\right) \tag{2.19}$$

With τ_n comprised between 0 and 1, ν_R and ν_D are the recombination and the diffusion velocity, respectively. For low recombination velocity, $\frac{\nu_R}{\nu_D}$ is negligible and can be considered ~ 0. Eventually, the barrier height in a tunnelling MIS structure is equal to :

$$\phi_b = -k_B T \left(\ln\left(\frac{j_0}{A^* T^2}\right) - \ln\left(\tau_n\right)\right) \tag{2.20}$$

Equation 2.20 shows that determining the barrier height in the silicon is not straightforward. It requires to estimate or to measure the tunnelling probability (τ_n) beforehand. If this is not taken into account, the barrier height in the tunnelling MIS structures can be over-estimated. Moreover, according to the equation 2.20, it could be expected that the addition of another tunnelling dielectric material on top of the tunnelling SiO_2 would reduce the measured exchange current because of a decrease of the tunnelling probability τ_n and not necessarily because of an increase of the barrier height. Therefore, to distinguish the tunnelling probability from the built-in voltage is difficult based on IV measurements.

Mott-Schottky plots

At a MIS structure, using small AC signals (e.g.: Impedance Spectroscopy), the capacitance (C_{scr}) arising from the addition of charges ($\widetilde{Q}$) at the edge of the space charge region in the semiconductor can be measured and formalised as following:

$$\widetilde{Q} = C_{scr}\widetilde{U} \tag{2.21}$$

Also, the capacitance due to the space charge region formed in the semiconductor can be treated as a standard parallel plate capacitive element:

$$C_{scr} = \frac{\varepsilon_{Si}\varepsilon_0}{d_{scr}} \tag{2.22}$$

With ε_0 being the vacuum permittivity, ε_{Si} the relative permittivity of silicon

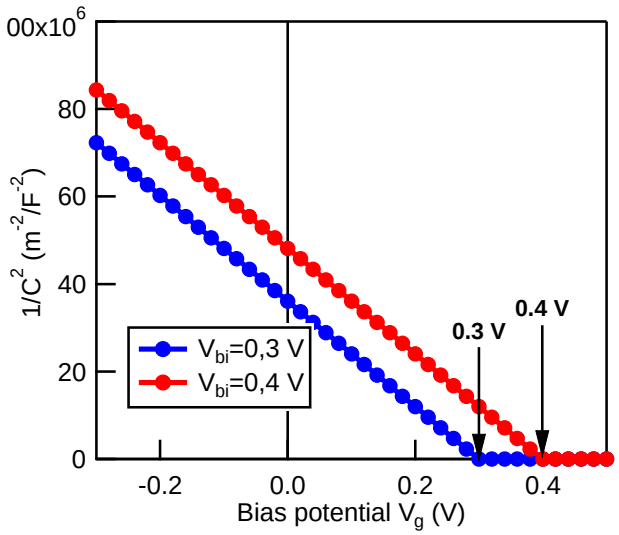

Figure 2.14: Theoretical Mott-Schottky plot for a perfect semiconductor/metal junction for two different built-in voltages. The intersection with the x-axis of the linear part in reverse bias provides the value of the built-in voltage (V_{bi}).

and d_{scr} the thickness of the space charge region. Solving Poisson's equation in silicon, the thickness of the space charge region d_{scr}, can be obtained by the following equation in n-type silicon:

$$d_{scr} = \sqrt{\frac{2\varepsilon_{Si}\varepsilon_0(V_{bi} - V_g)}{q\,N_d}} \tag{2.23}$$

With N_d is the donor density and q the absolute charge of an electron. Finally, one can obtain the well-known Mott-Schottky relation, which provides the relationship between the capacitance C_{scr} and the built-in voltage V_{bi}:

$$\frac{1}{C_{scr}^2} = \frac{2}{q\,N_d\varepsilon_{Si}\varepsilon_0 A^2} \times (V_{bi} - V_g) \tag{2.24}$$

This equation can be used to extract the built-in voltage as it would be determined by the value indicated by the linear intersection with the x-axis of the $\frac{1}{C^2}$ vs V_g plot in reverse bias (Figure 2.14). Unfortunately, the presence of trapped charges render the approach more complex. This case is treated in Chapter 11.

2.4 The solid-liquid interface

Fundamental studies of the interaction of water on oriented NiO surfaces have been carried out in-situ in DAISY-MAT and in an electrolyte, which were then followed by electrochemical characterization towards the oxygen evolution reaction (OER). The aim being to study in a stepwise way surface orientation properties when the NiO based catalyst is brought to its final use: its implementation as catalyst for the oxygen evolution reaction.

2.4.1 Adsorption on a metal oxide surface

Adsorption reaction

Water dissociation on a metal oxide surface produces protons and hydroxide ions. The protons and the hydroxides will adsorb preferentially onto Lewis basic and acid sites, respectively. Thus, the protons (H^+) would likely anchor on anionic sites while the hydroxides (OH^-) onto cationic sites of the NiO surface [58, 68, 135, 136] (Figure 2.15).

The electronic interaction between the adsorbate and the electrode surface can be of two types: physical adsorption (physisorption) and chemical adsorption (chemisorption). Physisorption designates weak interaction of the chemical species with the surface electrode due to the lack of a true chemical bond and would be seemingly associated with the van der Waals interaction. Physisorption is characterized by a narrow energy band (few meV) when measured e.g.: by EELS at low temperature (< 150 K) [69, 137]. Chemisorption (e.g.: electron exchange or electron pairing) induces electronic orbital coupling between the adsorbate and the anchoring site. It induces

Figure 2.15: Representation of adsorption of water molecules on a metal oxide surface. The protons and the hydroxides would anchor preferably onto the anionic and the cationic sites, respectively.

strong chemical bonds, for which the band width, contrary to physisorption, is about a few eV [69]. Thus, chemisorbed species can be detected by XPS. At room temperature, the sticking probability of non-dissociated species can be considered as 0, otherwise it can be taken equal to 1 [136]. It means that at room temperature the adsorbates, which are observed, are likely in strong interaction with the substrate. It should be mentioned that adsorbate are stable intermediates and cannot be compared to radical species.

For a neutral chemisorption process, protons and hydroxides are adsorbed in equal amount ($[H^+_{ads}] = [OH^-_{ads}]$) and it can be assumed, at first sight, that this is the case when the metal oxide surface is exposed to a water vapour phase. If immersed in solution, the activity of the species on the surface can be tuned according to the pH of the solution. For instance, it can be imagined that strong alkaline solution would lead to the removal of adsorbed protons and $[H^+_{ads}] < [OH^-_{ads}]$. This should result in an excess of negative charges on the electrode surface [135]. A strong acidic solution would leave a net positive charge and $[H^+_{ads}] > [OH^-_{ads}]$ [135]. The resulting charge on the metal oxide surface is compensated by a space-charge below the surface and by ionic species in the solution (K^+, SO^{2-}_4...). The ionic species in the solution lead to the formation of a charged double layer known as the Helmholtz double layer. The pH, for which the potential drop through the Helmholtz double layer is zero (V_h=0), is commonly called the isoelectronic point (IEP) or point of zero zeta potential (PZZP) [135]. The pH for which protons and hydroxides are adsorbed in equal amounts ($[H^+_{ads}] = [OH^-_{ads}]$) is termed point of zero charge (PZC) [135]. The two cases do not necessarily coincide at the same pH value because of the presence of others species in the solution, which can interact with the electrode surface [135].

The adsorption process happens when the metal oxide electrode is immersed in water or when the surface is exposed to a water vapour phase. For the latter, hydroxides and protons are likely adsorbed in equal quantities (neutral chemisorption process, with $[H^+_{ads}] = [OH^-_{ads}]$). Ni 3d-bands are more narrow and less dispersive than O 2p bands [138,139]. Hammer *et al.* [138] pointed out that adsorption processes interacting with d-bands would lead to the formation of bonding and anti-bonding states as for a two-state problem (Figure 2.16). The resulting state of the adsorption process on d-bands would produce well

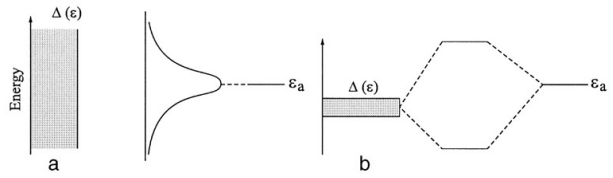

Figure 2.16: Density of state distribution for an adsorbate interacting (a) with a broad band (e.g.: O 2p) or (b) a narrow band (e.g.: Ni 3d), which leads to the formation of a bonding and anti-bonding state. Taken from Hammer et al. [138].

localized bonding and anti-bonding orbitals, whereas adsorption on O 2p bands would give rise to a broad feature [138]. Therefore, we assume that adsorbed species on Ni cationic sites would produce well defined electronic orbitals but it is very unlikely to measure the energy level of adsorbed species onto oxygen adsorbing site. Hydroxide (OH^-) d-band interaction provides two distinctive electronic states in the valence region and are labeled 3σ (bonding orbital) and 1π (anti-bonding orbital) [68, 140]. The d-1π hybridization in the valence region leads to numerous electronic states, which are partially filled according to the position of the d-band center [140]. The closer the d-band center to the valence band maximum the higher the electron occupancy in the anti-bonding state, which in turn reduce the substrate-adsorbate interaction [140].

The Helmholtz double layer

The Helmholtz double layer designates two planar charged layers, where the layers are of opposite sign, which forms at a solid-liquid interface. It is actually made of charges from the solid (electrons, holes, trapped charges) facing charges from the solution (ions) [135]. The distance between the two layers is only few atomic units ($\sim$ 3-5 Å) but it might vary according to the polarization of the solid surface (e.g. with an external bias). The space between the two charged layers is supposedly filled with polarized water molecules for which the dielectric permittivity is $\varepsilon = 5$ (for non polarized water molecules, $\varepsilon = 80$). Eventually, the Helmholtz double layer can be addressed as a parallel plate capacitor:

$$C = \frac{\Delta Q}{\Delta V} = \frac{A\varepsilon\varepsilon_0}{d} \tag{2.25}$$

With A being the surface of the electrode, d the distance between the two layers, ε_0 the vacuum dielectric permittivity, ΔQ the net quantity of charges in one layer and ΔV the potential drop through the double layer. From equation 2.25, one can derive the electric field arising at the Helmholtz double layer :

$$E = \frac{\Delta V}{d} = \frac{\Delta Q}{A\varepsilon\varepsilon_0} \tag{2.26}$$

The electric field in the Helmholtz double layer can be extremely high. For instance, in considering an excess of charges equivalent to 0.01 to 0.1

monolayers on the surface (e.g.: $[H^+_{ads}]$ or $[OH^-_{ads}]$) [135], the electric field E can be as high as 10^9 V/m [135]. It means the potential drop ΔV through the double layer is in the 0.1 to 1 V range, which is considerable.

It is important to point out that, for pure metallic electrodes and in the absence of electrochemical reaction, the Helmholtz double layer is driven by the difference in the *workfunction* between the surface of the solid and the electrolyte [135]. In equilibrium, for an uniform metallic electrode in contact with an electrolyte, anodic and cathodic current compensate each other and no net current flows through the interface. A Helmholtz potential drop built-up at the interface, which theoretically corresponds to the difference in workfunction on both side of the interface. The Helmholtz double layer can be, in theory, eliminated in polarizing the surface potential in order the *Fermi energy* position of the surface material and of the electrolyte are the same before contact.

In the case of a semiconductor, as for transition metal oxide materials, the Helmholtz double layer is controlled by the adsorption/desorption reactions on the surface, and not necessarily by the *workfunction* difference as for a metallic surface. Indeed, considering a free charge density of 10^{16}-10^{17} charges m^{-2}, the contribution of the free charges in the Helmholtz potential built-up is of the order of $\sim$ 10 mV [135]. Thus, the Helmholtz potential would arise from charged adsorbate site on the semiconductor surface as described in Section 2.4.1. Therefore, the nature of the adsorbing site on the semiconductor surface would define the properties of the Helmholtz double layer.

A schematic representation of a semiconductor/electrolyte interface is represented in Figure 2.17.

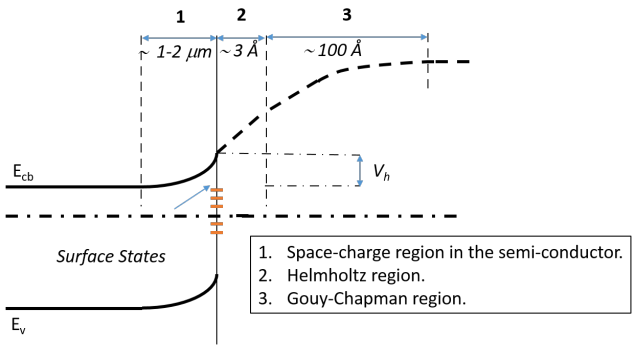

Figure 2.17: Typical band-diagram of a solid-liquid junction where the solid side is a n-type semiconductor. The thicknesses of the layers are taken from [135]. The space-charge region, surface state and the Helmholtz double layer have been detailed along this thesis. The Gouy-Chapman region corresponds to a charge gradient in diluted solution. This has been ignored in this thesis as the electrochemical experiments were realized in concentrated solution (pH=13-14).

2.4.2 Electrochemistry

Electrochemical reaction

Generality
Electrochemistry aims at studying the electronic charge transfers at solid-liquid interfaces. The solid side and the liquid side are called the electrode and the electrolyte, respectively. Electrochemical reactions involve the transfer of charges from or to the electrolyte and the modification of the oxidation state of the electrochemically active species. If an electron is added to the electrochemically active species, this is referred to as a reduction reaction. On the contrary, if an electron is added, this is referred to as an oxidation reaction:

$$Red.^{n} \underset{Reduction}{\overset{Oxidation}{\rightleftharpoons}} Ox.^{n+z} + z\,e^{-} \tag{2.27}$$

With n being the oxidation state of the reduced species *Red.* (having the lowest oxidation number) and z the number of charges exchanged during the reaction. *Ox.* stands for the oxidized species, the one having the highest oxidation number. The reduced and oxidized species form an electrochemical Redox couple [135]. The electrode where the oxidation reaction occurs is called a cathode, while if a reduction reaction occurs the electrode is called an anode.

The electrochemical reaction can be associated to a standard potential, which represents the electron electrochemical potential in the material [135]. As seen previously, if two materials of different nature are put into contact, the electron will flow to the material having the lowest Fermi energy position unless a potential build up at the interface or a chemical gradient appears [135]. The same occurs at a solid-liquid interface and electrons would naturally flow to the lowest energy level or, in the electrochemical language, to the highest equilibrium potential which is the equilibrium potential balanced by the partial activities of each species.

Standard and equilibrium potential
The energy of an electrochemical reaction can be calculated from a quantity called the electrochemical potential $\bar{\mu}$. It includes the elemental work of all the species participating in the reaction (Equation 2.27). The electrochemical potential of a species can be determined with the partial molar Gibbs energy μ_i of the element i and the local electrostatic potential of the electrons φ following:

$$\bar{\mu_i} = \mu_i + m_i F \varphi \tag{2.28}$$

where m_i is the oxidation number of the element i and F the Faraday constant. The partial Gibbs energy μ_i can be approximated by:

$$\mu_i = \mu_{i0} + RT \ln(a_i) \tag{2.29}$$

with a_i the partial activity of the element i and μ_{i0}, the partial molar Gibbs energy in standard condition. In equilibrium, the electrochemical potential

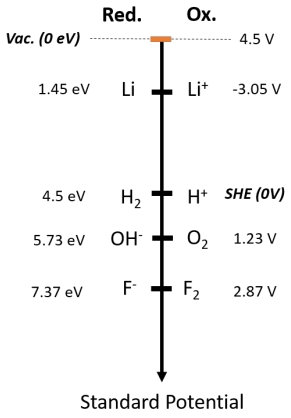

Figure 2.18: Standard electrochemical potential for some remarkable RedOx couples relative to the standard hydrogen electrode (SHE) or the electron energy in vacuum (Vac.). The Li/Li^+ and the F^-/F_2 RedOx couples provide the lowest and the highest electrochemical standard potential of all the RedOx couples, respectively. The H_2/H^+ and the OH^-/O_2 RedOx couples are the couples implicated in the water-splitting reaction in particular for the hydrogen reduction reaction (HRR) and the oxygen evolution reaction (OER), respectively.

is equal on the left and right-hand side of the reaction (Equation 2.27) and assuming the local electrostatic potential is the same everywhere:

$$\Sigma s\bar{\mu_i} = 0 \Leftrightarrow \varphi = -\frac{1}{zF}\Sigma s\mu_i \tag{2.30}$$

With s being 1 for chemical species in the final chemical state or -1 of the chemical species are in the initial chemical state and z the number of electrons exchanged during the reaction (Equation 2.27). Therefore, from the partial molar Gibbs energy, it is possible to derive the electrical potential φ in equilibrium. Under standard condition of temperature and pressure and partial activity equal to 1, the potential φ is called the standard potential of the couple Red/Ox and is referred to as $E^0_{Red/Ox}$ in electrochemistry. In real conditions, the partial activities of the species involved in the reaction is not equal to 1. It implies that the local electrostatic potential deviates from the standard potential $E^0_{Red/Ox}$. This can be corrected by including the partial activities of each species:

$$E_{Red/Ox} = E^0_{Red/Ox} + RT\ln\left(\frac{a_{Ox}}{a_{Red}}\right) \tag{2.31}$$

with $E_{Red/Ox}$ the equilibrium potential, $E^0_{Red/Ox}$ the standard potential, R the gas constant in the ideal gas law, T the temperature in Kelvin, and a the partial activity of the species involved in the reaction. The electron energy $qE_{Red/ox}$ represents the energy level of the highest occupied energy level in solution. This is therefore a similar quantity as the Fermi energy introduced in solid materials (Part 2.1.1). In electrochemistry, the potential of an electron

$E^{eq}_{Red/ox}$ is given against the standard hydrogen electrode (SHE) (Figure 2.18) as the fabrication of a hydrogen based electrode compatible with an electrolyte is convenient. However, it has been determined that the energy of the standard hydrogen electrode (RHE) relatively to electron vacuum energy is 4.5 eV [135]. Thus, the expression of standard electrochemical potential relatively to the electron vacuum energy $E^{abs}_{Red/Ox}$ should be:

$$E^{abs}_{Red/Ox} = E^{SHE}_{Red/ox} + 4.5V \tag{2.32}$$

As an example, Figure 2.18 provides standard potentials of some RedOx couples relative to the standard hydrogen electrode (SHE) or relative to the electron energy in vacuum.

The Butler-Volmer equation and the Tafel slope

If an external bias V is applied on the electrode (the solid surface) relative to the electrolyte, electrons on the electrode side acquire the energy qV. Depending on the sign of the external potential V, the equilibrium condition is displaced triggering an electrochemical reaction at the interface. For reversible electrochemical reactions and in the case there is no diffusion limitation of the chemical species, the evolution of the anodic and cathodic current are described by the theoretical Butler-Volmer equations:

$$J_c = -J_0 \exp\left(-\frac{\alpha z q \eta}{k_B T}\right) \tag{2.33}$$

$$J_a = J_0 \exp\left(\frac{\beta z q \eta}{k_B T}\right) \tag{2.34}$$

where the currents J_c and J_a stand for the cathodic current density and the anodic current density, respectively. In other words, J_c corresponds to the reduction reaction and J_a to the oxidation reaction in the equation 2.27. J_0 is the exchange current density at equilibrium. For the rest, q is the charge of an electron, z is the number of electrons exchanged during the reaction, α and β are symmetry factors of the reaction, which fulfil the equation $\alpha + \beta = 1$, k_B is the Boltzmann constant, T the temperature in Kelvin and η is the overpotential $V = E_{Red/Ox} + \eta$, with $E_{Red/Ox}$ the electrochemical potential of the RedOx couple calculated at equilibrium in equation 2.31. The current density is the sum of the anodic and cathodic contribution:

$$J = J_a + J_c = J_0 \left(\exp\left(\frac{\alpha z \eta}{k_B T}\right) - \exp\left(-\frac{(1-\alpha) z q \eta}{k_B T}\right)\right) \tag{2.35}$$

for $|\eta| >> 0$, the equation 2.35 can be simplified into the sole contribution of either the anodic current or the cathodic current, depending on the sign of η. Therefore, represented in logarithmic scale and for $|\eta| >> 0$, the IV curves are a straight lines of slope $\frac{\alpha z}{k_B T}$ for the anodic potential and $-\frac{(1-\alpha) z q}{k_B T}$ for the cathodic potential. This slope is called the *Tafel slope* and is generally expressed in dec/mV, which is an indication of how much potential the electrochemical system needs to increase the current density by one order of magnitude.

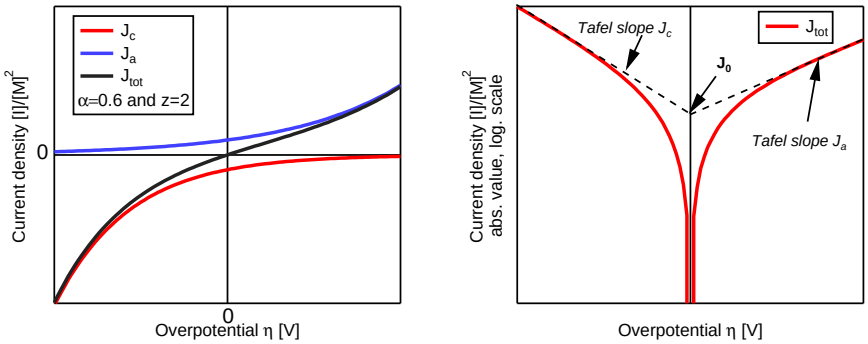

Figure 2.19: Left: Theoretical IV curves for an electrochemical reaction having a symmetry factor α=0.6 and a number of exchanged electron z=2. The total current is the sum of the contribution of the anodic current and the cathodic current. Right: Log. plot of the absolute value of the total current density from the left plot. For $\eta >> 0$ the curve can be linearised. The slope of the linear fit is called the Tafel slope. The intersection of the linear part with the Y-axis gives the exchange current density J_0.

Electrochemical Impedance Spectroscopy

Principles

Electrochemical Impedance Spectroscopy (EIS), which can be equivalently referred to as Electrical Impedance Spectroscopy or simply as Impedance Spectroscopy (IS), is a powerful non-destructive technique to determine properties of solid/solid and solid/liquid interfaces. The technique is based on transient signals (AC signals) where device response is evaluated over a wide range of frequency (in general 0.1 Hz to 1 MHz) and the results are analyzed in terms of the impedance of equivalent electrical circuits (Figure 2.20). Employed primarily in electrochemical systems (hence the term electrochemistry), the measurement technique has been used to quantify surfaces towards electrochemical reactions (catalyst, corrosion, batteries, capacitive elements) but it spreads into the solar cell field in particular concerning perovskite and silicon based structures [141–145]. Therefore, EIS can be used to characterize as much solid/liquid interfaces as solid state interfaces.

The method relies on the use of AC signals and the comparison of current and potential going through the sample in the frequency domain. In general, the AC signal is a single sinusoidal potential $E(\omega t) = A\cos(\omega t)$ with an amplitude A=10-20 mV RMS. The response in current to the potential excitation can be written as $I(\omega t) = Z\,E(\omega t)$, with Z being the complex impedance. For instance, in the case of a purely ohmic element, Z is real and the current and the potential flow are in phase with an amplitude ratio proportional to the ohmic resistance $|Z|$. In the case of a capacitive element, Z is equal to $\frac{1}{jC\omega}$. It

implies that the current phase is shifted by 90° from the phase of the potential, while the amplitude of the current depends on the frequency. As example, the phase and amplitude of standard electrical elements are listed in Table 2.2.

Element	Impedance Z	Amplitude (Z)	Phase (Z)
Resistance (R)	Z=R	R	0
Capacitive (C)	Z=$\frac{1}{jC\omega}$	$\frac{1}{C\omega}$	-90°
Inductive (L)	Z=$jL\omega$	$L\omega$	+90°

Table 2.2: Impedance, amplitude and phase delay of basic electrical elements under AC measurements. j is the complex imaginary part equal to $\sqrt{-1}$.

Solid/solid and solid/liquid interfaces rarely show an electrical response of a pure electrical element as displayed in Table 2.2. Instead, it can be assumed that the interfaces can be represented by an equivalent electrical circuit where different standard electrical elements are connected in parallel or in series. Fitting programs are implemented in electrochemical software to estimate parameters of equivalent electrical circuits. Fitting iteration between electrical equivalent model and experimental results needs to be performed until the model provides satisfactory results (see Figure 2.20).

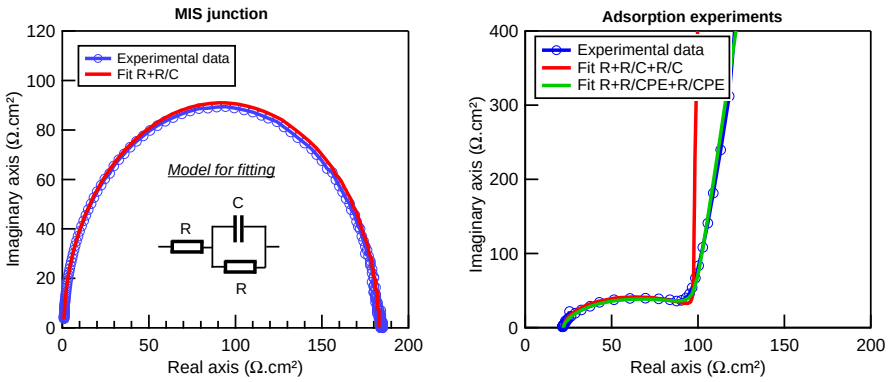

Figure 2.20: Nyquist representation of impedance spectroscopy data with the experimental results obtained with (left) one of the $Si/SiO_2/Pt$ MIS structures studied in Chapter 13, and during (right) the electrochemical adsorption experiments realized in Chapter 8. Electrical equivalent fits are also represented. It can be seen that whereas standard R and C elements are sufficient for quantifying the results obtained with the MIS structure, it is necessary to use CPE elements for the electrochemical experiments.

The Constant Phase Element

In electrochemistry, at first sight, it can be thought that an

electrode/electrolyte interface shows some capacitive behavior when measured by EIS because of the Helmholtz double layer at the solid-liquid interface. Practically, in most cases, the EIS measurements deviate from nominal capacitance fingerprints. It has been proposed that the capacitive element is not constant with frequency due to a distribution of time constants on the electrode surface. This can arise from surface heterogeneity, roughness, porosity and slow adsorption process [146]. To take into account capacitive dispersion, the Constant Phase Element has been introduced. It is formulated as following:

$$Z_{CPE} = \frac{1}{Q(j\omega)^{\alpha}} \quad \text{with} \quad j = \sqrt{-1} \quad \text{and} \quad \omega = 2\pi f \tag{2.36}$$

where Q is the numerical value of the admittance $(1/\|\mathrm{Z}\|)$ at $\omega = 1$ rad/s and α a parameter defining deviation from a pure capacitive behaviour. From equation 2.36, it can be said that for $\alpha = 0$, the CPE element behaves like a resistor, if $\alpha = 1$ like it behaves as a pure capacitive element and for $\alpha = 0.5$, the CPE corresponds to a Warburg element in the case of a semiinfinite linear diffusion [147]. All other cases in between arise from non ideal behaviour. It is worth mentioning that the impedance spectroscopy did not reveal large time-constant dispersion when realized on the MIS Schottky structure contrary to most of the electrochemical experiments where it was necessary to adopt the CPE elements during the electrical equivalent fitting (Figure 2.20). Therefore, the CPE element was only used to fit EIS measurements in an electrochemical cell.

CHAPTER 3

Methodology

Summary

In this chapter the methods and the conditions related to the deposition of the thin films and the growth of the silicon dioxide layer on top of silicon are detailed. Also, the different experimental methods which were employed along this thesis to characterize the samples as for X-Ray photoelectron spectroscopy, X-Ray diffraction, electrical, electrochemical and in-situ stress measurements are described.

This chapter is split into four parts: the first deals with the deposition of the thin films, the second with the Si/SiO_2 sample preparation, the third to the surface characterizations and the fourth to the bulk characterizations.

3.1 Thin film deposition

3.1.1 Magnetron DC-sputtering

Thin films in the nanometre range have been prepared at UCL and TU-Darmstadt. For instance, thin films have been used to study the surface properties of a certain orientation of NiO or to create Schottky junctions on top of the Si/SiO_2 interface. A thin film can be either prepared by Chemical Vapor Deposition (CVD) or Physical Vapor Deposition (PVD). The technique used in both universities during the thesis is commonly called cathodic magnetron sputtering and is categorized in the PVD class deposition techniques.

As represented in Figure 3.1, thin film deposition by cathodic magnetron sputtering relies on the bombardment of a material, called the target, and maintained at negative potential, by positively ionized particles, in general Argon as it is inert chemically, formed in a plasma and accelerated towards the negative potential value. The plasma is confined in the vicinity of the target with a set of magnets situated in the back of it. During the reaction, the kinetic energy from the positively ionized particles is transmitted to atoms on the surface of the target, which are in turn ejected from the surface. In the meantime, during the bombardment of the target by the positive ions, secondary electrons are emitted from the target surface (ion Induced Secondary Electron Emission - ISEE) [148]. The ISEE are accelerated towards increasing potential but are retained by the magnetic field near the cathode region where they collide and produce a number of ions [148].

The reaction produces *somewhat* a cloud of atoms, which diffuse through the deposition chamber. The ejected atoms then condensate with any surface in the deposition chamber and so form what is called a thin film. Therefore, the thin film base-material is determined by the target material. In general, the process is realized at relatively low pressure (1-10 Pa) in order to ignite the plasma and to allow an acceptable deposition rate (1-10 nm/min).

Sputtering can be realized from a DC and RF power supply and in general, in laboratory, from a planar target. DC sputtering consists in maintaining the cathode potential at a constant negative value to force positive particles to hit the target surface. This is mostly used when the cathode is metallic as they are very conductive. On the contrary, for lowly conductive targets (e.g.: metal oxide, ITO target), RF sputtering, where cathode potential alternates at 13.56 MHz, is preferred.

The stoichiometry of the deposited film can be tuned by modifying the composition of the atmosphere of the deposition chamber with a non-inert gas (O_2, N_2, H_2O...). For instance, from a metallic target one can obtain metal oxide thin films by adding a small amount of oxygen (5-15 %) to the atmosphere of the deposition chamber. In such case, this is referred to as

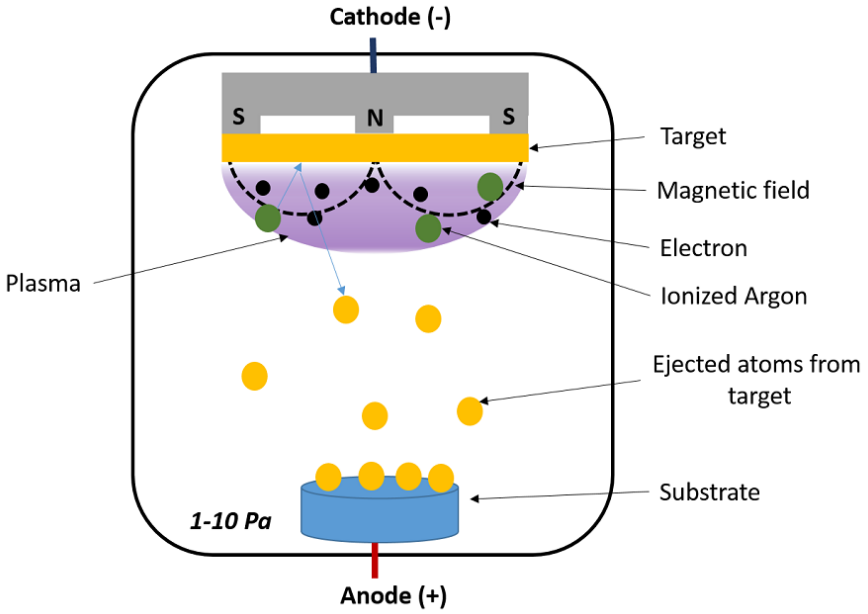

Figure 3.1: Simple schematic representation of the sputtering process. A plasma composed of negative particles (e.g.: O^-, e^-) and positive particles (Ar^+) is formed in the vicinity of the target. The positive particles are accelerated towards the target and the accumulated kinetic energy is transferred to the atoms from the target, which are eventually ejected into the volume of the chamber. A thin film is then formed on any exposed surfaces of the chamber.

reactive sputtering.

To summarize, Argon is required to produce the positive ions, which will sputter the target material in the chamber without reacting chemically. Depending on the conductivity of the target one will choose RF or DC sputtering and if the stoichiometry of the thin film needs to be adjusted, a non-inert gas can be added to Argon in the deposition chamber.

3.1.2 Nickel oxide deposition

Nickel oxide (NiO) thin film deposition is realized by DC reactive sputtering in Argon/Oxygen atmosphere from a pure metallic target. Deposition chambers at UCL or at TU-Darmstadt were not exactly the same, e.g.: chamber geometry, magnet configuration etc. and reproduction of experiments is rendered complex. Thus, the work has been split in two: on the UCL side, all the prepared NiO thin films were non-oriented and polycrystalline, while on the TU-Darmstadt side, the thin films are mostly oriented and polycrystalline. As the thesis started at UCL, the conditions of deposition were set at UCL while the conditions of deposition at TU-Darmstadt were chosen to be as close

as possible to the UCL ones, in particular concerning the deposition rates and the discharge curves.

Nickel cathode Discharge

Cathode discharge versus oxygen concentration was measured for each deposition chamber used in both universities. The cathode potential would be proportionally related to the inverse of the ion Induced Secondary Electron Emission (ISEE) of the target material [148, 149]. In the presence of oxygen in the chamber, the composition of the surface of the target can be modified over 1-2 nm [148]. It would result in a different ISEE yield. This change would affect the plasma impedance, which can be indirectly measured by the value of the cathode potential [148]. Thus, for a metallic nickel target, the plot of the cathode potential as a function of the oxygen pressure in the chamber evidences three regions (Figure 3.3 and Figure 3.2). According to what can be found in the literature, each region can be associated to a specific deposition regime [150]:

- the first region starts at 0% oxygen until the cathode potential reaches a minimum. This region might be defined as the *metallic* regime, although the deposited thin film might be instead oxygen deficient.
- the second region corresponds to the part of the curve at higher oxygen concentration relative to the first region. It is marked by a strong increase of the potential. This transitional region is referred as being the *semiconducting* regime as the thin film composition is likely close to stoichiometry. This region is also remarkable for having an hysteresis behaviour with the oxygen concentration.
- the third and last region is the part of the plot marked by an almost constant potential. The target is likely totally oxidized, and the deposited thin film might be metal deficient. This region is then labelled as the *oxidized* regime.

Setting up deposition conditions at UCL

Nickel oxide (NiO) thin films were reactively DC sputtered from a metallic nickel target in a AJA sputtering system[1]. For any deposition, the target-to-substrate distance is fixed to 122 mm.

At UCL, cathode power and pressure in the deposition chamber have been varied and the cathode potential has been measured accordingly. Experimentally, it has been observed that an increase of power or a decrease in pressure enlarges the regions (Figure 3.2). Finally, power and pressure were set respectively to 50 W and 2 mTorr for which the metallic regime is found between 0 and 10 % of oxygen concentration, the semi-conducting mode between 10 and 20 % and the fully oxidized target regime above 20 % (Figure 3.3). The idea being that a discharge curve spreading over a large

[1] `http://www.ajaint.com/`

oxygen concentration range enables to explore more accurately the properties of each region and might be more resilient to small changes in experimental conditions, for instance ageing of the target.

Prior to each series, the target is cleaned for 1-5 min in the same gas mixture selected for the deposition. This operation is supposed to remove any possible organic contaminant from the target and to offer a steady-state Ni-target surface.

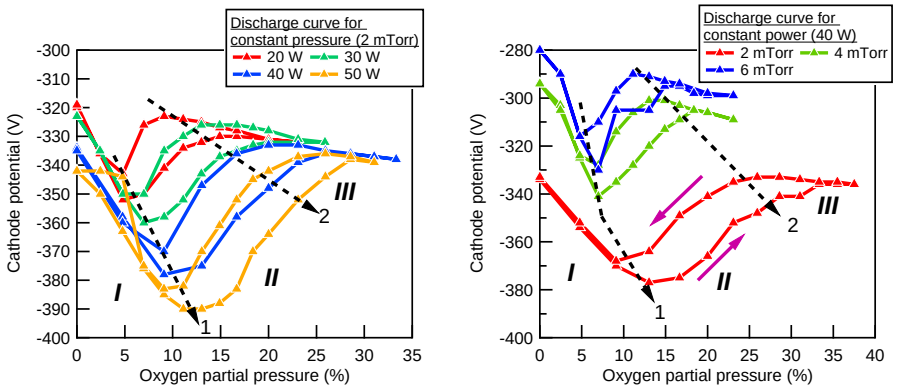

Figure 3.2: Discharge curve obtained at UCL for different cathode power at constant pressure (left) and at different atmosphere pressure for constant power (right). Each point is obtained after one minute of waiting time. The regions I, II and III stands for the metallic, semi-conducting (transition) and the fully oxidized regime, respectively. The regions are delimited by the arrows 1 and 2. The measurements are realized for increasing and decreasing oxygen pressure, hence the hysteresis behaviour. Decreasing oxygen partial pressure produce a curve shifted upward on the plots in comparison to the curve obtained for increasing oxygen concentration (indicated by the purple arrows on the right plot).

Nickel oxide deposition at TU-Darmstadt

At TU-Darmstadt, the conditions of deposition were chosen in order to reach similar deposition rate and discharge curve as set at UCL. After several tests, the parameters of deposition are set to 0.5 Pa (7.5 mTorr) for the pressure, 40 W for the power and the target-to-cathode distance is fixed to 14 cm. The discharge curves display similar regimes than in UCL but the metallic region is slightly smaller. The metallic region can be defined from 0 to 5% of oxygen, the second region from 5 to 15% and above 15% one can recognize the fully oxidized target region (Figure 3.3, left).

3.1.3 Platinum deposition

Platinum has been extensively used for preparing on one side oriented platinum thin films and on the other side for the interface experiments carried out on

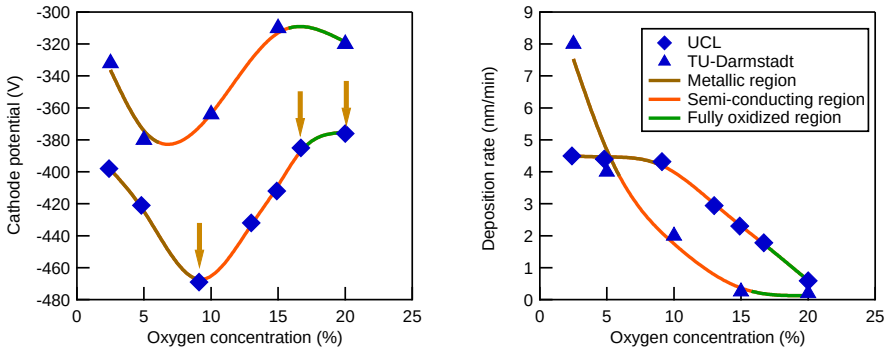

Figure 3.3: Discharge curve (left) and deposition rate (right) for the nickel target in UCL and in TU-Darmstadt. Discharge curves are recorded at constant power and pressure while oxygen concentration is varied. The plot is obtained from the cathode potential at the end of each deposition (several minutes). Regarding the discharge curve, three regions can be delimited (vertical arrows) : the metallic (0-10 %), semi-conducting (10-17 %) and oxidized region (> 17%).

Si/SiO_2 substrates. In both cases, the platinum deposition is realized in an Argon atmosphere from a metallic target by DC sputtering.

In order to carry out in-situ XPS measurements and electrochemical measurements an oriented platinum thin films have been used as buffer layer for in-plane conduction between the substrates (MgO, Sapphire) and the NiO thin films, which are both not conductive. Moreover, the relative low lattice mismatch between the substrate (MgO, Sapphire), platinum and NiO enables to tune NiO orientation in simply selecting the surface orientation of the substrate material. In that way, the structure allowed to study NiO surface properties according to one orientation with both in-situ XPS/UPS and electrochemical measurements. NiO thin film thickness was kept to less than 150 nm in order to limit potential losses during out-of-plane charge transfer from the platinum layer to the NiO surface.

It is worth mentioning that many alternatives to platinum exist for growing oriented NiO thin films and could even provide better NiO thin film quality (See Chapter 7). Nevertheless, the ESM group of TU-Darmstadt has developed the competence to grow oriented platinum thin films [151] and the use of an another oriented conductive buffer layer could have been time-consuming to handle. Overall, the use of platinum enables to obtain reasonably NiO oriented thin films and to provide some hints on NiO surface properties relative to the surface orientation (See Chapter 8 and 9).

Oriented platinum thin films were realized on specific oriented substrates commercially available. Sapphire (0001) or MgO (111), MgO(110) and MgO(100) were used to grow respectively Pt(111), Pt(110) and Pt(100)

Table 3.1: Lattice parameters of different materials on which it could be possible to obtain oriented NiO thin films. Lattice mismatch relatively to the NiO structure is indicated in %. and is calculated according to the crystallographic lattice constants from XRD PDF files.

Element	Lattice constant (A)	Lattice mismatch relatively to NiO
MgO	4.21	1%
NiO	4.168	0%
Ag	4.085	2%
Pt	3.924	6%
Pd	3.891	7%
Ni	3.524	15%

oriented thin films. The relatively low lattice mismatch between the base substrate and the platinum favours the growth of oriented platinum thin films. Deposition conditions are summarized in Table 3.2.

Table 3.2: Deposition conditions for platinum at TU-Darmstadt.

Substrate	Power (W)	Temp. (°C)	Pres. (Pa)	O_2 conc. (%)	Dist. (cm)	Dep. rate (nm/min)
Sapphire (0001)	5	600	0.5	0	7.5	3.6
MgO (111)	5	600	0.5	0	7.5	3.6
MgO (110)	5	600	0.5	0	7.5	3.8
MgO (100)	5	650	4	10	7.5	2.6
Si/SiO_2	5	RT→450	1→6	0	Max.	<0.5

Prior to each platinum deposition on oriented substrates, the substrates were kept for 30 min in the desired deposition condition without platinum sputtering. The aim being to clean out the surface from hydrocarbon contaminants and also, even though this has not been verified, this is supposed to (re-)crystallize the surface of the substrate. Indeed, because of the fabrication process, the oriented substrate might be delivered slightly amorphous at the surface. The relatively high temperature chosen for the deposition of the oriented platinum thin film might crystallize the surface of the oriented substrate.

For interface experiments on Si/SiO_2 substrates, the platinum is deposited at high pressure and long target-to-substrate distance (Table 3.2). The aim being to reduce the kinetic energy of the sputtered platinum atoms and to provide a smooth platinum deposition. Thus, it was decided to choose a working pressure above 1 Pa and a target-to-substrate distance of 15 cm. Deposition

rate was less than 0.5 nm/min.

3.2 Si/SiO_2 sample fabrication

Si/SiO_2 samples for interface experiments were all prepared at UCL in the Wallonia Infrastructure for Nano FABrication (Winfab) platform from a n-type FZ silicon purchased from Sil′tronix and delivered in the form of wafers, 3 inches in diameter, and 360 μm thick. Sheet resistance measured with a van der Pauw geometry is 10.1 Ω cm and donor density is estimated to be 4.4×10^{14} /cm^3 in the n-type silicon. The Si/SiO_2 substrates were used for in-situ XPS interface experiments in DAISY-MAT and the MIS fabricated junctions were also electrically characterized. In order to provide a high quality tunnelling Si/SiO_2 interface, specific fabrication processes have been elaborated.

Basically, the main steps for the Si/SiO_2 sample preparation are:

- Surface cleaning to remove both carbonated contaminant and the native silicon dioxide layer.
- Formation of a n-rich region by phosphorus enrichment for the ohmic back-contact. This step is only required for performing electrical characterization.
- Growth of a high quality tunnelling silicon dioxide (< 3 nm) on the non-doped side of the silicon.

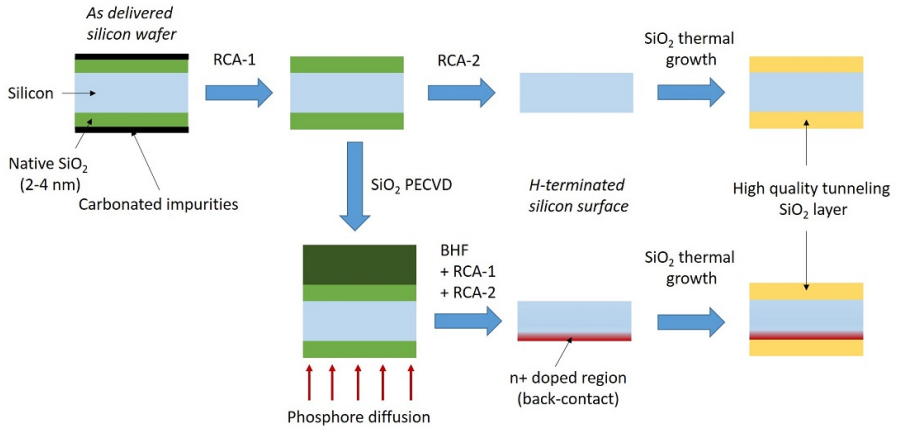

Figure 3.4: Schematic of the fabrication process of Si/SiO_2 samples. Two types of samples have been fabricated: with and without ohmic back-contacting. An ohmic back-contact was necessary for electrical characterization of the samples whereas the others were mostly used for in-situ XPS experiments.

3.2.1 Chemical surface cleaning

Surface cleaning is chemically performed and follows standard procedures developed at the WinFAB platform in UCL. To ensure a perfect clean surface out of any carbonated compounds or oxides, Piranha (H_2O_2:H_2SO_4, 5:2) bath for 10 min followed by 60 sec dips in hydrofluoric acid (HF 2%) bath are processed. The samples are extensively rinsed for 10 min with DI water between each bath and at the end of the cleaning process. A hydrophobic silicon surface, visually observable, is obtained after the chemical treatment, which is a clue of a H-terminated oxide free surface. In the presence of a thicker silicon dioxide layer (e.g.: PECVD SiO_2) a buffered hydrogen fluoride (BHF) bath is performed instead to reduce the silicon dioxide thickness.

3.2.2 Sample back-contacting

This step is only required when electrical measurements are carried out to characterize the front contact. Indeed, any contact on a lowly doped silicon will lead to the formation of a non-ohmic Schottky contact. For instance, in the beginning of the thesis, In-Ga eutectic has been tested as back contact material for electrical measurements. However, impedance measurements highlight the presence of two semi-circles, which can be associated to the presence of two rectifying contacts: one on the front and one in the back of the silicon (Figure 3.5). The problem can be solved by the diffusion of phosphor at high temperature into the silicon, which leads to the creation of a n-rich region not thicker than few μm. The n-rich region suppresses a rectifying contact to be formed. TLM measurements have carried out as well on non-doped oxide free n^+-Si surface and oxide free n-Si surface as presented in Appendix A.1. The results show that the superficial diffusion of Phosphor in n-Silicon helps to suppress rectifying junction and to obtain contact resistance in the 1 $\Omega\,cm^2$ range. In addition, impedance spectra only provide one semi-circle, confirming that the diffusion of phosphor leads to the formation of an ohmic back contact (Figure 3.5). Moreover, as measured at UCL, symmetrically enriched silicon wafers provide a charge carrier life-time of 500 μs. It proves that, in addition to suppressing barrier height, the process also passivates the surface of the back-contact, which is compatible with solar cell application.

The process to create an ohmic back contact can be detailed as following:

- The native oxide is chemically removed following the procedure described in previous part.
- A thick sacrificial silicon dioxide layer ($\sim$150 μm) is deposited by PECVD on one side of the sample.
- Phosphor diffusion in silicon is realized at 900°C for 5 min in a furnace under nitrogen on the unprotected side of the sample.
- The chemical baths are performed again to remove the as-grown oxide.

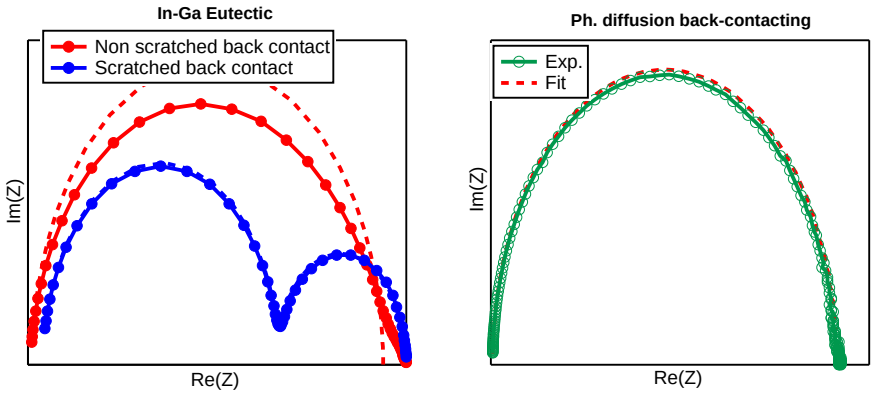

Figure 3.5: Nyquist representation of EIS measurements for In-Ga eutectic back-contacting (left) and for phosphor diffusion back-contacting (right). Fits (dotted lines) are attempted with electrical equivalent circuits including exclusively pure capacitive and resistive elements. The comparison of the measurements with the fits highlights that In-Ga eutectic fails to create an ohmic back-contact. On the contrary n^+ back contact obtained by phosphor diffusion on one side of the silicon helps to provide a single semi-circle where the fit gives a reasonable good result, suggesting the back contact is ohmic and so there is only one rectifying junction (the front contact).

- BHF bath is then performed to remove the poly-silicon-glass formed during the phosphorus diffusion step. Additional time is required to remove completely the thicker sacrificial PECVD SiO_2 layer. The BHF bath lasts until the interference fringes due to the thick silicon dioxide layer are visually not observable. The sample is then abundantly rinsed in de-ionized water.

3.2.3 SiO_2 thermal growth

Silicon dioxide is a widely studied material in MIS technologies. It has the advantage to be easily produced when a silicon substrate is oxidized. Also its use on the silicon surface enables to obtain a lowly defective interface particularly after hydrogen passivation. Therefore, along this thesis, the SiO_2 layer is thermally grown in a furnace in the WinFAB platform at UCL but surface passivation with atomic hydrogen is realized in the Daisy-MAT system at TU-Darmstadt (see Section 3.2.4). However, particular procedures have to be followed to produce a high quality silicon dioxide layer, especially:

- Cross-contamination from other elements, e.g.: metal, must be avoided.
- An abrupt transition between silicon and silicon dioxide might be desired to reduce the number of defective site, in particular uncoordinated silicon bonds, at the Si/SiO_2 interface, which can act as interface trap level.

The two requirements above aim at reducing defective states at or near the Si/SiO_2 interface. Indeed, defect levels can act as recombination centers for

minority charge carriers, could modify the charge transfer mechanism through the interface and pin the Fermi level of the silicon to an undesired position. Thus, it has been assumed that the silicon dioxide layer should be grown on an oxide free silicon wafer in a well controlled condition. Therefore, the as-delivered silicon wafer is first cleaned following the chemical bath recipe described in section 3.2.1. Then, a thin silicon dioxide layer is thermally grown in the WinFAB Koyo VP1000 furnace in dry gas (nitrogen or nitrogen/oxygen mixture). The program of the process is basically made of four steps as represented in Figure 3.6:

- the sample is kept at 700 °C for 30 min in dry nitrogen to homogenise the temperature in the furnace and purge the chamber.
- the temperature in the furnace is ramped up in dry nitrogen until the annealing temperature is reached.
- the annealing temperature is held on for a desired period of time. During this period the annealing atmosphere can be selected between pure nitrogen and a nitrogen/oxygen gas mixture.
- the temperature is ramped down from the annealing temperature to 700 °C in dry nitrogen.

In general, one cycle takes approximatively 2 hours. Although a high quality silicon dioxide layer can be obtained at high temperatures, the silicon dioxide layer has to be thin enough (<2.5 nm) to allow tunnelling of the charge carriers. To obtain a thin tunnelling SiO_2 layer becomes more difficult to achieve with increasing annealing temperature, but after furnace calibration (see Chapter 11), it has been assumed that the desired SiO_2 layer could be obtained at 1000 °C with no annealing period in dry nitrogen. It is believed that the oxygen participating in the SiO_2 growth process originates from oxygen desorption from the furnace wall during the thermal cycling. An approximatively 2.3 - 2.5 nm silicon dioxide layer is obtained with this thermal program on top of silicon, which is compatible with charge tunnelling. The Si/SiO_2 base substrate is then later stored in air.

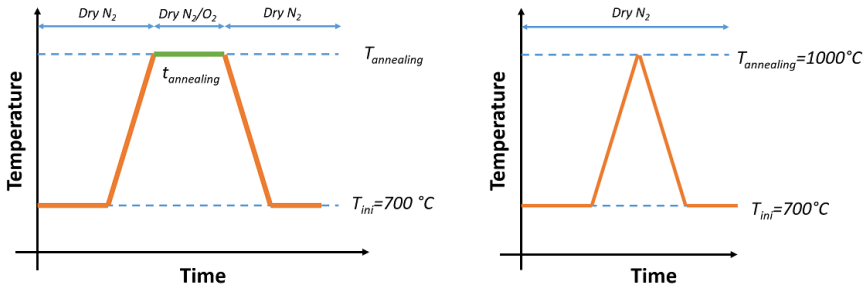

Figure 3.6: Left: Typical furnace profile. Right: Profile used to obtain a thermally grown tunnelling SiO_2 layer at 1000 °C on silicon during this thesis.

3.2.4 In-situ plasma cleaning and hydrogen surface passivation

A hydrogen plasma source (Tectra Gen2 Hybrid Atom/Ion Source) was used for both surface cleaning and passivation of the Si/SiO_2 samples as detailed in Chapter 11. Atomic hydrogen is obtained by cracking dihydrogen molecules in the plasma chamber set on atomic mode for which the current was set to 30 mA and the gas pressure to 0.2 mbar. The hydrogen cleaning step is realized at about 250 °C for 10 min and allows to remove efficiently carbonated contaminants and possibly hydroxilated compounds, which are present on the surface because of air exposure of the Si/SiO_2 samples. An additional 45 min hydrogen plasma exposure is necessary at higher temperature for the hydrogen passivation step according to reports found in the literature regarding Si/SiO_2 passivation [123, 152, 153]. As the temperature range was limited in the setup, the temperature for hydrogen passivation was set to 350 °C . To avoid possible hydrogen desorption from the sample, the plasma is maintained until the sample holder temperature reaches ∼150 °C.

3.2.5 Alumina deposition by ALD

Alumina layers deposited by Atomic Layer Deposition (ALD) have been performed on top of the hydrogen passivated Si/SiO_2 structure in the DAISY-MAT system at TU-Darmstadt [154]. The alumina layer is obtained by the alternative deposition of TMA (trimethylaluminum) and its oxidation by water. One ALD cycle consisted in a TMA and water pulse lasting respectively 80 ms and 150 ms, which are separated by an pumping period of 5 min in vacuum.

As the alumina layers have been deposited on the hydrogen passivated Si/SiO_2 samples, a low temperature for the alumina deposition was preferred. The reason, even though this was not proven at this level, is that it would limit the risk of the depassivation of the Si/SiO_2 structure. Thus, the temperature during the ALD process was constrained from room temperature to 200 °C in this thesis.

3.3 Surface characterization

3.3.1 X-Ray and UV photo-spectroscopy

Technical description

This part is only intended at providing a brief understanding of the photo-electron spectroscopy techniques, however detailed informations can be obtained in the book of S. Hüfner, "*Photoelectron Spectroscopy – Principles and Applications*" [155].

The main components in photoemission technique are the photon source, which can be a X-Ray or a UV light source, directed towards the sample, and the energy analyser which collects the electrons (Figure 3.7, left). An analyser,

composed of several electro-magnetic lenses, allows to filter the electrons having a specific kinetic energy and to count their quantity. Ultra High Vacuum (UHV) is required to reduce the electron scattering when the electron travels from the surface of the sample to the analyser. Thus, measurements in the Daisy-MAT system are carried out in the 10^{-8}-10^{-9} Torr range.
The technique allows to determine the electron binding energy ($E_{B.E}$) of the electrons participating in the electronic structure of the material. Basically, the technique measures the kinetic energy (E_k) of the electrons after photo-emission according to:

$$E_{B.E} = h\nu - E_k - \Phi \tag{3.1}$$

with $h\nu$ the photon energy emitted from the photon source (e.g.: X-Ray, UV light) and Φ the screening potential of the photo-emitted electrons with the local environment. Φ can be determined, for post-data correction, in measuring the energy levels (e.g.: Fermi energy) of reference samples such as Ag, Au and Cu.

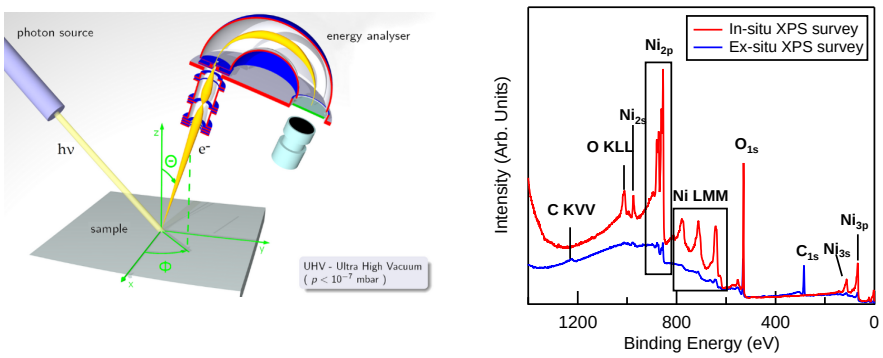

Figure 3.7: Left: schematic representation of XPS/UPS under operation. X-rays are directed towards the sample which in turns emits electrons (taken from Wikipedia [2]). The photoemitted electrons are quantified in the analyser. Right: Typical XP survey spectra of a NiO thin film; in red the sample has been produced in-situ in the Daisy-MAT system and in blue the NiO thin film has been exposed to air. Core level of NiO O 1s, Ni 2p are visible and carbon contamination (C 1s) is visible for the ex-situ sample. Also, Auger lines of Ni LMM, and O KLL are particularly visible on the in-situ sample. The in-situ XPS spectra is sharper and more intense than the ex-situ measurements as a thin contaminated layer is formed on the NiO surface of the ex-situ sample. The background increases to higher binding energy because of the number of scattered electrons increases.

Three types of photoemitted electrons can be identified: direct and indirect emitted electrons and scattered electrons. Direct and indirect emitted electrons are related to elastic processes (no energy is dissipated). The direct emission defines the emitted electrons *directly* originating from an electronic orbital under photo-excitation (e.g.: O 1s, C 1s, Ni 2p electrons...), while in indirect

emission the emitted electron acquires energy through another excited electron (e.g.: Auger emission). The scattered electrons arise from energy dissipation through inelastic collision of the emitted electrons. The scattered electrons are responsible for the background intensity particularly at high binding energy. Finally, the contribution of the three type of photoemitted electrons provide typical X-ray photoelectron (XP) spectrum as represented in Figure 3.7 (right).

Photoemission from a material follows standard Beer-Lambert optical law, where the ratio of the emerging (photoemitted electrons) over the incident (the photons) flux at a certain depth in a material exponentially decays:

$$\frac{I_{out}}{I_{in}} = \exp\left(\frac{-t}{\lambda}\right) \tag{3.2}$$

where I_{out} and I_{in} are the emerging and the incident flux, respectively. The parameter t is the the depth from the surface material and λ is the attenuation length, also referred as the inelastic mean free path (IMFP) which is a parameter quantifying the inelastic process between the incident photon and the material. The higher the IMFP, the deeper the information depth. The information depth can be determined as being $t_{max} = 3\,\lambda$ which corresponds to the depth where the intensity of the emerging flux is only 5 % of the photon intensity. The IMFP depends on the material but also on the photon source. Thus, on platinum, for photons having an energy of 50 eV, the IMFP is 0.5 nm but can reach up 2.2 nm for photon having an energy of 2000 eV (Figure 3.8). It turns out that the information depth is about 1.5 nm at 50 eV but is 6.6 eV at 2000 eV.

XPS and UPS are based on the same principles but use two different photon sources, $\sim$ 1000-2000 eV for X-Ray sources (XPS) and $\sim$ 5-50 eV for UV sources (UPS). XPS can provide an information depth of a few nanometers (max: 10 nm) and can eject electrons from the materials having high binding energy. Thus, XPS is more adequate for studying the core electronic structure or for interface experiments. On the contrary, UPS is much more surface sensitive. UPS can bring valuable information about the electronic structure in the valence band and the surface electronic structure dependence on the surface termination. In addition, along this thesis, UPS measurements were performed to also determine the workfunction.

DAISY-MAT system description

DArmstadt's Integated SYstem for MATerial Science (DAISY-MAT) is an UHV integrated system where deposition chambers and XPS/UPS chambers are all interconnected (Figure 3.9). This means that the vacuum is not broken when samples are transferred from, e.g., the deposition chambers to the XPS/UPS. The system has the great advantage to be able to study the surface electronic structure of the material by photoemission without surface contamination (C, OH, H_2O...). Thus, surface properties are not hindered by

[2] https://en.wikipedia.org/wiki/Photoemission_spectroscopy/

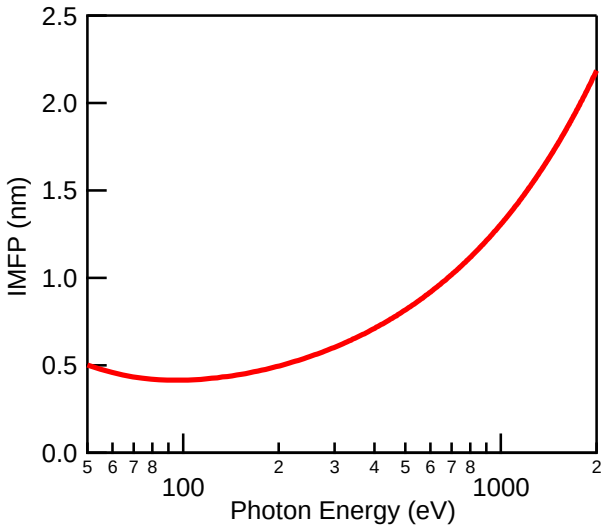

Figure 3.8: Inelastic Mean Free Path (λ) in platinum according to photon energy as determined by Powell et al. [156]. High energy photons possess a higher attenuation length than low energy photons. Note the minimum around 100 eV.

external compounds.

In the DAISY-MAT system, the Fermi energy can be determined either by in-situ XPS or in-situ UPS. The Fermi energy was estimated by extrapolating or fitting the edge defining the highest occupied electronic state (the valence band maximum) of the photo-emission spectra (Figure 3.10).

Another properties which can be measured accurately in the DAISY-MAT system is the workfunction ϕ. This was realized by in-situ UPS. The workfunction was determined with the sharp edge provided by the secondary emission electron cut off (Figure 3.10, right). The sharp cut off arises when the energy of scattered electrons interacting with the surface material is lower than the workfunction. Physically, in the vicinity of the surface of the material, the electrons with low energy are captured and cannot escape the surface.

Furthermore, because of the specific architecture of Daisy-MAT, it is possible to interface two materials of different nature and observe how bands align at the interface under the consequence of the electrostatic strength between the two materials. The experimental procedure rely on the use of XPS which has a deeper information depth. The idea being to deposit on one material a thin layer of another material (<1 nm) and observe how the electronic states shifts. In increasing sequentially the thickness of the deposited material, one can observe a gradual shift of the binding energy of the electronic states at the interface. From this experiments, it is possible to determine the band alignments at the interface [9, 100].

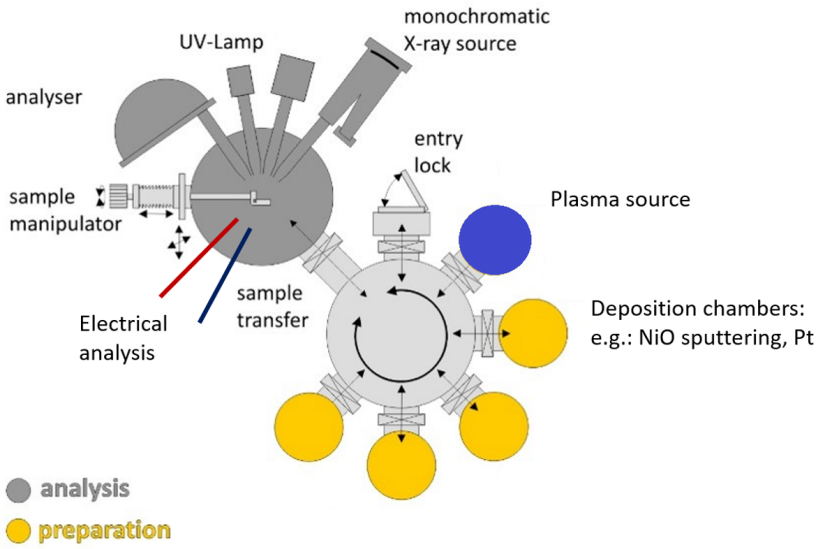

Figure 3.9: Schematic of the DAISY-MAT system: the deposition chambers are coloured in yellow, the distribution chamber in light grey and the XPS/UPS chamber in dark grey. All parts are maintained in UHV condition allowing to transfer samples from one part of the system to the other without breaking the vacuum.

XPS and UPS setups in DAISY-MAT

Photo-electron spectroscopy is performed in the DAISY-MAT system with an angle of 45 ° between the incident photon beam and the normal of the sample surface. The angle between the incident photon beam and the analyzer is fixed to 90°.

XPS was operated using Al K-α monochromatic X-Rays ($h\nu$=1486.6 eV). For surveys, the whole spectral region is analysed (Figure 3.7, right). The pass energy and step width of the scans were respectively set to 187.85 eV and 0.185 eV. Insight in the core levels and valence region were obtained by restraining the binding energy range to a narrow window around the state of interest as shown in left plot in Figure 3.10. Thus, pass energy and step width of the scans were set to 5.85 eV and 0.05 eV, respectively. During the measurements, the XPS chamber pressure is maintained in the 10^{-9} Torr range.

UPS uses a Helium discharge lamp emitting UV radiation of $h\nu$=21.22 eV. Pass energy is set to 2.95 eV but step width is kept at 0.05 eV. A bias of -4 V is applied to the sample in order to provide additional kinetic energy to the electrons escaping the sample surface, particularly for the electrons having a binding energy close to the secondary emission cut off. UP spectra are constantly measured at 4.5×10^{-8} Torr.

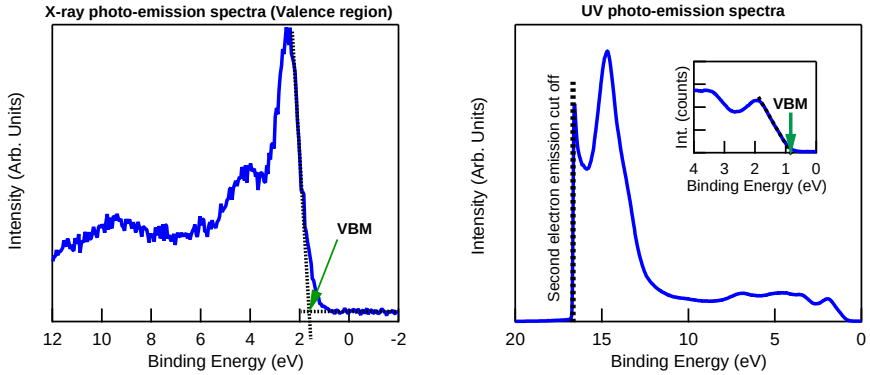

Figure 3.10: Left: Typical in-situ XP spectra near the valence band maximum (VBM) of a NiO thin film. Extrapolation of the VBM value is realized by linear extrapolation of the VBM edge (doted line). Right: Typical in-situ UPS spectra. VBM is also determined by linear extrapolation of the VBM edge (subwindow) and workfunction is measured according to the value of the secondary electron emission cut-off.

Silver standard is measured daily for calibration of the XPS/UPS. After Argon plasma cleaning for 10 min, Fermi edge and Ag 3d peak position values are recorded with XPS/UPS. The values obtained with the Ag standard are used to correct experimental data with a dedicated home-made IGOR[3] macro.

3.3.2 Electrochemical measurements

Introduction

The NiO thin films and the photo water-splitting devices were studied towards their Oxygen Evolution Reaction (OER) performance by electrochemical means.

During electrochemical characterization of a material, electrochemical reactions on its surface are generated and measured. The experiments are realized in an electrochemical cell filled with an electrolyte. The electrochemical cell is made of three electrodes [135]: the working electrode (the studied sample), the counterelectrode (generally a platinum wire) and the reference electrode as depicted in Figure 3.11 (left). The electrochemical characterization is driven by a potentiostat. The potentiostat can be simply represented as an operational amplifier, which adjusts the current going through the working electrode such that the potential relatively to the reference electrode is equal to the input signal provided by the user (Figure 3.11, left). In general, a commercial potentiostat can work with both DC and AC signals. Thus DC mode is used to realize cyclic voltammetry, which basically consists in obtaining current-voltage characteristic of the working electrode, and the AC mode is used to study the

[3] `https://www.wavemetrics.com/`

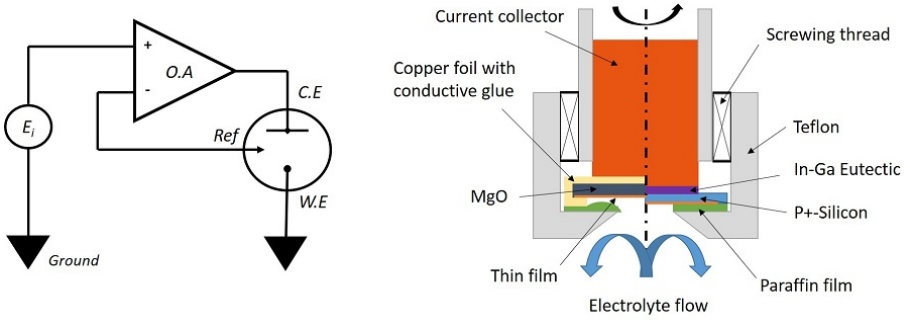

Figure 3.11: Left: electrical representation of the electrochemical cell with the working electrode (WE), counter-electrode (CE) and the reference electrode (Ref) with its electronic hardware (the potentiostat) simplified into an operational amplifier driven by a potential input (E_i). Right: schematic representation of the rotating disk electrode for, the left half, in-plane (MgO/Pt) conductive substrate or for, the right half, out-of-plane (p^+-silicon) .

sample with transient current, e.g.: Electrochemical Impedance Spectroscopy (EIS). Electrochemical characterization can be made of different steps, which aim at conditioning the cell and quantify different properties of the working electrode.

Electrochemical cell design

Two electrochemical cells have been used to characterize the samples. Both of them allow to study the sample in the dark and under illumination.

The first design (Figure 3.12, left) was elaborated at UCL and enabled to expose to a beam of light a sample mounted on a rotating disk electrode (RDE). This mounting system enabled to flush out bubbles formed by the OER from the sample surface and to reduce diffusion limitation issues at high over-potential. A gas inlet was also integrated in order to work with an O_2 saturated solution or with an O_2 depleted solution. In the former case, humid O_2 (saturated with H_2O) was bubbled and for the latter this was humid N_2. Saturating the gas with water beforehand is necessary. Otherwise dry gas would evaporate water from the solution and the solution concentration would evolve over time. The samples mounted on the RDE are back-contacted with In-Ga eutectic if p^+-silicon substrate is used and front-contacted with conductive copper tape for the MgO/Pt based samples Figure 3.11, right). The sealing in both mounting system is realized with a paraffin film[4], which is heavily pressed by screwing the top part of the RDE tip (Figure 3.11, right).

The second electrochemical cell design is commercially found under the

[4]Note from the author: During the private defense, Pr. M. Chatenet raised concern about the fact that the paraffin could poison the electrode. Paraffin might be not the best material for sealing the front of the tip of the rotating disk.

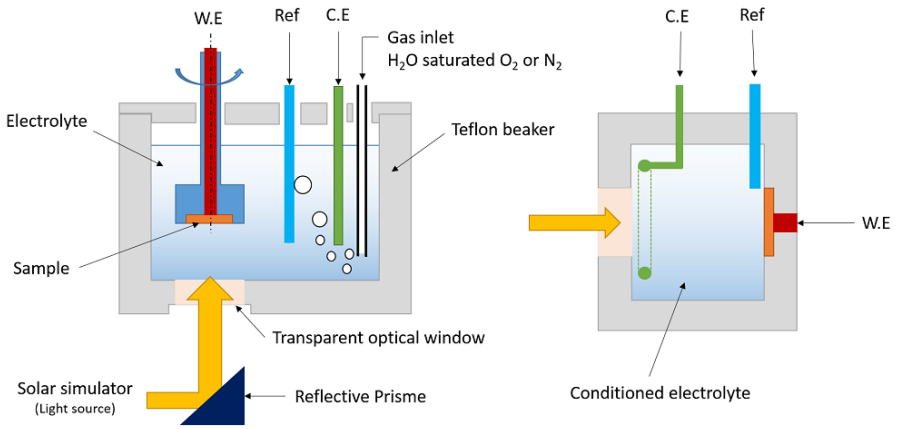

Figure 3.12: Electrochemical cell design at UCL (left) and at TU-Darmstadt (right). UCL design rely on the use of a RDE and sample is illuminated from the bottom. Contrary to UCL design, in the TU-Darmstadt electrochemical cell design the electrolyte is not bubbled and no electrolyte flow is forced but the reference electrode is located near the sample surface. Therefore, UCL design has been mainly used for OER characterization and the TU-Darmstadt one for adsorption reaction characterization.

name PECC-2 (Zahner PEC-Cell)[5] and is available in the electrochemical laboratory at TU-Darmstadt (Figure 3.12, right). In this design, the sample is static and no flow is forced in the electrolyte. Thus, the electrolyte is conditioned before being inserted into the electrochemical cell in bubbling either humid nitrogen or humid oxygen for several minutes in a beaker.

The first cell design has been used to perform the OER characterization of the samples, whereas the second design was focused with experiments related to the adsorption processes in the window stability of water. Unfortunately, because of lack of time, no experiments under light have been carried out with the first design to evaluate the performance of the final PEC water-splitting structure. Instead PEC water splitting characterization was roughly assessed with the second design taking as solar simulator a LOT-quantum 51 $\times$ 51 mm^2 field.[6]

As the temperature of the room at UCL was not regulated, the temperature of the solution is adjusted with a self-regulated hot plate. Thus, the temperature of the electrolyte was maintained to 25°C, which was supposed to be the maximum temperature reached during summer period. On the contrary, at TU-Darmstadt, the room temperature is maintained to 20°C and so the temperature of the electrolyte did not need to be regulated.

[5] `http://zahner.de/products/photoelectrochemistry/pec-cells.html`
[6] `https://lot-qd.de/en/`

3.3.3 Atomic Force Microscopy

Atomic Force Microscopy (AFM) is a high resolution scanning-probe microscopy method. The resolution can be as low as a few nanometers and allows to obtain high quality topographic images of the surface and also to determine material properties, in particular inhomogeneities (grain boundaries, stiffness, conductivity...). AFM can be found in a variety of configurations and can be used to study soft materials (stem cells, polymer) and harder material (thin films) as well. It can be adapted to study samples in solution or in air[7].

The setup used to take AFM images of the NiO thin film employed piezoelectric excitation of a cantilever, for which interaction to the sample surface is measured by the deflection of a laser in air. Phase and height images were obtained in tapping mode and measurement was set so that the cantilever works in repulsive condition.

The AFM images were obtained with a μmasch (HQ:NSC15/Al-BS) cantilevers. The free amplitude of the cantilever is 1500 mV, the scan rate during acquisition is 5 μm/sec, the amplitude sensitivity is 69 nm/V and the thermal tune of the cantilever is 46.5 N/m.

3.4 Bulk characterization

3.4.1 In-situ stress measurements

The AJA sputtering system at UCL is equipped with a Multi-beam Optical Stress Sensor (MOSS) setup which allows in-situ stress measurement during the film growth. A detailed explanation of the method and the setup used at UCL has been extensively described by Proost *et al.* [157].

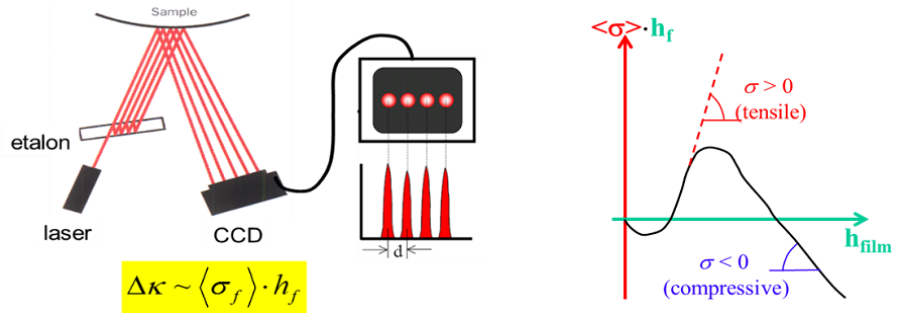

Figure 3.13: Left: schematic representation of the in-situ stress measurements setup on the sputtering chamber in the UCL. Right: typical in-situ stress measurements where a positive slope denotes a tensile regime and a negative slope a compressive regime. Taken from Proost et al. [157].

[7] https://en.wikipedia.org/wiki/Atomic_force_microscopy

Basically the preparation of an hetero-junction can lead to the formation of an internal stress. It can have diverse origins: defects in the thin film, lattice mismatch between the two materials, wetting properties of the substrate, intercalation of energetic particle on the top of the thin film growth... Thus, the internal stress developed in the thin film can produce at a macro-scale a curvature of the substrate. The curvature can be monitored in time with the MOSS system at UCL. The principle consists in producing an array of lasers directed onto the sample surface (Figure 3.13). The relative spacing $D(t)$ of the reflected arrays over time is directly related to the evolution of the internal stress developed in the thin film. Having D_{t_0} the initial position of the centroid (center of spots before thin film deposition), G the optical constant defining the MOSS set-up (determined as being 0.68 m at UCL), the relationship between $\Delta K(t)$, D_{t_0} and $D(t)$ is given by:

$$\Delta K(t) = G\,\frac{D(t) - D_{t_0}}{D_{t_0}} \tag{3.3}$$

Using the Stoney equation, it is possible to access the average internal stress $< \sigma_f >$ at any time t:

$$\frac{Y_s\, h_s^2}{6}\Delta K(t) =< \sigma_f(t) >\ h_f(t) = \int_0^{h_{f(t)}} \sigma_f.dh_f \tag{3.4}$$

With Y_s being the biaxial modulus of the substrate taken equal to 182 GPa for silicon (100), h_s and h_f are respectively the substrate and the thin film thickness, and $< \sigma_f >$ the mean stress in the NiO thin film. For having a better readability of the data, it is common to plot the stress thickness $< \sigma_f > .h_f$ against film thickness h_f. According to the slope of the stress thickness product, it is possible to identify different deposition regimes and to determine the type of stresses developing in the thin film. Thus a positive slope highlights tensile stress whereas a negative one highlights compressive stress (Figure 3.13, right). Compressive stress can be related to lattice mismatch at the interface and impinging of energetic particle in the top 3 nm of the already formed thin film (shot-peening effects) [158], or an excess of adatoms at grain boundaries for high adatom surface mobilities [159]. On the contrary tensile stress can be produced if the substrate surface tension is lower than the deposited thin film which would generate in the early stage of the film formation the so-called Volmer-Weber growth zipping process [158, 160].

3.4.2 X-Ray Diffraction measurements

X-Ray Diffraction (XRD) aims at studying crystallographic structure of materials and can provide information about average grain size, amorphousness, internal stress and, over all, the surface orientation.

The technique uses X-rays for which wavelengths are short enough to interact with the atomic spacing of the material (elastic scattering). If the material adopts a regular structure with specific interatomic planes, then the

X-rays can be constructively diffracted, as represented in Figure 3.14 (left), following Bragg's law[8]:

$$2d \sin\theta = n\lambda \tag{3.5}$$

With d the interplane distance, θ the angle of incidence (and reflection), λ the X-ray wavelength and n an integer.

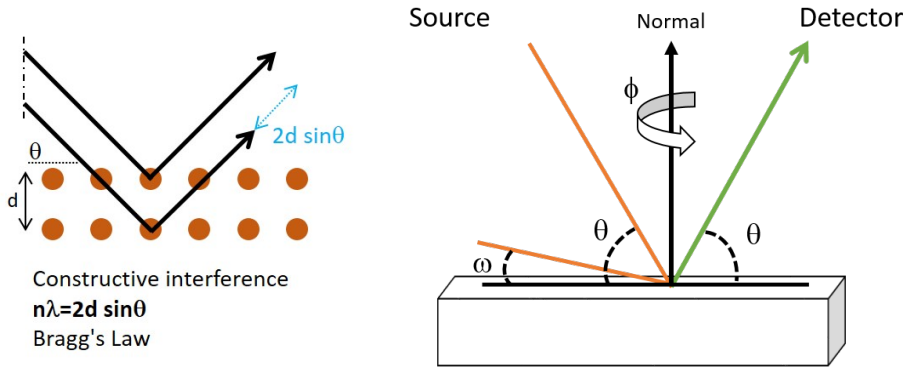

Figure 3.14: Left: X-Ray diffraction principle in a regular crystal structure according to Bragg's equation. Right: representation of the angles, relative to the normal of a surface, defining XRD measurements.

The $\theta/2\theta$ scan

When the angle of incidence θ of the X-Ray source is varied, e.g.: from 20° to 90°, any time Bragg's law is fulfilled a diffracted X-ray is detected. According to the position of the reflected X-ray relative to the incidence angle θ, it is possible to calculate the interplane distance of the material. The measurement is often referred to as $\theta/2\theta$ scan as the incident to diffracted X-ray angle is 2θ (Figure 3.14, right). From the resulting pattern, one can assess what is the preferential thin film orientation but also the measurement can be used to quantify further the thin film crystallographic structure, in particular the residual thin film stress, the grain size and the amorphousness.

- Stress: interplane distance can be shortened or extended depending if the film is under compressive or tensile stress, respectively, along the normal of the surface of the sample. In such case, the diffraction angle θ would be shifted to higher or lower angle relative to the reference angle. The reference angle is the angle for an interplane distance where the material is not subjected to strain. The thin film stress can be estimated if the interplane distance for a perfect crystallographic structure and the

[8] `https://en.wikipedia.org/wiki/Bragg's_law`

Young modulus are known beforehand. Then the out-of-plane stress can be calculated as follows:

$$\sigma = E\frac{d - d_0}{d_0} \tag{3.6}$$

Where E is the Young modulus of the material, d_0 the interplane distance for a stress-free condition and d the interplane distance for the constrained material. This method could not be applied to NiO, as there was too much uncertainty on both the d_0 value (see Section 2.2.1) and its Young modulus. However, XRD peak deviation to lower diffraction angle would indicate out-of-plane tensile stress and, reciprocally, a peak deviation to higher diffraction angle would indicate out-of-plane compressive stress.

- Grain size: average grain size of nanocrystalline compounds can be estimated from the Scherrer equation taking the FWHM of the diffracted peak[9]:

$$\tau = \frac{K\lambda}{\beta cos(\theta)} \tag{3.7}$$

Where τ is the average grain size, K a shape factor, λ the X-ray wavelength, β and θ are respectively the FWHM and angle position of the diffracted peak. Although this formula has been used to determine grain size in thin film, it might be rather risky. Indeed, the FWHM broadening can also arise from stress inhomogeneity, defects (dislocation, stacking fault) etc... and these factors can have a relatively large weight in thin films. Instead, the Scherrer equation might be more adequate to be used for quantifying powder. For this reason, the Scherrer equation has not been used to determine average grain size in the NiO thin films.

The ω scan

In complement to the $\theta/2\theta$ scan, surface texture can be estimated by grazing incidence XRD (GIXRD). It consists of an asymmetric scan where the angle ω of the incident light to the surface of the sample is fixed, while the detector angle varies by an angle θ (Figure 3.14, right). For low ω angle ($< 5\,^\circ$) the diffracted angle arises from tilted orientation (not normal to the surface). For instance in the NiO non-oriented poly-crystalline thin films, the angle of diffraction of the 111, 100 and 110 can be measured as the thin film is not textured along the normal to the surface. On the contrary, for highly oriented thin films, being textured in the direction of the normal to the surface, no diffraction angle can be observed for the 111, 100 and 110 orientations. Thus low ω angle scans have been performed, in particular, to evaluate the quality of the oriented thin films in Chapter 7.

XRD setup

At UCL, the XRD device is a Bruker, D8 Advance using a Cu X-ray source of 8.04 keV, which corresponds to a wavelength of 1.5406 Å. The measurements were restrained into the collection of $\theta/2\theta$ scans of non-oriented NiO thin

[9] `https://en.wikipedia.org/wiki/Scherrer_equation`

films.

As the work in TU-Darmstadt was mainly focused on the study of oriented NiO thin films, in complement to $\theta/2\theta$ scans, ω scans were carried out. XRD $\theta/2\theta$ scans were performed with a Seifert PTS 3003 diffractometer using a Cu anode and an X-ray mirror on the primary side. On the secondary side, a long soller slit and a graphite Monochromator were used to separate the Cu K-α line. The XRD was operated at 40 mA and 40 kV.

3.4.3 UV-VIS measurements

The reflectance measurement was realized with a 6° angle between the incident light and normal of the surface, while for the transmittance measurement, the incident light is set parallel to the normal of the surface.

The absorption coefficient (α) was determined from the transmittance ($T(\lambda)$) and the reflection ($R(\lambda)$) (λ is the wavelength), following the equation:

$$\alpha(\lambda) = \frac{1}{t} \ln\left(\frac{1 - R(\lambda)}{T(\lambda)}\right) \tag{3.8}$$

with t being the thickness of the thin film and λ the wavelength. The optical band gap (E_g) was derived from the adsorption coefficient using the so-called Tauc's relationship [161]:

$$(\alpha h\nu)^{1/n} = \alpha_0(h\nu - E_g) \tag{3.9}$$

where n is the power factor of the transition mode, h is the Planck constant, ν the frequency and the product $h\nu$ is the energy of the photon. Regarding nickel oxide, it seems that the adequate value of the power factor n is 1/2, which corresponds to a direct optical transition accross the band gap [90, 94, 96, 162]. Extrapolating the linear part of the $(\alpha h\nu)^{1/n}$ edge to zero provides the optical band gap E_g of the material [96, 161].

3.4.4 Electrical measurements

Four probes measurements

The nickel oxide thin films deposited on insulating substrate were electrically characterized with a four probe setup (also called Four Point Probe Resistivity Measurements) when the thin films conductivity was high enough. As the name indicates, the setup is made of four probes, aligned and equally spaced, where the two outer probes are used as current source and the two inners probe are used for voltage measurements (Figure 3.15, left). In this way, the outer probes measure a potential drop generated by the current source in the thin films. The relationship between the thin film resistivity(ρ), the thin film thickness (t), the voltage (V) and the current (I) is:

$$\rho = \frac{\pi}{\ln(2)} \left(\frac{V}{I}\right) t \tag{3.10}$$

Transmission line measurements

When the NiO thin films were not enough conductive enough, the transmission line measurement (TLM) was instead adopted. The TLM method consists in depositing, e.g.: by sputtering, parallel metallic stripes on the NiO thin films where the space between each stripes increases but the dimensions of the stripes are identical (Figure 3.15, right). By measuring the total resistance (R_T) for different spacing between stripes (d), it is possible to determine the contribution of the contact resistance (R_c), between the metallic contacts and the thin film, from the thin film resistivity (ρ) following [132]:

$$R_T = 2\,R_c + \frac{\rho}{W\,t}d \tag{3.11}$$

with t the thickness of the thin film and W the length of one stripe. Plotting $R_T = f(d)$ provides a linear curve where the intercept with the Y-axis corresponds to $2\,R_c$ and the slope is equal to $\rho/(W\,t)$. This method enables to measure thin film resistivity where the four probes measurement method fails. The reason could be that the surface of the contact between the probes and the thin film is higher for the TLM method as the contact is defined by the area of the metallic stripes, whereas for the four probes measurement, the contact is reduced to a point.

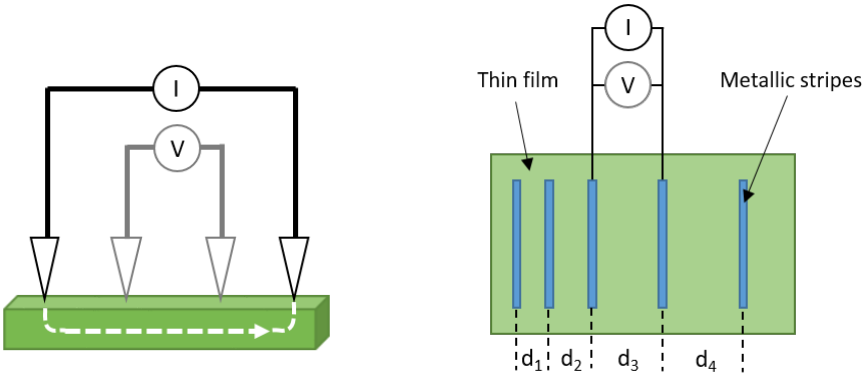

Figure 3.15: Schematic of the setup for the four probes measurements (Left) and the transmission line measurements (Right).

Temperature dependent conductivity measurements

Temperature dependent conductivity measurements have been conducted on NiO thin films at TU-Darmstadt. The setup can measure conductivity in a controlled atmosphere in a furnace regulated by an Eurotherm temperature controller [11] (Figure 3.16). Beforehand, platinum contacts are deposited at

the corners of the sample in the Van der Pauw geometry. Once the sample is mounted on the sample holder specially designed for the measurements and inserted in the furnace, a programmed thermal cycle is ran and conductivity is measured in the span time. For the NiO samples produced along this thesis, the temperature is ramped up to 500 °C at 1 °/min, then the temperature is held at 500 °C for 1 h before that the furnace is cooled down at 1 °/min. Two atmospheres have been used: pure Argon and 10 % oxygen (1:9, O_2/Ar). A more detailed description of a similar setup for conductivity temperature dependence experiments is presented in the work of Hohmann *et al.* [11].

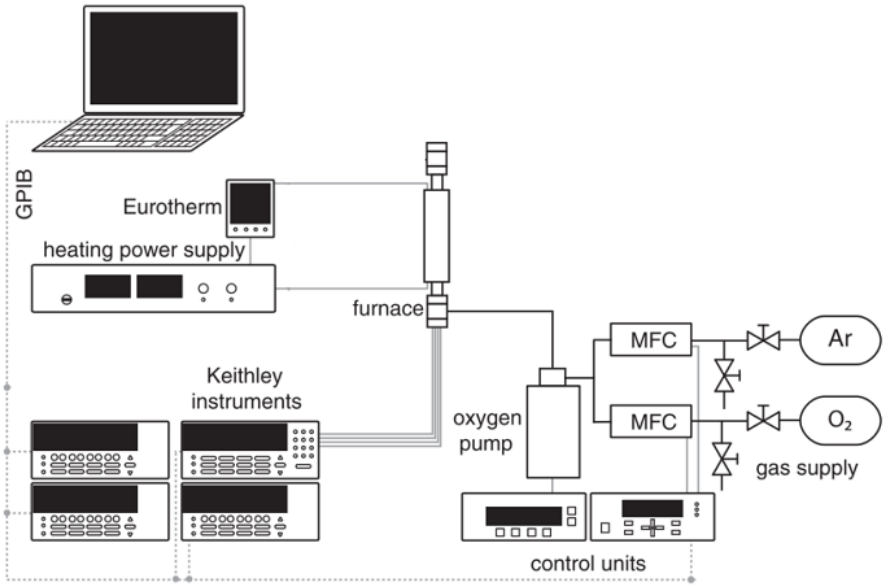

Figure 3.16: Schematic representation of the conductivity temperature dependence setup. The schematic has been adapted from the work of Hohmann et al. [11].

Electrical impedance spectroscopy and IV curves

Electrical impedance spectroscopy and IV measurements were performed on the Schottky junction which back-contacting by phosphor diffusion beforehand. Both measurements were conducted in the same probe station for electrical characterizations (Figure 3.17).

The measurements were realized in the dark with an Agilent 4294A impedance analyser from 40 Hz to 10 MHz at different polarization potential in four probes configuration terminal. Fitting of the impedance spectra is made with simple Randles elements with, after files conversion, the Echem Analyst Software. From the electrical impedance spectroscopy, the contact resistance (R_c), the equivalent capacitive element C_{meas} and the equivalent resistance at the Schottky diode R_{meas} were determined by fitting the experimental data

with a simple R+R//C circuit as presented in Figure 2.20 of the Section 2.4.2. Fitting provided error value representing less than 0.1% of the absolute values, which meant that the fits were reliable.

The IV curves were obtained with an Agilent 4156C semiconductor parameter analyser in a two probes configuration and the potential was swept from -1 V to 0.5 V. Although the connectors were not absolutely the same, it has been assumed that the value of the contact resistance (R_c) estimated by impedance spectroscopy could be used for iR correction of the IV curves.

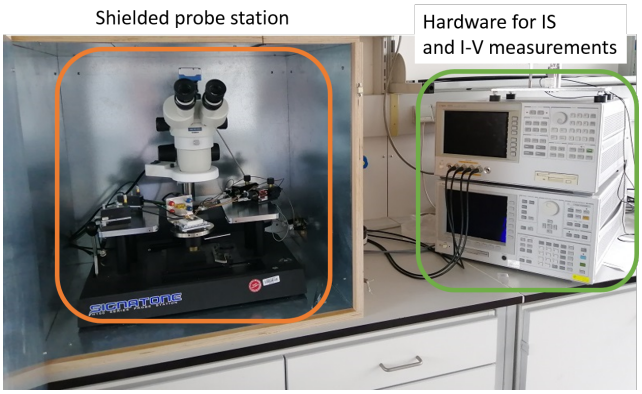

Figure 3.17: Picture of the electrical setup for the electrical impedance spectroscopy (IS) and the IV measurements. The samples are measured in the electromagnetic-shielded probe station.

CHAPTER 4

Defects and charge compensation in nickel oxide

Summary

Let's start to introduce the results obtained during this thesis by a general approach of the NiO thin films surface properties. In this chapter the numerous in-situ UPS/XPS measurements acquired on NiO thin films reactively deposited by DC-sputtering are compiled. The study endeavour at unveiling relationship between the workfunction, the Fermi energy, and electronic features in the O 1s region and the Ni 2p region.

Defective states, named O 1s(Def.), have been observed which would arise because of the introduction of defects. The defective state O 1s(Def.) can be eliminated at high temperature and low oxygen concentration (10 %) in the deposition chamber but it is prominent at room temperature and high oxygen concentration (20-25 %). The weight of the O 1s(Def.) in the O 1s region would define the surface electronic properties of NiO:

- at low O 1s(Def.) weight the measured workfunction is about 4.5 eV and the Fermi energy is about 1.1 eV above the valence band maximum.
- with increasing O 1s(Def.) weight the Fermi energy is reduced and the workfunction increases to $\sim$ 5.2 eV.
- above a certain O 1s(Def.) weight the Fermi energy is pinned to $\sim$ 0.6 eV and the workfunction is constant ($\sim$ 5.2 eV)

Eventually, a charge compensation of the dopants (nickel vacancies and maybe oxygen interstitials) has been proposed and can be summarized as following:

- at low dopant concentration, charge compensation is obtained by free holes and positive charges localized on oxygen atoms.
- when the dopant concentration is large, the Fermi level position is pinned to 0.6 eV and the insertion of dopant is compensated by the formation of peroxy species O^- and probably to a lesser extent, by the formation of Ni^{3+}, but not necessarily by free holes.

4.1 Introduction

NiO is a transition metal oxide (TMO) having a wide optical band gap (3.6-4.3 eV) for which the resistivity, in a defect-free structure, can reach up to 10^{13} Ω cm [50] and 10^{7} Ω cm at 1 kHz [73]. However, when sputtered at low temperature ($\lesssim$ 200°C), NiO thin film conductivity in the 0.1-1 Ω cm range can be measured [87, 95, 163].

NiO can be p-doped by holes in a metal deficient structure ($Ni_{1-\delta}O$), which can be obtained in an oxygen-rich environment. In such a case, NiO can be intrinsically doped by nickel vacancies (V''_{Ni}) or by oxygen interstitials (O''_i) [82, 83]. Moreover, for charge neutrality, intrinsic doping of NiO has to be compensated by positive charges, e.g. Ni^{3+}, O^{-}, holes [83], or oxygen vacancies. Taking Kröger-Vink notation, this can be formalized as following:

$$2\,[V''_{Ni}] + 2\,[O''_i] = [h^{\bullet}] + 2\,[V^{\bullet\bullet}_{O}] + [Ni^{\bullet}_{Ni}] + [O^{\bullet}_{O}] \tag{4.1}$$

where '[ ]' correspond to the concentration of the species per volume. Equation 4.1 is only a general view of the defect chemistry, which can develop in nickel oxide. The left-hand side of equation (4.1) are electronic defects (the dopants), which can be introduced in nickel oxide under oxygen-rich condition while the right-hand side represents the charge compensating species of the dopants.

Regarding the left-hand side (the dopants), Lany *et al.* have shown that in NiO crystal, under oxygen rich condition, nickel vacancies V''_{Ni} and not oxygen interstitials O''_i, are the defects leading to nonstoichiometry [82]. It is generally accepted that p-type conductivity in NiO originates from nickel vacancies V''_{Ni} [83, 164, 165]. However, in most cases, the NiO thin films produce grain boundaries and to the best of our knowledge, the possibility of stabilizing oxygen interstitials at the grain boundaries of a nickel oxide thin film has not yet been discussed in literature. Therefore, a non-stoichoimetry associated to oxygen interstial at the grain boundaries cannot be excluded as will be discussed in the Chapter 5.

Regarding the right-hand side of equation (5.1), associated to the compensating species, in reality the stability of each compound is not the same as charge compensation is driven by thermodynamic rules, which would promote the formation of charge compensation having the lowest formation energy. The question is therefore, what is the most stable charge compensation mechanism of intrinsic doping in nickel oxide?

The answer to this question in the literature might be elusive as the studies are often carried out on only one type of sample or in a limited range of conditions [83, 87]. However, it can be assumed that the formation of oxygen vacancies $V^{\bullet\bullet}_{O}$ in oxygen rich conditions, is very unlikely. Moreover, in a NiO thin film prepared at room temperature, it has been proposed that delocalized holes (free holes) would be interacting with oxygen atoms and localized holes might be found on both nickel and oxygen atoms [83]. These

results would suggest that the dopants in NiO (left hand side of equation (5.1)) can be compensated by free (delocalized) holes ($h^{\bullet}$) interacting with oxygen atoms, and by localized holes on oxygen ($O_O^{\bullet}$) and nickel ($Ni_{Ni}^{\bullet}$) atoms.

Although NiO can be adopted in various applications, clarification needs to be brought about the intrinsic charge compensation mechanism in nickel oxide. This chapter presents the compilation of results obtained by in-situ XPS/UPS measurements, realized in the DAISY-MAT system, with various NiO thin films prepared by reactive sputtering. Therefore, this chapter endeavours at emphasizing the impact of the temperature and the oxygen concentration during sample preparation on the measured surface electronic properties. The aim is to explore how the condition of deposition affects the NiO surface electronic properties measured by in-situ UPS/XPS. Eventually, the work provided enough clues to propose a charge compensation mechanism of nickel vacancies in NiO.

4.2 Experimental

The compilation includes the experimental results obtained with oriented NiO thin films and non-oriented polycrystalline NiO thin films deposited on silicon, fluorine doped tin oxide (FTO) and gold substrates. All the thin films were prepared in the DAISY-MAT system of TU-Darmstadt and measured in-situ by UPS/XPS as described in Chapter 3.

The oxygen concentration in the atmosphere of deposition ranges from 5 % to 20 % if the thin films are deposited at room temperature. If deposited at 200 °C and 400 °C, only results of samples prepared with more than 10 % of oxygen are selected. The orientation of the thin films and the nature of the substrate were not treated as being a significant factor. Therefore this chapter is primarily focused on the workfunction, Fermi energy values and the electronic features in the O 1s region and the Ni 2p region.

4.3 Results

4.3.1 The O 1s spectra

The O 1s spectra (Figure 4.1) are basically composed of two components. The O 1s photoemission from oxygen atoms in the lattice (O^{2-}), labelled O 1s(Main), is the most intense peak with a binding energy of about 529-530 eV (Figure 4.1). At higher binding energy to the main peak, a shoulder is observed, which is assigned, in this thesis, to defective electronic states (labelled O 1s(Def.) in Figure 4.1). The spectra in Figure 4.1 are arranged according to the weight of the O 1s(Def.), which can vary from $\sim 0\%$ to about 30% depending on the condition of preparation. The defect emission is particularly prominent for samples prepared at room temperature and high oxygen concentration. Its intensity is likely correlated with both temperature and oxygen concentration

in the deposition process. It is evident from Figure 4.1 that, for moderate O 1s(Def.) weights, the peak position O 1s(Main) shifts to lower binding energy with increasing O 1s(Def.) weight.

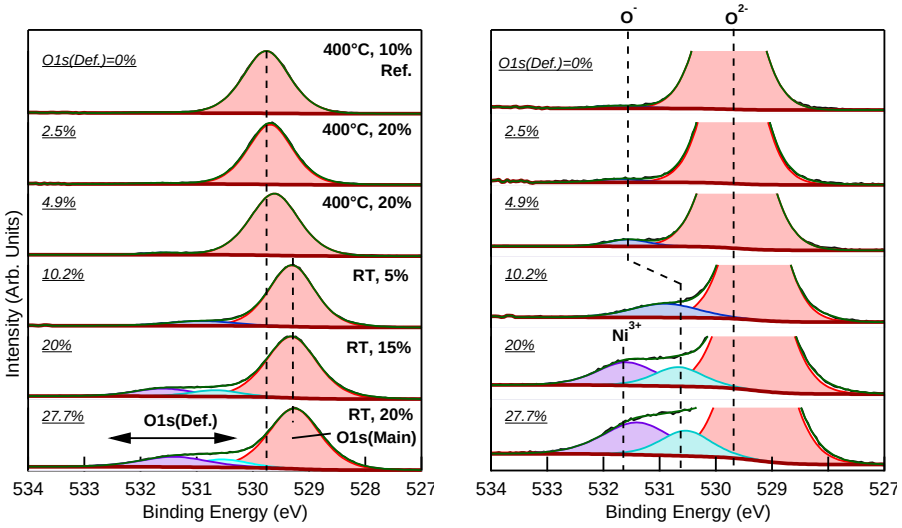

Figure 4.1: O 1s region measured by in-sity XPS. The spectra can be decomposed into photoemitted electrons from NiO crystal structure (O^{2-}) and from defective electronic state (O 1s(Def.)). The patterns are sorted out with increasing O 1s(Def.) weight (%) calculated over the total O 1s region. With increasing O 1s(Def.) weight, it can be seen that the O 1s(Def.) region is composed of one component in the beginning but of two components for larger O 1s(Def.) weights. Temperature of deposition and the oxygen concentration in (%) during the thin film preparation are indicated in the right part of the left plot. The right plot is a magnified view into the O 1s region deconvolution. The assignment of the electronic states in the O 1s(Def.) region are discussed further in the chapter.

More details of the O 1s spectra are given in the right plot of Figure 4.1. Results evidence that the shape of the O 1s(Def.) region can change substantially. For instance, for low O 1s(Def.) weight, the O 1s(Def.) region can be fitted with a single Gaussian-Lorentzian curve but, at higher O 1s(Def.) weight, it seems obvious that there is more than one component. The nature of the shoulder will be detailed further along this chapter but it could be assumed, at first sight, that the O 1s(Def.) region to be associated to peroxo species (O^-), as peroxo species are typically found at higher binding energy than the O 1s(main) peak for transition metal compounds [166].

4.3.2 The Ni 2p spectra

As detailed in Section 2.2.3 and following the work of Taguchi *et al.* [81], the Ni 2p XPS spectra can be decomposed into three main components, which are

assigned to the Ni $2p^5 3d^9 Z$, Ni $2p^5 3d^9 L$ and the Ni $2p^5 3d^8$ orbitals [81](Figure 4.2). Two minor peaks are found in the 864-970 eV regions, their nature have not been identified but their presence were found to be necessary to obtain reasonable fitting of the Ni 2p region. The FWHM of the Ni $2p^5 3d^9 Z$ peak with 1.05 eV is relatively narrow in comparison to the Ni $2p^5 3d^9 L$ and the Ni $2p^5 3d^8$ peaks which are 3 eV and 4.2 eV wide, respectively. In the rest of the study, for simplification, the Ni $2p^5 3d^9 L$ state will be referred to as the satellite peak Ni 2p(Sat.) and the Ni $2p^5 3d^9 Z$ state as the main peak Ni 2p(Main).

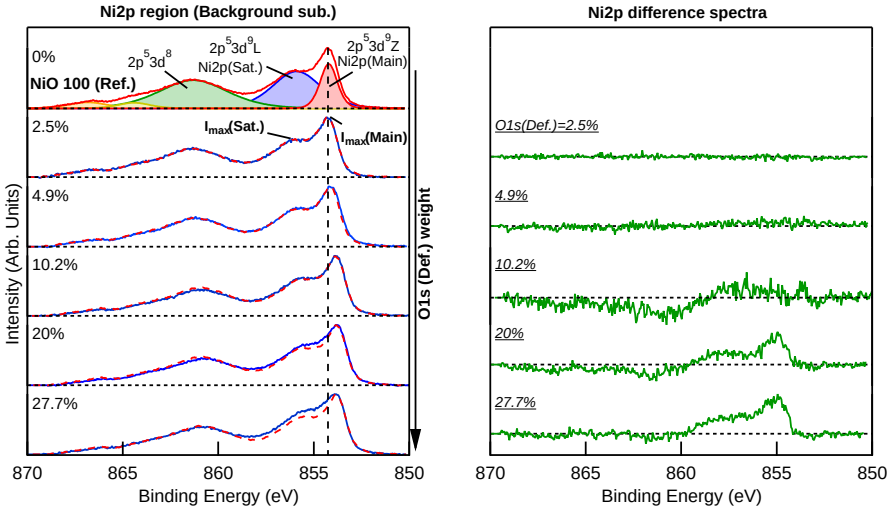

Figure 4.2: Ni 2p region measured by in-situ XPS. The spectra are sorted out according to the weight O 1s(Def.) in the O 1s region (see Figure 4.1). The top spectrum on the left plot is the spectra obtained with a 100 oriented NiO thin film prepared at 400 °C and with 10 % of O_2. This sample has been used as a reference spectra as it is supposed to provide a defect free thin film (see Figure 4.1). The reference spectra has been duplicated and aligned with the main Ni 2p peak of the other Ni 2p spectra. The right plot represents the differences between the actual spectra and the spectrum of the film prepared at 400° C with 10% O_2 (0 % O1s(Def.)). Shirley background subtraction has been used for the XPS data. The conditions of preparation of the samples are indicated in Figure 4.1.

It should be mentioned that the Ni 2p(Sat.) peak cannot be associated to the presence of Ni^{3+} in NiO, contrary to numerous reports misleading the XPS spectra assignment of the Ni 2p region. However, it can be noticed that, with the increase of the O 1s(Def.), the intensity ratio of the Ni 2p(Sat.) over the Ni 2p(Main) increases. As evidenced in the left plot of Figure 4.2, the Ni 2p region is gradually distorted in comparison to the reference sample with increasing O1s (Def.). The difference of spectra with a Ni 2p spectra obtained with a thin film producing no O1s(Def.) emission, evidences the gradual built-up of an extra electronic state between 855 and 860 eV, especially for high

O1s (Def.) weight (Figure 4.2, right). The assignment of this extra-electronic state will be discussed later.

To simplify the notation and to compare the results obtained in the Ni 2p region, the ratio of the maximum intensity between the Ni 2p(Sat.) over the Ni 2p(Main) will be denoted as R_{Ni}:

$$R_{Ni} = \frac{I_{max}(Sat.)}{I_{max}(Main)} \tag{4.2}$$

4.3.3 The valence band spectra

Figure 4.3 provides the valence band spectra obtained with the NiO thin films introduced in Figure 4.1 and Figure 4.2. The shape of the valence band spectra is complicated to interprete, particularly because of the charge-transfer nature of nickel oxide leading to numerous final state transitions during photoexcitation [70, 76–78, 81] (see Section 2.2.3). The nickel oxide valence band is a mixture of $Ni3d^8$ and $O\,2p^6$ orbitals, and, according to literature, the $Ni3d^8$ states are positioned above the $O\,2p^6$ energy band [70, 81]. Again, following the work of Taguchi *et al.* [81], two main final states contribute to the valence band of nickel oxide: the first one arises from holes left in the $Ni3d^8$ orbital after the electron excitation and is denoted as $Ni3d^8Z$, while the second one is due to the transfer of charge from the oxygen (the ligand) to the nickel atom and is referred to as $Ni3d^8L$ if the state is filled by an electron (more details are given in Section 2.2.3). The $Ni3d^7$ orbital remains in its ground state and is located between 6-10 eV under the Fermi level [71] (Figure 4.3).

The valence band maximum can be determined by the linear extrapolation of the valence band edge. The intersection with the X-axis is supposed to provide the value of the valence band maximum (Figure 4.3, left). The method is rather common but zooming into the valence band edge, the recorded spectrum is not totally equal to zero above the VBM determined by extrapolation (Figure 4.3, right). Therefore, the determination of the VBM remains uncertain. However, for comparability reasons, the determination by linear extrapolation is adopted in this chapter.

For moderate O 1s(Def.) weight, as for the O 1s(main) peak, the valence band edge shifts to lower binding energy with increasing O 1s(Def.) weight (Figure 4.3). The valence band maximum is about 1.1 eV when no O 1s(Def.) shoulder is visible in the O 1s spectra. The VBM steadily decreases to 0.65 eV when O 1s(Def.) is $\sim$ 10 % of the total intensity in the O 1s region. Above $\sim$ 10%, only a minor change of 0.1 eV is observed.

4.3.4 The workfunction

The workfunctions measured by in-situ UPS in the DAISY-MAT system show a strong dependence on the temperature of deposition. Typical secondary

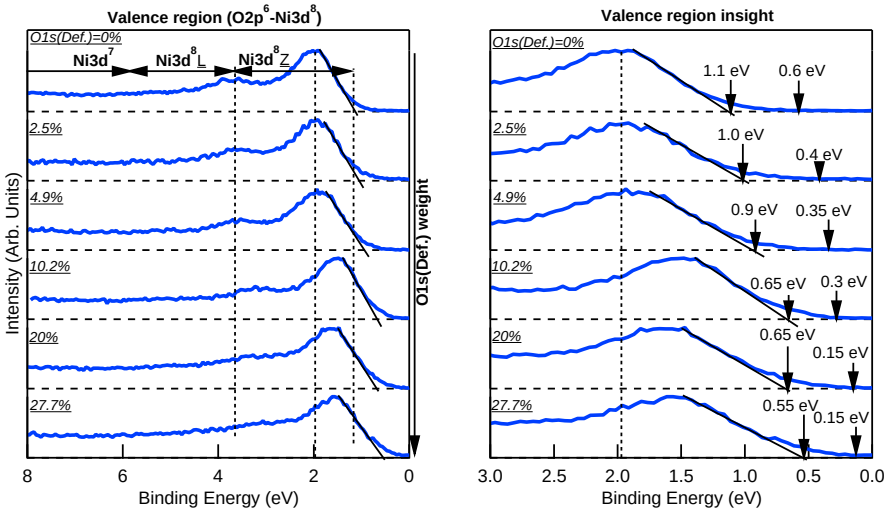

Figure 4.3: Valence band spectra measured by in-situ XPS. The spectra are sorted out according to the weight of the O 1s(Def.) electronic state in the O 1s region. The valence band maximum (VBM) is determined by linear extrapolation of the valence band edge. It can be noticed that the VBM gradually shifts from 1.1 eV to ∼ 0.6 eV with increasing O 1s(Def.) weight. The right plot is a magnified view of the valence band edge, it emphasizes that photoemission at lower binding energy than the VBM is realized. The conditions of preparation of the samples are indicated in Figure 4.1.

electron emission cut-offs obtained for samples prepared at room temperature and at high temperature are shown in Figure 4.4. At 400 °C and for an oxygen concentration larger than 10 %, the measured workfunctions lie around 4.5 eV while for samples prepared at room temperature the workfunction is around 5.2 eV.

The compilation of the workfunction values collected for the numerous samples prepared during the thesis show a clear dependence on the temperature of preparation (Figure 4.8, top). The workfunctions are 5-5.2 eV for the samples prepared at room temperature, while they are ∼ 4.5 eV if the samples are prepared at 400 ° C.

As detailed in the introduction, the deviation from stoichiometry in NiO thin films is mainly due nickel deficiency obtained in an oxygen-rich environment according to the literature. Thus, the accumulation of oxygen at the NiO surface could lead to an increase of the surface workfunction either because of the presence of peroxy species (O^-) on the NiO surface [68] or because of the increase of the cation electro-negativity when it gains oxidation state (e.g.: $Ni^{2+} \rightarrow Ni^{3+}$) [167]. In general, as a rule of thumb, more oxidized surfaces exhibit a higher workfunction as it would increase the ionization potential [168]. Therefore, it could be said that the higher workfunction could

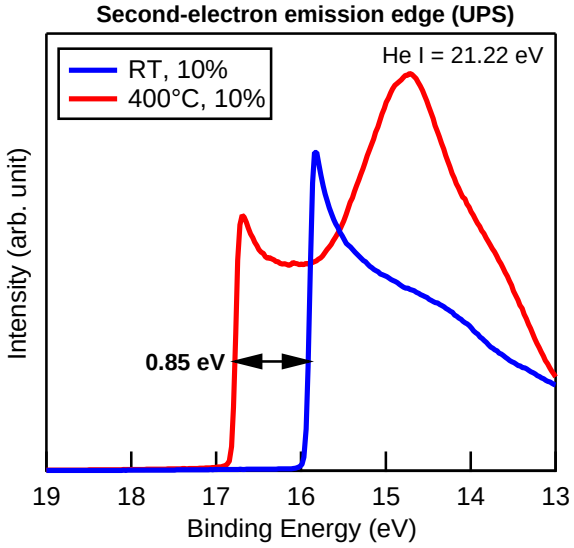

Figure 4.4: Secondary electron cut-offs measured by in-situ UPS for two samples prepared at room temperature and high temperature (400 °C). The secondary electron cut-off is at 0.85 eV higher binding energy for the sample prepared at high temperature in comparison to the sample prepared at room temperature.

arise from the accumulation of oxygen on the surface as the preparation of the samples at room temperature leads to the formation of more oxidized material. This could be put in perspective with the general rule that the heat tends to convert oxidized material into more reduced form, and so the most oxidized materials are obtained at low temperature.

4.3.5 Electrochemical measurements

Electrochemical experiments are realized on non-oriented polycrystalline NiO thin films ($\sim$ 50 nm) deposited on oxide free p^+-doped silicon. Two samples have been compared, for which one sample has been prepared at room temperature and 15% of oxygen whereas a second sample has been prepared at 400 °C and with 15% of oxygen. The results in this section are actually the data obtained in the activation part (first stage) of the electrochemical characterization of the samples towards the oxygen evolution reaction as detailed in Section 10.3.

The electrolyte was an ultra-pure 1.0 M KOH solution prepared from KOH pellets (Semi-conductor grade, 99.99% trace metals, Sigma-Aldrich). The samples were fixed at the tip of a rotating disk (2000 rpm) and measured against a Ag/AgCl reference electrode. The latter have a potential of 0.95 V vs RHE, measured experimentally with a hydrogen electrode. Electrochemical measurements were realized with a Metrohm Autolab PGSTAT302N

potentiostat at UCL where after an open circuit potential measurements, a cyclic voltammetry experiment at 100 mV/s for 10 scans have been carried out.

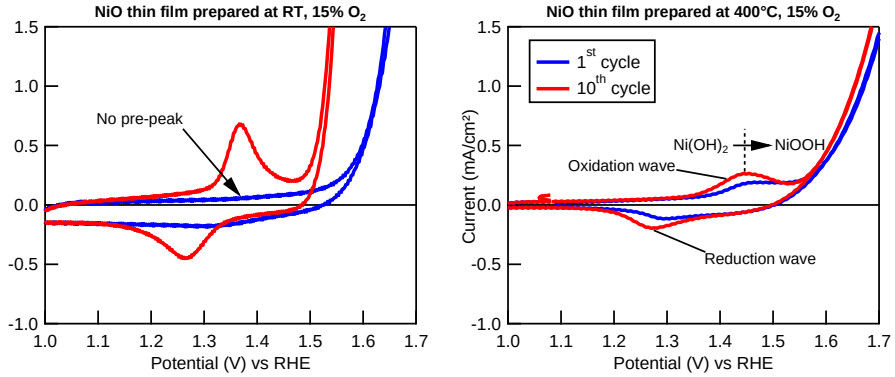

Figure 4.5: Cyclic voltammetry in 1 M KOH of the NiO thin film prepared with 15 % of oxygen and at room temperature (Left) or at 400 °C (Right). The sample prepared at high temperature shows the typical oxidation wave associated to the $Ni(OH)_2 \rightarrow NiOOH$ phase transformation already in the first cycle. On the contrary, the NiO thin film prepared at room temperature does not provide the oxidation wave in the first cycle.

The experiments show that the typical phase transformation of the nickel hydroxide ($Ni(OH)_2$) into nickel oxy-hydroxide (NiOOH) (for more details see Section 9) is present for the cyclic voltamograms realized on both sample (Figure 4.5). However, contrary to the sample prepared at room temperature, the sample prepared at 400 °C shows the typical oxidation wave associated to the nickel hydroxide phase transformation from the very first cycle. The oxidation wave gradually build-up with cycling for the sample prepared at room temperature.

The absence of the oxidation wave for the first cycle of the cyclic voltammetry experiment realized on the sample prepared at room temperature suggest that nickel oxy-hydroxide (NiOOH) is spontaneously formed on the surface when exposed to water and/or when immersed in the electrolyte. Thus, no nickel hydroxide ($Ni(OH)_2$) can be transformed into oxy-hydroxide (NiOOH) during the first cycle. According to literature, the nickel oxidation state in nickel oxy-hydroxide is supposed to be +III [169–171]. Therefore, it has been assumed that the spontaneous formation of nickel oxy-hydroxide on the NiO thin film surface prepared at room temperature might be triggered by the presence of triply ionized nickel atoms (Ni^{3+}) already present on the surface, following the reaction:

$$Ni^{3+}O^{2-} + H_2O \rightarrow NiOOH + H^+ \tag{4.3}$$

With similar reasoning, because of the presence of the oxidation wave typical of the phase transformation of $Ni(OH)_2$ for the sample prepared at high temperature in the first cycle of the cycling voltammetry (Figure 4.5), it has been assumed that the sample prepared at higher temperature would instead form spontaneously nickel hydroxide $Ni(OH)_2$ when exposed to water following the reaction:

$$Ni^{2+}O^{2-} + H_2O \rightarrow Ni(OH)_2 \tag{4.4}$$

Thus, the electrochemical results suggest that Ni^{3+} is present on the surface of the sample prepared at room temperature. On the contrary the surface of the sample when prepared at high temperature contains only regular Ni^{2+} atoms.

4.3.6 Optical measurements

Optical measurements have been realized on sputtered thin films at room temperature and 400 °C at TU-Darmstadt on fused silica. The measurements were performed with a Cary7000 optical bench in the 2500-200 nm wavelength spectral region.

The results show larger absorption coefficients in the band gap of the samples prepared at room temperature in comparison to what is measured for the sample prepared at high temperature (Figure 4.6). Also, it can be noticed that the higher the oxygen concentration during sample preparation at room temperature, the larger the absorption, whereas the samples prepared at higher temperature display only weak absorption in the band gap region. An excitonic peak at 3.25 eV [92], indicating the crystalline nature of the thin films, is even observed (Figure 4.6) .

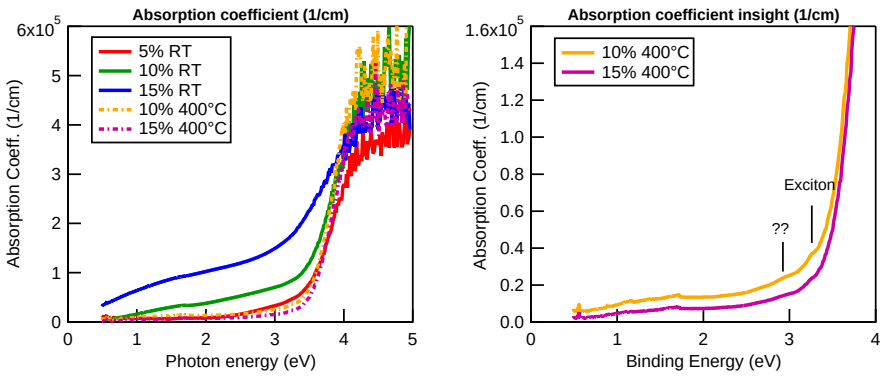

Figure 4.6: Absorption coefficients of NiO thin films determined from optical measurements. The NiO thin films have been deposited on fused silica. Samples prepared at room temperature display larger absorption coefficients within the band gap which increase with the oxygen concentration in the deposition chamber. On the contrary NiO thin films prepared at 400 °C provides low absorption coefficients within the band gap and a weak localized excitonic feature at 3.25 eV can be observed.

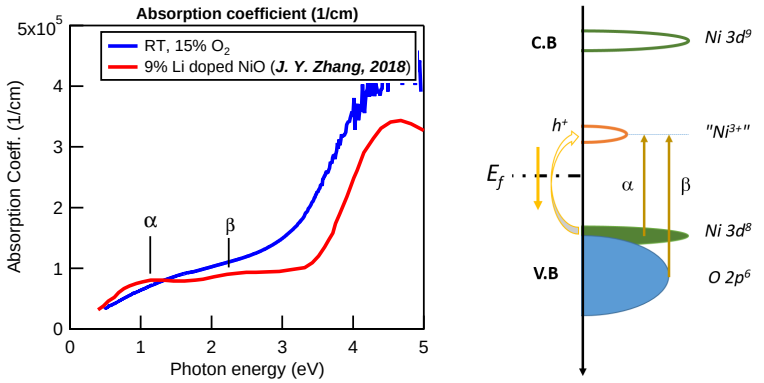

Figure 4.7: Left: Comparison of the optical absorption of the NiO thin film prepared at room temperature and 15 % oxygen with what can be obtained with an epitaxial Li doped NiO thin film prepared at high temperature [86]. Right: description of the doping mechanism in NiO which lead to the formation of an accumulation of holes in the band gap and the resulting α and β optical transitions. The α and β stand for the optical transitions between the Ni $3d^8$ and the O $2p^6$ orbitals, respectively, to the acceptor state (holes) in the band gap.

The literature reports that the optical properties of high quality NiO can be degraded by the creation of defects, such as nickel vacancies, or by the substitution of nickel by lithium (see Section 2.2.4). It has been reported that for crystalline Li-doped NiO, a double feature related to the possible presence of an acceptor state $\sim$ 1 eV above the valence band is observed [86]. The features denoted α and β are transitions between the Ni $3d^8$ and the O $2p^6$, respectively, to a hole state in the band gap (Figure 4.7, left). Our results do not show an as-well defined double feature as it has been obtained for the Li-doped NiO thin films [86]. The reason could be that the intrinsically doped NiO thin films are less crystalline, with potentially, a secondary oxygen-rich phase accumulating at the grain boundaries (see Section 5). This might favour a background absorption and an energy dispersion, in the band gap, of the double feature.

The presence of an acceptor state in the band gap of transition metal oxides when positively doped has been also observed in the thesis of K. Schuldt on Sr-doped $LaFeO_3$ [172]. As generally accepted, the lowering of the Fermi energy towards the valence band maximum would generate holes in the valence band. However, in the thesis of K. Schuldt, it has been assumed that for transition metal oxide, where the valence band edge is constituted of d-orbitals, a strong columbic repulsion may repel the holes in the d-band into the band gap. Eventually, the columbic reaction in the d-band would lead to the formation of an acceptor state in the middle of the band gap. Similarly, in NiO, when positively doped, the resulting holes would be repelled from the Ni $3d^8$ orbitals and would accumulate above the Fermi energy (Figure 4.7,

right). Thus the α and β transition could be assigned to the emergence of the so-called Ni^{3+} in doped NiO.

4.4 Discussion

4.4.1 Surface electronic properties of NiO thin films

The numerous data collected along this thesis are plotted against the O 1s(Def.) in Figure 4.8. Two regions can be identified for the VBM. The first one is characterized by a decreasing VBM with increasing O 1s(Def.) shoulder, for moderate O 1s(Def.) weight (0-10 %), where largest VBM are attained with the samples prepared at high temperature (above 200°C). The second region is marked by an almost constant valence band maximum around 0.6 eV.

In the meantime, still with increasing O 1s(Def.) weight, two regions can be identified to describe the evolution of the R_{Ni} ratio. The first region, for O 1s(Def.) weight between 0 and 10 %, is characterized by a constant R_{Ni} ratio of $\sim$ 0.625 (Figure 4.8, bottom). The second region, is characterized by an increasing R_{Ni} ratio with increasing O 1s(Def.) weight.

Also, three regions can be identified if the workfunction is plotted against the O 1s(Def.) weight (Figure 4.8, top). The first one, for O 1s(Def.) weight between 0 % and 5 %, is characterized by a constant workfunction of 4.5 eV. The second region, for O 1s(Def.) weight between 5 % and 10 %, constitutes a transition region, in which the workfunction increases from 4.5 eV to 5.2 eV. The third region, for O 1s(Def.) weight above 10 %, is marked by an almost constant workfunction of 5.2 eV.

Therefore, for convenience, the results obtained in Figure 4.8 can been delimited in three regions as defined by the evolution of the workfunction with O 1s(Def.): two domains with a constant workfunction separated by a transition region for O 1s(Def.) comprised between 5 % and 10 % (Figure 4.8).

In addition, the ionization potential (I), which represents the position of the valence band edge relative to the electron energy in vacuum, has been determined from the workfunction (ϕ) and the valence band maximum (VBM) following the relationship I=VBM+ϕ (see Section 2.1.3). The evolution of the ionization potential evidence the formation of a dipole δ of about 0.3 eV when the samples are prepared at room temperature in comparison to the samples prepared at high temperature. As detailed before, the dipole on the NiO thin film surface might be likely related to the accumulation of oxygen species or the presence of Ni^{3+}.

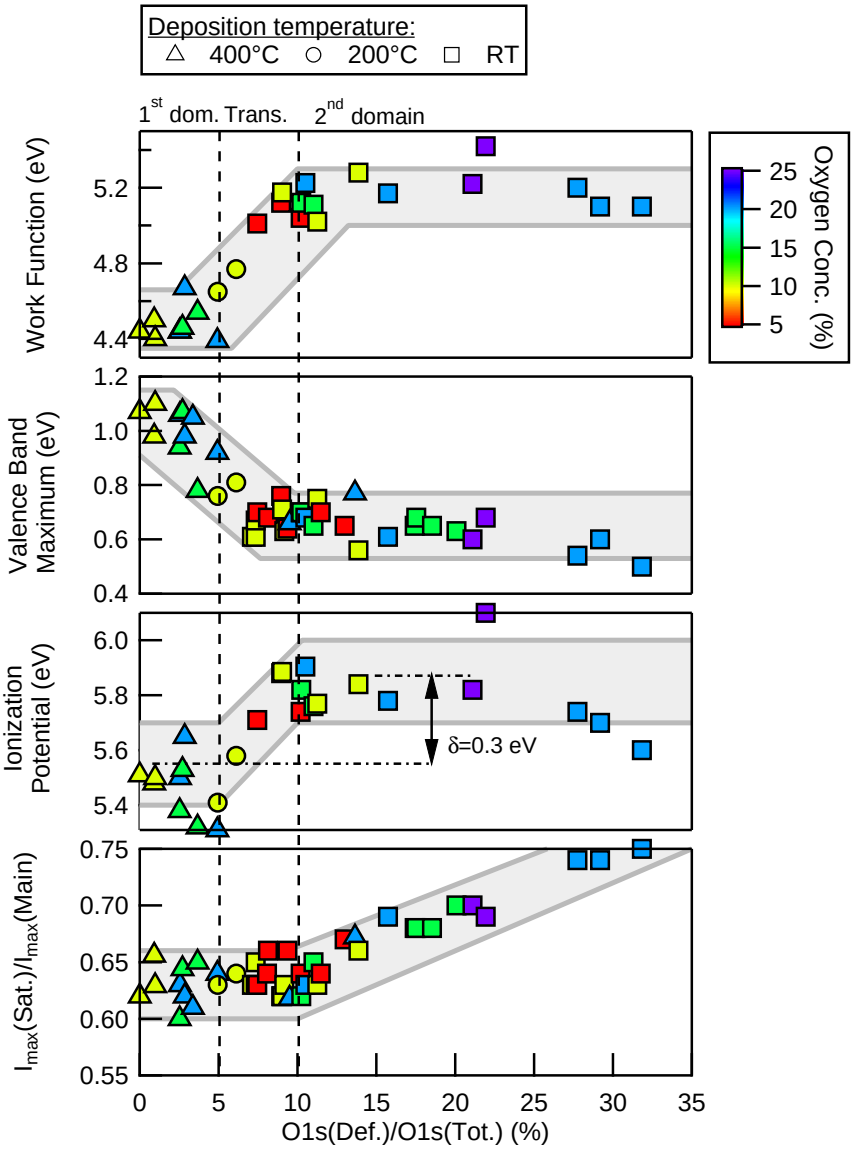

Figure 4.8: Workfunction (ϕ), valence band maximum (VBM) position (see Figure 4.3), ionization potential (I=VBM+ϕ) and relative peak intensity R_{Ni} of the satellite peak over the main peak in the Ni 2p(3/2) region (see Figure 4.3), as a function of the weight of the electronic state assigned to defects in the O 1s region (see Figure 4.1). The plots are realized in compiling numerous in-situ XP spectra of NiO thin films reactively sputtered on various substrates, temperature and oxygen concentration. It appears that the parameters impacting the surface properties of the NiO thin films are the oxygen concentration (color scale) and the temperature (markers).

4.4.2 Overall view

Observing the general view of Figure 4.8, one can notice that the first domain (O 1s(Def.) weight $< 5\%$) is exclusively made of the samples prepared at high temperature. It is characterized by a low workfunction, a decreasing Fermi energy and a constant R_{Ni} value, whereas the second domain (for O 1s(Def.) weight $> 10\%$), consisting mostly of samples prepared at room temperature, is characterized by a large workfunction value, an almost constant Fermi level position and a continuous increase of the R_{Ni} ratio with increasing O 1s(Def.) weight. The two domains are separated by a transition region located between 5 % and 10 % where, in particular, the workfunction value increases.

Looking at the oxygen color scale of Figure 4.8, it can be observed that, in both domains, the O 1s(Def.) weight in the O 1s region is somewhat correlated to the oxygen concentration in the deposition chamber: the larger the oxygen concentration, the larger the O 1s(Def.) electronic density. Thus, for samples in the 1^{st} domain, prepared at 400 °C, the O 1s(Def.) is almost completely suppressed if deposited with 10% of oxygen concentration and increases up to 4-5 % if prepared with 15-20 % of oxygen. For samples from the 2^{nd} domain, prepared at room temperature, the O 1s(Def.) weight varies from 10 to 35% when oxygen concentration is increased from 5-10% to 20-25%.

4.4.3 Charge compensation mechanism of defects in NiO

High temperature preparation

First of all, as seen on Figure 4.8, the samples of the 1^{st} domain are exclusively samples which were prepared at high temperature ($\geqslant$ 200 °C). As discussed in Chapter 10, a high temperature of deposition favours a more crystalline and more homogeneous thin film structure.

The first domain is characterized by a high valence band maxima, which tend to decrease with increasing O 1s(Def.) weight (Figure 4.8). It means, following Fermi statistics, the concentration of holes in the valence band maximum increases. Also, higher O 1s(Def.) weights are obtained at high oxygen concentration during thin film fabrication. This would support the assumption that the thin films are intrinsically doped by an excess of oxygen. Thus, the experiments suggest that in the first domain higher hole concentrations are attained with increasing O 1s(Def.) weight. Thus charge compensation of the dopant, formed at high oxygen concentration, is realized through the formation of holes.

As explained in the introduction, the dopant can be either a nickel vacancy or an oxygen interstitial. In bulk NiO, nickel vacancies are the only dopant but, as no detailed literature treated this case yet, it is assumed that oxygen interstitials can be present at grain boundaries. Chapter 5 will highlight that the grain boundaries accumulate oxygen species if the thin film is prepared at room temperature, but the temperature erases the oxygen-rich

grain boundaries and might convert the thin film to a more stoichiometric crystallographic structure. Therefore, we assert that holes in the valence band of the NiO thin films prepared at high temperature originate from nickel vacancies and not from oxygen interstitial.

Meanwhile, the Ni 2p region is not particularly affected by the increase of the O 1s(Def.) weight as the R_{Ni} ratio is constant as seen in Figure 4.8. Supported by the fact that the difference of spectra of the samples having an O 1s(Def.) weight of 2.5% and 4.9 % with the reference sample (O 1s(Def.)=0%) do not evidence an obvious change in the electronic structure in the Ni 2p region (Figure 4.2, right), that the cyclic voltammetry realized on a sample prepared at high temperature discards the presence of Ni^{3+} on the surface (see Section 4.3.5) and finally that the low workfunction value of the samples from the 1^{st} domain indicates that the formation of Ni^{3+} or O^{-} is limited (see Section 4.3.4). Therefore, it is assumed that the NiO thin films produced at high temperature do not contain the charge compensating species Ni^{3+}.

It has to be mentionned that at the minimum, in the 1^{st} domain, the Fermi energy is 0.6 eV when determined by linear extrapolation (or 0.35 eV in taking the threshold where no photo-emission is detected, Figure 4.3) for the samples from the 1^{st} domain. This means that the ratio $h^{\bullet}/N_v$, which can be determined from equation 2.1.2 is at best 10^{-6}-10^{-3}. Therefore, the holes/oxygen interaction cannot be detected by in-situ XPS (the accuracy of the XPS is at least 1%). Thus the O 1s(Def.) cannot be related to holes but could be associated with peroxo species present in small quantity. Thus, it is assumed that the O 1s(Def.) observed for sample prepared at high oxygen concentration and high temperature of deposition might be related to the formation of a peroxo species which would accumulate primarily at the grain boundaries (see Chapter 5).

Moreover, as detailed in Section 2.2.1, NiO is a charge transfer material. It means that charges are compensated through Ni^{2+}/O^{2-} interaction. As a nickel vacancy (V''_{Ni}) replaces a lattice nickel atom, the charges of nickel vacancies might also be compensated by V''_{Ni}/O^{2-} interactions. Therefore, it would make more sense that missing nickel atoms are compensated by positive charges localized on the surrounding oxygen atoms. Thus, the negatively charged nickel vacancies V''_{Ni} would interact electronically with the six surrounding oxygen atoms and so charge compensation by holes would be primarily localized on the oxygen atoms.

As the Fermi energy decreases with increasing O 1s(Def.), and as it is very unlikely that Ni^{3+} can be created in the samples prepared at high temperature, we propose that, for the first domain, the compensation of nickel vacancies is realized by the formation of holes:

$$Ni^{\times}_{Ni} + O^{\times}_{O} + \frac{1}{2}O_2 \rightarrow NiO + O^{\times}_{O} + V''_{Ni} + 2\,h^{\bullet} \qquad (4.5)$$

and also by peroxo species:

$$\mathrm{Ni}_{\mathrm{Ni}}^{\times} + \mathrm{O}_{\mathrm{O}}^{\times} + \mathrm{O}_2 \rightarrow \mathrm{NiO} + 2\,\mathrm{O}_{\mathrm{O}}^{\bullet} + \mathrm{V}_{\mathrm{Ni}}'' \tag{4.6}$$

Room temperature deposition

The 2^{nd} domain (Figure 4.8) is characterized by an almost constant Fermi level position, an increasing R_{Ni} ratio and a high workfunction. Although the O 1s(Def.) increases with oxygen concentration during sample preparation, the almost stable Fermi level position would suggest the addition of defects does not necessarily create more free charge carriers. A convincing demonstration that holes are not created when the NiO thin film is prepared at room temperature is given in Chapter 5.

Contrary to samples prepared at high temperature, samples prepared at room temperature of the 2^{nd} domain are highly defective where an oxygen-rich secondary phase accumulate at the grain boundaries (see Chapter 5). Therefore, also with respect to what has been written in the previous part, the implication of oxygen interstitials in the non-stoichiometry of these sample cannot be totally discarded.

Regarding the charge compensating species in the 2^{nd} domain, it can be noticed that the R_{Ni} ratio increases with increasing O 1s(Def.) weight. In particular, the differences of the Ni 2p XP spectra with the Ni 2p reference spectra (O 1s(Def.)=0 %) evidence an additional electronic component (Figure 4.2). The additional component might be attributed to Ni^{3+}. Indeed, the XPS spectra of NiOOH, where nickel is formally in the +III state, as for lithium doped NiO, provides a more prominent Ni 2p(Sat.) peak in comparison to the Ni 2p(Main) peak [173, 174]. Thus we attribute the swelling of the Ni 2p(Sat.) peak with increasing oxygen concentration in the process for samples prepared at room temperature, as a fingerprint of the presence of Ni^{3+} species.

This might be in line with the electrochemical measurements (Figure 4.5) and, to a lesser extent, with the optical measurements (Figure 4.6), which would suggest that triply ionized nickel atoms (Ni^{3+}) are present on the surface and in the bulk of the thin films prepared at room temperature. Also the high workfunction value reported for the samples of the second domain (Figure 4.8) can be related to both Ni^{3+} and O^{-} species (see Section 4.3.4). Finally, as detailed in Chapter 5, the thin films prepared at room temperature would accumulate oxygen species at the grain boundaries that would eventually lead to the formation of nickel peroxide NiO_2. An XAS study on NiO thin films prepared at room temperature suggested that charge compensation of dopants is dominantly carried by peroxo species (O^{-}) and to a lesser extent to Ni^{3+} [83]. Therefore, we propose the charge compensation mechanism in RT-NiO thin films to be:

$$5\,\mathrm{Ni}_{\mathrm{Ni}}^{\times} + 4\,\mathrm{O}_{\mathrm{O}}^{\times} + O_2 \rightarrow NiO + 4\,(1-\delta)(Ni_{Ni}^{\bullet} + O_O^{\times}) + 4\,\delta(O_O^{\bullet} + Ni_{Ni}^{\times}) + V_{Ni}'' + O_i'' \tag{4.7}$$

with δ a parameter comprised between 0 and 1 to take into account charge compensation discrepancy over oxygen and nickel atoms.

Looking at the O 1s region for the samples of the second domain, the deconvolution reveals that the O 1s(Def.) shoulder is composed of at least two electronics states (Figure 4.1). As the Ni 2p spectra, the electrochemical measurements and the high workfunction value suggest the presence of Ni^{3+} in the NiO thin films prepared at room temperature, it is assumed that the additional O 1s(Def.) component at high binding energy, for the samples of the second domain, is indirectly related to the presence of Ni^{3+}. In crystalline structure, the emergences of Ni^{3+} is very unlikely as the Ni $3d^7$ state is too deep to be raised to the Fermi energy. Thus, we assume that the presence of the Ni^{3+} is rendered possible due to the amorphousness of the NiO thin films prepared at room temperature.

To summarize, for the samples from the second domain, the charge carrier concentration (h^+) does not necessarily increase with increasing number of nickel vacancies and oxygen interstitials, but instead the results might suggest that nickel vacancies and oxygen interstitials are compensated by the formation of peroxo species (O^-) and by the oxidation of nickel atoms into Ni^{3+}.

4.5 Conclusion

Numerous in-situ UPS/XPS measurements, which were carried out on NiO thin films deposited by reactive DC-sputtering, have been compiled. It appears that the workfunction and Fermi level of NiO can be tuned by varying growth temperature and oxygen concentration during deposition. Samples prepared at high temperature exhibit workfunctions of about 4.5 eV while, if prepared at room temperature, the workfunction is about 5.2 eV. In the meantime, the Fermi level can be tuned from about 1.1 eV to 0.6 eV above the valence band maximum, particularly by increasing the oxygen concentration in the deposition chamber, which would entail the formation of nickel vacancies. Also the formation of a dipole is observed on the surface of the NiO thin films prepared at room temperature which results in about 0.3 eV in the increase of the surface workfunction.

In comparing in-situ XPS/UPS measurements with optical and electrochemical measurements, a charge compensation mechanism in NiO has been proposed and can be summarized as following: in relatively stoichiometric NiO structure, the nickel vacancies are the dominant dopant and the charge compensation is obtained by holes and to a certain extent by peroxo species (O^-). For a highly defective nickel oxide structure, the dopant could be both the nickel vacancies and the oxygen interstitial. As we found that the Fermi level position is pinned to about 0.6 eV for high doping concentration, it has been assumed that the dopants are compensated by the formation of peroxo species and to the formation, in a lesser extent, of Ni^{3+} species but not necessarily by free holes.

CHAPTER 5

Origin of the conductivity of reactively sputtered nickel oxide thin films at room temperature

Summary

Literature reports that nickel oxide (NiO) thin films deposited by reactive sputtering at room temperature display, in comparison to pure NiO, a high conductivity and a low electrical activation energy. Herein, for such thin films, we evidence the presence of an oxygen-rich secondary phase accumulating at the grain boundaries before appearing in the bulk of the grain with increasing oxygen partial pressure. Fingerprinting by electron energy loss spectroscopy indicates that the secondary phase has a high electrical conductivity. The comparison of in-situ electrical measurements with in-situ X-ray photoemission spectroscopy highlights a pinning of the Fermi energy to 0.6 eV for any NiO thin films prepared by reactive sputtering at room temperature whereas the conductivity continuously increases with oxygen concentration during sample preparation. Thus, the introduction of defects can not be compensated by positive charges in the form of free holes but rather in the form of localized holes on oxygen atoms or on nickel atoms. Finally, we ascribe the reported high conductivity to a lowering of the electrical activation energy during polaron electrical displacement, which implies an increase of the charge carrier mobility, at the oxygen-rich grain boundaries or by the creation of an alternative electrical path supported by the positive compensating species Ni^{3+} or O^{-}.

This chapter includes the results obtained by TEM/EELS measurements realized by Gunnar Lumbeeck and Nicolas Gauquelin from the EMAT group of the University of Antwerp. Also the work realized by Jonas Hunka at TU-Darmstadt contributed to the scientific input of this chapter.

Large parts of this chapter are based on the draft of an article under submission:

R. Poulain, G. Lumbeeck, J. Hunka, J. Proost, H. Idrissi, D. Schryvers, A. Klein and N. Gauquelin. **Origin of high conductivity in oxygen-rich room temperature nickel oxide thin films**. *In preparation.*

5.1 Introduction

When sputtered at low temperature ($\lesssim$ 200°C), NiO thin film resistivity in the 0.1-1 Ω cm range has been reported [87, 95, 163] while electrical activation energy (E_A) can be astonishingly close to 0-0.15 eV [150, 175]. This can be surprising, owing to the fact, that pure nickel oxide (NiO) is supposedly highly resistive in nature with up to 10^{13} Ω cm while E_A reaches 0.6 eV [50]. Although NiO can find numerous applications, the understanding of the underlying mechanism which would clarify the origin of the conductivity of NiO thin films prepared at room temperature by reactive sputtering has not been elucidated yet.

In this chapter, we focused at evidencing the reasons of the high electrical conductivity for NiO thin films prepared in oxygen-rich condition at room temperature (RT-NiO thin films) by reactive sputtering. The thin films are characterized by in-situ electrical measurements, in-situ X-ray photoemission spectroscopy(XPS), by electron loss energy spectroscopy (EELS) and transmission electron microscopy (TEM). The results obtained by EELS-TEM reveals the presence of a secondary phase accumulating at grain boundaries before appearing in the bulk of the grain with increasing oxygen concentration where, in particular, the EELS pattern of the secondary phase possesses features found in conductive NiO based materials. Also, as seen in Chapter 4, the in-situ XPS measurements show that the Fermi energy is pinned around 0.6 eV for any RT-NiO thin films whereas the electrical in-situ characterization on the same thin films evidences that the conductivity can increase by three orders of magnitude.

Thus, from the confrontation of the in-situ XPS measurements with the in-situ electrical characterizations, we demonstrate that charge compensation of defects, either nickel vacancies ($V_{Ni}^{''}$) or oxygen interstitial ($O_i^{''}$) for which formation cannot be excluded at the grain boundaries, is realized by a positive chemical species, as for peroxo ($O_O^{\bullet}$) or Ni^{3+} ($Ni_{Ni}^{\bullet}$) compounds, but not by the creation of free holes ($h^{\bullet}$) with increasing oxygen partial pressure. Eventually, the increase of the conductivity is explained by a lowering of the energy barrier in the secondary phase during the polaron hopping mechanism of the charge carrier in the valence band of the RT-NiO thin films or by the creation of an alternatuive electrical path supported by the positive compensating species Ni^{3+} or O^{-}. Finally, the results presented in this chapter on RT-NiO thin films can provide hints in the understanding of electrical transportation mechanisms in the RT-NiO thin films especially to what concern the importance for differentiating the electrical activation energy (E_A) from the Fermi energy (E_F).

5.2 Experimental

5.2.1 Deposition chambers

NiO thin films ($\sim$ 50 nm) were prepared by reactive DC magnetron sputtering at room temperature from a pure Ni target (99.9%). Two sputtering chambers have been used in this chapter. The first one, part of the deposition system at UCL, was used to deposit the NiO thin films on an oxide-free H-terminated p^+-silicon surface for scanning transmission electron microscopy (STEM), electron energy loss spectroscopy (EELS) and Automated Crystal Orientation Mapping (ACOM-TEM) measurements. The second chamber is part the DAISY-MAT system at TU-Darmstadt [168] which is an ultra-high vacuum system where the samples can be transferred without breaking the vacuum to different platforms to characterize the thin films for, i.e.: in-situ XPS and in-situ electrical measurements (see Section 3.3.1). In this chapter, all XPS measurements are performed in-situ in the DAISY-MAT system.

5.2.2 Sample preparation for STEM and EELS measurements

Czochralski (CZ)100-double polished p^+-silicon (381 μm thick, 0.004-0.008 Ω cm) were chemically cleaned to ensure a perfect oxide free H-terminated silicon surface (See Section 3.2.1).

NiO thin films were deposited at UCL on the oxide free H-terminated p^+-silicon sample at 50 W, 0.26 Pa (2 mTorr), with a target-to-substrate distance of 12.2 cm and at 2.5%, 17% and 20% of oxygen concentration.

5.2.3 STEM-EELS and ACOM-TEM measurements

STEM, EELS and Automated Crystal Orientation Mapping (ACOM-TEM) studies were realized on the three samples prepared at UCL after few months following the deposition. The thin films have been likely subjected to the electrical ageing process reported for RT-NiO thin films (see Chapter 6), but it has been assumed that it cannot modify the conclusion drawn in this chapter.

Prior to TEM measurements, cross-sectional samples were prepared with the "lift-out" method, using the focused ion beam (FIB) procedure. A narrow carbon layer followed by a thick platinum protective layer was added on top of the NiO film before cutting out the sample to ensure the crystallographic integrity of the NiO layer while thinning the film for minimal grain overlap.

EELS was performed on an aberration corrected FEI Titan Cubed microscope operated at 300 kV with a 19 mrad convergence angle equipped with a Gatan Enfina ER EEL spectrometer. The experiments were conducted with a monochromated beam in scanning mode (STEM) yielding a 1 Å fine probe size with a 125 meV energy resolution and a beam current of 50 pA. Annular

dark field (ADF) STEM images were simultaneously acquired during the EEL spectrum imaging on the DF4-detector of the microscope (yielding a 20 mrad inner semi-collection angle). By using a collection angle of 47 mrad, nearly all scattered electrons can be captured through the EELS entrance aperture. For recording the O-K edge spectra, an exposure time of 200 ms/pixel and a dispersion of 0.05 eV/pixel were used. The EELS map scaling was set to ∼4 Å/pixel, while a map size of 30 pixels × 100 pixels was chosen. A standard power-law background subtraction [176] was applied on the O-K edge spectra obtained from the EELS data. Raw data are presented without any post-processing.

The procedure for the ACOM-TEM measurements has been detailed elsewhere by Lumbeeck *et al.* [177].

5.2.4 Sample preparation for in-situ electrical and XPS measurements

The conditions of deposition at TU-Darmstadt were set to match the discharge curve and deposition rate obtained at UCL (See Section 3.1.2). Thus, deposition conditions at TU-Darmstadt were set to 40 W, 0.5 Pa and the target-to-substrate distance to 14 cm. With these parameters, the NiO thin films have been produced with 5 %, 10 % and 15 % of oxygen concentration.

At TU-Darmstadt, the thin films were deposited on gold patterned contacts, on top of fused silica for the in-situ conductivity and in-situ XPS measurements.

5.2.5 In-situ electrical measurements

The in-situ electrical characterization of as-deposited RT-NiO thin films prepared at at TU-Darmstadt was performed by a two probe setup (gold contact on fused silica) in the DAISY-MAT system. The contribution of the contact resistance (R_c) from the total thin film resistance (R_{tot}) has been determined by stepwise in-situ electrical measurements with increasing thin film thickness.

Assuming the resistivity to be homogeneous in the experimental thickness range (50-300 nm), the total resistance is considered as being $R_{tot} = R_c + \rho\frac{L}{tW}$ where R_c, ρ, t, L and W stand for the contact resistance, the thin film resistivity, the thickness, the length between two gold stripes and the width of one gold stripe, respectively. As represented in Figure 5.1, the plot of R_{tot} as a function of $1/t$ would enable to discriminate the contribution of the contact resistance (R_c) from the measured resistance (R_{tot}) and to extract the thin film resistivity ρ.

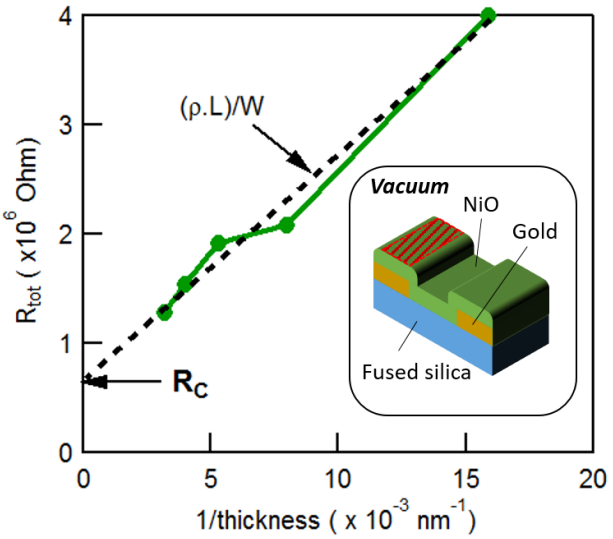

Figure 5.1: Representation of the method employed to determine, with a two probe configuration, the in-situ thin film resistivity in DAISY-MAT. The thin film is sequentially deposited on gold patterned stripes on fused silica. Fr this plot the oxygen concentration during deposition is 5%. The width of a stripe is W and the length between two stripes is L. The total resistivity is measured for increasing thin films thickness. The linear extrapolation of R_{tot} as a function of the inverse of the thin film thickness enables to remove the contribution of the contact resistance and to estimate the thin film resistivity. The measurements are realized in-situ on as-deposited thin films without breaking the vacuum. The red-shaded area indicates where the in-situ XPS measurements are performed subsequently to the in-situ electrical measurements.

5.3 Results

5.3.1 In-situ electrical measurement

As displayed in Figure 5.2, the in-situ sheet resistivity of the RT-NiO thin films prepared at TU-Darmstadt displays a clear dependency on the oxygen concentration during reactive sputtering. Thus, the conductivity increases by 3 orders of magnitude when the oxygen concentration varies from 5 % to 15 %. At 15 % of oxygen concentration, the conductivity is about 6.5 $S.cm^{-1}$. The conductivity obtained for the samples prepared for the in-situ electrical measurements is in the same order of magnitude to what can be found in the literature [87, 95, 163].

5.3.2 In-situ photoemission

The in-situ photoemission spectra obtained in the DAISY-MAT system on the samples from chamber #2 at 5%, 10% and 15% of oxygen concentration

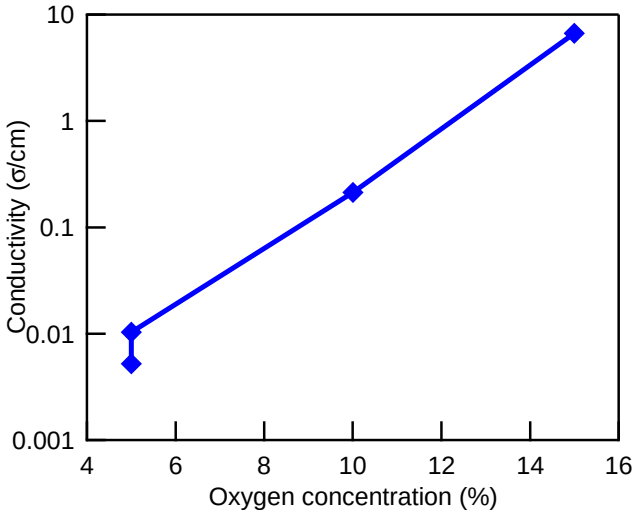

Figure 5.2: In-situ conductivity measurements of the NiO thin films deposited at TU-Darmstadt on gold patterned fused silica substrates.

are displayed in Figure 5.3. Three regions have been measured: the valence band, the O 1s and the Ni 2p regions. More details about the XP spectra in the measured region are given in Chapter 4. Thus, the Ni 2p region is made of the the Ni $2p^5 3d^9 Z$, Ni $2p^5 3d^9 L$ and the Ni $2p^5 3d^8$ orbitals [81] (Figure 5.3). In the rest of this chapter, for simplification, the Ni $2p^5 3d^9 L$ state will be referred to as the satellite peak Ni 2p(Sat.) and the Ni $2p^5 3d^9 Z$ state as the main peak Ni 2p(Main) (Figure 5.3). The O 1s region is composed of the prominent photoemission from lattice oxygen (O^{2-}) denoted O 1s(Main) and, at a higher binding energy, a shoulder can be observed which increases with increasing oxygen concentration. Following Chapter 4, the shoulder at higher binding energy to the main peak in the O 1s region has been labelled O 1s(Def.).

The position of the edge of the valence band is an indication of the Fermi energy [9]. The latter has been determined by the intersection of the linear extrapolation of the valence band edge with the background emission in the bandgap. It can be observed that the Fermi energy is relatively constant for the three samples and is consistently about 0.60-0.67 eV.

It should be mentioned that the Ni 2p(Sat.) peak cannot be spontaneously associated to the presence of Ni^{3+} in NiO contrary to numerous reports misleading the XPS spectra assignment. However, it can be noticed that, with increasing oxygen concentration, the valley between the Ni 2p(Main) peak and the Ni 2p(Sat.) peak becomes less pronounced (Figure 5.3).

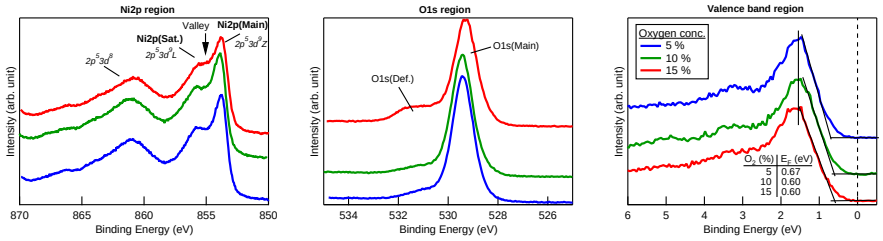

Figure 5.3: In-situ photoemission spectra of a) the Ni 2p, b) the O 1s and c) the valence band regions. The measurements are realized on the samples of chamber #2 after in-situ electrical measurements (see Figure 5.2). The Fermi energy is determined by linear extrapolation of the valence band edge to the X-axis. It can be seen that there is no obvious reduction of the Fermi energy (E_F) with increasing oxygen concentration.

5.3.3 NiO thin films prepared on silicon

The thin films structure

As shown by the ACOM-TEM images in Figure 5.4, the RT-NiO thin films are about 50 nm thick and adopts a poly-cristalline structure. In line with literature [150, 178], the thin films include numerous grain boundaries at any oxygen concentration during the sample preparation. Also, the grains are more dense and noticeably elongated along the direction of growth at high oxygen concentration (17 % and 20 %).

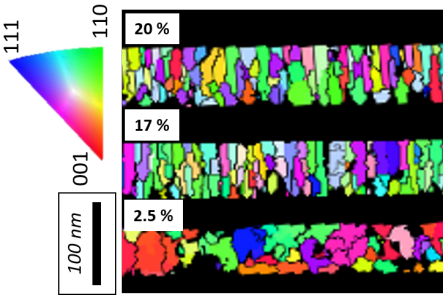

Figure 5.4: ACOM cross-sectional image of the three studied RT-NiO thin films (2.5%, 17% and 20% of oxygen concentration) prepared on oxide free silicon sample at UCL.

Presence of electronically active defects

STEM-EELS measurements provided information about the electronic inhomogeneities at the grain size level in the NiO thin films and emphasized the presence of a specific pre-peak at 529 eV in the O K edge, which is particularly observed at the grain boundaries of the sample prepared with 17 % and 20 % oxygen concentration and in the bulk of the grain if prepared with 20 % oxygen concentration (Figure 5.5). XAS-literature reports that spectra

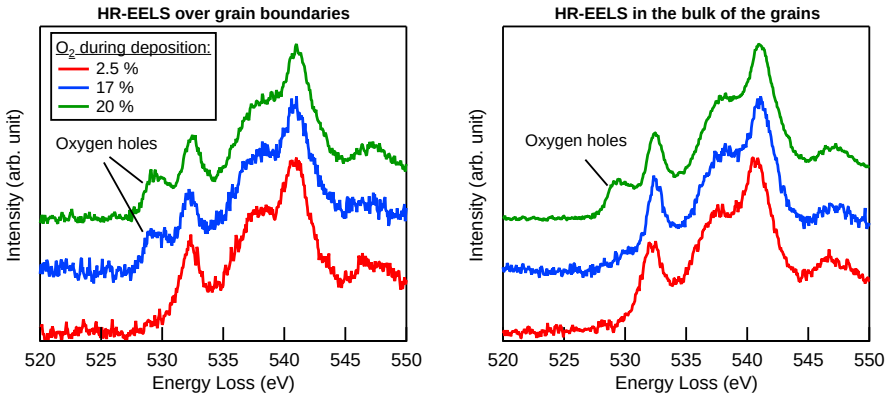

Figure 5.5: EELS obtained on a) grain boundaries and b) in the bulk of the grains for the three NiO thin films deposited on silicon at room temperature at 2.5 %, 17 % and 20 % of oxygen concentration at UCL.

of extrinsically or intrinsically doped NiO materials display a similar electronic feature at 529 eV in the O K edge region and so could be the fingerprint of a higher conductivity [83, 84, 86]. Although the exact nature of this feature is controversial, its presence has been related to positive charges in nickel oxide [83, 84, 86–88] and might be more appropriately denoted as a hole in the Ni $3d^8$L orbital, with L the oxygen ligand [179]. Therefore, the feature observed in the O K edge region at 529 eV will be labelled as an *oxygen hole* in the rest of this chapter.

Measurements show that these oxygen holes are promoted at high oxygen concentration as the pre-peak at 529 eV is not visible for the sample prepared with 2.5 % (Figure 5.5). The oxygen hole feature tends to accumulate at the grain boundaries before also being observed in the bulk of the grain at higher Oxygen concentration. Indeed, the sample produced at 17% oxygen concentration only provide the feature associated to holes if EELS is performed at grain boundaries. Taking the sample prepared at 20 % oxygen concentration, it can be seen that the feature is visible the boundaries and in the bulk of the grains (Figure 5.5).

Bicolor images have been realized from EELS measurements on the NiO/silicon samples (Figure 5.6) using the region corresponding to the oxygen holes in the O K edge spectra (energy window from 528 to 530 eV). These bicolor maps clearly evidence a chemical homogeneity of the sample prepared with 2.5 % of oxygen, whereas the samples prepared with 17 % and 20 % have a more pronounced pre-peak at 529 eV over the grain boundaries (Figure 5.6).

As the oxygen hole pre-peak has been reported in doped NiO but not in pure NiO (without dopant), its presence could be an indication of higher conductivity. Therefore, the heterogeneity revealed in the bicolor images of

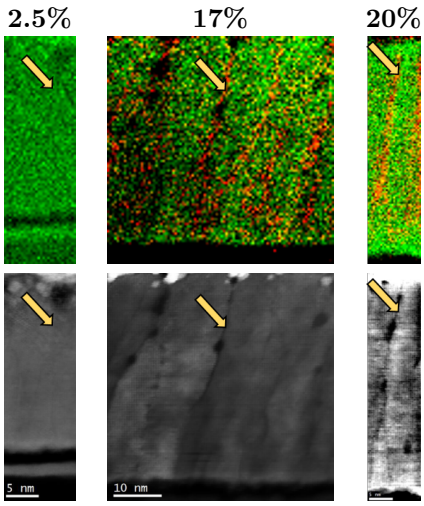

Figure 5.6: Top row: Bicolor images realized from the cross-sectional EELS measurements of the 2.5 %, 17% and 20% NiO thin film where the red color indicates where the pre-peak associated to oxygen holes is the strongest. The green color does not necessarily imply an absence of peak but only a reduction of the pre-peak intensity in comparison to the most intense region. Bottom row: Corresponding ADF images where grain boundaries are highlighted with a denser contrast. The yellow arrows indicate the position of the same grain boundary in the top and lower row for a given sample.

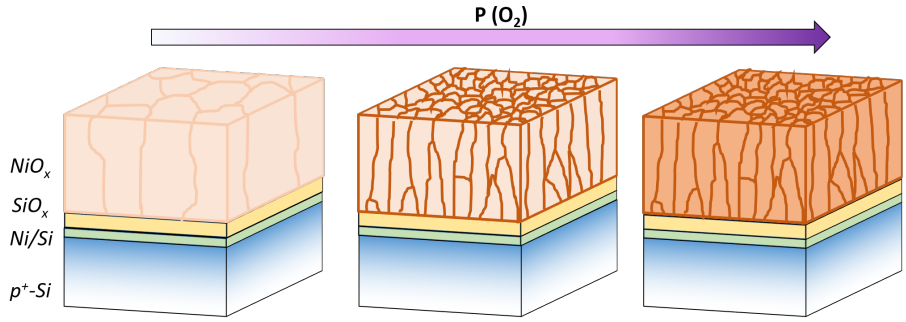

Figure 5.7: Schematic representation of the NiO thin film morphology deposited on silicon according to the oxygen partial pressure in the deposition chamber. The deeper the red, the more defects. At low oxygen concentration the thin film is considered to be homogeneous. When the oxygen concentration is increased the defects accumulate primarily at the grain boundaries before entering the whole crystal structure. As detailed in Appendix A.2, cationic inter-diffusion occurs at the interface which leads to the formation of a SiO_x layer on top of a nickel rich region.

the samples prepared with 17% and 20% of oxygen concentration indicates that the grain boundaries would primarily support electrical conductivity of the RT-NiO thin films.

A schematic representation of the distribution of the chemical species responsible for the oxygen hole in the NiO thin film has been represented in Figure 5.7 according to the oxygen content in the deposition chamber. With regards to the STEM-EELS measurements, the oxygen hole can be considered as absent if the thin film is prepared at low oxygen concentration but gradually appears at grain boundaries before being present in the whole structure at higher oxygen concentration. The threshold when the oxygen holes appear in the bulk of the grain can be triggered when grain boundaries are saturated with oxygen holes.

5.4 Discussion

5.4.1 Defects and charge compensation in NiO

NiO can be p-doped by holes in a metal deficient structure ($Ni_{1-\delta}O$). This can be obtained in an oxygen-rich environment which would lead to intrinsic doping by nickel vacancies $V_{Ni}^{''}$ or by oxygen interstitials $O_i^{''}$. Moreover, for charge neutrality, intrinsic doping of NiO has to be compensated by positive charges e.g: Ni^{3+} ($Ni_{Ni}^{\bullet}$), peroxo species O^- ($O_O^{\bullet}$), holes ($h^{\bullet}$) [83], or by oxygen vacancies ($V_O^{\bullet\bullet}$). This can be formalized as follow:

$$2\,[V_{Ni}^{''}] + 2\,[O_i^{''}] = [h^{\bullet}] + 2\,[V_O^{\bullet\bullet}] + [Ni_{Ni}^{\bullet}] + [O_O^{\bullet}] \tag{5.1}$$

where the brackets '[ ]' correspond to the defect concentration per volume. Equation (5.1) is only a general view of the defect chemistry which can develop

in nickel oxide. The left-hand side of equation (5.1) are electronic defects (the dopants) which can be introduced in nickel oxide under oxygen-rich condition while the right-hand side represents the charge compensating species of the dopants.

Regarding the left-hand side (the dopants), it is generally accepted that p-type conductivity in NiO originates from nickel vacancies $V_{Ni}^{''}$ [83, 164, 165]. Thus, Lany *et al.* have shown that in NiO crystals, under oxygen-rich conditions, nickel vacancies $V_{Ni}^{''}$ and not oxygen interstitials $O_i^{''}$, are the defects leading to nonstoichiometry [82]. However, in most cases, the NiO thin films contain grain boundaries and to the best of our knowledge, the possibility of stabilizing oxygen interstitials at grain boundaries in a nickel oxide thin film has not yet been discussed in literature. In addition, it has been reported that the grain boundaries differ from bulk NiO as this is a structure where, in comparison to bulk NiO, the defect formation energy might be lower [38] and the mobility of nickel vacancies is larger [180]. So a non-stoichiometry associated to oxygen interstitial at the grain boundaries has to be considered in this chapter.

Regarding the right-hand side of equation (5.1), associated to the compensating species, it is expected that the formation of one compound to be driven by thermodynamic rules. This would promote charge compensation mechanisms having the lowest formation energy. For instance, the formation of oxygen vacancies, $V_O^{\bullet\bullet}$, in oxygen-rich conditions is very unlikely. Also for room temperature (RT) NiO thin films, it has been proposed that delocalized holes (free holes) would be interacting with oxygen atoms and localized holes might be found on both nickel and oxygen atoms [83]. These results available in literature would suggest that dopant in NiO (left hand side of equation (5.1)) can be compensated by free (delocalized) holes ($h^{\bullet}$), by localized holes on oxygen ($O_O^{\bullet}$) and nickel ($Ni_{Ni}^{\bullet}$) atoms.

5.4.2 Charge compensation in NiO

As a charge transfer material [75, 77, 79], the mobile charges in the valence band of a pure crystallographic NiO structure are transferred continuously from $\mathrm{O\,2p^6}$ to $\mathrm{Ni\,3d^8}$ bands during electrical displacement. Therefore, the charges have to overcome a potential barrier and this can be done with the help of thermal energy in the form of a phonon [97, 98]. The addition of the energy of the phonon to the charges (hole) produce what is called a polaron.

The conductivity (σ) is the product of the contribution of the number of charge carriers (holes) and their mobility:

$$\sigma(T) = e\, p, \mu_p \tag{5.2}$$

with p the hole density, e the elementary charge and μ_p the hole mobility. According to Fermi statistics, the concentration p of holes in the valence band

is:

$$p = N_v \exp\left(-\frac{E_F}{k_B T}\right) \tag{5.3}$$

with N_v the effective density of states in the valence band, E_F the Fermi energy, T the temperature and k_B the Boltzmann constant. Temperature activation of the mobility μ_p for a polaron hopping transportation in NiO follows an Arrhenius law [97, 98] following:

$$\mu(T) = \frac{\mu_0}{T} \exp\left(-\frac{E_A}{k_B T}\right) \tag{5.4}$$

Where μ_0 is a temperature-independent pre-factor and the activation energy E_A is basically the required energy for the charge carrier to overcome the barrier between two energy wells [97, 99]. It should be mentioned that as the Fermi energy E_F and the activation energy E_A can be both determined with temperature dependent conductivity experiments, these parameters can be easily inter-mixed.

Right-hand side of equation (5.1)

In-situ XPS measurements of the samples prepared in chamber #2 suggest that the Fermi energy is not lowered with increasing oxygen concentration during preparation of the samples (Figure 5.3). Moreover, looking at the in-situ electrical measurements realized on the samples prepared in chamber #2 (Figure 5.2), the conductivity increases by three orders of magnitude when the oxygen concentration increases from 5 % to 15 %.

Assuming a constant hole mobility, according to equation 5.2, the increase of the conductivity would originate from an increase of the charge carrier density p in the valence band. It would imply that:

$$E_{F,15\%} - E_{F,5\%} = -k_B T \ln\left(\frac{p_{15\%}}{p_{5\%}}\right) \tag{5.5}$$

Therefore, an increase of the holes in the valence band by three orders of magnitude should be accompanied by a decrease of the Fermi energy by about 0.2 eV. This is not what is observed experimentally. In Figure 5.3 the Fermi energy is rather constant for the three samples. In RT-NiO thin films, the charge carrier concentration is therefore expected to be independent to the defects concentration. Eventually, the comparison of the in-situ XPS measurements and the in-situ electrical measurement would discard that the charge compensation is realized by holes ($h^\bullet$). The remaining possibilities are the formation of a positive charge on oxygen which lead to the formation of peroxo species($O_O^\bullet$) or on nickel which would form Ni^{3+} ($Ni_{Ni}^\bullet$). Thus, to explain the increase of the conductivity, the mobility of the charge carrier has to increase with increasing oxygen concentration or that the compensating species ($O_O^\bullet$ and $Ni_{Ni}^\bullet$) can be also considered as a charge carrier having a certain mobility.

The XPS data of the O 1s region (Figure 5.3) display a shoulder (O 1s(Def.)) which has been associated in literature to peroxo species ($O_O^{\bullet}$) [166]. Also the O 1s(Def.) intensity increases with increasing oxygen concentration in the chamber. It might correlate with the appearance of the oxygen holes peak at 529 eV in the O-K edge spectra obtained by EELS, especially at high oxygen concentration. Therefore, the oxygen holes could be related to positive charge on the oxygen ($O_O^{\bullet}$) arising from the charge compensation of the dopants.

However, the presence of Ni^{3+} ($Ni_{Ni}^{\bullet}$) in the thin film cannot be completely discarded as the Ni 2p region provides a more shallow valley with increasing oxygen concentration (Figure 5.3). Indeed, materials having formally nickel in the +III state, as for NiOOH and Li doped NiO, the Ni 2p spectra provides a more prominent Ni 2p(Sat.) peak in comparison to the Ni 2p(Main) peak [173, 174]. Thus, the disappearance of the valley between the Ni 2p(Sat.) peak and the Ni 2p(Main) peak with increasing oxygen concentration, may be related to the presence of positive charges on nickel ($Ni_{Ni}^{\bullet}$). It should be mentioned that the Ni^{3+} species might be controversial as its energy of formation could be relatively high in a pure NiO crystal structure [70]. However, we assume that positive charge compensation over nickel might be possible at or nearby grain boundaries.

Left-hand side of the equation (5.1)

STEM-EELS measurements highlight that the charge compensating species accumulate primarily at the grain boundaries before entering in the bulk of the grains with increasing oxygen concentration (Figure 5.6 and Figure 5.7). Assuming that the charge compensating species are formed in the proximity of the dopants, it implies that dopants would accumulate also at the grain boundaries. This assumption makes it difficult to determine what the majority dopant in RT-NiO thin films. Indeed, as detailed above, the stabilization of oxygen interstitials at the grain boundaries cannot be discarded. Therefore, no conclusion can be reached about the true nature of the dopant in RT-nickel oxide at this stage and it is assumed that both nickel vacancies (V_{Ni}'') and oxygen interstitial (O_i'') can dope a RT-NiO thin film.

5.4.3 Doping mechanism in RT-NiO thin films

Finally, as detailed above and in line with the Chapter 4, the dopant might be compensated by positive charge on oxygen $O_O^{\bullet}$ and to a lesser extent by a positive charge on nickel $Ni_{Ni}^{\bullet}$ but not by holes ($h^{\bullet}$). Also, the identification of the dopant in the RT-NiO thin film is not obvious and we assume that nickel vacancies can coexist as much as oxygen interstitial at the grain boundaries. Thus, as already shown in Chapter 4, the charge compensation mechanism in RT-NiO thin films must be:

$$\begin{aligned} 5\,\mathrm{Ni}_{\mathrm{Ni}}^{\times} + 4\,\mathrm{O}_{\mathrm{O}}^{\times} + O_2 \rightarrow & NiO + 4\,(1-\delta)(Ni_{Ni}^{\bullet} + O_O^{\times}) \\ & + 4\,\delta(O_O^{\bullet} + Ni_{Ni}^{\times}) + V_{Ni}'' + O_i'' \end{aligned} \tag{5.6}$$

with δ a parameter comprised between 0 and 1 to take into account charge compensation discrepancy over oxygen and nickel atoms.

5.4.4 Mechanism of conductivity in RT-NiO thin films

As represented in Figure 5.7, the oxygen holes would first accumulate at the grain boundaries before appearing in the bulk of the grain with increasing oxygen concentration. As it can be assumed that p-type doping is obtained in an oxygen-rich thin films, the RT-NiO thin films must be also oxygen-rich and these electrically active oxygen holes can be related to the accumulation of an oxygen-rich species at the grain boundaries. Although this hypothesis cannot be directly supported by EELS measurements, where the determination of the chemical composition is not accurate enough to emphasize an oxygen concentration distribution of less than 10 % inside the thin films [176, 179], it has been assumed that that higher conductivity is supported at the grain boundaries by the oxygen-rich secondary phase.

As mentionned above, charge transportation in NiO is in theory realized through the polaron hopping mechanism [73]. It means that charges in NiO (holes) need to gain enough thermal energy (phonon) to overpass an energy barrier E_a (see equation 5.4) located over a nickel atom separating two energy wells situated over oxygen atoms [97, 98] (Figure 5.8). Interstingly, literature reports low electrical activation energy in the 0-0.15 eV range for RT-NiO thin films [150, 175] whereas for pure NiO, the activation energy is higher with at least 0.6 eV [50].

Moreover, the pinning of the Fermi energy for the RT-NiO thin films suggests that the creation additional positive species in the valence band with temperature would lead to the formation of peroxo O^- or Ni^{3+} species. So for such materials as RT-NiO thin films, the concentration of charge carrier in the valence band is temperature independent which means that p in equation 5.2 is constant. Therefore, the activation energy reported in RT-NiO thin films could be related to the energy barrier that mobile charges as to overcome in the RT-NiO thin films.

As detailed previously, the interpretation of the in-situ electrical and in-situ XPS data suggests that the increase of the conductivity of RT NiO thin films with increasing oxygen concentration can be associated to an increase of the mobility of the charge carriers or that the compensating species provide support for conductivity.

Regarding the mobility of holes in the valence band, as the grain boundaries is supposedly an oxygen-rich material, it means that the alternative transfer from cationic to anionic site, typical of polaron hopping, could be replaced by a continuous band such as, for example, an O 2p band at the grain boundaries. Thus, E_A is reduced at the grain boundaries while it would have a higher value in the bulk of the grain. The low E_A for RT-NiO thin films would suggest that the energy barrier provided by the nickel atoms, and seen by the polarons, is

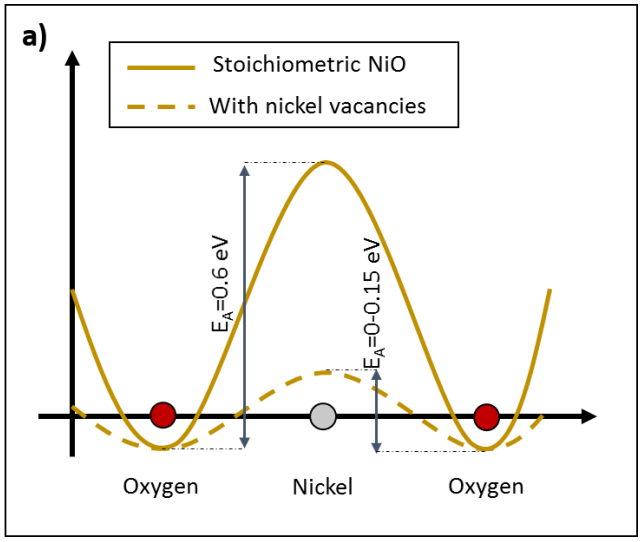

Figure 5.8: Schematic representation of the potential profile encountered by a charge in a stoichiometric NiO structure or in the case of the presence of a nickel vacancies. The electrical activation energy E_A value are taken in literature [50, 150, 175].

substantially reduced and the charges can flow from atoms to atoms without encountering substantial energy barrier (Figure 5.8).

Regarding the fact that the compensating species can also participate in the conduction process, as mentionned in the Chapter 4, as reported by optical adsorption measurements on Li doped NiO, a double feature is observed in the bandgap and can be assigned to the presence of an acceptor state $\sim$ 1 eV above the valence band [86]. This acceptor state could be made of the species compensating defects for RT-NiO thin films and could be also an alternative electrical path to the charges participating in the conduction process.

Eventually, the assumption that grain boundaries support electrical path correlates also with the reported dependence of the conductivity on the thin film thickness for the RT-NiO thin films in the 100 nm – 1000 nm range, where it can be observed that the thin film conductivity decreases with thickness [87, 150]. Indeed, as seen previously, when deposited by sputtering, the RT-NiO thin films are polycrystalline and composed of elongated grains (Figure 5.4). As proposed by Deuermeier *et al.* for Cu_2O thin films, it can be assumed that the grain boundary density is inversely proportional to the thin film thickness [181]. Therefore, similarly with NiO, in assuming that the quantity of grain boundaries decreases with thickness, as the results in this chapter supports the fact that grain boundaries are the main conduction paths, it can explain why the RT-NiO thin films conductivity decreases with thickness.

5.5 Conclusion

In conclusion, for the RT-NiO thin films prepared by reactive sputtering, the results of this chapter evidence the presence of a secondary phase, associated to an oxygen-rich material, accumulating first at the grain boundaries with increasing oxygen concentration before appearing in the bulk of the grain. The secondary phase, when measured by STEM-EELS, is characterized by an oxygen hole feature typical of higher conductivity in NiO.

In comparing in-situ electrical and XPS measurements, it has been unveiled that the charge compensation of defects in RT-NiO thin films is not realized through the formation of free holes (non-localized holes) but, instead, the dopant would be compensated by a positive charge localized on oxygen, which can convert into a peroxo species (O^-), or to a lesser extent by positive charges on nickel atoms (Ni^{3+}). The nature of the dopant, because it accumulates at the grain boundaries, could be both nickel vacancies and oxygen interstitial.

In the secondary phase, it is proposed that the charge carriers flow through a continuous energy band, likely the O 2p band or that it offers specific electrical path supported by the compensating species Ni^{3+} or O^-. This can explain the increase of the conductivity with oxygen in the process even though the quantity of charge carriers is constant for any NiO thin films prepared at RT.

CHAPTER 6

On the electrical instability of reactively sputtered nickel oxide thin films prepared at room temperature

Summary

Literature reports an electrical instability over time of the RT-NiO thin films. In the meantime, the Chapter 5 evidences the presence of an oxygen-rich secondary phase accumulating at the grain boundaries of such thin films. In this chapter, we demonstrate that the reported RT-NiO thin films electrical instability can be related to the instability of the oxygen-rich secondary phase. Thus, Nickel oxide thin films have been reactively sputtered at room temperature on non-conductive substrate (soda-lime, fused silica). It could be also observed an electrical instability with time of our synthesized RT-NiO thin films and with temperature. The study emphasizes at evidencing the structural modification of the RT-NiO thin films after thermal annealing and to detail the underlying mechanism for the reported electrical degradation. Thus, EELS, STEM, electrical, XRD and optical measurements have been performed. The study shows that the electrical instability of such thin films is intimately related the properties of the oxygen-rich secondary phase segregating at the grain boundaries highlighted in Chapter 5.

This chapter includes the results obtained by TEM/EELS measurements realized by Gunnar Lumbeeck and Nicolas Gauquelin from the EMAT group of the University of Antwerp. Also the work realized by Henri Savolainen at TU-Darmstadt contributed to the scientific input of this chapter.

6.1 Introduction

Literature reports that NiO thin films prepared at room temperature by reactive sputtering are subjected to electrical ageing especially when exposed to air [163, 182–184], contrary to NiO thin films prepared at high temperature [183]. This might be due to the desorption of oxygen from an oxygen-rich RT-NiO thin film over time [182]. The ageing process can be particularly enhanced if the RT-NiO thin film is exposed to a reducing atmosphere such as hydrogen (H_2), carbon monoxide (CO) or a humid atmosphere [185]. On the contrary, an oxidizing atmosphere (O_2) or inert atmosphere (Ar) do not degrade substantially the RT-NiO thin film conductivity [185]. This suggests that the RT-NiO thin films might be oxygen-rich and the excess of oxygen is decreased when the thin films is exposed to a reducing agent.

In the Chapter 5, it has been demonstrated the presence of an oxygen-rich secondary phase accumulating at the grain boundaries which is responsible to the high electrical conductivity and low activation energy reported for RT-NiO thin films. Thus, this chapter is intended at evidencing that the electrical instability over time of RT-NiO thin films prepared by reactive sputtering is intrinsically related to the desorption of the oxygen-rich secondary phase from the thin films.

6.2 Experimental

6.2.1 Deposition chambers

NiO thin films ($\sim$ 50 nm) were prepared by reactive DC magnetron sputtering at room temperature from a pure Ni target (99.9%). Two sputtering chambers have been used for this article.

The first one, which is the deposition chamber at UCL, was used to deposit the NiO thin films on soda lime substrate for ex-situ electrical measurements. As described in Section 3.4.1, the at UCL is endowed with a Multi-beam Optical Stress Sensor (MOSS) setup allowing to measure in-situ the stress developing during the thin film deposition [157]. NiO thin films were deposited at UCL on soda-lime substrate without any specific surface treatment and the NiO deposition was realized at 50 W, 0.26 Pa (2 mTorr), with a target-to-substrate distance of 12.2 cm and for oxygen concentration varying between 2.5 % and 20 %.

The second chamber is part of the DAISY-MAT system at TU-Darmstadt(see Section 3.3.1)where the thin films were prepared on fused silica for electrical temperature dependance measurements, optical, XRD and for high resolution transmission electron microscopy (HR-TEM), high resolution electron energy loss spectroscopy (HR-EELS) and Automated Crystal Orientation Mapping (ACOM-TEM) measurements. The conditions of deposition at TU-Darmstadt

were set to match the discharge curve and deposition rate obtained at UCL. Thus, deposition conditions at TU-Darmstadt were set to 40 W, 0.5 Pa and the target-to-substrate distance to 14 cm. With these parameters, the NiO thin films have been produced with 15 % of oxygen concentration on fused silica.

6.2.2 Ex-situ electrical measurements

Electrical characterization of the NiO thin films deposited on soda lime at UCL were conducted ex-situ (after exposure to air) with standard four probe measurements when freshly deposited (see Section 3.4.4). Conductivity measurements on the aged sample were performed with the Transmision Line Measurements method as the conductivity was too low to be measurable with our standard four probe setup (see Section 3.4.4).

6.2.3 In-situ stress measurements

In-situ stress measurements have been performed during the growth for a RT-NiO thin film deposited with 15 % oxygen on oxide free H-terminated p^+-silicon (see Section 3.2.1). Once the deposition is terminated, the temperature of the sample is manually increased in a stepwise-fashion until $\sim$ 200 °C in vacuum. The exact temperature on the sample is not known as no temperature calibration was available, therefore the indicated temperature is the temperature which has been set on the temperature controller of the system.

6.2.4 Temperature dependent conductivity measurements

Temperature dependent conductivity measurements have been performed on one sample prepared with 15 % oxygen at TU-Darmstadt on fused silica. The measurement is carried out in O_2/Ar (ratio 1:9) atmosphere in van der Pauw geometry (platinum contact). The temperature is cycled from RT to 500 ° C at 1 ° C/min with an holding period of one hour at 500 ° C. A complete set-up description is detailed in Section 3.4.4. The thermal cycle can be considered as an annealing process.

6.2.5 Optical measurements

Ultra-Violet VISible Spectroscopy (UV-VIS) measurements have been conducted with a Cary 7000 spectrophotometer in the 250-2500 nm wavelength range. The reflectance measurement was realized with a 6° angle between the incident light and normal of the surface, while for the transmittance measurement, the incident light is set parallel to the normal of the surface. A more complete description of the methods used for the optical measurements is given Section 3.4.3.

6.2.6 STEM, EELS, ACOM-TEM, XRD and GIXRD measurements

XRD $\theta/2\theta$ scans and GIXRD were performed following description of the TU-Darmstadt setup in Section 3.4.2 for XRD and GIXRD measurements.

Experimental details about the STEM, EELS and ACOM-TEM measurements have been described in Chapter 3.3.1.

6.3 Results

6.3.1 Instability of NiO thin films prepared at RT

Instability with time

The Nickel oxide thin films produced at room temperature have been electrically characterized at three different stages: directly after deposition (in-situ, TU-Darmstadt, see Chapter 5), freshly deposited but exposed to air (ex-situ, UCL) and after storing the samples for several months in air (ex-situ, UCL). The results (Figure 6.1) show that the thin films are not stable over time, and freshly deposited thin films are more conductive than samples exposed to air for 6 months. The difference in conductivity can be up to 5 orders of magnitude. This electrical degradation is refereed in the literature as electrical ageing [163, 182–184]. Thus, the conductivity of the thin films prepared with 15% of O_2 is about 6 S/cm when measured in-situ at TU-Darmstadt, but with the same oxygen concentration prepared at UCL and exposed to air for 6 months, the conductivity is only $\sim 10^{-4}$ S/cm. From Figure 6.1 it is obvious that RT-NiO thin films are unstable over time when exposed to air, even at room temperature. This instability complicates any comparison of values with literature. Nevertheless, it can be noticed that the conductivity increases with increasing oxygen concentration during sputtering for the NiO thin films prepared in both deposition chambers (Figure 6.1). This might indicate that the oxygen concentration during deposition plays a fundamental role for the conductivity of the NiO thin films. The trend in conductivity with the oxygen concentration is preserved at any moment of the ageing process.

Instability when annealed

When heated up to $\sim$ 200 °C, in-situ stress measurements of the RT-NiO thin film prepared with 17 % of oxygen in the deposition chamber displays a compression-to-tension transition (Figure 6.2). Such a transition can occur if the thin film loses material in vacuum (e.g. desorption of oxygen species) and also if the sample becomes more densely packed (e.g. higher degree of crystallinity). Therefore, in addition to the ageing process over time, the heat could be another factor of instability for the NiO thin films prepared at room temperature. The degradation of the conductivity observed with time in Figure

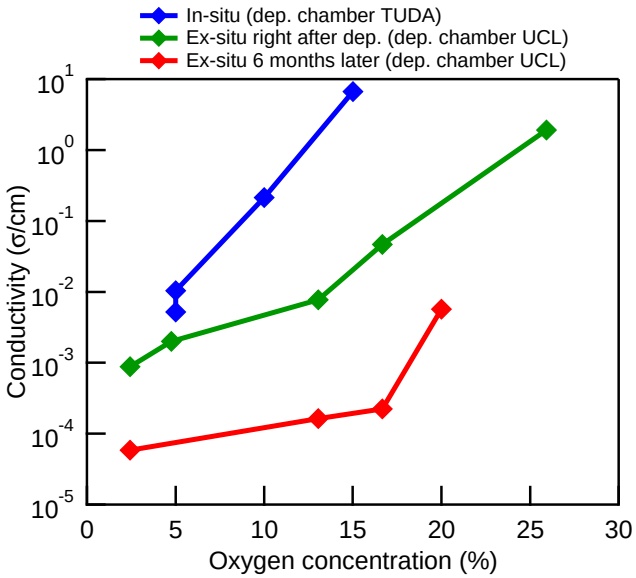

Figure 6.1: In-situ conductivity measurements of the NiO thin films deposited at TU-Darmstadt on gold patterned fused silica substrates (see Chapter 5) and conductivity measurements of the RT-NiO thin films deposited at UCL on soda lime substrates directly after deposition (4 probes measurements) and after 6 months (TLM).

6.1 or with temperature in Figure 6.2 lead us to question the stability of the NiO thin films sputtered at room temperature.

6.3.2 Temperature dependent conductivity measurements

Temperature dependent conductivity measurements of the sample prepared at room temperature on fused silica show a non-reversible transition occurring at 150-200 °C when the sample is heated up during the first cycle (Figure 6.3). After the first cycle, the electrical conductivity loses up to two orders of magnitude and does not return to the initial value before annealing, which was about 1 S/cm. This result is in-line with literature, where it has been reported that the conductivity of NiO thin films abruptly decreases by 3 orders of magnitude when the NiO thin film is prepared above 200 °C in comparison to room temperature preparation [95].

Interestingly, the conductivity of the NiO thin film is affected by the presence of oxygen in the atmosphere during the thermal cycle. At the end of the second cycle, performed in pure Argon, the conductivity is decreased by another order of magnitude in comparison to its value at the end of the first cycle, which has been performed in 10 % O_2 atmosphere (Figure 6.3). On the contrary, at

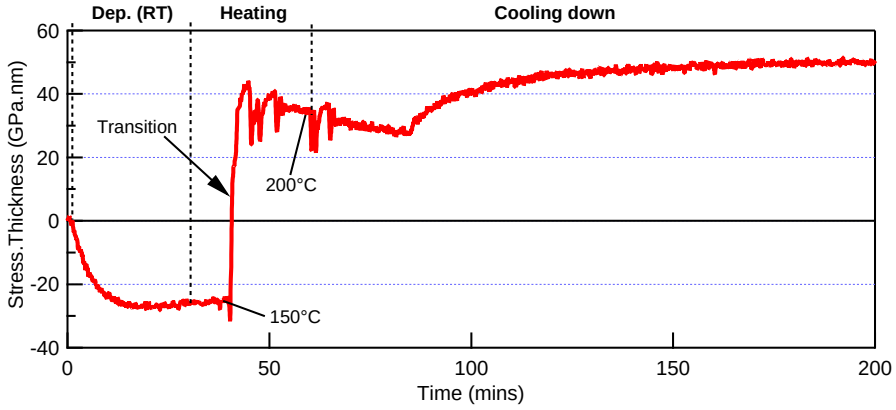

Figure 6.2: In-situ stress measurement of a sample prepared at UCL with 17 % oxygen concentration and annealed stepwise in vacuum directly after the deposition. Compressive-to-tensile transition is observed between 150-200 °C. The increase of the tensile stress during the cooling might be assigned to the difference in thermal coefficient of the NiO thin film and the silicon substrate. Sample thickness after deposition is about 100 nm here.

the end of the third cycle, carried out in 10 % oxygen, the conductivity value is identical to the conductivity obtained at the end of the first cycle (Figure 6.3). This indicates that the presence of oxygen in the annealing atmosphere can balance the conductivity in the NiO thin film. Thus, it could confirm the p-type nature of the conductivity in NiO with nickel vacancies (V''_{Ni}) or oxygen interstitial (O''_i) as intrinsic dopants. Also, the first and the third cycle, realized in 10 % oxygen, display a feature during the heating up at around 200 °C, which is not visible during the second thermal cycle in Argon. As the first and third cycle are both realized in the presence of oxygen, the feature around 200 °C could be related to adsorption/desorption process of oxygen on the nickel oxide surface.

6.3.3 NiO thin film structure on fused silica

The NiO thin film deposited on fused silica is morphologically identical to the ones deposited on silicon discussed in Chapter 5. Indeed, in the as-grown film, as for the NiO thin films deposited on silicon (see Chapter 5), the ACOM-TEM images of the NiO thin film display elongated grain along the direction of growth (Figure 6.4). In addition, the pre-peak at 529 eV in the O-K edge spectra, assigned to the presence of a larger conductivity and labelled as an oxygen-holes (see Chapter 5), is detected primarily at the grain boundaries but not in the bulk of the grain (Figure 6.5). It indicates that the NiO thin films deposited on non-conductive substrate can be considered as similar as what was obtained on silicon in Chapter 5 with elongated grain structure including a high density of grain boundaries in the thin film and the oxygen-hole feature

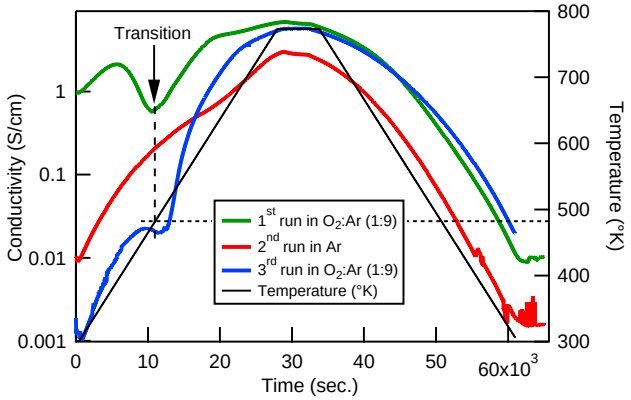

Figure 6.3: Temperature dependence of conductivity for NiO thin films prepared at RT at TU-Darmstadt with 15% oxygen in the deposition chamber. The temperature is indicated by the black curve.

in the O K edge spectrum present at the grain boundaries.

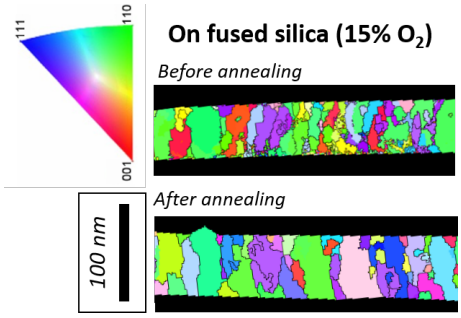

Figure 6.4: ACOM image of NiO thin film deposited at RT on fused silica before (top) and after annealing (bottom). The thin film is deposited at TU-Darmstadt with 15 % oxygen.

After the annealing of the sample prepared on fused silica, although the ACOM-TEM structure dhows well defined grain domain similar to what was observed before the thermal cycle (Figure 6.4), the EELS spectrum over a grain boundaries does not display the feature assigned to the oxygen-holes (Figure 6.5). Therefore, the thermal cycle might suppress the defects formed at the grain boundaries during the reactive DC-sputtering at room temperature, while preserving the morphology as well as restoring stoichiometry homogeneity.

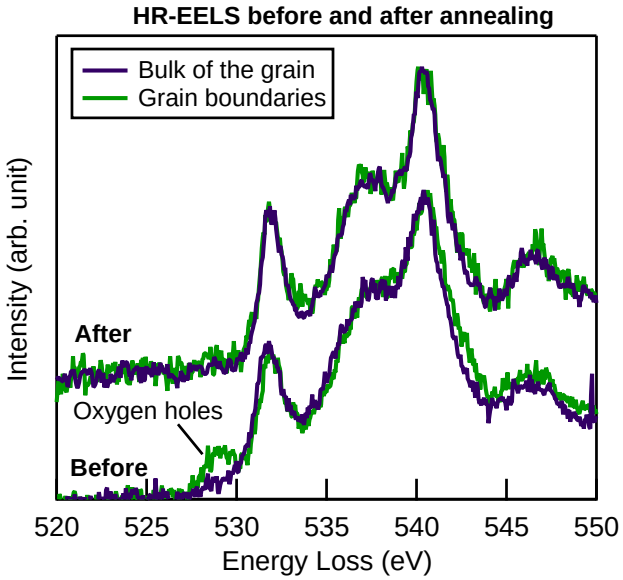

Figure 6.5: HR-EELS spectra obtained in the bulk of the grain (Black) and at the grain boundaries (Green) for the thin film deposited on silica at room temperature before and after annealing. Before annealing the oxygen hole is observed at grain boundaries but the feature at 529 eV is suppressed after annealing.

6.3.4 XRD and optical measurements

The X-Ray diffractogram presented in Figure 6.6 shows a dominantly NiO (111) oriented thin film before and after annealing. However, the intensity of the (111) peak is increased and is shifted to the right after the sample is annealed for both XRD and GIXRD patterns. It would mean that an out-of-plane tensile strain is relaxed after heating and probably the thin film structure reorganizes towards a less defective (and less amorphous) crystallographic structure. This is in-line with the compressive stress measured in-plane by an in-situ stress measurement on the NiO thin films deposited on silicon (see Chapter 10). This means that the volume of the crystal structure is compressed in the plane and is extended along the direction of growth. The stress measured in NiO thin films might arises from the presence of the defects in the thin film accumulating at the grain boundaries.

Optical measurements show that the non-annealed sample prepared at room temperature has a higher optical absorption coefficient in the bandgap in comparison to the annealed sample (Figure 6.7). Concurrently, although this might not be substantial, the optical bandgap increases from 3.6 eV to 3.75 eV (Figure 6.7). The higher optical absorption observed for the sample prepared at RT might be partly related to the oxygen hole species evidenced by STEM/EELS and segregating to the grain boundaries. Indeed, for the

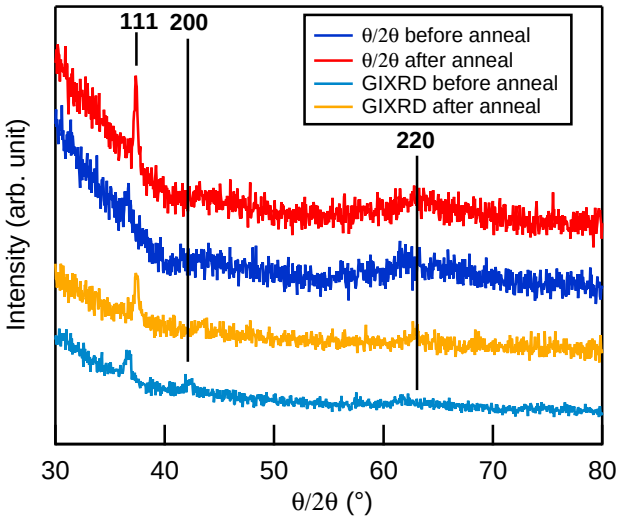

Figure 6.6: XRD and GIXRD patterns of the NiO thin film deposited at room temperature on fused silica before and after annealing.

annealed sample, the absorption in the bandgap is substantially improved while the oxygen hole pre-peak is removed (Figure 6.5).

As already mentioned in Chapter 4, it has been reported that, for Li-doped NiO single crystal, a double feature is observed and could be related to an acceptor state about 1 eV above the valence band [86]. The features denoted as α and β are the transition between the Ni $3d^8$ and the O $2p^6$ orbitals, respectively, to the acceptor state in the bandgap. Our results do not show similar well defined double feature and the reason could be that the intrinsically doped RT-NiO thin films are less crystalline with, in particular, a secondary oxygen-rich phase accumulating at the grain boundaries. This might favour a background absorption and an energy dispersion in the bandgap of the double feature.

6.4 Discussion

In line with literature, our experiments show that RT-NiO thin films are electrically unstable over time and with temperature (Figure 6.1 and Figure 6.3). In Chapter 5, an oxygen-rich secondary phase has been evidenced by STEM/EELS measurements at the grain boundaries which support an electrically active species in the name of oxygen-holes. In this chapter, the experiments demonstrate that the oxygen-rich secondary phase can be suppressed upon heating. Indeed, the EELS measurements on an annealed RT-NiO thin film (Figure 6.5) does not display the oxygen holes which was detected before annealing at the grain boundaries. Concurrently, it is observed

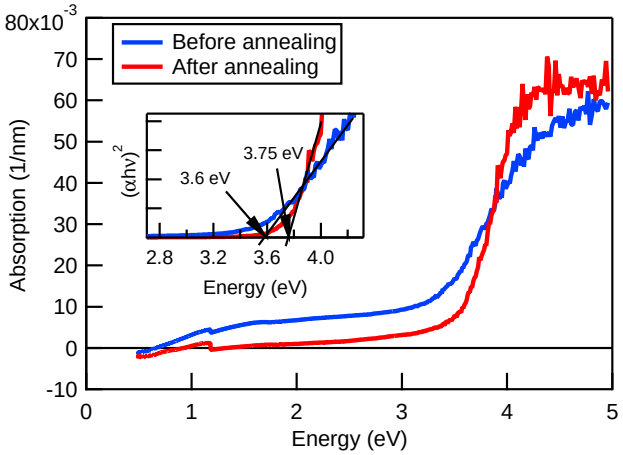

Figure 6.7: Absorption coefficient of the RT-NiO thin film deposited on fused silica at TU-Darmstadt with 15% oxygen. The measurements are carried out before and after annealing. Tauc plot is represented in the inset where optical bandgap before and after annealing is determined as being 3.6 and 3.75 eV, respectively.

an inflexion in the temperature dependent conductivity measurements around 200 °C in the heating stage of the first thermal cycle (Figure 6.3). After the first thermal cycle, the conductivity is substantially lowered and it cannot recover the high conductivity measured before. The inflexion in conductivity around 200 °C and the loss in conductivity after a thermal cycle can correspond to the suppression of the oxygen-rich secondary phase carrying the oxygen-holes. Thus the electrical instability with heating can be associated to the desorption of the excess of oxygen presents at the grain boundaries.

Moreover, the XRD measurements (Figure 6.6) and the optical measurements (Figure 6.7) suggest that the RT-NiO thin film is subjected to a high internal stress and possess a certain degree of amorphousness. After the thermal cycle the RT-NiO thin films are relaxed and are converted towards a more stoichiometric and homogeneous film. Thus, it could be assumed that the oxygen-rich secondary phase is highly disordered and amorphous in nature as both the secondary phase and the amorphousness of the film are suppressed with heating.

It could be assumed that the desorption of the oxygen-rich phase at the grain boundaries, observed with heating, is also the underlying mechanism of the reduction of the conductivity with time of the RT-NiO thin films as represented in Figure 6.8. Finally, a schematic of the annealing process and the ageing process on a RT-NiO thin film prepared by DC reactive sputtering in a relatively high oxygen concentration, is proposed in Figure 6.8.

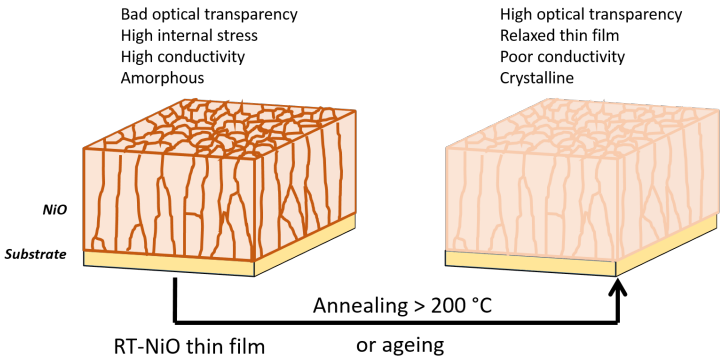

Figure 6.8: Illustration of the RT-NiO thin film modification after annealing above 200 °C or with ageing. The amorphous oxygen-rich secondary phase which accumulate primarily at the grain boundaries, the reddest part on the schematic, is suppressed and after the process, the NiO thin film leans towards a more stoichiometric and relaxed morphology.

6.5 Conclusion

In this chapter, it has been demonstrated that the oxygen-rich secondary phase evidenced in Chapter 5 and accumulating at the grain boundaries is amorphous, not stable with temperature if heated above $\sim$ 200 °C and by extension is not stable with time. It has been assumed that the secondary phase desorbs from the thin film prepared at room temperature following a stoichiometry recovery mechanism. Thus after annealing no secondary phase is detected by EELS over the grain boundaries, the thin film is relaxed, the optical transparency is improved but the conductivity is substantially reduced. Finally, the results suggest that the intrinsic properties of the oxygen-rich secondary phase is related to the stability of the RT-NiO thin films with temperature and with time.

CHAPTER 7

Growth of oriented nickel oxide thin films

Summary

Surface properties can become a fundamental issue in any application where surfaces or interfaces are involved as for the solid-electrolyte junctions and the solid-state junctions [186]. The understanding of the surface properties might bring valuable information to improve the performance of a device. However as NiO is highly resistive, a conductive underlayer is necessary to study the surface by e.g. in-situ UPS/XPS or electrochemically

Therefore, in this chapter, because of the relatively low lattice mismatch NiO thin films have been grown on oriented platinum thin films (100, 110 and 111) by DC sputtering in the DAISY-MAT system at TU-Darmstadt. The aim of this part is to determine what are the conditions of preparation favouring the obtention of an oriented NiO thin film (100, 110 or 111). The effect of the conditions of preparation on the thin film orientation was explored into two parts. In a first part the temperature of deposition is set to 400 °C and the oxygen concentration is varied from 2.5 % to 20 %, while in a second part the oxygen concentration in the deposition chamber is fixed to 10 % and the temperature is increased from room temperature to 500 °C. In the first part the thin films morphologies and structures were assessed by atomic force microscopy (AFM) and by X-ray diffraction (XRD) measurements, while the thin films produced in the second part were assessed only by AFM measurements. It will be shown that for (100) oriented NiO thin films can be obtained at 400 °C and 10 % of oxygen on (100) oriented Platinum substrates, and fully (110) and (111) oriented NiO thin films can be obtained at 400 °C and 20 % of oxygen on (110) and (111) oriented Platinum substrates, respectively. It has also been observed that an increase of temperature helps to obtain a more crystalline surface. Thus, as revealed by AFM, surfaces without well-defined morphology are observed at room temperature while sharp structures on the thin films surface could be visualized if prepared at 500 °C.

7.1 Introduction

An oriented substrate with low lattice mismatch is necessary to favour the growth of oriented NiO thin films. Therefore, the growth of (111) oriented NiO thin films might be promoted on non-conductive materials as α-sapphire(0001) [52,187–190] and MgO(111) [54], and on conductive materials as Pt(111) [191], Au(111) [52,192], Ni(111) [52,58,61], Cu(111) [52], Rh(111) [193], Mo(110) [194]. NiO (100) oriented layers were successfully obtained on non-conductive surfaces of MgO 100 [55, 195, 196] and on the conductive surface of 3 nm-MgO(100)/Mo(100), Mo(100) [194], Ag(100) [192, 197–200], Ni(100) [63], Pt-Ir(200) [201]. To our knowledge only one study coped with the growth of NiO (110) oriented thin film, which was made on a MgO (110) single crystal [55].

Little information is available regarding the oriented NiO thin films microstructure, which could unveil grain boundaries or dislocations. However, using PLD at 300 °C and in pure oxygen, Kawai *et al.* could successfully obtain homogeneous NiO (100) thin films without apparent dislocations on Pt-Ir 200/STO (100) substrates [201]. On α-sapphire(0001), Lee *et al.* [189] deposited NiO (111) oriented films by RF-sputtering from a NiO target in pure O_2 atmosphere at 15 mTorr. It was found that NiO adopts a cubic grainy structure if deposited at 400 °C and a rhombohedral structure if deposited at 600 °C. Finally, Warot *et al.* grew NiO (111) on MgO (111) by RF sputtering from NiO target at 10% oxygen concentration and at high temperature (700-900 °C). They found that, on MgO (111), the deposited NiO (111) thin film developed triangular (100) faceting of tetrahedral nature when prepared at 900 °C but not at 800 °C [54]. Similarly, on MgO 110, the NiO (110) oriented thin film adopts elongated pyramidal reconstruction into (100) facets [55]. Yamauchi *et al.* obtained flat NiO (111) surface on sapphire (0001) after RTA treatment at 1373 K for 60 seconds with some discontinuity emerging at substrate irregularity [190].

7.2 Experimental

As detailed in Section 3.1.3, oriented Platinum (100), (110) and (111) thin films ($\sim$ 50-100 nm) were prepared on MgO 100, MgO (110) and Sapphire(0001) (CrysTec), respectively. Platinum deposition is realized at high temperature (600 - 650 °C) and low deposition rate (2-4 nm/min) by DC-sputtering at 5 W in 0.5 Pa Argon atmosphere for the deposition on Sapphire and MgO(110) and 4 Pa (1:9) O_2:Ar atmosphere for Platinum deposition on MgO(100).

The NiO thin films ($\sim$ 50-150 nm) are DC-reactively sputtered onto the oriented Platinum thin films at 400 °C, the power is set to 40 W, the pressure to 0.5 Pa and the target-to-substrate distance to 14 cm. The samples have been produced for 2.5 %, 5 %, 10%, 15 % and 20% of Oxygen concentration in the deposition chamber. It has been found that, if the oxygen concentration was too low, metallic nickel could be formed in the thin film. Having at

least 10 % oxygen was sufficient to produce NiO without metallic nickel. It is worth mentioning that the 10 % value corresponded to the middle of the transition regime of the cathode discharge curve of the deposition chamber at TU-Darmstadt (see Section 3.1.2). After deposition, sample cooling is realized in the same atmosphere as the deposition atmosphere, the reason being to avoid any drastic surface modification or/and change in stoichiometry if the samples are exposed to vacuum while the sample temperature is still hot. The samples prepared at 400 °C were studied by AFM (see Section 3.3.3) and XRD measurements at TU-Darmstadt (see Section 3.4.2).

A series of NiO thin films deposited on oriented Platinum has been prepared where the oxygen concentration is fixed to 10 % but the temperature is varied from room temperature to 400 °C. This series has not been studied by XRD and only AFM images related to this second series will be shown.

7.3 Results

7.3.1 Surface morphology of oriented Pt thin films

The XRD patterns of the final structure containing the Platinum thin films show that the Platinum thin films are oriented according to the substrate orientation. Indeed, looking at the Figure 7.2 and Figure 7.3, no other Platinum peaks than the desired ones can be observed on the XRD patterns. It means that the (100) oriented Platinum layer is obtained on MgO (100), the Platinum (110) layer on MgO (110) and the Platinum (111) layer on Sapphire.

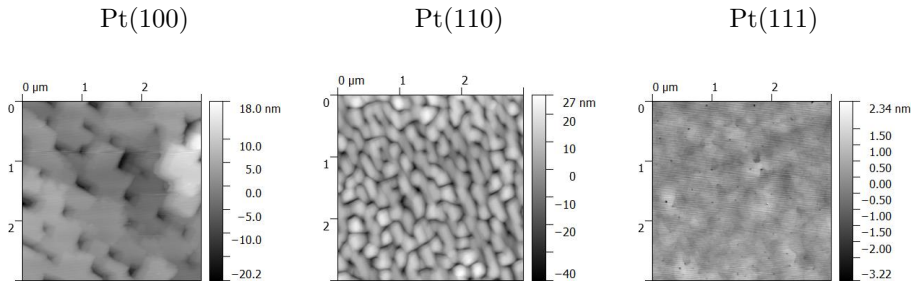

Figure 7.1: AFM height images (3×3 µm) of oriented Platinum thin films grown on oriented MgO(100), MgO(111) and α-Sapphire (0001). Measured at TU-Darmstadt.

However, the AFM images of the Platinum thin films highlight that the surfaces might include step-like patterned surfaces, as for (100) surface and (110) surface, or some dot-like irregularities as for the (111) surface (Figure 7.1). Thus, the Platinum thin films are oriented as desired, but in looking at the AFM images, it can be seen that the surface is not perfectly flat (Figure 7.1). The (111) oriented Platinum thin film presents the flattest surface among all while the (100) and (110) oriented Platinum thin films are seemingly exposing

more patterned surfaces. It should be mentioned that the irregularities can affect the growth of the NiO layer as it could favour the emergence of stress leading to the formation of similar irregularities in the NiO thin film.

7.3.2 NiO thin films deposited at 400 °C

General observations

XRD patterns of the NiO thin films deposited on top of the oriented Platinum thin films are displayed on Figure 7.2 and Figure 7.3. The lattice mismatch of MgO being only ~ 1 % with NiO, the differentiation of the XRD MgO peak and NiO peak was not possible when MgO was used as base substrate. However, NiO orientation other than the MgO orientation would be clearly visible, if present. In case no XRD NiO orientation is visible outside the intense region were the XRD MgO peak dominate, the sample is assumed to be dominantly oriented according to the substrate orientation. Thus, totally oriented NiO thin films are obtained on the MgO(110)/Pt(110) and α-Al_2O_3(0001)/Pt(111) if the concentration of oxygen is 20% (Figure 7.2), and on MgO(100)/Pt(100) if the concentration of oxygen is 10 % (Figure 7.3). Thus, the (100) orientation is favoured at lower oxygen concentration and the (111) and (110) at higher oxygen concentration. This might be in-line with what is predicted for at least the (100) and (111) orientations, which are supposed to be favored in low and high oxygen concentration, respectively [183, 202].

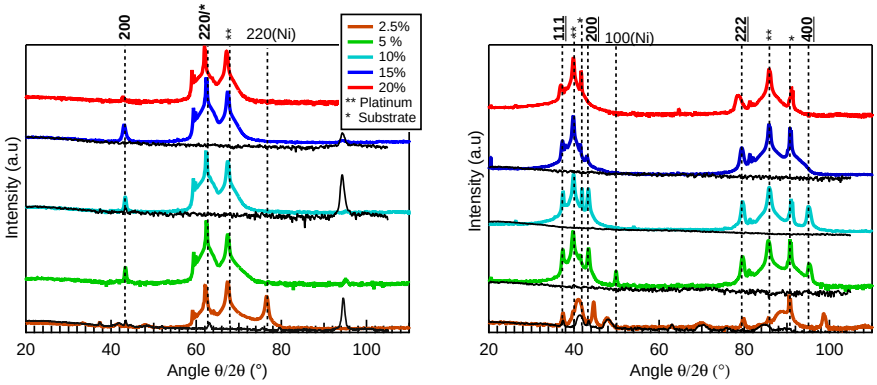

Figure 7.2: θ/2θ XRD scans of NiO thin films deposited at 400 °C on Pt/MgO(110) substrates (left) and Pt/α-Sapphire (0001) (right). The black curve accompanying the θ/2θ represents the omega scan where the angle ω is 2 ° (see Section 3.4.2). Measurements realized at TU-Darmstadt.

Under 10 % oxygen concentration, the thin films might include a metallic phase. The metallic phase is well visible at 2.5 % and it tends to vanish for the samples prepared with 5 % oxygen. With at least 10 % of oxygen in the deposition chamber, the XRD feature associated to metallic nickel is

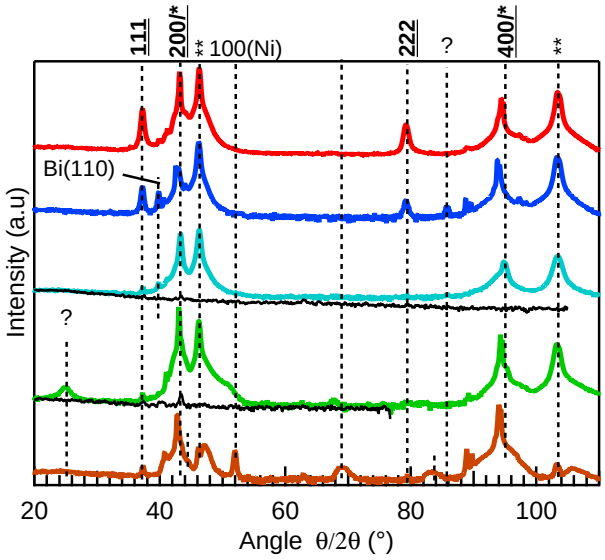

Figure 7.3: $\theta/2\theta$ XRD scans of the NiO thin films deposited at 400 °C on Pt/MgO(100) substrates (left) and at various oxygen concentration. The NiO thin film deposited on Pt/MgO(100) with 15 % oxygen concentration suffered from bismuth cross-contamination during the deposition. The black curve accompanying the $\theta/2\theta$ represents the ω=2 ° scan. Measurements were realized at TU-Darmstadt. For the legend to reader is invited to refer to Figure 7.2.

suppressed (Figure 7.2 and Figure 7.3). The samples prepared with 2.5 % of oxygen might be an amorphous or not well defined crystalline structure of NiO. Indeed, the AFM images of the sample prepared with 2.5 % on Pt(111) shows large and rough domains (Figure 7.4). Moreover, the ω scan of the samples prepared with 2.5 % of oxygen display peaks aligned with the $\theta/2\theta$ scan peaks, which might indicate a tilted crystal structure not aligned with the oriented Platinum thin films. However, XPS spectra, not displayed here, did not show any trace of metallic Ni for the samples prepared with 2.5% and 5% oxygen in the deposition chamber. This is likely due to the fact that the surface oxidises after the deposition as the sample is maintained in the deposition atmosphere until this is cold enough to be transferred to the XPS chamber. The partial oxidation has been assumed to be realized with respect to the dominant orientation as the metallic domain might adopt an oriented growth as well.

Also, the XRD patterns highlight the inclusion of the NiO (111) orientation for the NiO thin film deposited on Platinum (100) above 10% of oxygen concentration (Figure 7.3). Non-desired (100) orientations also appear for samples prepared on Platinum (110) and (111) for lower oxygen concentration than 20 % (Figure 7.2) where the non-desired (100) phase gradually disappears with increasing oxygen concentration. Regarding the non-desired orientations

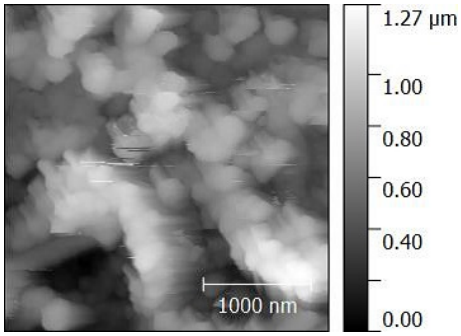

Figure 7.4: AFM height image of a NiO thin film prepared on (111) oriented Platinum surface at 400 °C and 2.5 % of oxygen concentration.

in any thin films, if the oxygen concentration is at least 5%, the ω scans at 2° do not show of diffraction peak aligned with the $\theta/2\theta$ diffraction angles of the non-desired orientations (Figure 7.3 and Figure 7.2). This indicates that the non-desired orientations grow parallel to the substrate surface.

The AFM images obtained with the NiO thin films deposited on oriented Platinum thin films at 400 °C (Figure 7.5), show patterned surfaces where the height amplitude can vary up to 100 nm. This might not be representative of the real height of the structure on the surface as the thin films were sometime only 50 nm thick, as for the sample prepared with 20 % of oxygen concentration (Figure 7.5). However, the AFM images enable to evaluate the quality of the surface and to assess the structure developing according to both the oxygen concentration and the substrate dominant orientation.

NiO thin films deposited on Pt (100)

In the series of samples obtained at 400 °C, the most (100) oriented NiO thin film on (100) oriented Platinum has been obtained with 10 % of oxygen concentration (Figure 7.3). The XRD patterns show also that the thin films prepared with 2.5 % and 5 % might include a metallic nickel secondary phase while for oxygen concentration higher than 10 % a non-desired (111) orientation appears. As seen in Figure 7.5, the surface morphology gradually changes to a more grainy structure with increasing oxygen concentration. At low oxygen concentration a very flat surfaces co-exist with sharp cubic-like structures and some areas which look like pin-holes in the thin films. With increasing oxygen concentration the pin-holes tend to disappear and the sharp cubic-like structures are replaced by rounded grains when the thin film is prepared with more than 15 % of oxygen concentration. The sharp cubic-like structure and the pin-holes observed at lower oxygen concentration might arise because of the irregularities observed in the AFM image of the (100) oriented Platinum thin film (Figure 9.6). At higher Oxygen concentration, as it has been seen in Chapter 4, the thin films include larger quantity of electronic defects. Thus

the introduction of defects in the thin film may accommodate the irregularities in the structure originating from the Platinum thin film, and so the rounded shapes observed at high oxygen concentration (Figure 7.5), which does not correspond to a regular cubic crystallographic structure, might arise because of the inclusion of defects in the thin film at such oxygen concentration.

NiO thin films deposited on Pt (110)

Best (110) oriented samples are obtained for high oxygen concentration (20 %). At lower oxygen concentration the thin films are a mixture of (110) and (100) orientation. It should be mentioned that the NiO (100) orientation grows along the growth direction as indicated by the absence of peak in the ω scan for the NiO (100) diffraction peak (Figure 7.3). The deposition of the NiO thin films on (110) oriented Platinum thin films at 400 ˚C provided a rough surface for any oxygen concentration in the deposition chamber (Figure 7.5). However, the samples prepared with 10 % and 15 % seem to develop regular patterns. In particular, with 15 % of oxygen concentration the surface produce elongated structures, which could remind the (100) surface faceting of the (110) surface observed at high temperature in the literature when the thin film is directly prepared on MgO (110) [53]. Also at 500 ˚C and with 10 % of oxygen concentration, the surface of the thin film deposited on (110) oriented Platinum thin film displays sharper edges along the elongated structure (See Section 7.3.3). It could mean that a similar surface morphology observed on MgO (110) could be obtained when the thin film is deposited on (110) oriented Platinum. With 20 % of oxygen concentration and at 400 ˚C the surface of the thin film shows a grainy morphology (Figure 7.5). Similarly to the NiO thin films prepared on (100) oriented Platinum thin film at high oxygen concentration, the grainy surface obtained for the 110 oriented thin film at 20 % Oxygen would appear because of crystallographic defects accommodating rounded shape grains which is not typical of cubic crystallographic structure.

NiO thin films deposited on Pt (111)

The AFM images of the NiO thin films deposited on Platinum (111) reveal two types of domains for oxygen concentration between 5 % and 10 % (Figure 7.5). One is extremely flat, while the second one is grainy. The height difference between these two structures does not excess more than 7 nm. The flat surface being in any case at lower level than the rough one. The area fraction of the flat surface decreases with increasing oxygen pressure. At 5 %, 10 % and 15 % of oxygen concentration, the flat surface account for 47 %, 25 % and 2 %, respectively. The flat surface is then totally absent from the AFM image obtained with the sample prepared with 20 % of oxygen.

Thus, because of mutual disappearance of the flat surface on the AFM images and the NiO (100) peak on the XRD patterns with increasing oxygen content for NiO thin films grown on Pt(111) thin film (Figure 7.2), it is reasonable to assert that the flat and the grainy morphology are related to the NiO (100) and the NiO (111) orientations, respectively. However, the

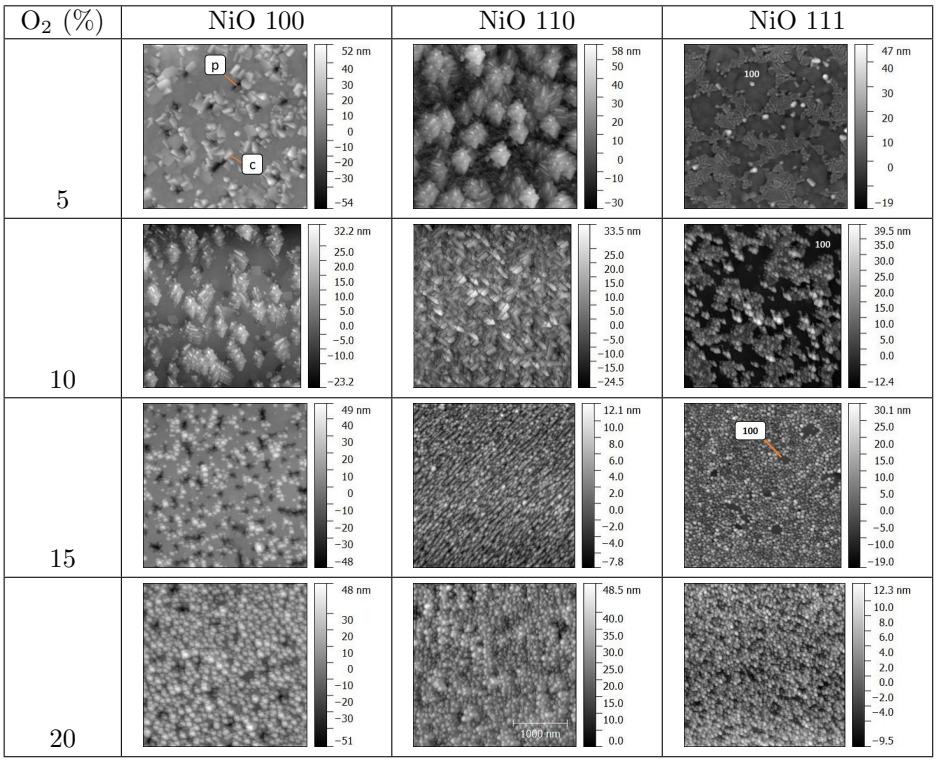

Figure 7.5: AFM height images (3×3 µm) measured at TU-Darmstadt of the NiO thin films grown on (100), (110) and (111) oriented Platinum thin films at 400 °C and at various oxygen concentration. The label p and c indicate a pin-hole and a cubic-like morphology, respectively. Regarding the NiO thin films deposited on Platinum (111), the flat area associated to the (100) orientation is indicated by the label 100, the grainy surface being associated to the (111) orientation.

interplanar distances of the (100) and (111) planes are 0.208 nm and 0.12 nm, respectively. The (111) orientation is thus more packed than the NiO (100) along the growth direction. With respect to the interplanar distance, it would be expected that, for a homogeneous growth, the (100) phase is more elevated than the (111) one. However, the AFM images show the contrary. This indicates that the growth rate along the (111) direction is faster than along the (100) direction. Instead, the thicker (111) region could correlate with the higher surface energy of the (111) orientation over the (100) one. Indeed, high surface energy surfaces tend to increase adatom formation while low surface energy surfaces reduce adatom formation as calculated for oriented aluminum surfaces [203]. The absence of peaks aligned with the NiO (100) orientation in the ω scan of the NiO thin films deposited on Platinum (111) (Figure 7.2) suggests that the NiO (100) domain can grow parallel to the surface defined by the Platinum (111) substrate.

Because of dipole formation perpendicular to the surface, a specific surface termination is required to stabilize the (111) surface. NiO (111) can be stabilized in vacuum either by (100) pyramidal faceting [54], or by a p(2×2) octopolar reconstruction [52, 57–59]. Both seem to require considerable amount of heat to be formed. Pyramidal faceting of oriented thin films has been obtained at 500 °C and 10 % oxygen (see Section 7.3.3). Unfortunately, the sample coul not be exploited as it was cross-contaminated by bismuth as revealed by in-situ XPS (not shown in the thesis). For the sample prepared at 400 °C, at high oxygen concentration, a grainy surface can be observed, probably resulting from a columnar thin film structure (Figure 7.5). This structure has been encountered also on α-sapphire(0001) by Lee *et al.* [189] who deposited NiO (111) oriented films by RF-sputtering from a NiO target in pure O_2 atmosphere at 15 mTorr. Thus, it could be assumed that the grainy surface obtained with 20 % of oxygen originates from the surface stabilization by defects, which might be formed at such high oxygen partial pressure. Therefore, a specific surface stabilization of the NiO (111) orientation could be obtained at high oxygen concentration at 400 ° C without surface reconstruction into (100) facets or formation of a flat p(2×2) octopolar structure.

7.3.3 AFM images for films grown at different temperatures

The series of NiO thin films prepared on oriented Platinum thin films with a fixed oxygen concentration (10 %) and at different temperature has been studied by AFM only. The height images of the surfaces are displayed in Figure 7.6. It can be observed that the surfaces which are not defined at room temperature, produce rounded patterns, with well defined grain boundaries, at 200 °C. At 400 °C and 500 °C, sharp structures on the surfaces can be obtained. Interestingly, the NiO thin films deposited at 500 °C on (110) and (111) oriented Platinum, could be (100) faceted. For instance, the thin films deposited on (100) oriented Platinum seems, apart from some irregularities, to be relatively

T (° C)	NiO (100)	NiO (110)	NiO 111
RT			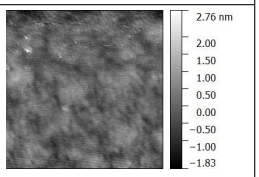
200 °C		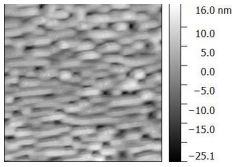	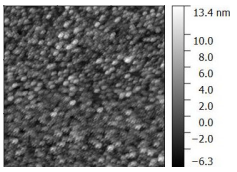
400 °C	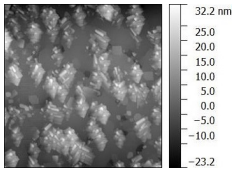	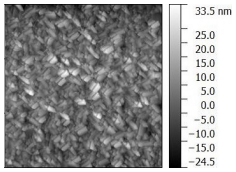	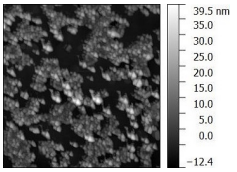
500 °C	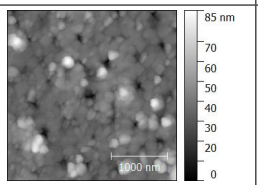	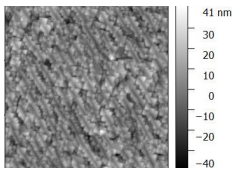	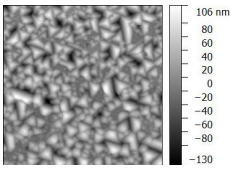

Figure 7.6: AFM height images (3×3 µm) measured at TU-Darmstadt of the NiO thin films grown on oriented Platinum thin films (100, (110) and 111) with 10 % oxygen and for various temperature of deposition.

flat, whereas the NiO thin film deposited on (110) oriented Platinum produces elongated features having teeth like shape. This could remind the (100) faceting of the (110) thin films when directly grown on MgO (110) substrate as reported in the literature [53]. Finally, when deposited on (111) oriented Platinum, the surface of the NiO thin film likely produce a (100) faceted pyramidal structure as it could be expected for classical (111) surface reconstruction. However, for the latter, the thin film has been cross-contaminated by bismuth as measured by XPS (not shown here) but the AFM image is shown only as indication to understand the effect of the temperature on the morphology of the surface of NiO thin films deposited on (111) oriented Platinum thin films.

7.4 Conclusion

The XRD measurements reveal that fully oriented NiO thin films can be obtained on (100) oriented Platinum with 10 % of oxygen and, on (110) and (111) oriented Platinum with 20 % of oxygen concentration when the temperature is fixed to 400 °C. At such temperature, under 10 % of oxygen, the thin films might include a metallic secondary phase and, when prepared at 2.5 % of oxygen, the structure of the thin film is highly disordered and not well defined. If sufficient oxygen concentration is brought in the deposition chamber, mixed oriented thin films can be obtained but the thin films remain well oriented along the direction of growth. For the series of samples prepared at 400 °C, the AFM surface images highlight that the most (100) oriented NiO thin film presents a flat surface combined with sharp cubic patterns and, the most (110) and (111) oriented NiO thin films display grainy surfaces, which could originate from the formation of defects in the thin film at high oxygen partial pressure.

The measurements on the series obtained with 10 % of oxygen where the temperature was increased from room temperature to 500 °C suggest that sharper surface structure is obtained with increasing temperature. The thin films prepared at room temperature produce somewhat a non well defined flat surface. The AFM images obtained with the NiO thin films deposited at 500 °C on (110) and (111) oriented Platinum could be interpreted as if there is a (100) surface faceting, which is not observed at lower temperature.

CHAPTER 8

Adsorption of water on oriented Nickel oxide thin films

Summary

It is generally accepted that the chemical surface properties can be either tuned by the surface orientation and/or by the presence of coordinately unsaturated defect sites [204, 205]. This part aims at unveiling NiO surface properties according to one dominant orientation and also to estimate the importance of defects. The experimental plan consisted, after having produced oriented NiO thin films by reactive DC sputtering (Chapter 7), to study the surface activity towards water adsorption and as presented in the next chapter (Chapter 9), towards the oxygen evolution reaction .

The studied oriented NiO thin films are analyzed in-situ using photoelectron spectroscopy (XPS/UPS) before and after surface exposure to water in vacuum and by electrochemistry in an oxygen-poor, 0.1 M NaOH, solution for which the experiments are carried out in the window stability of water.

Specific features in the electronic surface properties of the as-prepared sample surfaces are evidenced by in-situ UPS. Some electronic features can be associated to a specific surface orientation. The experiments in vacuum might suggest that the water is absorbed in a bi-layer fashion, for which the first layer is made of dissociated water molecules and the second layer is made of non-dissociated water molecules interacting with the first layer. Also, it has been observed that the valence band maximum position to the Fermi level is less affected by water exposure in vacuum on the dominantly (100) oriented thin film in comparison to the (110) and (111) dominantly oriented thin films. Supported by electrochemical measurements, the reason could be that dominantly (100) oriented thin films adsorb in equal amount positive (H^+) and negative charges (OH^-) originating from water dissociation on the NiO surfaces. On the contrary the dominantly (110) and (111) sample would likely adsorb primarily hydroxide (OH^-) but to a lesser extent positive charges (H^+). Finally, the presence of defects on the surface might be indispensable to enhance adsorption reactions on the NiO surfaces as the samples prepared at large oxygen concentration develop electrochemical features suggesting that larger adsorption activity of the surfaces are attained.

8.1 Introduction

The adsorbates on the surface of a material are important intermediates for catalytic and electrocatalytic reactions. The study of hydroxyl and molecularly adsorbed water might provide valuable information on the surface reactivity [58, 140]. The adsorption reactions are generally, at least for Nickel oxide, theoretically studied or experimentally studied in UHV system by Electron Energy Loss Spectroscopy (EELS) or Photo Electron Spectroscopy (PES). However, for a defined surface, the link between in-situ adsorption reaction and electrochemical properties is not obvious. Therefore, we propose in this section to study the surfaces of the oriented NiO thin films prepared with 10 % and 20 % of oxygen concentration (See Chapter 7) towards in-situ water adsorption in vacuum and towards adsorption reactions in an electrochemical cell. Finally, this section will endeavour at unveiling NiO surface properties according to the surface orientation and also according to the defects introduced in the thin films during the deposition.

8.2 Water adsorption in vacuum

8.2.1 Experimental

In the following part, from the whole batch of NiO thin films deposited on oriented platinum produced in Chapter 7, only the NiO thin films prepared at 400 °C with 10 % and 20 % oxygen concentration in the chamber are studied. In particular, it has been found that a fully (100) oriented NiO thin film was obtained with 10 % oxygen and, fully (110) oriented and (111) oriented NiO thin films were obtained with 20 % oxygen. The idea of the work presented in this chapter was to evidence the properties of a specific NiO orientation and also to bring valuable information if defects are introduced in the thin films when prepared at high oxygen concentration. In order to simplify the text, the samples, although not always totally oriented, are labelled according to the main desired orientation (the orientation of the platinum thin film, see Chapter 7) and the oxygen concentration as detailed in Table 8.1.

Table 8.1: Summary of the different samples studied in this chapter.

Name	Substrate	% O_2	Orientation
NiO(100)-10%	MgO(100)/Pt(100)	10	Dominantly (100)
NiO(100)-20%	MgO(100)/Pt(100)	20	Mixed (100) & (111)
NiO(110)-10%	MgO(110)/Pt(110)	10	Mixed (110) & (100)
NiO(110)-20%	MgO(110)/Pt(110)	20	Dominantly (110)
NiO(111)-10%	α-Al_2O_3(0001)/Pt(111)	10	Mixed (111) & (100)
NiO(111)-20%	α-Al_2O_3(0001)/Pt(111)	20	Dominantly (111)

Surface exposure to water was realized in a UHV chamber of the DAISY-MAT system (see Section 3.3). The experiments consisted in pulsing 15 times de-ionized water for 500 ms in vacuum at RT. A pumping period of one minute in vacuum separate each pulse.

For the UP and XP spectra, a Shirley background subtraction was used when necessary. For UPS measurements, the background subtraction is made into two regions: between 0 and ∼8.5 eV and between ∼8.5 and ∼16 eV.

8.2.2 Results

In-situ UPS on as deposited sample

Electronic states on NiO(100)-10%
The UP spectra of the as-deposited NiO(100)-10% sample shows four features between 0 and 9 eV (Figure 8.1). In literature, UP spectra on (100) cleaved NiO single crystals also display four distinctive peaks in the 0-9 eV range near the valence band [68, 137]. The two peaks at lowest binding energy are associated to screened Ni 3d orbitals while the two others found at higher binding energy to O 2p[x/y] and O 2p[z] orbitals [137]. As detailed in Section 7.1, the NiO(100)-10% sample is dominantly (100) oriented and it displays a flat surface alternating with structured irregularities. Overall the UPS measurements would suggest that although the sample surface is not perfect, the electronic states on the NiO(100)-10% sample originates from the (100) exposed facet.

For binding energies higher than 7.5 eV, an intense peak at 15 eV can be seen but its origin has not been elucidated.

Electronic states on NiO(110)-10% and NiO(111)-20%
Regarding the UP spectra of the NiO(110)-20% and the NiO(111)-20% samples, the valence band is composed of three states (Figure 8.1). In comparison to the NiO(100)-10% sample, the absence of the O 2p[z] state on dominantely (111) oriented surface is also observed in literature [64, 194]. As detailed in Section 7.1, the NiO(111)-20% sample is dominantly (111) oriented but contrary to the NiO(100)-10% sample, the surface of the NiO(111)-20% sample is grainy. However, as the UP spectra of the NiO(111)-20% sample provides similar spectra in the valence band as what is reported in the literature [64, 194], it could be assumed that, as for the NiO(100)-10% sample, the observed electronic state originate from the dominant surface orientation of the thin film. By extension, the same reasoning is applied on the dominantly (110) oriented NiO(110)-20% sample.

As for the NiO(100)-10% sample an intense peak is visible between 10 and 15 eV for the NiO(110)-20% and the NiO(111)-20% samples (Figure 8.1). Interestingly, to the right of the intense peak, a shoulder, lower in intensity, can be observed for both NiO(110)-20% and the NiO(111)-20% samples. This feature is positioned for the NiO(110)-20% and NiO(111)-20% samples at 10

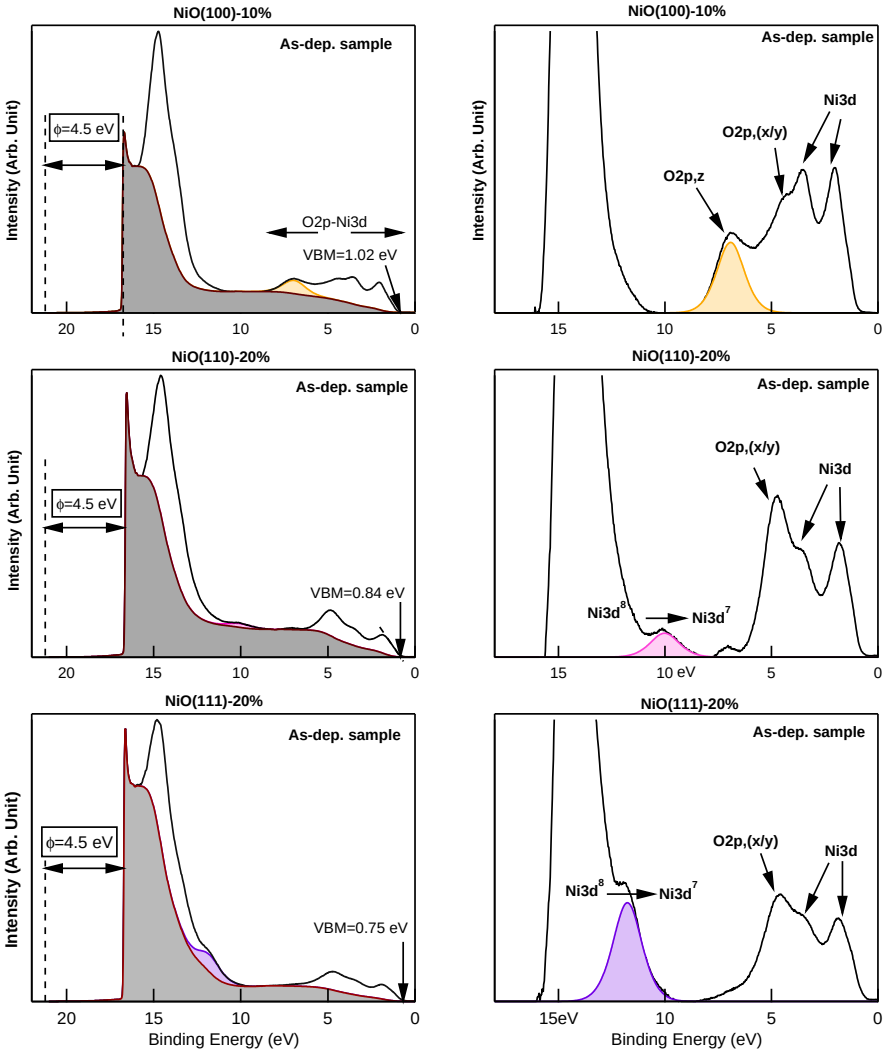

Figure 8.1: In-situ UPS measurements of as-deposited NiO(100)-10%, NiO(110)-20% and NiO(111)-20% samples. The left column shows the full spectra, while the right column is an insight, after background subtraction, of the states observed by UPS. The workfunction ϕ is given relative to the He I energy (21.22 eV). To evidence the differences in spectra, three regions have been coloured. Between 5 and 8 eV a surface electronic state on the NiO(100)-10% sample is found, which has been assumed to be unique to the (100) orientation (yellow) assigned to the O 2p[z] electronic state. On the NiO(110)-20% sample an electronic state around 10 eV (pink) is found while for NiO(111)-20% sample a prominent electronic state appears between 11 and 12 eV (purple). The specific states observed on the dominantly (110) and (111) oriented sample, although this might be not true, were associated to a $Ni3d^8 \rightarrow Ni3d^7$ transition.

and 11.7 eV, respectively (Figure 8.1). Although this cannot be said with confidence, the peak found on the fully (110) and (111) oriented thin films might be related to the Ni $3d^8 \rightarrow$ Ni $3d^7$ transition [70].

Electronic states on mixed surface orientation

In the case of mixed oriented polycrystalline thin films, the surface properties of the thin films might combine the intrinsic properties of each orientation. For instance, according to XRD measurements (Figure 7.2 in Chapter 7), the NiO(111)-10% sample is a mixture of the (100) and (111) orientations. In the meantime, the UP spectra obtained with this sample provides the Ni $3d^8 \rightarrow$ Ni $3d^7$ transition typical of the (111) orientation and the O 2p[z] orbitals near the valence band edge typical of the (100) orientation (Figure 8.2). This result strengthens the idea that the O 2p[z] orbitals is typical of (100) orientation and that at least the Ni $3d^8 \rightarrow$ Ni $3d^7$ transition can be associated to the (111) orientation. Finally, it could be said that the electronic states specific of each orientation are superimposed to form the final UPS spectra.

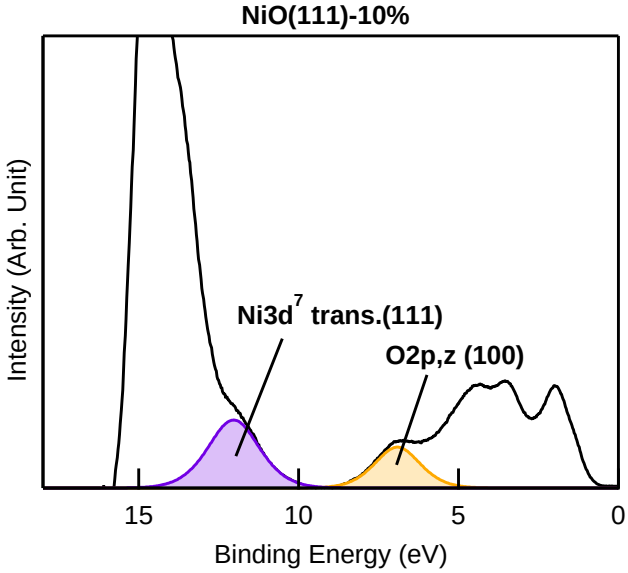

Figure 8.2: UP spectrum after background subtraction of the NiO(111)-10% sample. As indicated by XRD, this thin film includes both the (100) and the (111) orientation. Interestingly, the UP spectrum combine the electronic features specifically found for fully oriented (100) and (111) NiO thin films (see Figure 8.1).

Workfunction and Fermi energy

The workfunction measured by UPS on as-deposited samples from Table 8.1 is about 4.5 eV for all samples, while the Fermi energy varies between 0.75 and 1 eV (Figure 8.1). As seen in Chapter 4, a low workfunction ($\sim$ 4.5 eV) and

a high Fermi energy ($\sim$ 1 eV) are typical of NiO thin films prepared at high temperature.

In-situ UPS on surfaces exposed to water

UP spectra after water exposure of the dominantly oriented sample have been measured and, after Shirley background subtraction, compared to the UP spectra obtained before water exposure (Figure 8.3). The difference of the spectra shows three distinctive peaks at 4-7 eV, 8-11 eV and 11-15 eV.

Although this is not absolutly clear, the peak at 4-7 eV and at 8-11 eV have been assigned to the bonding (3σ) and anti-bonding (1π) orbitals of the hydroxide (OH^-). Indeed, in the work of Xin *et al.*, the anti-bonding states have energy levels near the valence band edge while the bonding states occupy energy level about 5 eV below the anti-bonding state [140].

Even though this is less clear, the 12-15 eV region has been assumed to be related to the $1b_2$ states of water (H_2O). Indeed, the electronic structure of ice (T $<$ 150 K) by photo-emission mainly evidence the presence of three components: the $1b_1$ anti-bonding state ($\sim$ 5-8 eV), the $3a_1$ bonding and anti-bonding state ($\sim$ 8-12 eV) and the $1b_2$ bonding state ($\sim$ 12-15 eV) [136]. For some reasons, only the $1b_2$ bonding state may be seen at room temperature in the spectra of Figure 8.3.

Thus, after spectra subtraction, it appears that the bonding state (3σ) and the anti-bonding state (1π) are equal in intensity for the dominantly (100) oriented NiO(100)-10% sample. But on the contrary, the bonding state (3σ) of hydroxide dominates over the anti-bonding states (1π) on the NiO(110)-20% and the NiO(111)-20% (Figure 8.3). Following the work of Xin *et al.* [140], it could mean that the hydroxide on the NiO(100)-10% has a lower interaction with the surface of the sample contrary to the two other samples. Thus, the hydroxide bond length with the surface might be shorter on the NiO(110)-20% and the NiO(111)-20% samples than on the NiO(100)-10%. Although the assignment is speculative, it will be seen later that it could make sense to a certain extent in comparison to the electrochemical results.

The work function

The workfunction, after water exposure, is reduced in comparison to the as-deposited sample (Figure 8.3). Thus, when the workfunction is 4.5 eV for the as-deposited samples, after water exposure, the workfunction is equal to 3.9 eV for the NiO(100)-10% sample, 3.8 eV for the NiO(110)-10% samples and 3.5 eV for the NiO(111)-10%.

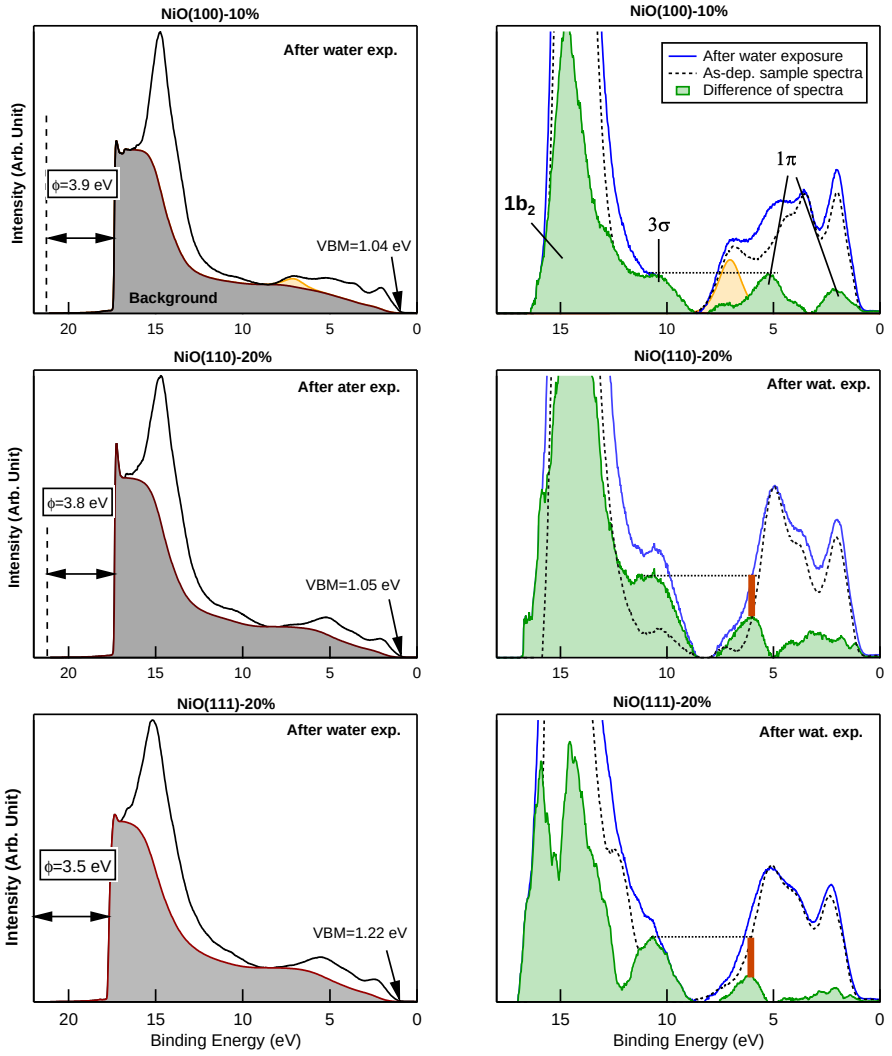

Figure 8.3: In-situ UPS measurements of the NiO(100)-10%, NiO(110)-20% and NiO(111)-20% samples after surface exposure to water. The density of state of the bonding (3σ) and anti-bonding state (1π) is about the same for the NiO(100)-10% sample whereas the bonding state is higher than the anti-bonding state on the NiO(110)-20% and the NiO(111)-20% samples. The workfunction χ is given relative to the He I energy (21.22 eV). The vertical brown line for the right plots related to the NiO(110)-20% and NiO(111)-20% has been drawn to evidence the difference in intensity between the bonding and anti-bonding states.

In-situ XPS on as deposited sample

As for the UP spectra, the XPS measurements of NiO are complex to interpret, mainly near the valence band edge and in the Ni 2p region due to the numerous electronic transitions during photo-excitation [70, 76–78, 81]. As detailed in Chapter 4, the Ni 2p region is made of three components, which are assigned to the Ni $2p^5 3d^9 Z$ (state in the $3d^9$ band), Ni $2p^5 3d^9 L$ (state arising from the hybridization of the $3d^9$ band with the ligand) and the Ni $2p^5 3d^8$ bands [81] (Figure 8.4, top). Similarly to the UPS measurements of the as-prepared samples, the valence band region obtained by XPS result from the hybridization of the O $2p^6$ and Ni $3d^8$ orbitals. The Ni $3d^8$ states dominate the valence band edge, while the O $2p^6$ orbitals occupy higher binding energies. However, the O 2p states in the valence band region are not as visible as with the UPS measurements when XPS measurements are carried out. The reason is that the photoemission cross-section favors the electrons from the Ni 3d orbitals over the O 2p orbitals when high energy photon sources are used [68]. Therefore, the resulting spectra when measured with an X-ray source, would originate, in taking the notation of Taguchi *et al.* [81] (see Section 2.2.3), from the Ni $3d^8 Z$, Ni $3d^8 L$ and Ni $3d^7$ orbitals (Figure 8.4, bottom).

The O 1s region is simpler (Figure 8.4, middle): a main peak is found in the 529-531 eV range and account for the lattice O^{2-} from the NiO crystal. The main peak can be easily fitted with a single Gaussian curve. For the NiO(110)-20% and the NiO(111)-20%, a shoulder at higher binding energy can be seen in the O 1s region (Figure 8.4) and account respectively, after background subtraction, for 4.3% and 5.2 % of the total intensity in the O 1s region (Figure 8.4). A summary of the O 1s(Def.) in the O 1s region for the samples prepared with 10 % and 20 % of oxygen is given in Table 8.2. As detailed in Chapter 4, this shoulder has been assigned to the presence of defective sites (O 1s(Def.)) in the NiO thin film and might be associated to the presence of nickel vacancies in the thin film when the thin films are prepared at high oxygen concentration and high temperature. Thus, lower Fermi level position is observed ($\sim$ 0.9 eV) for both samples prepared at high oxygen concentration when measured by XPS, in comparison to the dominantly (100) oriented sample NiO(100)-10%, which provides a XPS Fermi level of 1.1 eV above the valence band maximum (Figure 8.4 and Figure 8.5).

For the NiO(100)-20% sample, no substantial shoulder associated with the presence of nickel vacancies is measured (Table 8.2). It might be due to a higher diffusion coefficient of the chemical species [38, 180], especially along (100) high angle grain boundaries [180]. Indeed, when the sample is still hot after deposition, the defect density might be mitigated by diffusion of species along the grain boundaries, and high angle grain boundaries might provide a channel for stoichiometry recovery.

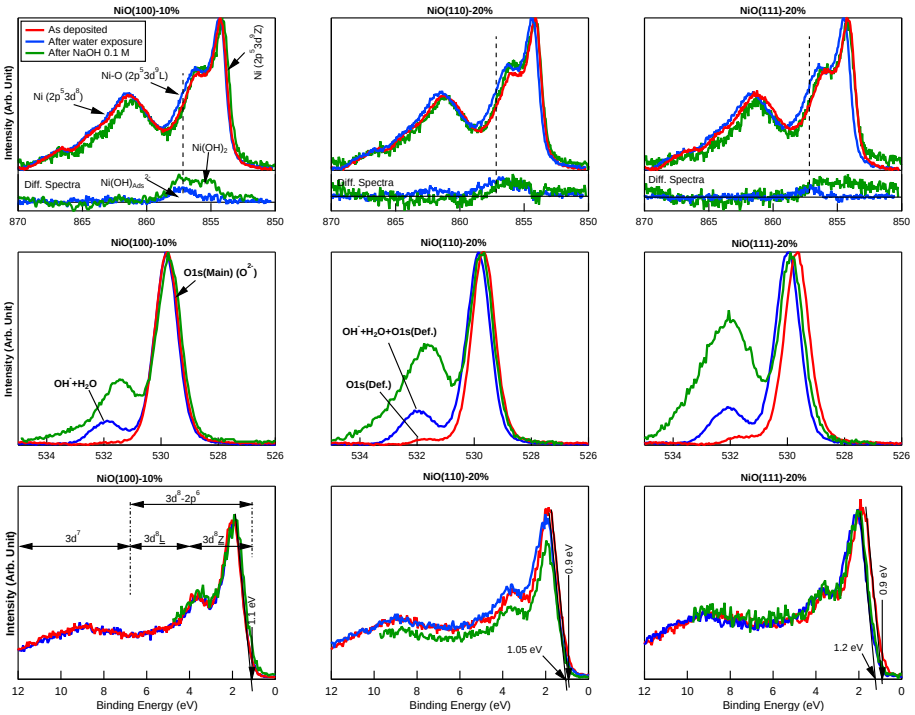

Figure 8.4: XPS measurements (DAISY-MAT) of the NiO(100)-10% (left column), NiO(110)-20% (middle column) and the NiO(111)-20% (right column) thin films before and after water exposure in vacuum (in-situ measurements) and after electrochemical adsorption experiments (ex-situ measurements). The Ni 2p and the O 1s region are plotted after Shirley background subtraction.

Table 8.2: Weight of the shoulder to the left of the main peak in the O1s region before and after exposure of the sample surface to water. Before water exposure, the shoulder is assigned to the presence of defects whereas after water exposure the shoulder accounts for the photoemission contribution of hydroxide and water adsorbed on the NiO surface.

Sample	Before (%)	After (%)	Difference (%)
NiO(100)-10%	∼0	13.5	13.5
NiO(110)-10%	0.9	14.3	13.4
NiO(111)-10%	0.9	12.8	11.9
NiO(100)-20%	1.9	17.3	15.4
NiO(110)-20%	4.3	19.2	14.9
NiO(111)-20%	5.2	20	14.8

In-situ XPS on surfaces exposed to water

O 1s region: Presence of a double layer of water
After surface exposure to water of the NiO thin films in the DAISY-MAT system, a shoulder at higher binding energy to the main O 1s peak emerges in the O 1s region (Figure 8.4). The shoulder can be attributed to the formation of hydroxide [166, 206] due to the reaction of water on the surface of the sample as detailed in Section 2.4.1, but also, as it will be seen later, it could originate from non-dissociated water molecules on the surface.

It is important to mention that the shoulder in the O 1s region, accounting for hydroxide and water molecules, is found for any prepared NiO thin films (Figure 8.4). Thus, after subtracting the contribution of the defective electronic states measured before water exposure, the shoulder at higher binding energy associated to hydroxide [166, 206] and water [136] accounts for 12 to 15 % (Table 8.2). This difference would be the equivalent of 0.15 nm of water or about 1.5 to 2 layers of water. It shows that at least there is more than one monolayer of water adsorbed on the surfaces.

Literature reports that, similar to metals, when a metal oxide surface is exposed to water, the chemical transition occurs within the two first layers of adsorbed water [136]. At low temperature (∼ 150 °C), Thiel *et al.* described the first layer as being bound by direct chemisorption bonds on the surface, and so water would dissociate within the first layer. On the contrary, the second layer is made of undissociated water molecules retained by two or three hydrogen bonds to the first layer molecules [207]. Thermal excitation would eliminate water molecules bound by weak interactions to the substrate and only water molecule having a strong interaction with the surface or dissociated water molecules might remain at room temperature in a vacuum environment [208, 209].

According to literature and as it has been estimated that more than

one monolayer of water molecules would remain after surface exposure to water, it could be assumed that the water molecules are adsorbed in a bi-layer fashion on the surface of the NiO thin films at room temperature for the samples studied in this chapter. The first layer would be composed of dissociated water molecules and the second layer would be made of non-dissociated water in strong interaction with the first layer.

Ni 2p region: hydroxide
Comparison of the Ni 2p spectra before and after water exposure in vacuum highlights the presence of an additional electronic state in the 855-860 eV range, which overlaps the Ni $2p^5 3d^9 L$ electronic states (Figure 8.4). Literature reports that nickel hydroxide compounds as for $Ni(OH)_2$ and NiOOH provide an electronic state in this binding energy range [173]. Moreover, as seen in Section 4, the oxidation of Ni^{2+} to Ni^{3+} is very unlikely for NiO thin films prepared at high temperature. Therefore, it has been assumed that the extra electronic state in the 855-860 eV range, after water exposure, could arise from the formation of an hydroxide species similar to nickel hydroxide on the NiO thin films after water exposure and this would correspond to the first layer of adsorbed water on the NiO surface.

Fermi level shift
Figure 8.5 shows the variation of the Fermi energy relative to the valence band edge before and after water exposure for the oriented samples listed in Table 8.1. The variation of the Fermi position is limited for the sample prepared on the MgO(100)/Pt(100) substrate, especially to what concerns the NiO(100)-10% sample, which looks completely unaffected by the water exposure in vacuum (see also Figure 8.4). On the contrary, when prepared on MgO(110)/Pt(110) and particularly on Sapphire/Pt(111), the NiO thin films displays broader variation in the Fermi position when exposed to water.

The accumulation of negative charges in NiO on the dominantly (110) and (111) oriented thin film could be a reason why the Fermi energy increases after water exposure in vacuum. From ~ 0.9 eV, the Fermi energy raises to 1.05 eV and 1.2 eV for the NiO(110)-20% and the NiO(111)-20% samples, respectively (Figure 8.4). On the contrary, the unchanged Fermi level position after water exposure on the dominantly (100) oriented NiO(100)-10% sample would suggest there is no net accumulation of charges on that surface.

8.2.3 Discussion

Fermi energy shift and surface orientation

The in-situ XPS measurements suggest that more than one monolayer of water is interacting with the surface of the oriented NiO thin films. As seen above, the first layer might be made of dissociated water molecules while the second is not dissociated but would be in strong interaction with the first layer.

As seen in Figure 8.4 and Figure 8.5, if dominantly (100) oriented, the

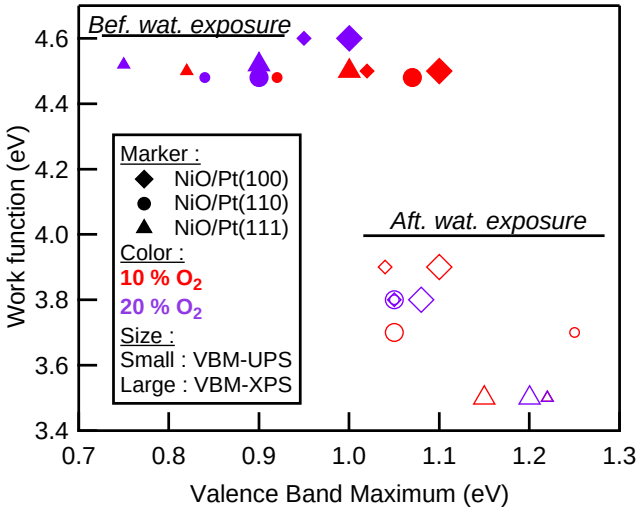

Figure 8.5: Comparison of VBM values obtained either from the XPS or the UPS measurements for the oriented samples prepared at 400 °C listed in Table 8.1. Full and open markers represent data obtained before and after water exposure, respectively. It can be observed that the workfunction decreases for all the surfaces after water exposure, but to a larger extent for the dominantly (110) and (111) oriented sample. The Fermi energy of the dominantly (100) oriented sample is almost unchanged after water exposure whereas it varies more for dominantly (111) oriented samples.

Fermi energy is not substantially affected by water exposure. This would suggest that water adsorption on the dominantly (100) oriented surface does not result on an accumulation of electrical charges on the surface of the thin film. However, the first layer of water must be dissociated as the Ni 2p spectra suggest the formation of a species similar to nickel hydroxide. Moreover, as it will be presented in Section 8.3, a non-dissociated first layer of water in vacuum on the dominantly (100) oriented surface would not correlate with the higher electrochemical activity observed for both hydroxide (OH^-) and hydrogen (H^+) of dominantly (100) oriented surface, in comparison to the other oriented samples. So, at first sight, the water molecules would be dissociated into hydroxides and protons, which would be equally adsorbed within the first water layer on the (100) oriented surface.

Contrary to the dominantly (100) oriented thin films, the increase of the Fermi energy for the dominantly (110) and (111) oriented thin films after water exposure indicates an accumulation of electrons at the surface of the NiO thin film. This can originate from electron injection in the NiO electronic structure due to the oxidation of hydroxides ($OH^- \rightarrow OH_{Ads} + e^-$) or because of the presence of a net positive charge building up outside the surface. In the meantime, larger Fermi energy shifts are accompanied by a lower workfunction value in comparison to the dominantly (100) oriented thin films (Figure 8.5).

Assuming that dominantly (100) oriented thin films do not produce specifically a dipole, the lower workfunction value could mean that a dipole with negative charges oriented towards the sample surface might arise within the first layer of adsorbed water molecule. As there are negative charges accumulating in the NiO surface, the most probable solution is that the hydroxide injects electrons in the NiO crystal structure ($OH^- \rightarrow OH_{Ads} + e^-$) leaving in the first water layer a positive charge (H^+). The electrons and the protons would then build-up a dipole structure within the first layer of water molecule, on the dominantly (110) and (111) surfaces.

In looking back at the adsorption of water on the dominantly (100) oriented surfaces, as no Fermi energy shift is observed after water exposure, and that the (100) oriented surfaces provides adsorbing sites for both the hydroxide (OH^-) and the protons (H^+), then it could be assumed that the resulting electron from hydroxide adsorption: $OH^- \rightarrow OH_{Ads} + e^-$ is captured by a proton following: $H^+ + e^- \rightarrow H_{ads}$. Eventually, no electrons are injected in the NiO if (100) oriented as the electron would directly be captured by the adsorption reaction of protons. It would explain why no shift in the Fermi energy is observed on dominantly (100) oriented surfaces.

Workfunction shift and surface orientation

Undissociated water molecules in the second layer might adopt a certain order where, in particular, the oxygen atoms would point inward and the O-H bonds would point outward [69, 136]. Thus the outer layer (the second layer) of adsorbed water could lead to the formation of a dipole in the vicinity of the surface.

In this context, Reissner *et al.* reported that the workfunction of (100) oriented NiO single crystal surfaces can decrease down to 2 eV if the surface is exposed to water at 143 K, but the workfunction is higher with $\sim$ 3.5 - 4 eV if the same experiments are realized at 120 K [200]. The reason would be that a crystalline ordered structure is obtained at 143 K whereas amorphous water structure is obtained at 120 K [200]. Thus, the ordering of the water molecules in the second layer can have significant consequences on the value of the workfunction. Also, it has been reported that the more normal to the surface the water molecule in the outer monolayer, the larger is the dipole [136].

The workfunction of the as-deposited samples lie around 4.5 eV for any studied sample but it decreases to 3.9 eV, 3.8 eV and 3.5 eV if the NiO thin films are prepared respectively on MgO(100)/Pt(100), MgO(110)/Pt(110) and Sapphire/Pt(111) samples (Figure 8.5). As the measured workfunction, after water exposure, is not reduced to lower values than 3.5 eV, with respect to the value obtained by Reissner *et al.* [200] (see above), it could be assumed that the non-dissocated layer at room temperature is amorphous in nature.

Schematic representation of water adsorption in vacuum

Figure 8.6 represents how the structure resulting from water adsorption is, according to the interpretation made from the measurements in vacuum. As suggested by the in-situ XPS measurements, the adsorption of water on the NiO surfaces would be realized in a bi-layer fashion. The inner water layer would be made of dissociated water molecule, while the outer layer would be made of undissociated and polarized water molecules.

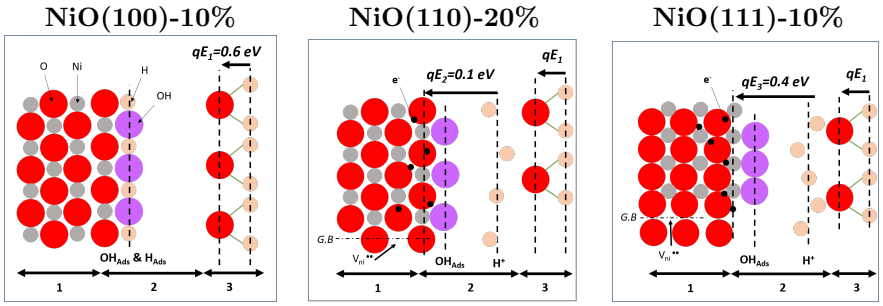

Figure 8.6: Schematic cross-section of the final chemical surface state after water exposure of the (100), (110) and (111) oriented thin film. Region 1 stands for the NiO oriented thin films structure near the surface, region 2 for the adsorbate originating from the reaction of water onto the surface and region 3 represents the amorphous polarized water molecule layer during the photoelectron emission measurements. "G.B" stands for grain boundary.

The Fermi level shifts to higher value on the dominantly (110) and (111) oriented thin films. It has been interpreted as the negative hydroxide ions inject electrons in the crystal structure ($OH^- \rightarrow OH_{Ads} + e^-$). However, these electrons remains in interaction with the positive proton left behind in the first water layer and could lead to the building up of a dipole layer within the first layer of adsorbed water molecules (Figure 8.6). This dipole layer would be made of electrons and protons and could be responsible for the lower workfunction values observed for the dominantly (110) and (111) oriented thin films, in comparison to the dominantly oriented (100) thin films (Figure 8.5). For the latter, the electron injection would be compensated by an electron capture by the adsorption reaction of protons ($H^+ + e^- \rightarrow H_{ads}$). Thus no substantial Fermi energy shift is observed on the dominantly (100) oriented NiO thin film after water exposure in vacuum. Both protons and hydroxide would be equally adsorbed on the NiO (100) surface (Figure 8.6).

Finally, the interpretation of the measurements presented above, implies that the dominantly (100) oriented surface produced in this study provides adsorption sites for both hydroxide and protons, whereas the dominantly (110) and (111) oriented surfaces might only expose adsorption sites towards hydroxides. We will see in the next section that indeed, taking the samples

studied in-situ in vacuum towards water adsorption, the electrochemical characterization of the adsorption reactions in an electrolyte shows that the dominantly (100) oriented samples might provide active sites for hydrogen adsorption that the two other orientations do not have.

8.3 Adsorption reaction in an electrolyte

8.3.1 Experimental

After in-situ measurements of surface exposure to water in vacuum on dominantly oriented NiO thin films, the samples listed in Table 8.1 have been characterized in an electrolyte in the stability window of water in order to study the adsorption reactions.

Thus the electrochemical surface characterization was carried out in the stability window of water in a 0.1 M NaOH solution where nitrogen has been bubbled for 10 mins to remove oxygen from the solution beforehand. The aim being to study only the adsorption reaction and to avoid any electrochemical reactions, such as the oxygen evolution reaction (OER) and the oxygen reduction reaction (ORR). For instance, the OER could lead to the formation of a thick hydroxide layer and so adsorption reactions would not be related to the nickel oxide surface itself but rather to the nature of the hydroxide growing on top (See Section 9).

Equilibration of the electrode is realized by cycling the surface potential 20 times at (100) mV/sec from 0.1 to 1.1 V vs RHE. After this first step, the electrode is considered as being in steady-state condition (see Appendix A.5). Electrochemical measurements started by a cyclic voltammetry with a low sweep rate (10 mV/sec) between 0.1 to 1.1 V vs RHE, subsenquently followed by the Electrochemical Impedance Spectroscopy (EIS) measurements realized stepwise from 0.1 to 1.1 V vs RHE where potential equilibration is made beforehand for 30 seconds (Quasi-static measurements). EIS results are fitted with simple electrical equivalent circuits. The contact resistance (R_c) is placed in series with a constant phase element (CPE) (see Section 2.4.2) in parallel with a resistance (R_{cpe}) as following: R_c-[CPE/R_{cpe}]$_n$. The number n is fixed according to the number of semicircles visible on the Nyquist plot (see Appendix A.6).

The CPE element measured by EIS is converted into a capacitive equivalent following the formula:

$$C_{eq} = \frac{(Q_\alpha R_{cpe})^{\frac{1}{\alpha}}}{R_{cpe}} \tag{8.1}$$

where Q_α and α are defined in Section 2.4.2.

After the electrochemical experiments, the surface of the samples are analysed by XPS as represented in the Figure 8.4. The measured surface is

supposed to be the electrochemical surface condition obtained when the surface is in open circuit potential in 0.1 M KOH in an oxygen-rich electrolyte[1]. In general the open circuit potential is about 0.6-0.9 V vs RHE.

8.3.2 Results

Electrochemical cyclic voltammetry, quasi-static experiments and EIS enable to characterize in-operando the surface properties of the different synthesized NiO thin films towards the hydroxide (OH^-) and the hydrogen (H^+) adsorption reactions. The results of the experiments are all gathered in Figure 8.7.

Two regions, where events in current occur, are identifiable: the region in the 0.1 to 0.3 V vs RHE potential range and the region in the 0.8 to 1.1 V vs RHE potential range (Figure 8.7). The low potential region was ascribed to the reactions related to hydrogen adsorption reaction while the high potential region was associated to the hydroxide adsorption reaction. The events in current could be associated to adsorption reactions without electrochemical discharge (e.g.: $H^+ \rightarrow H^+_{Ads.}$ or $OH^- \rightarrow OH^-_{Ads.}$). This assumption is detailed by the following arguments:

- First, the potential range for the study is limited to 0.1 to 1.1 V vs RHE. No electrochemical reaction, such as the oxygen evolution reaction (OER, +1.23 V vs RHE) and the hydrogen evolution reaction (HER, 0 V vs RHE), are expected. However, the oxygen reduction reaction (ORR, $(1/2)O_2 + 2\,e^- + H_2O \rightarrow OH^-$) might occur for potential lower than +1.23 V vs RHE. This possibility is discussed in Appendix A.5. It must be mentioned that the shoulder to higher binding energy in the O 1s spectra after the electrochemical measurements is increasing (Figure 8.4), but not as much as was observed when the oxygen evolution reaction was carried out on oriented NiO thin films [210]. Thus the event in current cannot be associated to a standard electrochemical reaction.

- Second, the quasi-static points (black dots in the cyclic voltammetries of Figure 8.7) show that the current decays to 0 with time in the potential range where events in current are seen. It means that the events related to the peak in current are limited and decay with time when the quasi-static measurements are carried out. This can happen for a blocked electrochemical reaction (only intermediate steps are realized) or when the current arises from the charging of the Helmholtz double layer capacitive element, but certainly not because of a continuous electrochemical reaction.

- Third, in the case there is an electrochemical discharge, the exchange of the electronic charges would lead to the formation of non charged adsorbed species (e.g.: $OH^-_{Ads} \rightarrow OH_{Ads} + e^-$ or $H^+_{Ads} + e^- \rightarrow H_{Ads}$),

[1] After the experiments in oxygen poor electrolyte, characterization have been carried in an oxygen rich solution. However, it is assumed that the concentration in oxygen of the solution should not modify drastically the electrode surface with regard to the XPS measurements.

which would in turn reduce the charge of the Helmholtz double layer. For instance, when the OER is carried out on the NiO surface, a decrease of the associated equivalent capacitive element has been observed (Figure 9.11 in Section 9), which is due to a high occupation of adsorbing site. Instead, the increase of events in current at low or high potential range is accompanied by an increase of the equivalent capacitive element (Figure 8.7). This suggests that the ions in the solution are interacting stronger with the surface but the electrical charge might be not transferred to the electrode.

Therefore, it has been assumed that the events in current observed in Figure 8.7 in the 0.8 to 1.1 V vs RHE potential region and in the 0.1 to 0.3 V vs RHE potential region, with regards to the quasi-static and EIS measurements, cannot be associated to an electrochemical reaction involving a charge transfer between the ions and the electrode. Instead, the analysis of the electrochemical results indicates that the events in current observed in the studied potential window are related to the early stage of an adsorption reaction without charge discharge.

The events in current can be related to the increase of the capacitive element associated to the Helmholtz double layer when species are adsorbed on the NiO surface. Indeed, during cyclic voltammetry the relationship between the current I, the equivalent capacitance of the Helmholtz double layer C_h and the sweep rate $v_s = \frac{dV}{dt}$, which is constant during the measurements, is:

$$I = C_h v_s \tag{8.2}$$

Therefore, an increase of the capacitive element C_h would necessarily be measured by an increase of the current during the cyclic voltametry. For this reason, the cyclic voltammetry and the EIS measurements are intimately related. In the meantime, the EIS measurement evidence a sharp increases of C_h in the potential region where the events in current are observed. The capacitive nature of the events in current explains why the variation in current is seen only during the cyclic voltammetry and not during the quasi-static measurements (Figure 8.7). The increase of the equivalent capacitance might be generated by a decrease of the distance between the two layers forming the Helmholtz double layer or an increase of the number of charged adsorbed species.

Eventually, the event in current observed in the 0.8-1.1 V vs RHE potential region has been assigned to the adsorption/desorption of charged hydroxide species: $OH^- \rightarrow OH^-_{Ads}$ and the event in current in the 0.1-0.3 V vs RHE potential range have been assigned to adsorption/desorption process related to protons where the reaction is: $H^+ \rightarrow H^+_{Ads}$. The charged adsorbates (OH^-_{Ads} and H^+_{Ads}) would be responsible for the increase of the equivalent capacitive element measured in the low and high potential region (Figure 8.7).

At intermediate potential(0.3 to 0.8 V vs RHE) a negative current is measured by cyclic voltammetry but does not vanish on the quasi-static

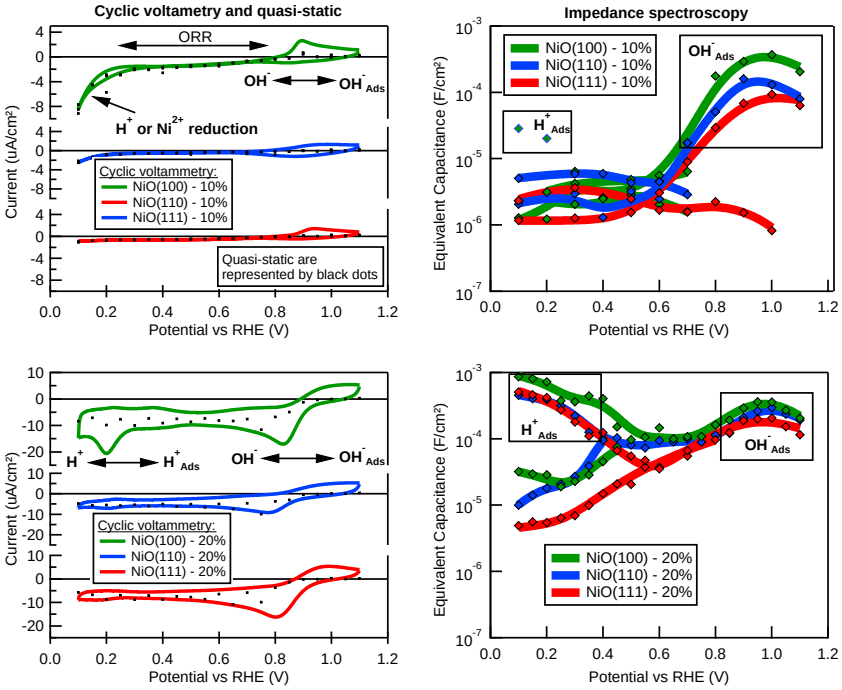

Figure 8.7: Representation of the electrochemical surface characterization of the differenly oriented NiO thin films prepared at 400 °C and at 10 % and 20 % of oxygen concentration. The left side is related to the cyclic voltammetry (10 mV/sec) and the quasi-static measurements (black squares) and the right side to the equivalent capacitive element measured by EIS and derived from fitting of the Nyquist plots (See Appendix A.6). ORR stands for the oxygen reduction reaction after comparison of the data with what can be obtained in an oxygen rich electrolyte (see Appendix A.5)

measurements (Figure 8.7). This is a fingerprint of an electrochemical and non-limited reaction. As shown in the Appendix A.5, this has been assigned to the oxygen reduction reaction (ORR) following the reaction: $\frac{1}{2}O_2 + H_2O + 2\,e^- \rightarrow 2\,OH^-$ where the oxygen comes from the remaining dissolved oxygen molecules in the electrolyte.

8.3.3 Discussion

Effect of the oxygen concentration during sputtering

At first sight, the electrochemical results display larger differences depending on oxygen content than in dependence on the orientation of the thin films. When the thin films are prepared with 10 % oxygen, the cyclic voltammetry looks relatively inert towards the adsorption reactions in comparison to what has been obtained with the samples prepared with 20 % oxygen during the film fabrication (Figure 8.7). For instance, the maximum current density does not exceed more than 4 $\mu A/cm^2$ and the minimum current density is -8 $\mu A/cm^2$ (obtained with the NiO(100)-10% sample) whereas with samples prepared with 20% oxygen concentration the maximum in the oxidation current density is slightly increased with $\sim$ 5 $\mu A/cm^2$ but the reduction peak can be as low as -20 $\mu A/cm^2$. Moreover, the difference between the forward current and the backward current is larger at intermediate potential (0.4-0.6 V vs RHE) when the sample is prepared with 20% of oxygen concentration than with 10% oxygen concentration (Figure 8.7). Concurrently, EIS shows an obvious fingerprint of a higher hydrogen adsorption in the low potential range for the samples prepared with 20 % of oxygen in contrast to the samples prepared with 10 % of oxygen in the deposition chamber.

In the beginning of this chapter, it has been highlighted that the AFM images of the samples prepared with 20% of oxygen in the deposition chamber are more grainy and they do not adopt a regular pattern as the samples prepared with 10% of oxygen concentration (Figure 7.5). Moreover, the in-situ XPS measurements on the as-prepared sample evidence the presence of an additional electronic state at higher binding energy in the O 1s peak when prepared at high oxygen concentration (Figure 8.4). As seen in Chapter 4, the shoulder in the O 1s region can be associated to defects such as nickel vacancies. Therefore, it could be assumed that the larger electrochemical activity towards adsorption reactions of the samples prepared with 20% oxygen concentration is related to higher defect density on the surface of the samples. Also, the measured equivalent capacitance of the Helmholtz double layer is definitely higher in the potential region of the H^+ and OH^- adsorption reaction for the samples produced with 20% of oxygen in the deposition chamber in comparison to the samples prepared with 10% of oxygen (Figure 8.7).

Effect of the surface orientation

Looking into details of the electrochemical results displayed in Figure 8.7, when the NiO is deposited on MgO(100)/Pt(100) substrates, the cyclic voltammetry highlights stronger adsorption features related to the adsorption of protons (H^+) in the 0.1-0.3 V vs RHE potential range, in comparison to the sample prepared on MgO(110)/Pt(110) or on α-Sapphire(0001)/Pt(111) either the samples are prepared with 10 % of oxygen or with 20 % of oxygen. For the NiO(100)-10% sample, it should be mentioned that the decrease in current down to -8 $\mu A/cm^2$, in the 0.1-0.3 V vs RHE potential range, as the current measured with quasi-static experiments and cyclic voltmetry are similar (Figure 8.7, left part). At such potential, the hydrogen reduction reaction is very unlikely. Thus, the continuous reduction of protons could be associated to a non limited reduction reaction: $H^+ + e^- \rightarrow "H"$ but the final product cannot be assigned to a chemical compound with certitude. In addition, the partial reduction of surface Ni^{2+} could also be another option to explain the current behaviour of the NiO 100-10% surface.

For the samples prepared with 10% of oxygen concentration, the EIS results show that seemingly hydrogen is adsorbed for the dominantly (100) oriented thin film but not for the other orientations (Figure 8.7, right upper part). The affinity of the dominantly (100) oriented sample towards hydrogen adsorption over the other orientations is also noticed when the sample is prepared with 20% of oxygen in the deposition chamber as the determined equivalent capacitive element is higher for the NiO(100)-20% sample than for the NiO(110)-20% and the NiO(111)-20% samples (Figure 8.7, right lower part). Moreover, the CV measurements display a more pronounced peak for hydrogen adsorption of the dominantly (100) oriented sample either prepared with 10 % of oxygen or with 20 % of oxygen (Figure 8.7, left part).

Therefore, it could be said that the (100) oriented sample has a sharper tendency to adsorb protons on its surface in comparison to the other orientations. This is in line with the in-situ XPS/UPS measurements (Section 8.2.3), which suggest that no charged layer is formed on the (100) surface and that hydrogen and hydroxide might be adsorbed equally on the (100) oriented surface. On the contrary, water adsorption experiments in vacuum on the (110) and (111) oriented NiO thin films could lead to the formation of a dipole where electrons are facing the positive hydrogen species (H^+) within the first layer of adsorbed water (Section 8.2.3). This assumption is supported by the electrochemical measurements, which show that these two surfaces are not that much interacting towards hydrogen adsorption.

XPS measurements after electrochemical characterization

Looking back at Figure 8.4, it can be observed that the valence band position after the electrochemical measurements is not modified in comparison to the valence band maximum measured after surface exposure to water in vacuum. Moreover, the difference of spectra of the Ni 2p region after electrochemical

measurement with as deposited thin film shows a marginal swelling of the density of state in the 855-860 eV region in comparison to the difference of spectra after surface exposure to water in vacuum. In the meantime, the shoulder at higher binding energy in the O 1s region is substantially increased. The increase of the shoulder is more important for the NiO(110)-20% and the NiO(111)-20% sample. Thus, it could be assumed that the intensity of the shoulder at higher binding energy in the O 1s spectrum, after the electrochemical experiments might be closely related to the presence of defects and not necessarily to the intrinsic properties of a specific surface orientation.

The difference of the Ni 2p spectra displays a slight increase of the photoelectron emission between 854 and 860 eV in comparison to the water exposure experiments in vacuum. It can be assumed that the layer of adsorbates leading to the a nickel hydroxide layer on the oriented NiO surfaces does not vary much during the electrochemical experiments. In comparison, the shoulder in the O 1s region increases substantially. Thus, it can be assumed that the electrochemical experiments generates additional adsorbate species but bonded to the hydroxide already adsorbed on the NiO surface. This additional layer of adsorbate would not directly interact with the NiO surface but could be mitigated in the presence of defects on the surface as this shoulder is larger if the defective state O 1s(Def.) is visible in XPS spectra of the as-deposited samples.

8.4 Conclusion

Differently oriented NiO films were prepared by reactive magnetron sputtering at 10 % and 20 % oxygen concentration onto heated Platinum (100), (110) and (111) oriented thin films grown onto MgO and sapphire substrates. The films are analyzed in-situ using photoelectron spectroscopy before and after surface water dissociation in vapour phase and by electrochemistry in an oxygen-poor and 0.1 M NaOH solution where experiments are carried in the window stability of water to study in-operando adsorption processes.

The similarity of the UPS results obtained on the most oriented thin films with what is provided in the literature suggests that an orientation could support a specific surface electronic fingerprints and even though our thin films are not perfect, their electronic surface properties could originate from the dominant surface orientation. In particular, the dominantly (100) oriented NiO thin films, displays a O 2p[z] electronic state not visible in dominantly (110) and (111) oriented NiO thin films.

The XP spectra reveal that water is absorbed in a bi-layer fashion on the as-prepared oriented NiO thin films. The first layer would be made of dissociated water molecules and the second layer, made of undissociated water molecules, is interacting with the first layer. The second layer forms a dipole structure (polarized water molecule), which would explain the decrease of the workfunction measured after water exposure. The dissociation of water within

the first layer leads to the formation of adsorbates. These adsorbates adsorb differently according to the dominant surface orientation. Thus, it has been assumed that hydroxides (OH^-) and protons (H^+) are adsorbed equally on the dominantly (100) oriented thin films but only the hydroxides might be adsorbed on the dominantly (110) and (111) oriented thin films.

Finally, the study of the adsorption reactions in the window stability of water evidences that the dominantly (100) oriented sample provide adsorption sites for hydrogen and hydroxide. On the contrary, the dominantly (110) and (111) oriented thin films show less reactivity towards the adsorption of hydrogen. Also, the presence of defects on the surface might be indispensable to enhance adsorption on the NiO surfaces as samples prepared at high oxygen concentration develop electrochemical features suggesting larger catalytic activity of the surfaces.

CHAPTER 9

Oriented NiO thin film activity towards the oxygen evolution reaction

Summary

Oriented NiO films (111), (100) & (110), reactively DC-sputtered on oriented platinum films on top of MgO substrates were studied electrochemically and were characterized on a rotating disk electrode for their performance towards the oxygen evolution reaction (OER). From the results, two electrochemical domains can be defined according to their catalytic activities: high overpotential ($>$ 1.55 V vs RHE) and low overpotential ($<$ 1.55 V vs RHE). We found that at low overpotential, electrochemical performances are rather similar for all orientations, but on the contrary, at higher overpotential, the (110) sample has the best electrochemical performance, followed by (111) and (100) samples. During OER, a thin hydroxide layer, about 1-2 nm thick growing on top of the thin film surfaces, has been identified as being the active material for the electrochemical reactions. The (111) and the (100) oriented thin film samples would produce a nickel hydroxide having the same catalytic properties, but the (100) oriented thin film would be less covered by the nickel hydroxide offering lower catalytic site density, and, on the other hand, (110) samples would form a more stable and more catalytically active nickel hydroxide material over both (111) and (100) thin films. The observed differences is ascribed to the formation of the β-Ni(OH)$_2$ phase on top of the (110) oriented thin film being more crystalline and more stable nickel hydroxide phase than the α-Ni(OH)$_2$, which is supposedly produced during the OER on the NiO(111) thin film and, to a lesser extent, on the NiO(100) oriented thin film.

The scientific material of this Chapter served to compose the article:

R. Poulain, A. Klein, and J. Proost. **Electrocatalytic Properties of (100)-, (110)-, and (111)-Oriented NiO Thin Films toward the Oxygen Evolution Reaction**. *The Journal of Physical Chemistry C*, 2018

Readable online: `https://doi.org/10.1021/acs.jpcc.8b05790`. The author of this manuscript, cited also as first author of the article above would like to point out he did not access the final version of the article.

9.1 Introduction

Although the hydrogen evolution reaction (HER) is efficient, the oxygen evolution reaction (OER) provides bottleneck issues and hinders greatly the performance of water splitting devices. Indeed, OER involves four electrical charges where HER only requires two, which could considerably decrease the kinetics of the reaction. However, among all the parameters that can be tuned to optimize the reaction, the material used as electrode can have a great influence on the OER mechanism and so on the performance of a water-splitting device.

The crystal orientation could be one aspect for optimizing the efficiency of an electrode towards an electrochemical reaction. For instance, it has been proven that the thermodynamically unstable (100) orientation of IrO_2 and RuO_2 structure is electrochemically more active towards OER than the (110) orientation [211]. Up to now, no experimental study has been carried out on the NiO surface orientation towards the OER activity. However, theoretical and experimental studies on adsorbates suggest a relatively great catalytic properties discrepancy between the three NiO dominant orientations [58, 61, 63, 65–67, 79, 212].

NiO is a stiff element, able to resist to relatively aggressive environment. Structurally, it adopts a stacked rocksalt like structure with a lattice constant of 4.17 Å. Dominant surface orientations for NiO are the (100), (110) and (111) in the (hkl) Miller index formatting. As seen before (see Section 2.2.1), the (100) and (110) surfaces are non-polar, which means the electric charge with the underlying plane is neutral, while the (111) surface is polar because of the formation of a dipole perpendicular to the surface [52].

Also, during electrochemical experiments on NiO, a thin nickel hydroxide layer might grow. Nickel hydroxide forms layers maintained by a weak OH-OH liaison and oxidizes to oxy-hydroxide above 1.1-1.4 V vs RHE. β/β refers to a hydroxide/oxy-hydroxide couple when no water or ions intercalate the structure. If water intercalates, hydroxide crystallinity decreases and the hydroxide is said to be turbostratic. In such case the hydroxide/oxy-hydroxide phase transformation involves the α/γ couple [171]. Oxidation state of cationic sites in γ-oxy-hydroxide phase is 3.66 and might be due to the intercalation of external compounds as potassium in the structure [170]. The whole picture between the four species is described by the so-called Bode scheme (Figure 9.1). The Nickel hydroxide properties towards the OER has been largely studied theoretically and experimentally, and could be one of the best base material as alternative to rare earth based catalyst [32–35, 213–216].

Although higher control on the material properties are achieved with sputtered thin films, only few reports have been found on the use of NiO thin films towards OER. The systematic study on NiO thin film carried out by Miller *et al.* [218] highlighted that OER activity is increased with NiO sputtered

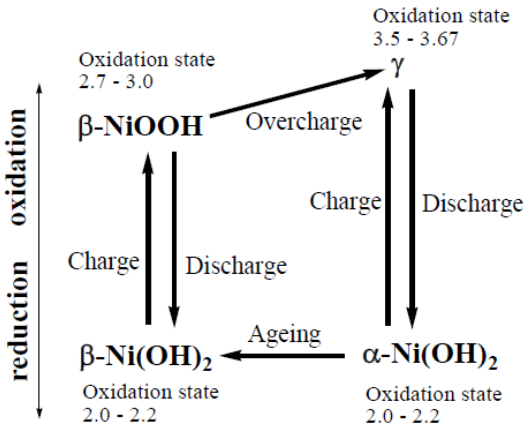

Figure 9.1: Bode diagram representing the phase transformation and relationship between the four states of nickel hydroxide derived compounds. Taken from Lyons et al. [217].

films when they present a high degree of crystallinity and when there is an excess of oxygen in the film composition. However, the study did not point out any relationship with the surface orientation and the hydroxide properties developing on top of the film.

Instead of carrying out a systematic study, we propose here to introduce electrochemical results obtained on oriented samples in order to give hints for preferential path for tailoring NiO based electrode for OER. Moreover, we would like to emphasize that NiO electrochemical properties might be closely related to the nature of the nickel hydroxide growing on the surface during OER.

9.2 Experimental

9.2.1 Sample preparation

100-150 nm NiO oriented thin films were deposited on Pt/MgO oriented substrates with (111), (110) and (100) orientation, which were prepared previously by the deposition of Pt thin films on MgO (111), (110) and (100) single crystals. NiO was then reactively DC sputtered at 500 °C from a Ni target (grade 99.9%). According to reports, the (100) and (111) orientation are favoured at relatively low and high oxygen concentration, respectively [183,202]. Although no ultimate optimization of deposition conditions was attempted, the (100), (111) and (110) samples were deposited with 10 % of oxygen for the (100) sample, and 20 % of oxygen for the (111) and (110) sample. All other sputtering conditions were the same for the three oriented samples, and

defined in Section 3.1.2. After deposition, the samples were cooled down to room temperature in the deposition atmosphere. The use of platinum as an underlayer is compatible with the fact that a Pt/NiO junction should create an ohmic contact. The workfunction of the p-type NiO is less than 5.2 eV (Chapter 4), while metallic Pt has a workfunction strictly above 5.2 eV. Therefore, an accumulation layer should be created in the NiO side at the NiO/Pt interface. Although the films are not single crystalline, the samples are referred by their dominant orientation in the following parts.

9.2.2 Electrochemical experiments

All experiments are realized at room temperature in ultra-pure 1.0 M KOH electrolyte (Semi-conductor grade, 99.99 % trace metals, Sigma-Aldrich). Samples were fixed at the tip of a rotating disk (2000 rpm) and measured against a Ag/AgCl reference electrode, the latter having a potential of 0.95 V vs RHE, measured experimentally with an hydrogen electrode. Electrochemical experiments were realized with a Metrohm Autolab PGSTAT302N potentiostat. As depicted in Figure 9.2, the electrochemical experiments consisted in a cyclic voltammetry activation at (100) mV/s for at least 10 scans, followed by a chrono-amperometry for 10 min at $\sim$ 1.6 V vs RHE to ensure the electrode is in equilibrium state, then a slow CV is realized twice at 10 mV/s, followed by a quasi-static experiment. The latter consisted in fixing the working electrode potential for 90 sec while the current is being measured. The current value at the end of the span time is then taken to plot IV curves.

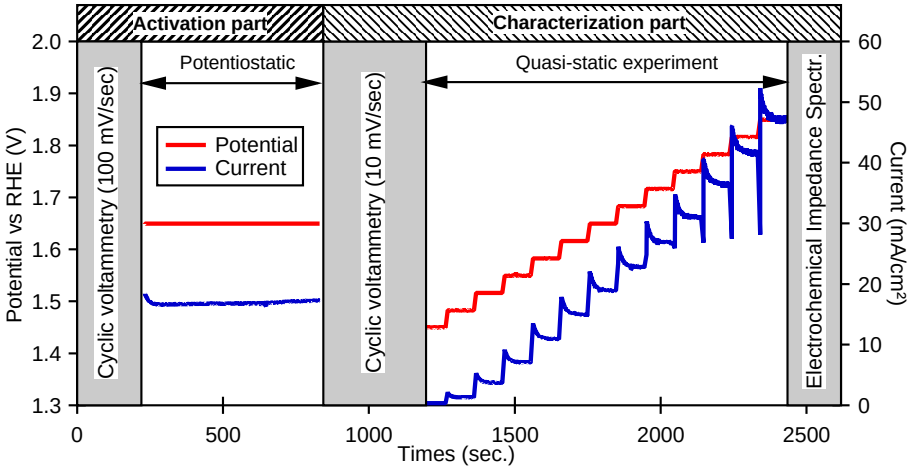

Figure 9.2: Typical experimental procedure for the electrochemical characterization of the NiO thin films towards the OER. The plan includes an activation part for about 20 min followed by the cyclic voltametry and the quasi-static measurements. The results are then iR_c corrected where the contact resistance R_c is determined by EIS measurements carried out at the final stage of the electrochemical characterization.

Finally, Electrochemical Impedance Spectra (EIS) are carried out from 1 MHz to 1 Hz at different potentials, from which the series resistance is determined for $iR_{c,tot}$ correction of the IV curves. Contrary to (111) and (110) samples, the (100) sample produces specific features at high frequency (>100 kHz) associated to electric charges in the NiO (Figure 9.3). The electrical model

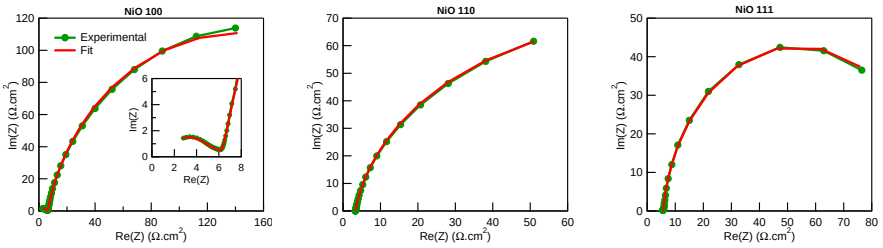

Figure 9.3: EIS realized at 1.45 vs RHE on a different sample in a Nyquist representation.

associated to the (100) oriented thin film is made of three elements in series, which are electrically defined as being a resistance R in parallel with a constant phase element (CPE). For the meaning of the CPE, see detailed description in Section 2.4.2. The equivalent electrical circuit was used to determine the ohmic losses for $iR_{c,tot}$ correction of the CV plot (Table 9.2). The ohmic losses being for the (100) sample: $R_{c,tot} = R_c+R_1+R_2$ for which R_1 and R_2 are the resistance associated to the semi-circle visible at high frequencies (>100 kHz). For the (111) and (110) samples, the EIS spectra were simply fit with a R_c+R_{ct}/CPE model where $R_{c,tot}=R_c$ (Table 9.2). Thus, the series resistance could be determined for $iR_{c,tot}$ correction (Table 9.1). Finally, from

Table 9.1: Value of the total contact resistance $R_{c,tot}$ determined by EIS for $iR_{c,tot}$ correction of the IV curves. Contrary to the (110) and the (111) samples, the contact resistance of the (100) sample has been found to be dependant on the electrode potential and an empirical law has been determined. The value are given in $\Omega\,cm^2$. E_{RHE} is the potential of the electrode relative to the RHE.

NiO (100)	NiO (110)	NiO (111)
$3.3\times\ (E_{RHE}\text{-}0.95)^{-0.864}$	2.8	2.3

the constant phase element associated to the Helmholtz layer, the equivalent Helmholtz capacitance (C_h) is calculated following equation 9.1, as proposed by Musiani *et al.* [146]:

$$C_{equivalent} = Q^{\frac{1}{\alpha}} \left(\frac{R_{c,tot} R_{ct}}{R_{c,tot} + R_{ct}} \right)^{\frac{1-\alpha}{\alpha}} \tag{9.1}$$

Where $R_{c,tot}$ is the resistance of the electrolyte and R_{ct} is the charge-transfer resistance (see Table 9.2).

Table 9.2: EIS equivalent electric model adopted in this part according to the NiO orientation.

100	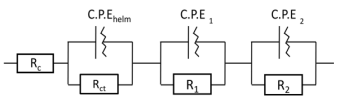
110 & (111)	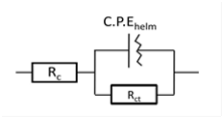

9.2.3 Structural and chemical characterization

The AFM (Section 3.3.3) and the XRD (Section 3.4.2) measurements were performed at TU-Darmstadt before and after electrochemical measurements, respectively. Chemical composition analysis of the surface was performed ex-situ after the electrochemical measurements by XPS at UCL. The electrode is supposed to be retrieved out of the electrolyte in OCV condition. The aim is to determine the elements present on the hydroxide surface and also to estimate the nickel hydroxide thickness. Ni 2p, Fe 2p and O 1s region were scanned in order to obtain quantitative data. XPS fitting was realized with CASA XPS software and was focused on the O 1s and the C 1s regions (Figure 9.4). Fitting in the O 1s region is carried out in order to take into account photoemission from oxygen in the crystal lattice of NiO, the hydroxide $Ni(OH)_2$ and carbonacious species (O-C, O=C). Thus the deconvolution consisted into four Gaussian-Lorentzian (GL–50) peaks (Figure 9.4, left). The peaks associated to O-C and O=C species are constrained to be in the 532.7-532.9 eV range where the O=C/O-C ratio is determined by the deconvolution of the C 1s region (Figure 9.4, right). Eventually, the O-H and O-Ni are constrained in the 530.9-531.9 eV and 529-530 eV range, respectively. It should be noted that these XPS measurements did not allow to differentiate the hydroxide phases, as vacuum would lead to water removal and nickel hydroxide crystallization in its β phase [219].

9.3 Results and Discussion

9.3.1 Structural characterization

The X-ray diffractogram in Figure 9.5 reveals in all cases oriented films along the c-axis, although the inclusion of non-desired orientations in (110) and (100) samples needs to be recognised. Indeed, in the (110) films a small fraction of (100) orientation can be seen while in the (100) film we observe (111) orientation. However, it remains marginal and it can be assumed that electrochemical properties will be mainly related to the main orientation. Also,

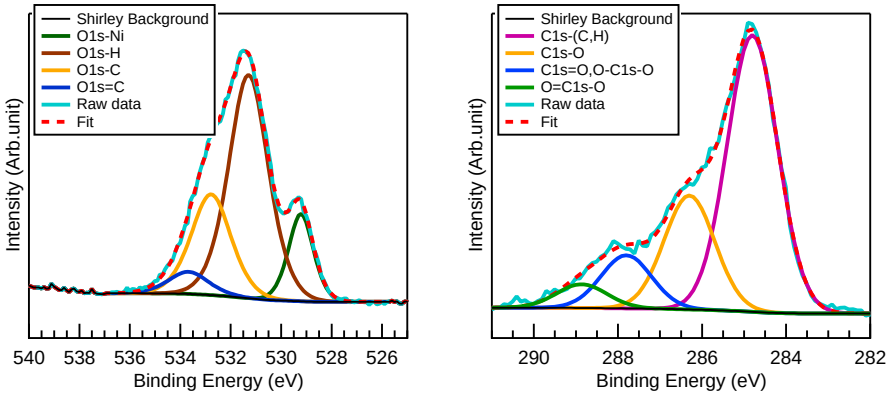

Figure 9.4: Typical O 1s and C 1s peak deconvolution realized after electrochemical reaction on the NiO (100) oriented sample. Shirley background is used as baseline.

the (100) sample includes a Ni^0 phase, which might originate because of the lower oxygen concentration during the film preparation for this orientation. However, in-situ XPS measurement (not shown here), did not show any metallic nickel at the surface probably because it has been oxidized during the cooling period during the sample preparation. Thus a stoichiometry gradient might arise at the surface of the (100) sample. Therefore, a less conductive layer would emerge between the bulk of the sample and the electrolyte, which might be the origin of the additional capacitive components at high frequencies as seen in the EIS spectra (Figure 9.3). The XRD patterns obtained with the (110) and the (111) oriented samples do not evidence the presence of a metallic phase. This might be due to the higher oxygen concentration during the sample preparation. It results that the (110) and the (111) oriented samples provide a simpler EIS spectra (Figure 9.3), for which the equivalent electrical fitting circuit is simplified in comparison to what it has been used for the (100) oriented sample (Table 9.2).

Before electrochemical characterization of the three studied samples, the AFM micrographs in Figure 9.6 show a relatively flat surface having likely cubic grain morphology for the (100) surface, which indicates that we have an excellent surface orientation, while the (110) sample displays more elongated grains on the surface adopting regular patterns and, finally, the (111) surface has the most surprising surface morphology. Indeed, the structure seems to combine two surface domains: one leading to an apparent (111) flat surface and the second leading to a rough surface without apparent surface faceting. The mechanism leading to such surface inhomogeneity is not elucidated and is out of the scope of this work but absence of facet for a (111) oriented NiO thin film correlate with what can be obtained if NiO is deposited on sapphire by RF-sputtering at high oxygen concentration [189]. However, before the electrochemical experiments, the flattest geometrical surface is obtained with the (100) surface, and in comparison, geometrical surfaces, or with others words the surface in contact

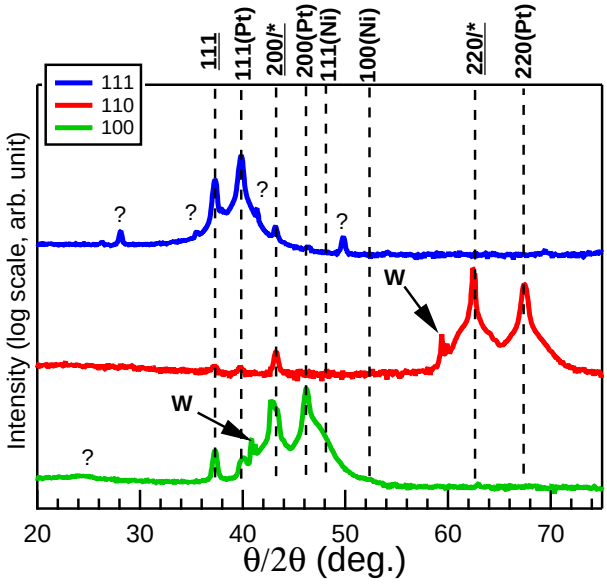

*Figure 9.5: X-ray diffractograms for the NiO (111), (100) and (110) samples after electrochemical experiments. NiO peaks are indicated by their orientation, W account for the Tungsten peak emerging from the XRD hardware and the symbol * for the MgO single crystal peak. Unidentified peaks might be associated to hydroxide or a trace of a polymer used to ensure sealing of the rotating electrode.*

with the electrolyte, are 2.2% and 4.7% higher for respectively (110) and (111) surfaces in comparison to the (100) NiO oriented thin film (Figure 9.6 and Table 9.3). We can therefore assume that the influence of the geometrical surface can be neglected when interpreting the electrochemical experiments [1].

	NiO (100)	NiO (110)	NiO (111)
RMS height (nm)	3	6.7	10.5
Geometrical surface ratio	1.021	1.024	1.066

Table 9.3: Root mean square (RMS) and geometrical surface ratio for the three oriented samples determined from the AFM images displayed in Figure 9.6

9.3.2 Presence of Nickel Hydroxide on NiO

The XPS measurements in Figure 9.7, which have been realized after electrochemical cycling, reveal noticeable differences between each sample. After deconvolution of the O 1s peak, a higher hydroxide coverage on the (110)

[1] However, Pr. M. Chatenet raised concern over the fact that an electrochemical methods can be more reliable to evaluate the active surface with the electrolyte e.g.: capacitive methods than with AFM.

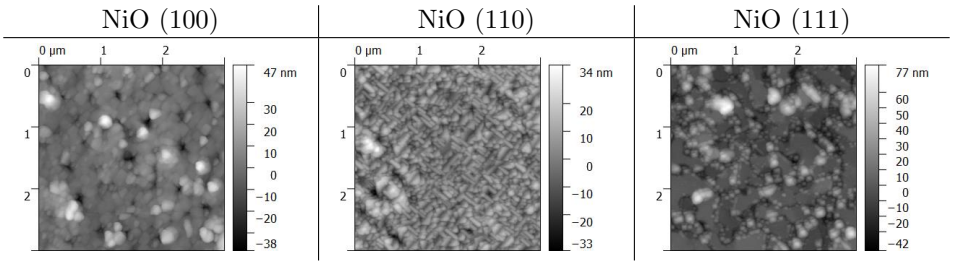

Figure 9.6: AFM height images before electrochemical cycling of the NiO (100), NiO (110) and NiO (111) sample.

over the (111) and (100) surface can be determined. The estimated thickness of the hydroxide layer growing on our (110), (111) and (100) surfaces is 2, 1.7 and 1.25 nm, respectively, while the carbonated layer is found to be relatively constant and is about 1.8 nm for all the samples (Table 9.4). XPS results suggest that hydroxides grow on all the studied samples but the (110) produces more hydroxide than the (111) and the (100) surfaces, the latter producing the lowest hydroxide amount, which is also confirmed by the spectra obtained in the Ni 2p region. Indeed, the peak in the 856 eV range assigned to nickel hydroxide and accompanying at higher binding energy the Ni 2p peak, is the strongest with the (110) surface followed by (111) and then by (100) surface (Figure 9.7).

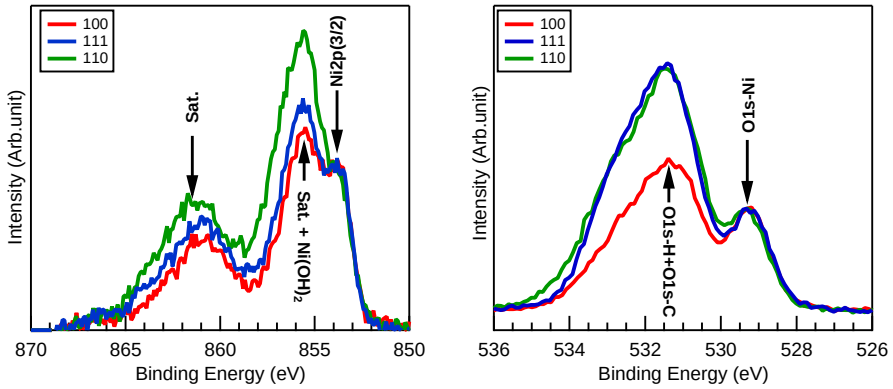

Figure 9.7: XPS profiles of Ni 2p (left) and O 1s (right) region for the (100), (111) and (110) samples.

Moreover, cyclic voltammetry experiments show an oxidation/reduction wave in the 1.1-1.4 V vs RHE range for the three samples which can be attributed to the nickel hydroxide/oxy-hydroxide phase transformation (Figure 9.8). Thus, the hydroxide observed by XPS is related to nickel hydroxide, and so the

Table 9.4: Area fraction extrapolated from XPS deconvolution on the different orientations.

Orientation	(100)	(111)	(110)
O-Ni (%)	23.6	16.3	13.7
OH-Ni (%)	47.7	56.8	55.6
O-C (%)	23.6	21.9	25.2
O=C (%)	4.9	4.8	5.5
Ratio OH-Ni/O-Ni	2	3.5	4.1
Estimated hydroxide thickness (nm)	1.25	1.7	2
Estimated carbonated layer (nm)	1.8	1.75	1.85

electrochemical reactions could be likely located on the nickel hydroxide phase growing on top of each surface but not necessarily directly on the dominant surface orientation.

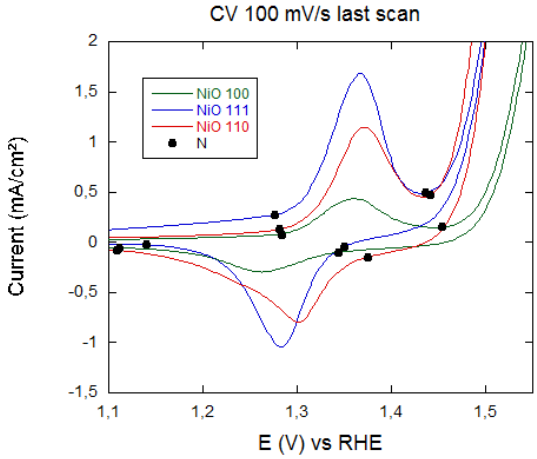

Figure 9.8: Cyclic voltammograms at (100) mV/s in the $Ni(OH)_2$ pre-oxidation wave region. Black dots represent boundaries for determining coulombic charges of the oxidation and reduction waves.

Moreover, taking the coulombic charge of the oxidation wave related to the $Ni(OH)_2 \rightarrow NiOOH$ phase transformation, the determination of the quantity of charges per cationic site on the NiO surfaces has been calculated and would discard completely the possibility that the electrochemical reactions happen on the NiO surfaces. Indeed, the coulombic charges of the oxidation wave is 231, 808 and 538 $\mu C/cm^2$ for the (100), (111) and the (110) samples,

respectively(Table 9.4). As detailed in Section 2.2.1, the (100), (111) and the (110) surfaces can provide theoretically 0.11, 0.13 and 0.08 cationic site/$Å^{-2}$, respectively. This calculation indicates that the cationic sites support 1.21, 3.75 and 4.07 charges on the (100), (111) and the (110) sample, respectively (Table 9.4). Ideally, if the reactions happen on the surface, there should be 1 to 1.66 charge per cationic site (depending on the phase, see Figure 9.1). The (110) and the (111) displays substantial higher charges per cationic site experimentally than what should be obtained for *planar* electrochemical reactions. Therefore, the only reasonable possibility is that the electrochemical reactions occur in a volume and not on a surface. Thus, it is assumed, that the electrochemical reactions are realized in a volume which is supported by the nickel hydroxide layer growing on top the nickel oxide surfaces during the OER. This could be rendered possible thanks to the weak OH-OH interaction in the nickel hydroxide, which would accommodate reactions in the $Ni(OH)_2$ structure.

Table 9.5: Main characteristics of the oxidation and reduction wave of the hydroxide/oxy-hydroxide reaction before OER. Raw data taken from cyclic voltammetry realized at (100) mV/s. The estimated hydroxide thickness is determined either for a β or a γ phase transformation.

Orientation	NiO (100)	NiO (111)	NiO (110)
FW peak ($\mu C/cm^2$)	231	808	538
Ni in NiO (e^-/cat) (FW)	1.21	3.75	4.07
Estimated $Ni(OH)_2$ thickness (nm) β/γ	0.54/0.32	2.11/1.27	1.27 / 0.76
BW peak ($\mu C/cm^2$)	-202 (87%)	-692 (85%)	-632 (115%)

Taking an average number of cationic site by volume of 0.026 atom.A^{-3} for $Ni(OH)_2$, the reaction depth into the hydroxide is estimated to vary from 0.3 to 1.9 nm from the top of the nickel hydroxide surface (Table 9.5). The reaction depth range correlate relatively well with the XPS measurements, which provides a hydroxide thickness of 1.4 - 2.1 nm. It proves that $Ni(OH)_2$ would provide the catalytic material in which electrochemical reactions happen in a small volume of few nanometre depth. Then it can be assumed that electrochemical reaction occurs at the interface between the nickel hydroxide and the electrolyte but not on the NiO surface.

9.3.3 Electrochemical measurements

Mass transport limitation

Electrochemical measurements of the oriented thin films prepared in this chapter, show a large discrepancy between the three orientations (Figure 9.9, left). At large overpotential, the performance towards the OER is higher on the (110) oriented sample, followed by the (111) oriented sample and then the (100) oriented sample. Plotting the IV curve in log scale (Figure 9.9, right), two regions can be defined. The first region, delimited by potential lower than 1.55 V vs RHE, provide a low Tafel slope, meaning that the increase of current is high for a given increment of potential. The second region, for potential higher

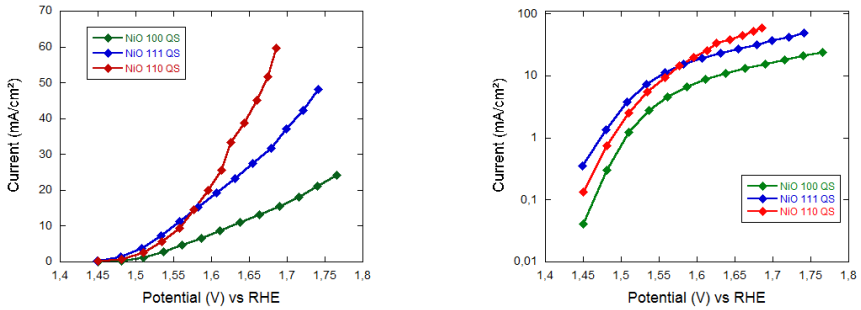

Figure 9.9: IV curves determined from the quasi-static measurements in linear scale (left) and logarithmic scale (right). The potential is iR corrected for each curves.

than 1.55 V vs RHE, is characterized by a high Tafel slope, meaning that the increase of current is low for a given increment of potential. The origin of the two regions will be discussed later but it can be said that, on a rotating disk electrode, mass transport limitation can be described by the Levich equation which is:

$$j_{LA} = 0.620\, n\, F\, D^{2/3}\, v^{-1/6}\, C_r\, \omega^{1/2} \tag{9.2}$$

with j_{LA} being the anodic limiting current, n the number of electrons exchanged (= 4), F the Faradic constant (= 96500 C/mol), D the diffusion coefficient of the hydroxides in water ($\sim 10^{-5}$ cm^2/s), C_r the concentration of active species (= 0.001 mol/cm^3), v the kinematic viscosity of water ($\sim 9.10^{-3}$ cm^2/s) and ω the angular rotation speed (210 rad/sec at 2000 rpm). For our setup, the calculations give an anodic limiting current j_{LA} of 3.53 A/cm^2. This value is far from the current range in which the setup is working ($<$ (100) mA/cm^2). The anodic current limitation is only calculted for a theoritical diffusion layer at the electrode surface but other factors as surface reduction because of micro-oxygen bubbles fixed on the rotating electrode or mass transport limitation within the nickel hydroxide layer should be considered as well.

Indeed, the Levich equation allows to assess limiting current for bulk mass transportation from the electrolyte, but diffusion of species through the hydrous hydroxide layer has to be considered. Diffusion of species can be assessed both by EIS or QS. Being not enough accurate because of the large current at high overpotential EIS does not provide satisfactory results, but QS data can provide an estimation of the diffusion of the chemical species in the hydroxide layer in applying the so-called Cottrell equation in the relevant transition part of each measured QS plot [220]. Cottrell equation describes

transitional current when a potential stair is applied to an electrode:

$$I(t) = n\,F\,A\,C_{OH^-}\sqrt{\frac{D_{OH^-}}{\pi\,t}} \tag{9.3}$$

with C_{OH^-} the concentration of hydroxide, D_{OH^-} the diffusion coefficient of the hydroxide and t the time. One can extract an estimation of the diffusion coefficient of the active species through the hydroxide layer by identifying the linear part of the $I(t) = f(t^{-1/2})$ plot (Figure 9.10, left). The interfacial concentration in hydroxide can be considered equal to bulk concentration as the experimental current density is much lower than the limiting current as determined by the Levich equation.

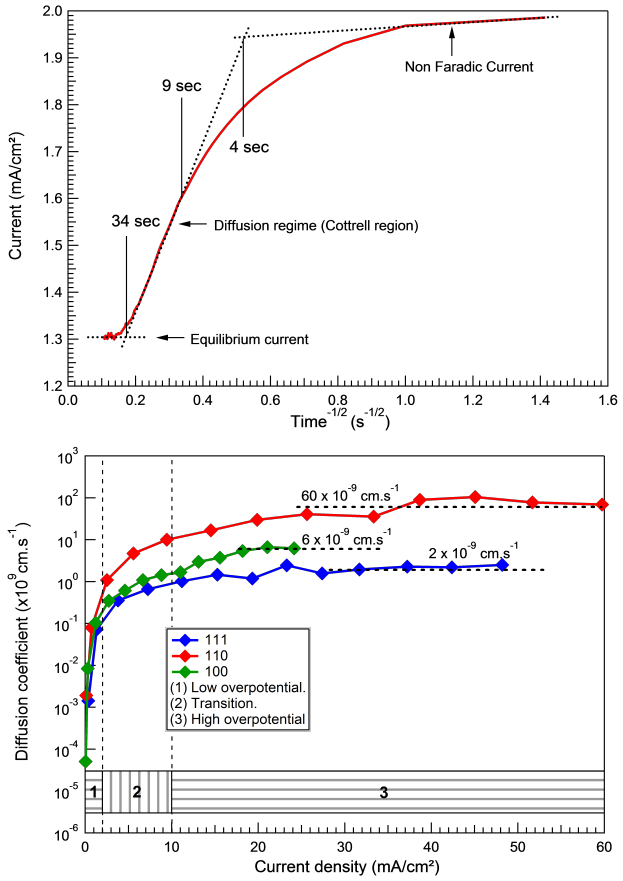

Figure 9.10: Top: Cotrell plot of the transitional regime during the quasi-static experiment (see Figure 9.2). The Cottrell region correspond to the linear part between 9 and 34 seconds. Bottom: extracted diffusion coefficient for the different sample for a concentration of reactant equal to 1 mol/L. The coefficient diffusion in the hydrous hydroxide layer is extracted for high over-potential (area 3). The area 1 and 2 has been excluded for the evaluation of the diffusion coefficient.

Thus, for the right plot of Figure 9.10 the extracted diffusion coefficient shows that hydroxide diffusion in the nickel oxy-hydroxide is about one order of magnitude higher for the (110) oriented NiO thin film than for both the (100) and (111) oriented thin films.

Tafel slope

In addition, it is observed that for the IV curve plotted in logarithmic scale that the curves obtained for the (111) and the (100) oriented sample are similar where the (111) curve resembles to a translation of the (100) curve to higher current (Figure 9.9, right). The IV curve in logarithmic scale obtained on the (110) oriented surface differs from the two other curves, especially at high overpotential where the Tafel slope is larger.

The Tafel slope determined from Figure 9.9 (right) at low ($<$ 1.55 V vs RHE) and high ($>$ 1.55 V vs RHE) overpotential are displayed in Table 9.6. At low overpotential, the Tafel slope can be considered as roughly similar for the three samples. On the contrary, the Tafel slope is the lowest for the (110) oriented sample (210 mV/dec), while it is higher for the (111) and the (100) oriented sample with 348 mV/dec and 373 mV/dec, respectively.

Table 9.6: Tafel slopes, expressed in mV/dec, obtained with the (100), (110) and the (111) oriented samples at low ($<$ 1.55 V vs RHE) and high ($>$ 1.55 V vs RHE) overpotential. The data are extracted from Figure 9.9 (right).

Potential (V) vs RHE	NiO (110)	NiO (111)	NiO (100)
$<$ 1.55 V	46	57	41
$>$ 1.55 V	210	348	373

9.3.4 110 vs 111

The (110) sample shows a higher catalytic activity for the OER particularly at high overpotential ($>$ 1.55 V vs RHE) composed to the (111) sample (Figure 9.9 and Table 9.6). Moreover, the comparison of the frontward and backward coulombic charge of the nickel hydroxide/oxy-hydroxide phase transformation gives a ratio equal to 85 % and 115 % for the (111) and the (110) sample, respectively. It can therefore be assumed that different nickel hydroxide species are produced for each orientation.

However, the equivalent capacitance of the Helmholtz double layer has a similar value for both samples (Figure 9.11) and the CPE α factor is above 0.9 (Table 9.7). These two observations could mean that the hydroxide layer homogeneity is similar on both surfaces with *somewhat* an equivalent number of adsorbption sites in contact with the electrolyte.

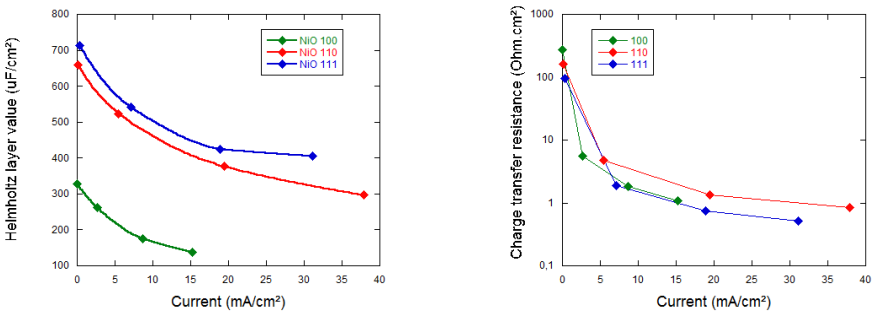

Figure 9.11: Equivalent capacitance values of the Helmholtz layer and charge transfer resistance values for the (100), (110) and (111) samples, as determined by EIS at different potentials.

Interestingly, the nickel hydroxide oxidation pre-step produces an equivalent coulombic charge higher on the (111) sample than on the (110) sample ($\times$ 1.5, Table 9.5) but the nickel hydroxide is thicker with the (110) sample than on the (111) sample with 2 nm against 1.7 nm, respectively (Table 9.4). This suggests that the (111) sample produces a thinner hydroxide layer for which, when oxidized, the cationic sites gain a higher oxidation number than the cationic sites from the hydroxide growing on top of the (111) oriented sample.

Table 9.7: α factor values of the Helmholtz double layer for the three oriented sample as determined after fitting of the EIS measurements.

Potential vs RHE (V), non iR corrected	NiO (110)	NiO (111)	NiO (100)
1.45	0.91	0.92	0.86
1.55	0.92	0.92	0.89
1.65	0.92	0.94	0.88
1.75	0.92	0.89	0.85

The estimated hydroxide thicknesses from the electrochemical pre-oxidation waves comply with the XPS measurements in assuming that the α-$NiO(OH)_2$ phase is present on top of the (111) oriented sample. Indeed, it has been found that the Ni oxidation state is 3.5-3.67 in a γ-NiOOH phase (oxidation of the α-$NiO(OH)_2$ phase) while the Ni oxidation state is 2.7-3.044 in the β-NiOOH phase (oxidation of the β-$NiO(OH)_2$ phase). Thus, the hydroxide thickness is 1.25 nm on top of the (111) oriented sample in assuming a α-$NiO(OH)_2$ $\rightarrow$ γ-NiOOH phase transformation but for the β-$NiO(OH)_2$ $\rightarrow$ β-NiOOH phase transformation the hydroxide thickness would be 2.1 nm (Table 9.5). However,

the XPS measurements suggest that the hydroxide thickness is about 1.7 nm on top of the (111) oriented sample (Table 9.4). In consequence, it discards the possibility to have the β-NiO(OH)$_2$ phase growing on top the (111) oriented sample. On the contrary, for the (110) oriented sample, the XPS and the electrochemical measurements do not discriminate between both α and β hydroxide phase.

Eventually, as the electrochemical reactions occur in the nickel hydroxide layer, the nickel hydroxide can be oxidized into two oxy-hydroxide phases (either the β or the γ phase). Also, the electrochemical performance of the oriented samples suggest that the nickel hydroxide layer on top of the (110) and the (111) sample are different, and the comparison with the XPS measurements, it can be estimated that the nickel hydroxide growing on top of the (111) sample provides an oxy-hydroxide counterpart with a higher oxidation state. Therefore, to comply with the Bode scheme (Figure 9.1), it can be consistent to assume that the (111) sample would produce an hydroxide mainly made of α-Ni(OH)$_2$, while the (110) sample would be likely producing the more stable β-Ni(OH)$_2$ phase.

9.3.5 100 vs 111

Taking a look at the fast CV scans at (100) mV/s with respect to the current wave typical of the nickel hydroxide/oxy-hydroxide phase transformation situated right before the OER (Figure 9.8 and Table 9.5), it is possible to evaluate the pseudo-capacitive properties of the nickel hydroxide material. It can be observed a clear difference between the three samples. The backward coulombic charges represent around 85-87 % of the measured forward coulombic charge for the (111) and (100) surfaces, while it reaches up to 115 % for the (110) sample (Table 9.5). Thus, the (100) and (111) sample produce a hydroxide with similar pseudo-capacitive properties.

Also, looking back at the IV curve in log scale of the (100) and (111) samples, one can notice similar shapes but the shape of the curve obtained with the (111) sample is shifted about 0.25 decades upwards in comparison to the curve obtained with the (100) oriented sample. The observed vertical translation in Figure 9.9 between the log(I) vs.V curves of (100) and (111) sample might be indicative for the fact that close catalytic activity is obtained for both surface orientations. In other words, the same active sites are present on both surfaces, but the amount of the active site on the surface might be higher on the (111) sample than on the (100) sample. Indeed, a translation in the Tafel plots can be interpreted by a higher exchange current density for the (111) sample, which can be either related to an increase of the geometrical surface or an increase of the number of active site density. Since AFM measurements before electrochemical experiments[2] do not highlight a clear increase of the geometrical surface for the (111) sample over the (100) sample

[2]Unfortunately AFM measurements after the electrochemical measurements have not been performed.

(only 4.7%, Figure 9.6 and Table 9.3), the translation could be attributed to an increase of the number of active sites on the (111) surface compared to the (100) surface. This increase is qualitatively in line with both the higher coulombic charge in the NiOOH $\rightarrow$ $NiO(OH)_2$ region of the (111) sample compared to the (100) ($\times$ 3.5, Table 9.5) and with the XPS measurements, which confirm a higher nickel hydroxide thickness on the (111) surface than on the NiO (100) ($\times$ 1.4, Table 9.5). Moreover, the equivalent capacitance of the Helmholtz double layer is higher on (111) sample than on the (100) ($\times$ 2.2, Figure 9.11).

These observations lead to the assumption that similar hydroxides grow on the (100) and (111) surfaces (same pseudo-capacitive properties and same catalytic activities) but the quantity of active material is lower on the (100) surface than on the (111) one (lower active site density, thinner hydroxide layer on the (100) surface).

In addition, on the (100) sample, the hydroxide layer might be inhomogeneous as suggested by the lower value taken by the α factor of the Helmholtz layer determined by EIS in comparison to the α factor for the (111) oriented sample (Table 9.7). The assumption that the (111) sample develops a more homogeneous hydroxide coverage than the (100) sample is consistent with the work of Cappus *et al.* which was realized in an UHV chamber [63]. His work suggested that hydroxyl groups do not bond to regular sites on a (100) surface, but rather on defective ones, while a full hydroxyl coverage is obtained with the (111) surface. Therefore, it would mean the hydroxide on the (100) sample could be inhomogeneous and can be found in higher quantity nearby crystallographic defective sites (e.g.: at grain boundaries) than on regular site. Instead hydroxides might bond on defective site and on regular sites for the (111) sample, providing a more homogeneous hydroxide layer.

Finally, it can be assumed that comparable hydroxides grow on both (111) and (100) oriented thin films but the (100) oriented sample is less covered than the (111) counterpart. As in the previous part, it has been assumed that the (111) oriented surface produces the α-$Ni(OH)_2$ hydroxide, by extension it is assumed that also the (100) oriented thin film develops the α-$Ni(OH)_2$ phase during the OER experiments.

9.3.6 Tafel slope insight

When plotting the resulting IV curves semi-logarithmically, two regimes of electro-catalytic activity are being highlighted (Figure 9.9). The first one, at low overpotential (1.45 – 1.55 vs RHE, $I < 2$ mA/cm^2) is characterized by a high electro-catalytic activity (low Tafel slope), while the second regime at potentials above 1.55 vs RHE ($I > 10$ mA/cm^2) develops lower electro-catalytic activity (high Tafel slope).

At low overpotentials, the Tafel slope lies in the 40-60 mV/dec range and can be considered to be similar for all surface orientations (Table 9.6). At

higher overpotential, large Tafel slopes are attained. (100), (110) and (111) samples have a respective Tafel slope of 210, 348 and 373 mV/dec. The change in the Tafel slope value at a electrode towards the OER has been already reported in literature [221, 222]. For instance, Nadesan *et al.* [221] observed three Tafel slopes with Li doped NiO, the first region being limited to currents below 5 mA/cm^2 is characterized with a low Tafel slope, which is about 43 mV/dec, then a region for which the current is comprised between 5 and (100) mA/cm^2 with a Tafel slope of 85 mV/dec, and the last region for currents higher than (100) mA/cm^2 where the Tafel slope is high and is about 132 mV/dec. This is however that what is obtained at high over-potential for the sample studied in this chapter.

Tafel slope at low overpotential

The low Tafel slope at low overpotential can be considered unexpected if the electrochemical reaction is supported by the hydroxide in a non-contaminated electrochemical setup. Indeed, the literature gives Tafel slopes which lie in the 120 mV/dec range for pure $Ni(OH)_2$ [34, 215, 216]. However, when other elements are incorporated in the nickel hydroxide structure, the Tafel slope can decrease substantially. For instance in the presence of iron, even in trace amounts, the Tafel slope of the nickel hydroxide can be as low as 40 mV/dec [34, 215, 216].

Also, Tafel slopes in the 43 mV/dec range have been reported for experiments realized with Li doped NiO [221]. Intrinsic/extrinsic dopants in the NiO crystal such as Li or nickel vacancies might be beneficial for the OER [218,221]. Thus, intrinsic contaminant as Li, could lead to the formation of Ni^{3+}, which could enhance the OER reaction [221]. Moreover, crystal discontinuities such as grain boundaries can concentrate catalytic sites [218].

With our samples, XPS measurements have been attempted in the Fe region after the electrochemical experiments to detect a possible iron contamination, but no signal has been detected (Figure 9.12).

Thus, as our samples are not Li doped, we could assume the enhanced electrochemical activity at low overpotential compared to what we could expect, might arise from the presence of defects, for instance nickel vacancies or crystal discontinuities at the electrode surface such as the grain boundaries as observed in the AFM images (Figure 9.6). However, XRD patterns of the (100) sample show a shoulder, which is interpreted as being a fingerprint from a vanishing Ni^0 phase trapped in the NiO structure. The presence of the Ni^0 phase in the NiO thin film would favour the idea that the surface is oxygen deficient, hindering the formation of nickel vacancies at the surface. Therefore, the crystallographic irregularities on the NiO thin film surface, and not the electronic defects such as nickel vacancies, would account for the enhanced OER activities on the surface of the electrode at low over-potential.

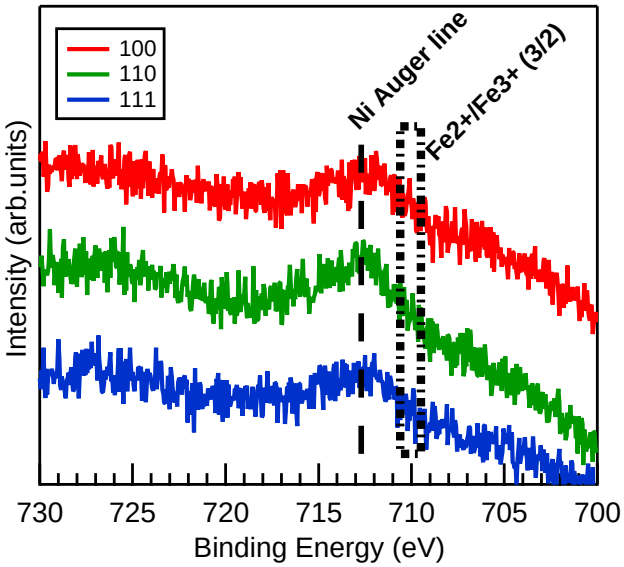

Figure 9.12: XPS profiles of the Fe 2p region for (100), (111) and (110) samples after the electrochemical characterization towards the OER. No iron could be detected by XPS.

Tafel slope at high overpotential

At high overpotential, a charge transfer limitation can be discarded as the fitting of the EIS measurements show that charge transfer resistance of the (100) and (111) samples is half of that of the (110) sample (Figure 9.11, right), which is in contradiction with the IV curves showing that the OER is more efficient for the (110) oriented sample.

A change in the reaction path is likely to happen at high overpotential, but the expected Tafel slope value should be at the maximum 120 mV/dec. At high overpotential a large portion of the surface will be subjected to the hydroxide discharge on the active site S following the reaction:

$$S + OH^- \rightarrow SOH + e^- \tag{9.4}$$

Therefore the surface is mainly covered by SOH [217, 222]. In the meantime, the Helmholtz double layer value decreases at high overpotential for the three samples, which would mean there are less absorbing sites available (Figure 9.11, left). Indeed, the SOH intermediate in equation 9.4 would reduce the number of free adsorbing site, where electric charges are facing ions (hydroxide) from the electrolyte. It results in a reduction of the Helmholtz equivalent capacitance when measured by EIS. Thus, a rate limiting step, where neutral SOH species decrease the number of adsorbing site might explain, to a certain extent, the large Tafel slope measured experimentally at high overpotential for the oriented samples prepared in this chapter.

Therefore, the high Tafel slope measured for large overpotential on the oriented NiO thin films is not really understood at this stage. But it cannot be totally explained by a rate determining step in the oxygen evolution reaction ans it must include other phenomenon such as mass transport limitation in the very close vicinity of the reaction site due to e.g. a decrease of the active surface because of micro-oxygen bubbles which did not reach the critical volume to be detached or mass transport limitation within the nickel hydroxide as it has been shown that the electrochemical should occur in volume and this cannot be assessed by the Levich equation.

Taking the Cotrell equation, it can be observed that the diffusion coefficient on the (110) oriented thin film is about 10 times higher than on the 100 and 111 oriented NiO thin films (Figure 9.10). Again, this results could correlate with the assumption a more crystalline β-phase could growth on the (110) surface and the (110) is able to stabilize the hydroxide layer, as a crystalline phase would allow higher diffusion rate of species over an amorphous structure such as a α-$NiOOH_2$/γ-NiOOH. The change in Tafel slope value at high potential might arise of a diffusion controlled reaction inside the hydrous layer but not from the bulk electrolyte. The difference in the diffusion rate might explain why the (110) is electrochemically more active than the (111) and (100) surface at higher over-potential. Using large NiO specific area electrode e.g : nano-powder where specific area can reach up to several square meter per gram of catalyst would avoid to enter in diffusion limiting regime at high over-potential because of diffusion limitation of the active species in the hydrous layer.

Finally, as explained before, the lower Tafel slope observed on the (110) sample in comparison to the two other orientations at high overpotential could be due to the formation of the β-$Ni(OH)_2$ phase for the (110) sample and the α-$Ni(OH)_2$ phase for the (100) and (111) samples.

9.4 Conclusion

In conclusion, we have presented experimental results showing that oriented NiO thin films have noticeable differences in their electrochemical properties towards the oxygen evolution reaction. Electrochemical activity might be closely related to the hydroxide forming on top of each surface. The (110) orientation gives the highest electrochemical activity over the (111) and (100) samples at higher overpotential. Unexpectedly, low Tafel slopes are obtained at low overpotential. As there is no indication of surface contamination by iron, it could originate from defects present at the surface or/and at the grain boundaries. The (100) sample might present an inhomogeneous stoichiometry at the thin film contrary to the (110) and (111) prepared at higher oxygen concentration. Finally, we assume that the (110) surface might be able to stabilize $Ni(OH)_2$ in its β form. On the contrary, our (100) and (111) would produce on their surface the same but least active hydroxide, which might be the α-$Ni(OH)_2$ phase. The hydroxide would be present in lower quantity on the (100) surface than the (111) one.

CHAPTER 10

Nickel oxide thin films on silicon: structural assessment and evaluation towards the oxygen evolution reaction

Summary

This chapter aims at assessing the NiO thin film preferential crystallographic orientation according to the oxygen partial pressure and the temperature in the sputtering chamber when prepared on oxide-free silicon. The thin films are then studied electrochemically towards the oxygen evolution reaction.

The samples were prepared at UCL on oxide free silicon heavily p^+-doped (CZ, (100) oriented, 0.004-0.006 $\Omega\,cm$). During the thin film deposition, the stress developping in the thin film was measured in-situ. This systematic study aims at exploring NiO thin film surface properties when deposited on silicon according to the conditions of preparation, especially with respect to the use as catalytic layer for the OER.

10.1 Introduction

In Chapter 9, it has been found that, when prepared at high temperature, the (110) oriented NiO thin films would provide the best catalytic performance in comparison to the (111) and (100) oriented thin films. The least desired surface orientation being the (100) facet. The oriented NiO thin films were obtained on oriented platinum. However, for the production of a practical device, the starting surface is rarely ideal for favouring a specific surface orientation. For instance, in this thesis, the nickel oxide thin films are expected to be used either directly on silicon or on silicon/silicon dioxide surfaces.

In Chapter 8, the results evidence that the thin films prepared at high temperature and high oxygen concentration are more active towards the adsorption of species because of the introduction of defective sites on the surface. Moreover, in Chapter 4, it has been shown that higher defect concentrations are attained when the thin films are deposited at room temperature and high oxygen concentration. Thus, it could be interesting to explore further the electrocatalytic properties of highly defective NiO thin films at low temperature.

Therefore, the surface orientation of NiO thin films deposited on oxide-free heavily p^+ doped silicon has been explored in this chapter according to the oxygen concentration and the temperature in the chamber. The thin films were then characterized towards the oxygen evolution reaction (OER). The idea has been to determine the conditions, which favour the growth of the (110) orientation, or minimizing the surface density of the (100) surface, and to assess the catalytic properties of NiO thin films prepared at room temperature.

The choice of working on oxide free silicon surfaces was motivated by the fact that when this study was carried out, the condition for growing a thin tunnelling silicon dioxide layer on silicon was not addressed, and so an oxide free silicon surface ensured that charge transfer from the silicon to the NiO layer is not hindered. Moreover, the heavily p^+ doped silicon would suppress the formation of any barrier height at the Si/NiO interface and so would provide an ohmic contact at the interface.

10.2 In-situ stress measurements and XRD

10.2.1 Experimental

Nickel oxide thin films were prepared by reactive sputtering at UCL (for the condition of deposition see Section 3.1.2) where in-situ stress measurements (see Section 3.4.1) were performed on oxide free silicon substrates (see Section 3.2.1) heavily p^+-doped (CZ, (100) oriented, 0.004-0.006 Ω cm). The influence of the oxygen concentration and the temperature in the deposition chamber has been evaluated during the growth of thin film by in-situ stress measurements and X-Ray diffraction measurements at UCL (see Section 3.4.2). For NiO, the

relative weight of each peaks in a XRD spectrum is calculated as following:

$$R_{hkl} = \frac{K_{hkl} \int I_{hkl}}{K_{200} \int I_{200} + K_{111} \int I_{111} + K_{220} \int I_{220}} \tag{10.1}$$

where hkl are the Millers index, I to the intensity of the XRD peak and K corresponds to the correction of the intensity where K_{200}=1, K_{220}=0.48 and K_{111}=0.65 as determined in Figure 2.4 of the Section 2.2.1.

10.2.2 In-situ stress measurements at room temperature

During in-situ stress measurement, the stress is typically composed of two regimes: an initial regime (σ_{ini}) with a large instantaneous stress and a final regime (σ_{fin}) characterized by a lower instantaneous stress (Figure 10.1). The transition between the two regimes occurs generally around 20 nm.

The transition between the initial and the final stage of the thin film growth (delimited by the transition from high to low instantaneous stress) can be related to broken columnar grains perpendicularly to the direction of growth as ACOM-TEM measurements suggest (see Figure 5.4 in Chapter 5) which is particularly pronounced with high oxygen concentration in the deposition chamber. Thus, stress relaxation can arise as the stress from the early stage of the thin film growth does not propagate through the columnar structure because of the presence of in-plane grain boundaries.

In-situ stress measurements for the samples prepared at room temperature (Figure 10.2) show, for any sample, a large instantaneous compressive stress at any stage of the thin film growth. However, while initial instantaneous stress (σ_{ini}) increases from -1.2 GPa to -2.5 GPa with increasing oxygen concentration, the final instantaneous stress (σ_{fin}), though compressive, reaches a minimum around 17% of oxygen concentration (Figure 10.2, right). Variation can be noticed with the ageing of the nickel target, particularly concerning the final instantaneous stress, which tends to by strongly reduced with ageing of the target. Compressive stress can be related to: the lattice mismatch at the interface, impinging of energetic particle in the top 3 nm of the already formed thin film (shot-peening effects) [158], or an excess of adatoms at grain boundaries for high adatom surface mobilities [159]. On the contrary, tensile stress can be produced on surfaces having low surface free energy. In such case, this would generate in the early stage of the thin film formation the so-called Volmer-Weber growth zipping process [158, 160].

The observation that the final instantaneous stress is more affected by target ageing might be due to the formation of a racetrack overtime on the nickel target surface [223], and in our experiments at target end-of-life the racetrack was quite pronounced in the UCL chamber. Because of the racetrack, the surface area perpendicular to the axis of deposition is diminished. It means that ejected particles from the target surface would collide more before reaching the surface of the substrate and thus impinging of energetic particles

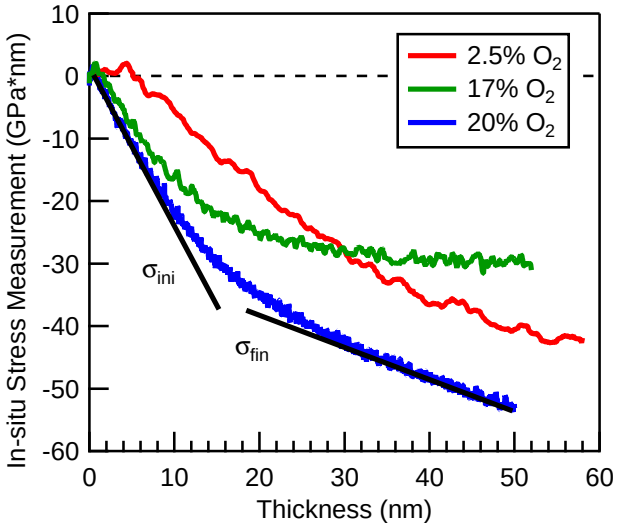

Figure 10.1: Raw in-situ stress measurements for the samples studied by TEM/EELS. Two stages are visible: the high instantaneous stress region where σ_{ini} is measured and the low instantaneous stress region where σ_{fin} is measured. The vertical arrow indicates the beginning of the stress evolution for the sample prepared with 2.6 % of oxygen.

is reduced with time [223].

Unlike the final instantenous stress, the initial instantaneous stress seems rather unaffected by target ageing. It would suggest that initial instantaneous stress is not, or to lesser extent, correlated with the amount of impinging particles.

When inserted in the chamber, the surface of the silicon is H-terminated and strongly hydrophobic. This would suggest the surface free energy to be extremely low. The substrate surface would have a poor wetting properties with any material deposited on top. Therefore, the Volmer-Weber growth mode should be favoured. Experimentally, initial instantaneous stress is triggered after a certain thickness and, in the elapsed time between the deposition start and the compressive stress development, no stress is measured. This is particularly visible with the 2.6% sample where compressive stress starts after 5 nm of deposited material (Figure 10.2, left).

Thus, it could be assumed that the surface free energy of the region between the silicon on the polycrystalline NiO thin film can be tuned according to the oxygen concentration in the chamber, and so the surface free energy would be increased with increasing oxygen concentration. This assumption can correlate with what has been reported in the literature for ZnO surfaces [224]. An higher surface free energy would increase the surface

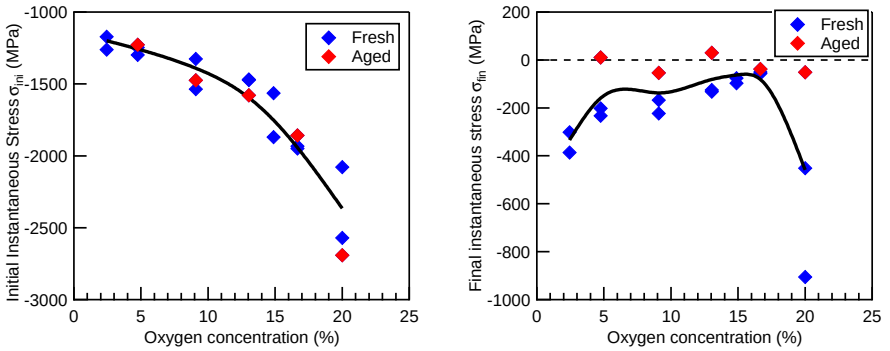

Figure 10.2: Left and right plots are about the initial instantaneous stress and final instantaneous stress, respectively, for thin films prepared at room temperature. In blue the data obtained from fresh nickel target and in red those from the aged target.

wetting properties of the interface towards the deposited thin film, meaning that the adatoms would have a lower surface mobility and layer-by-layer growth mode would be promoted at larger oxygen concentration. However, because of the large lattice mismatch of the substrate with the NiO rock-salt like structure, higher compressive stress in the initial stage of the thin film would be generated. On the contrary, lower oxygen concentration would promote high adatom mobility and islanding in the very early stage of the NiO thin film growth.

Eventually, the larger final instantaneous stress of the 20% sample over the 17% sample might be associated to defect spreading into the bulk of the grains as suggested by the HR-TEM/EELS measurements (see Chapter 5).

10.2.3 In-situ stress measurements and surface orientation

The properties of NiO thin films prepared at higher temperature (200°C and 350°C) have been evaluated with different oxygen concentration in the chamber at UCL. An overview of all the XRD patterns recorded is available in the Figure 10.3. For comparison, the relative weight of the intensity of each XRD peak for one spectrum is extracted and is displayed in Figure 10.4.

It can be observed, that while the (111) orientation dominates ($\sim$ 60%) at room temperature, but when prepared at 200 °C where it accounts for less than 30% of the weight intensity. At 350 °C, the (111) orientation weight strongly decreases from 70% to 20 % when the oxygen concentration in the deposition chamber is increased from 5% to 20%.

Meanwhile, the (100) and the (110) orientations are marginal at room temperature but the (100) orientation weight becomes more prominent with

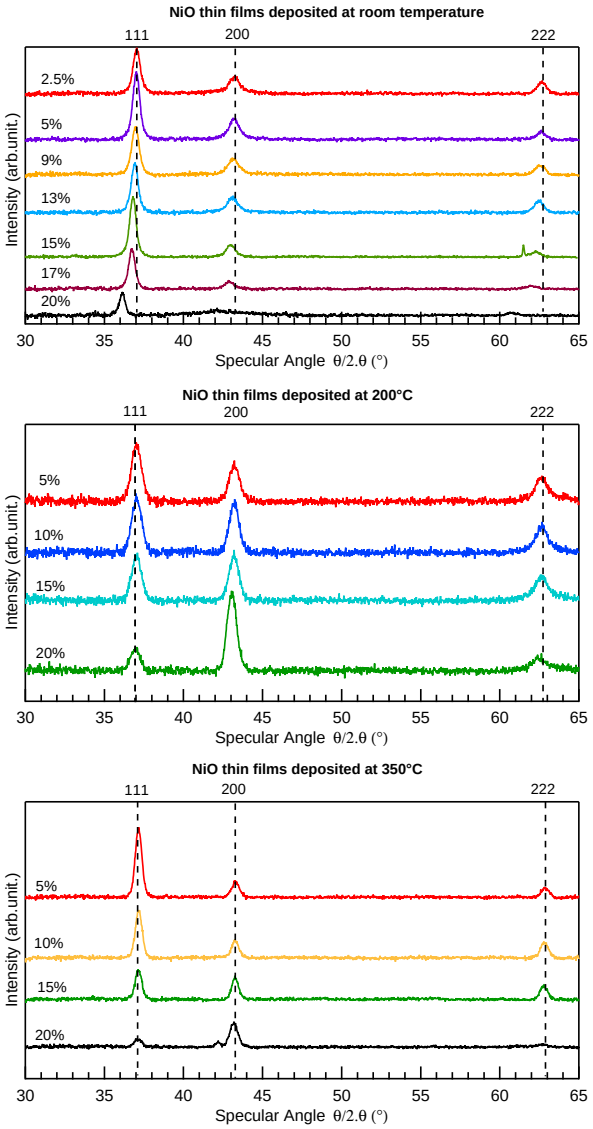

Figure 10.3: XRD patterns realized on NiO thin films deposited on oxide free silicon. The thin films have been deposited at room temperature (top), 200 °C (middle) and 350 °C (bottom). The oxygen concentration during sputtering is indicated in % in the left part of each plot.

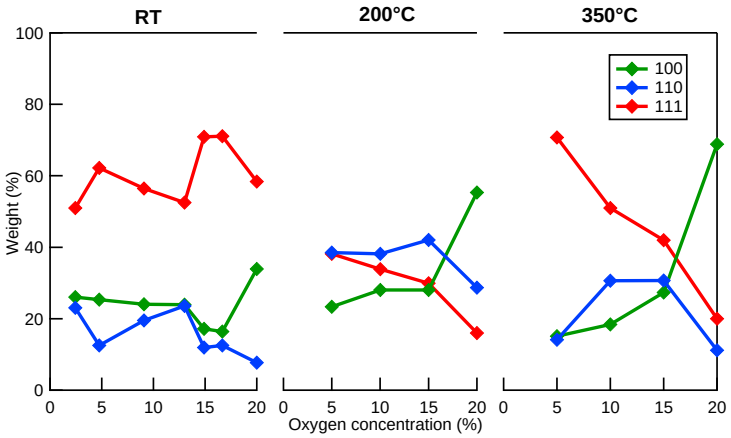

Figure 10.4: Relative (100), (110) and (111) weight determined from the XRD measurements of NiO thin films prepared on p^+-silicon. The weight of the peaks are evaluated by integrating the XRD peak intensities as described in equation 10.1.

temperature especially at large oxygen concentration. The (110) is found in larger quantity at intermediate conditions of deposition: 10-15 % oxygen in the deposition chamber and 200 °C. Eventually, as a rule of thumb, when NiO is deposited on (100)-silicon surface, it can be said that the (111) and (100) populations are inversely correlated: when the (111) dominates the (100) orientation is marginal and inversely.

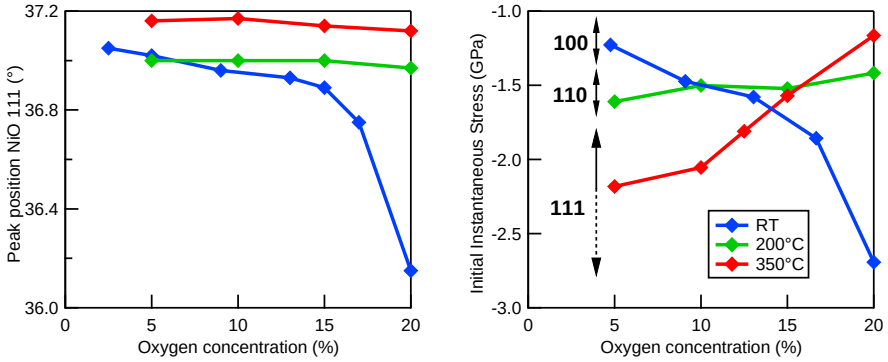

Figure 10.5: Peak deviation (Left plot) of the NiO (111) peak and initial instantaneous stress (Right plot) with oxygen concentration for thin films prepared at room temperature (RT), 200°C and 350°C. The data are derived from the XRD patterns displays in Figure 10.3

Considering the peak deviation of the (111) orientation on the XRD patterns (Figure 10.5, left), it can be seen that a larger peak deviation to lower

diffraction angles is attained with increasing oxygen concentration when deposited at room temperature. The trend suggests an increase of the inter-plane distance, which is compatible with the out-of-plane compressive stress measured with the MOSS setup for in-situ stress measurements (Figure 10.2).

During the experiments, a dependence has been noticed between the orientation of the deposited thin films measured by XRD and the initial instantaneous stress measured in-situ. For instance, when the (111) orientation dominates, it coincides with the highest initial instantaneous stress: at 350°C at low oxygen concentration and at room temperature (Figure 10.5 and Figure 10.4). Thus the (111) orientation dominates when the initial instantaneous stress is about -1.9 to -2.5 GPa. Inversely, a preferred (100) orientation is obtained when the initial instantaneous stress takes its lowest value (from -1.1 GPa to -1.4 GPa). Also when the (110) orientation dominates at 200°C, the initial instantaneous stress takes an intermediate value and only varies from -1.6 GPa to -1.4 GPa (Figure 10.5, right). Therefore, it can be concluded that dominantly (111) oriented thin films prepared on an oxide free silicon substrate are correlated with a large initial instantaneous stress (-2.2 GPa to -1.8 GPa), the (100) orientation prevails at lower initial instantaneous stress value (-1.3 GPa to -1 GPa) and the (110) orientation is favoured at intermediate initial instantaneous stress region (-1.7 GPa to -1.4 GPa)(Figure 10.5, right). This might be in-line with the fact that the surface energy of the polar (111) orientation is the highest followed by the non-polar (110) and the (100) orientation (see Section 2.2.1). The latter is supposed to be the most stable facet with the lowest surface energy value (see Section 2.2.1). Thus it could be said that the stress generated in the early stage of the thin film growth might promote a specific orientation.

10.3 Thin film characterization towards the OER

10.3.1 Experimental

Electrochemical performances of the NiO thin films deposited on p^+-silicon substrates have been evaluated towards the oxygen evolution reaction (OER). As described earlier, the samples were prepared by reactive DC sputtering at room temperature, 200 °C and 350 °C and the oxygen concentration in the deposition chamber could be varied from 3 % to 20 %. The NiO thin films were about 50 nm thick and all were polycrystalline randomly oriented although some orientations might dominate according to the condition of preparation (see previous section). Electrochemical setup is the one developed at UCL for OER characterization as detailed in Chapter 9.

10.3.2 Results

As seen in Figure 10.6 (left), the quasi-static plot shows that the samples prepared at room temperature provide similar catalytic properties. The Tafel slope at low overpotential ($<$ 1.55 V vs RHE as defined in Chapter 9) is about 30 mV/dec for any oxygen concentration during the deposition (Figure 10.6, right). In the high overpotential region ($>$ 1.55 V vs RHE as defined in Chapter 9) the best OER performance is obtained for the samples prepared with 17 % oxygen in the deposition chamber for which the Tafel slope is about (110) mV/dec.

The performances of the thin films are substantially degraded when the samples are heated during the fabrication (Figure 10.6, left). For instance, at high overpotential, the Tafel slope can reach up to 200 to 400 mV/dec where the lowest Tafel slope values are attained when the sample is prepared at high oxygen concentration in the deposition chamber (Figure 10.6, right).

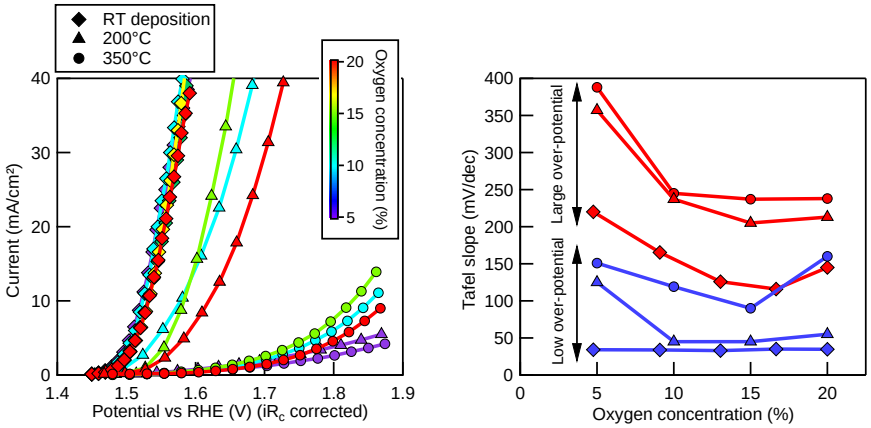

Figure 10.6: Left: Electrochemical IV curve obtained in quasi-static condition for the NiO thin films prepared on oxide free p^+-silicon according to the temperature (markers) or oxygen concentration (color scale). Right: Tafel slope either taken in the low or high overpotential region.

As seen in Chapter 4, low temperature and high oxygen concentration during the thin film deposition promote the inclusion of defects in the thin film. Therefore, as we observe that the OER performances are the best when the NiO thin films are prepared at low temperature or when prepared with high oxygen concentration during deposition, it is realistic to assume that the best OER performances can be obtained only by the introduction of defective sites on the surface of the thin films.

Taking the NiO thin films prepared at higher temperature, the low defect density in the thin film let the OER performances to rather be dominated

by the surface orientation. In our experiments, the XRD measurements show that the (110) orientation is prominent for samples prepared between 10-15 % oxygen concentration in the deposition chamber at 200°C and the (100) orientation particularly dominates for the sample prepared at 200°C and 350°C at 20 % oxygen concentration (Figure 10.4). Electrochemical measurements of heated samples prepared in 15-20 % of oxygen concentration, show better performance when the (110) orientation dominates either at low or high overpotential (Figure 10.6, right).

This can correlate with the finding of Section 9 that the (110) facet might provide the best orientation for the OER as it would stabilize the oxy-hydroxide it is β form. On the contrary, the (100) orientation is the least desired orientation for such reaction as it would promote the formation of γ-oxy-hydroxide, which is not the most electroactive hydroxide material for the OER. In addition, the (100) orientation provides a lower surface coverage of hydroxides in comparison to the other orientations, which would reduce even more its OER performances.

However, although the (110) facet could provide a base material for a more efficient OER reaction, the reaction is much more improved in the presence of a highly defective thin films as the one prepared at room temperature and high oxygen concentration.

It has to be mentioned that, even though not represented here, when assessed by XPS, the nickel hydroxide layer after the OER experiments is thicker for the NiO thin films prepared at room temperature in comparison to the sample prepared at high temperature. In Chapter 9, it has been assumed that at high over-potential, the electrode is subjected to mass transport limitation within the nickel hydroxide layer. Therefore, for the room temperature NiO thin films, at high over-potential, the mass transportation limitation could be reduced to a certain extent relatively to the NiO thin films prepared at high temperature. The analysis of the transitional regime of the quasi-static measurements with regards to the Cotrell equation (see Chapter 9), could have brought valuable information on the diffusion coefficient within the nickel hydroxide growing on top of the room temperature NiO thin films. However, this study has not been carried out at the time this manuscript has been submitted.

10.4 Conclusion

As measured by in-situ measurements, highly compressively strained thin films are obtained during the reactive sputtering of NiO on oxide free p^+-silicon. Two growth regimes were evidenced: the initial instantaneous stress regime and final instantaneous stress regime. Correlation could be obtained between the initial instantaneous stress and the preferred growth orientation during sputtering with the (111), (110) and (100) orientation dominating at high, intermediate and low initial instantaneous stress, respectively.

The NiO thin films provided best catalytic performance towards the OER when defects are introduced in the thin films particularly when prepared at room temperature and high oxygen concentration. This indicates that the OER requires a defective NiO material. Therefore, an efficient NiO based catalytic layer has to be prepared at room temperature while the surface orientation would have only a minor leverage on the optimization of the catalytic properties.

CHAPTER 11

Si/SiO_2 sample preparation and surface conditioning

Summary

This chapter deal with the fabrication and the surface conditioning of Si/SiO_2 samples in the aim of being implemented in tunnelling MIS structures. Thin tunnelling silicon dioxide layers (< 2.5 nm) have been thermally grown in a furnace at UCL. The best conditions for growing a SiO_2 layer on silicon fulfilling the specifications consisted in a thermal cycle at 1000 °C in nitrogen without annealing period. It has been assumed that the oxygen participating in the SiO_2 process originate from furnace wall desorption. In the purpose of being used in the DAISY-MAT system of TU-Darmstadt, specific surface conditioning procedure has been developed. Thus, after having assessed different methods, surface cleaning and surface passivation has been realized by exposing the samples to a hydrogen plasma source. The effectiveness of the passivation of the Si/SiO_2 samples is assessed by in-situ XPS/UPS measurements but also by electrochemical measurements in dark and under light. The interpretation of the electrochemical experiments could unveil the presence of a donor state in the silicon bandgap.

In addition to the growth of SiO_2 on top of silicon and the conditioning of the Si/SiO_2 samples, the preparation by ALD deposition and the conditioning of an thin alumina overlayer (< 1 nm) has been assessed.

11.1 Growth of silicon dioxide

11.1.1 Introduction

As detailed in the methodology part (see Section 3.2), a furnace calibration was necessary in order to figure out the right parameters to obtain a high quality tunnelling silicon dioxide layer on silicon. The silicon dioxide layer was choosen as buffer layer between the silicon and the front contact as Si/SiO_2 produces a high quality interface with a low defect states density (see Section 2.3.3). However, the silicon dioxide layer has to be thin enough to allow charge tunnelling from the semiconductor to the electrode.

11.1.2 Experimental

Silicon dioxide growth is realized on n-type FZ-silicon single crystal (100) wafers, chemically cleaned (see Section 3.2.1), for which the sheet resistivity is 10.1 Ω cm (determined with a van der Pauw method). Therefore, the doping concentration is estimated to be 4.4×10^{14} /cm^3 and so the Fermi level position is calculated to be 0.834 eV above the valence band maximum.

After the chemical surface cleaning, the silicon wafers are supposed to be H-terminated, and were immediately inserted in a Koyo VP1000 furnace (see Section 3.2.3). Heating and cooling period are realized in dry nitrogen at 10 °/min. Different program has been assessed where duration and the atmosphere for annealing period are varied in order to evaluate the parameters which influence the silicon dioxide thicknesses and properties. The atmosphere during the annealing period is in any case a dry gas which can contain a certain amount of oxygen. The quantity of oxygen could be intentionally set but, as it will be seen in the following part, it could originate from furnace wall desorption.

The quality of the silicon dioxide layer was then assessed by XPS at the UCL with an Al K-α monochromatic X-Rays source ($h\nu$=1486.6 eV) with an electron angle exit of 55 ° between the normal of the sample surface and the analyser.

The in-situ XPS measurements of the Si 2p region display typical features, which can be associated to the silicon and the silicon dioxide layer, distinctively. As seen in Figure 11.1 (left), the elemental silicon (Si^0) peak is in the low binding energy part of the Si 2p region, while at higher binding energy, the photo-emission from the silicon of the SiO_2 layer (denoted Si^{IV}) can be observed. It should be mentioned that the peak related to the elemental silicon (Si^0) is made of a double feature: the photo-emission of the Si 2p(3/2) orbital (the main peak) and the Si 2p(1/2) spin-orbit split components orbitals.

The silicon dioxide thickness was determined by the comparison of the photoemission intensity of the Si^{IV} and the Si^0 peaks in the Si 2p region (see Figure 11.1, left). Taking the Inelastic Mean Free Path (IMFP) of the

Si 2p photoemitted electrons through the silicon (λ^{Si}) and the silicon dioxide (λ^{SiO_2}), it is possible to determine accurately the thickness of the silicon dioxide layer [225, 226]. The formula used to determine the SiO_2 thickness was:

$$\frac{I_{Si^0}}{I_{Si^{IV}}} = \frac{C^{Si}\,\lambda^{Si}}{C^{SiO_2}\,\lambda^{SiO_2}} \frac{\exp\left(-\frac{t_{SiO_2}}{\lambda^{SiO_2}\cos(\alpha)}\right)}{1-\exp\left(-\frac{t_{SiO_2}}{\lambda^{SiO_2}\cos(\alpha)}\right)} \tag{11.1}$$

where I is the integrated intensity of the XPS peaks in the Si 2p region, C the atomic density of silicon, λ the inelastic mean free path of photoemitted electron in the Si 2p region, α the angle of the analyser with the normal of the sample surface and t_{SiO_2} the silicon dioxide thickness. The uppercase element is related to the layer which is considered, either the silicon wafer or the silicon dioxide.

11.1.3 Results and discussion

After the thermal cycle in the furnace, the silicon oxide thickness was estimated by XPS at UCL by evaluating the relative area of the Si^0 and the Si^{IV} peak [225] as detailed in the experimental part above. As the samples were contaminated by surface exposure to air and as it could not be cleaned in a proper way in the XPS chamber at UCL, the absolute Si^0 peak position could not be used for any quantitative assessment. However, the peak distance ΔSi 2p, corresponding to the distance between the Si^0 and Si^{IV}, was assessed (Figure 11.1, left) and plotted against the SiO_2 thickness. The result, as displayed in Figure 11.1 (right), suggests that ΔSi 2p increases primarily with the SiO_2 thickness and no significant dependence on annealing temperature is observed. Indeed, as seen in Figure 11.1 (right), for samples prepared at 1000°C, thickness and distance between the two peaks is relatively close to the samples prepared at lower temperature (700-800 °C). This indicates that the SiO_2 properties when assessed by XPS is the same when the SiO_2 is grown at 700°C and at 1000°C.

As seen in Figure 11.1 (left), longer annealing periods were required at lower temperature to reach a given thickness. However, as for the temperature of annealing, the annealing period is not estimated as a critical parameter in the XPS fingerprint of the silicon dioxide layer although it can determine the thickness of the layer. Also, the concentration of oxygen did not appear to be critical as it only affects the SiO_2 growth rate (higher oxygen concentration increases the growth rate).

Thus, the samples prepared at 1000°C were not annealed under oxygen but only in dry nitrogen (it is believed that oxygen desorbs from the furnace wall) and is realized without any annealing period. It turns out that the SiO_2 thickness is thin enough ($\sim$ 2.5 nm), compatible with the targeted application. Similar XPS fingerprint to the sample prepared at 1000 °C was obtained when the sample is prepared at lower temperature for a given thickness. It means, there could be two ways for producing a tunnelling SiO_2 layer, either the SiO_2

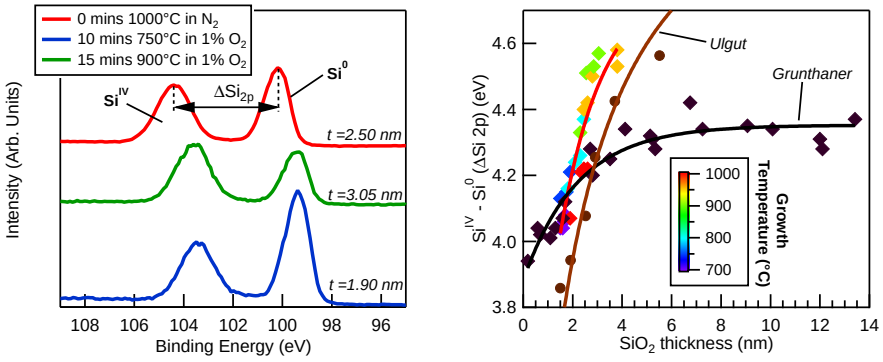

Figure 11.1: Left: Typical XP spectra of the Si 2p region (obtained at UCL). Two parts are evidenced: the photoemission from the silicon dioxide layer (Si^{IV}) and the photo-emission from elemental silicon Si^0 (the silicon wafer). The distance $\Delta Si\,2p$ between the Si^{IV} and the Si^0 peaks and the thickness of the silicon dioxide layer are evaluated from these measurements. Right: $\Delta Si2p$ versus silicon dioxide thickness. Coloured dots are measured during furnace calibration at UCL, in black are data taken from Grunthaner et al. [227] and in brown from Ulgut et al. [228].

layer is growth at high temperature in nitrogen without annealing period or it can be grown at low temperature with optionally both a small amount of oxygen and an annealing period.

However, literature provides some reports asserting that the higher the temperature the better the SiO_2 quality [132]. Therefore, although XPS measurements do not show an obvious difference in quality between the samples prepared at low or high temperature for a given SiO_2 thickness, it has been preferred to carry out the SiO_2 growth at 1000°C.

As reported in literature, photoelectron spectroscopy measurements on thin Si/SiO_2 interfaces highlight a film thickness dependence of ΔSi 2p [227–229]. However, the relationship between ΔSi 2p and the silicon dioxide thickness might depend on the Si/SiO_2 sample conditioning before the XPS measurements. As illustrated in Figure 11.1, similarly to Ulgut *et al.* [228], the evolution of ΔSi 2p with SiO_2 thickness is steeper for our batch of sample, in comparison to what was obtained by Grunthaner *et al.* [227]. The experiments of the latter consisted of chemical depth profiling of a thick SiO_2 layer, grown thermally on silicon, by diluted HF, followed by a cleaning step in ethanol, whereas our sample and the one of Ulgut *et al.* were characterized by XPS after being exposed to air and all impurities. With their results, Grunthaner *et al.*, defined two regions: the first region of a SiO_2 thickness of 0-30 Å is characterized by an increasing ΔSi 2p peak distance, while the second region in the 30-60 Å range is characterized by a constant peak distance ΔSi 2p value of 4.3 eV. They proposed that the first region corresponds to a highly disordered and strained layer, which might be

accompanied by the presence of under-coordinated Si^{3+} atoms. The second region would correspond to a more stoichiometric SiO_2 layer.

However, as described in Section 2.3.3, their assumption is discarded by more recent works, which suggests that the chemical transition between silicon and silicon dioxide is only few atomic layer thick [116]. In this thesis, we propose that the increase of the ΔSi 2p peak distance with thickness could alternatively be explained by the presence of an electric field as it will be discussed in Chapter 12.

11.2 SiO_2 surface cleaning and passivation

11.2.1 Introduction

As described before, samples used for Si/SiO_2 interface experiments in the DAISY-MAT system are prepared in a furnace at UCL. Their exposition to air during storage and transportation is then unavoidable. Various contaminants (hydrocarbons, hydroxides) are then found on the surface, which have to be removed in order to carry out interface experiments on controlled surfaces to reduce uncertainties and to improve reproducibility. Looking more into details of the XP spectra of the Si 2p region, one can notice differences in the Si^0 and Si^{IV} peak positions with regards to the cleaning method. In particular, the distance ΔSi 2p and the Si^0 peak position is of main interest. Calculated flat-band positions, where no charge accumulation (negative or positive) occurs at the silicon surface, has been calculated to be 99.574 eV in taking a Si^0 to the VBM distance of 98.74 eV [230]. It can be assumed that, if the Si^0 peak position deviates from the calculated flat-band position, the surface is charged and so surface conditioning is not ideal. Also, it is important that removal of the surface contamination has no detrimental effect on the interface quality, especially concerning energy trap levels. So an effective cleaning process, additionally to remove surface contamination has to preserve the sample surface quality and integrity. Therefore, three methods to clean up the surface have been employed and compared, where two of them relied on plasma exposure (see Section 3.2.4).

11.2.2 Experimental

Silicon dioxide growth is realized on n-type FZ-silicon single crystal (100) wafers, chemically cleaned (see Section 3.2.1), for which the sheet resistivity is 10.1 Ω cm (determined with a van der Pauw method). Therefore, the doping concentration is estimated to be 4.4×10^{14} /cm^3 and so the Fermi level position is calculated to be 0.834 eV above the valence band maximum.

After the chemical surface cleaning, the silicon wafers are supposed to be H-terminated, and were immediately inserted in a Koyo VP1000 furnace (see Section 3.2.3). Heating and cooling period are realized in dry nitrogen at 10 °/min. The thermal cycle is totally realized in dry nitrogen without

any annealing period where the SiO_2 layer is estimated to be 2.5 nm (see the previous section).

Surface conditioning of the Si/SiO_2 samples prepared in the furnace at UCL were realized in the DAISY-MAT system to be then, in particular, studied by in-situ XPS measurements. The three methods for the Si/SiO_2 surface preparation were the following:

- **Thermal surface treatment in Oxygen:** Although it is a slow reaction, the combination of heat (200 °C - 600 ° C) and oxygen (1-2 Pa) in one of the UHV chambers connected to DAISY-MAT could burn hydrocarbon species and remove hydroxides from the surfaces [231]. The surface treatment can take up to 2 or 3 h to totally suppress the carbon peaks in the XPS surveys (Figure 11.2). The reaction between the carbon and the oxygen likely produce carbon dioxide and water (CO_2, H_2O).

- **Oxygen plasma exposure:** highly reactive neutral particles (radical, O_3 ...) are created if oxygen is used in the plasma chamber. The oxygen plasma treatment is effective to remove carbonacious contaminants at both room and high sample temperature (Figure 11.2). However, if the treatment is realized at room temperature, the sample needs to be annealed to remove possible peroxides created on the SiO_2 surface. As for the annealing process, oxygen plasma removes adsorbated hydrocarbon contamination from the surface by forming likely carbon dioxide and water molecules (CO_2, H_2O).

- **Hydrogen plasma exposure:** substituting the oxygen by hydrogen, one can obtain a hydrogen plasma by cracking dihydrogen molecules. Hydrogen radicals are likely produced during the process, which react with the hydrocarbons on the sample surface to form methane and water (CH_4, H_2O). However, heat needs to be brought to sustain the reaction. If realized at room temperature, the hydrogen plasma had little effect on the cleaning. In contrast, ten minutes exposure at 200 °C to hydrogen plasma is sufficient to remove completely any traces of carbon from the sample surface (Figure 11.2). Moreover, as reported in literature (see Section 2.3.3), the Si/SiO_2 surface can be passivated by hydrogen and in particular it can be realized if the Si/SiO_2 surface is exposed a longer time and at higher temperature to a hydrogen plasma source. Thus a possibility of passivating the Si/SiO_2 surface with hydrogen has been also evaluated (more details in Section 3.2.4).

11.2.3 Results

XPS surveys

As it can be seen in Figure 11.2, after each treatment, no trace of carbon can be found in comparison to the ex-situ sample and only peaks of oxygen and silicon from the Si/SiO_2 sample are visible.

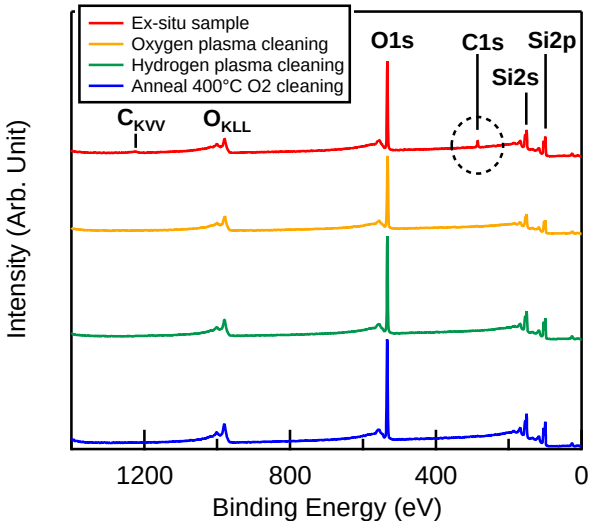

Figure 11.2: XPS surveys of Si/SiO_2 surfaces for an ex-situ sample and samples exposed to different surface cleaning. The ex-situ sample shows carbon contaminations while the cleaned samples are free of any contamination. The carbon peak in the XPS survey is removed by the cleaning.

Thermal surface treatment in Oxygen

XP spectra of the Si 2p regions after thermal cleaning of the Si/SiO_2 sample are displayed in Figure 11.3. Although the method helps to remove carbon contaminants, the ΔSi 2p distance is rather unaffected and the Si^0 peak position still deviates to higher binding energy. This means that positive charges are still present on the surface. The annealing reduces the Si^0 peak position to lower binding energy but not enough to reach flat band position. The reason might be that carbon species are still present on the surface but in such low quantity that they are not detectable by XPS. Annealing the sample in oxygen can be ineffective and time-consuming for removing the carbonacious contaminants, though it might be smooth and harmless to the sample surface. Finally, thermal surface cleaning has been considered as a not acceptable surface treatment for the purpose of the upcoming experiments.

Oxygen plasma exposure

On Figure 11.4 (left), typical XP spectra of the Si 2p region are displayed after oxygen plasma cleaning and after a post-annealing treatment. Directly after the oxygen plasma exposure, a drastic decrease of the ΔSi 2p distance from 4.5 eV to 3.9 eV is observed while the Si 2p peak position deviates from the flat-band position to lower binding energy ($\sim$ 0.1 eV) after plasma exposure. This might originate to the presence of negative charges trapped in or on the silicon dioxide surface after the oxygen plasma treatment, which would lead to the formation of a hole accumulation region in the silicon at the Si/SiO_2 interface. The

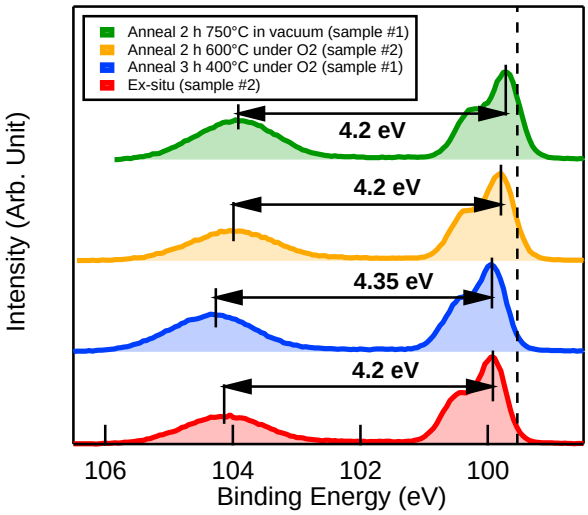

Figure 11.3: XPS spectra of the Si 2p region before and after annealing of the sample under oxygen at different temperature and exposure time. The vertical dashed line represents the calculated flat-band position.

negative charges might be due to the presence of peroxide species O^- left on the SiO_2 surface after the oxygen plasma exposure. When the sample is annealed, the ΔSi 2p distance retrieves larger value and the Si 2p peak position is found closer to the calculated flat-band position. This might arise from desorption of the peroxo species formed during the plasma treatment, which will reduce the amount of negative charge on the silicon dioxide surface. Therefore, the XP spectra indicate that the oxygen plasma cleaning followed by a annealing step enables to attain flat-band condition.

Hydrogen plasma exposure

Similar to the thermal cleaning in oxygen and the oxygen plasma cleaning methods, the hydrogen plasma cleaning method is a suitable method to get rid of carbon contamination (Figure 11.2). Figure 11.4 (right) shows XP spectra recorded in-situ after the surface treatment. It can be seen that the peak distance varies relatively little after hydrogen plasma cleaning, while the Si^0 peaks approaches flat-band position. Exposing the same sample a second time for a longer period of time ($\sim$ 45 min) and at higher temperatures ($\sim$ 350 °C) to the hydrogen plasma, an additional shift of the Si^0 peak position to lower binding energy is induced, finally getting very close to the calculated flat-band position. In comparison, the XP spectra of a HF cleaned silicon sample, which is supposed to be H-terminated and so passivated [232], provides a Si^0 peak position rather aligned to the one of the hydrogen passivated Si/SiO_2 sample.

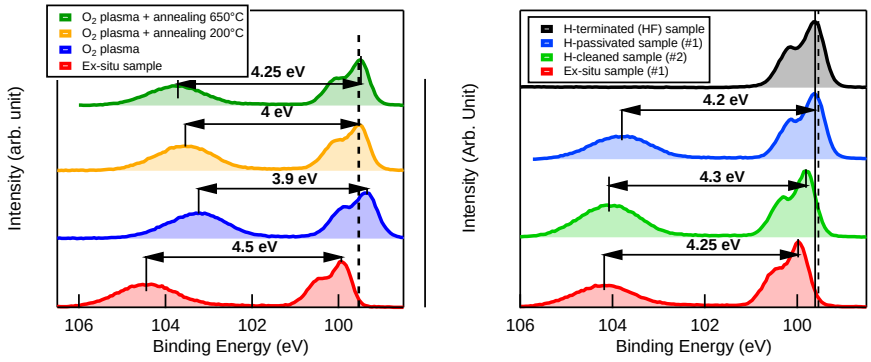

Figure 11.4: Left: XPS spectra of the Si 2p region before and after exposure to the oxygen plasma realized at RT and when samples are annealed afterwards at different temperature. Right: after surface cleaning by exposing the surface to a hydrogen plasma source and after hydrogen passivation. In black, a H-terminated sample is shown for comparison (Note the absence of Si^{IV} peak). The vertical dashed line represents the calculated flat-band position.

11.2.4 Discussion

Figure 11.5 provides an overview of the ΔSi 2p peak distance in relation to the Si^0 peak position. Ex-situ Si/SiO_2 samples are found to the very left of the plot and are about 0.4 eV to higher binding energy than the calculated flat-band position. It would mean that surface contaminants bring positive charges attracting electrons to the surface of the silicon (downward band bending in silicon). Surface cleaning, which removed carbonacious and hydroxide contaminants, shifts the Si^0 to the right and reduces the ΔSi 2p peak distance. Hydrogen plasma treated surfaces, after surface passivation, are less scattered and show Si^0 peak positions close to the calculated flat-band position.

Thus, the surface cleaning with a hydrogen plasma has the advantage to be non-destructive to the sample surface while removing effectively carbonacious species and further exposure at higher temperature leads to the surface passivation by atomic hydrogen. As detailed in Section 3.2.4, this method is in-line with literature where Si/SiO_2 sample passivation is traditionnaly obtained by the implantation of atomic hydrogen at high temperature in the SiO_2 layer [103, 104, 122].

As passivation by the introduction of atomic hydrogen in the Si/SiO_2 has been already reported in the literature, it has been decided that surface cleaning and surface passivation of the samples will only be realized by surface exposition to the hydrogen plasma source in the DAISY-MAT system. In the rest of this thesis, hydrogen passivation of the surface will be directly refereed with the term *passivation* and hydrogen passivated surfaces will be refereed as

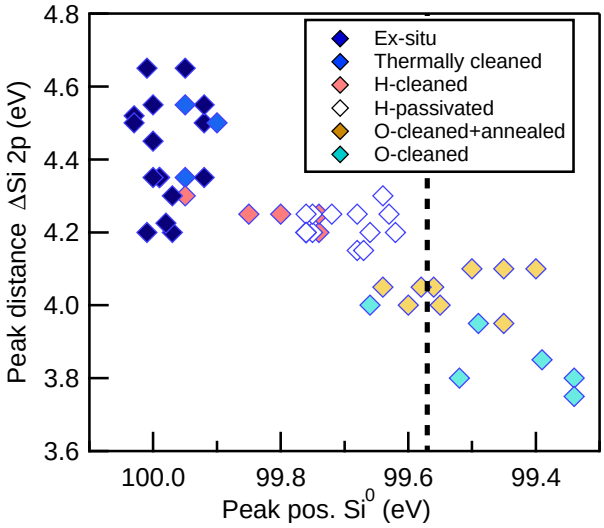

Figure 11.5: Compilation of the $\Delta Si\,2p$ peak distance according to the Si^0 peak position for different Si/SiO_2 surface preparation. The vertical dashed line represents the calculated flat-band position of the Si^0 main peak.

passivated surfaces following the procedure detailed in Section 3.2.4.

11.3 UPS characterization of the SiO_2 and the Al_2O_3 surfaces

11.3.1 Experimental

UPS measurements have been realized in the DAISY-MAT system (see Section 3.3.1) on surface cleaned but non-passivated Si/SiO_2 sample, passivated Si/SiO_2 sample and passivated Al_2O_3 layer grown at 50°C by ALD as detailed in Section 3.2.5 under two different conditions: without electron exposure and with electron exposure from an electron gun during UPS measurement.

As detailed previously, the SiO_2 layer is grown thermally at 1000 °C in dry nitrogen in a furnace without annealing period on n-type silicon where the overall thickness is estimated by XPS to be about 2.5 nm. The thickness of the Alumina layer is about 1 nm. For the preparation of the passivated SiO_2 the reader is invited to read the previous ssections of the chapter and for the preparation of the alumina layer to read Section 3.2.5 and Appendix A.3.

11.3.2 Results and discussion

Figure 11.6 and Table 11.1 present the different results of the experiments. The experiments emphasize in particular the presence of an additional contribution

at 15.2 eV in the UP spectra, for which the intensity is sensitive to electron exposure, especially for non-passivated SiO_2 surface (Figure 11.6, left). The decrease in intensity of the additional peak at 15.2 eV after hydrogen passivation is not understood but it can be taken as a clue that surface hydrogen passivation modifies the electronic structure of the silicon dioxide. The SiO_2 surface properties before and after hydrogen passivation varies only slightly. Thus, the workfunction and the valence band maximum for the SiO_2 surface are about $\sim$ 4.8 eV and $\sim$ 5.5 eV, respectively.

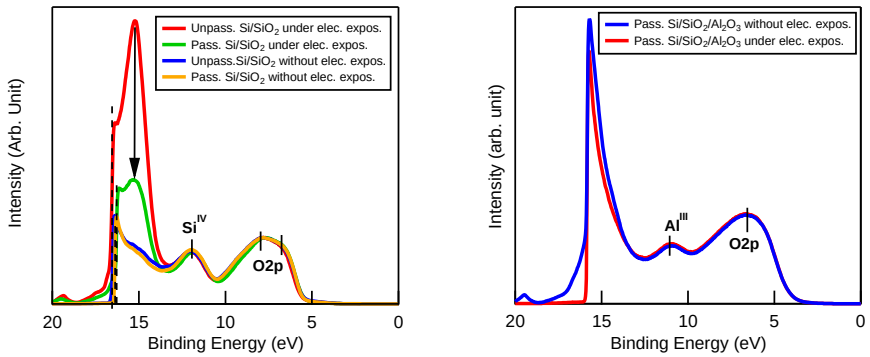

Figure 11.6: UPS measurements realized with He I (21.22 eV) exposure for different surface composition (SiO_2, Al_2O_3), preparation (passivated and non-passivated) and condition of measurement (with or without surface exposure to electron bombardment). The results with the SiO_2 sample are shown on the left and with Al_2O_3 samples on the right.

Regarding the passivated Al_2O_3, no particular change can be noticed when the sample is exposed to the electron beam. VBM ($\sim$ 4.1 eV) and workfunction ($\sim$ 5.4 eV) are unchanged and the UPS profiles are similar for both measurement conditions (Figure 11.6 and Table 11.1). The interfacing of a passivated SiO_2 surface and a passivated Al_2O_3 surface might lead to a valence band offset $\Delta_{VBM} = VBM_{Al_2O_3} - VBM_{SiO_2}$=0.4 eV. The Alumina layer provide a higher workfunction ($\sim$ 5.4 eV) than the SiO_2 surface ($\sim$ 4.8 eV), the implication of such difference is not very clear at this stage. However, as alumina cannot accept mobile charge, the creation of an electron depleted layer in the silicon, as it would be the case if a large workfunction metal (e.g.: Platinum) is contacted on Si/SiO_2, is unlikely. Maybe, in the case that two insulators with different workfunction are contacted, the difference in workfunction is compensated by the transfer of chemical compounds (e.g.: cations, Oxygen...) at the interface but not by the transfer of mobile charges.

Table 11.1: Extracted parameters from Figure 11.6 when the samples are not exposed electron.

Surface	Workfunction (eV)	Valence Band Maximum (eV)
Non-passivated Si/SiO_2	4.7	5.5
Passivated Si/SiO_2	4.8	5.5
Passivated $Si/SiO_2/Al_2O_3$	5.4	4.1

11.4 Electrochemical characterization of non- and passivated Si/SiO_2 samples

11.4.1 Experimental

Silicon dioxide growth is realized on n-type FZ-silicon single crystal (100) wafers, chemically cleaned (see Section 3.2.1), for which the sheet resistivity is 10.1 Ω cm (determined with a van der Pauw method). Therefore, the doping concentration is estimated to be 4.4×10^{14} /cm^3 and so the Fermi level position is calculated to be 0.834 eV above the valence band maximum.

After the chemical surface cleaning, the silicon wafers are supposed to be H-terminated, and were immediately inserted in a Koyo VP1000 furnace (see Section 3.2.3). Heating and cooling period are realized in dry nitrogen at 10 $^\circ$/min. The thermal cycle is totally realized in dry nitrogen without any annealing period where the SiO_2 layer is estimated to be 2.5 nm (see the previous section).

Electrochemical characterization of passivated and non-passivated Si/SiO_2 samples were performed in 0.1 M KOH solution. The experiments were simple and were made, in a first stage, of a Cyclic Voltametry (CV) experiments at various sweep rate from 0.1 to 1.1 V vs RHE and, in a second stage, of an Open Circuit Voltage (OCV) measurement for two minutes. Experiments are repeated in the dark and under light using an electrochemical solar simulator setup at TU-Darmstadt (see Section 3.3.2).

The samples were back-contacted by platinum deposited by sputtering on a n^+ rich region obtained by phosphor diffusion (see Section 3.2.2). This kind of structure ensures the formation of an ohmic junction.

11.4.2 Results and discussion

Presence of a donor state

Looking at the CV measurements realized in the dark, a feature can be observed between 0.6 and 0.8 V vs RHE (Figure 11.7, left). The total number of charges associated to this feature, estimated by Coulombic integration, is about 1.03-1.35$\times 10^{12}$ charges per cm^{-2} for the non-passivated Si/SiO_2 sample, whereas, in comparison, the passivated sample provides almost two times less charges with 6-6.7$\times 10^{11}$ charges per cm^{-2}.

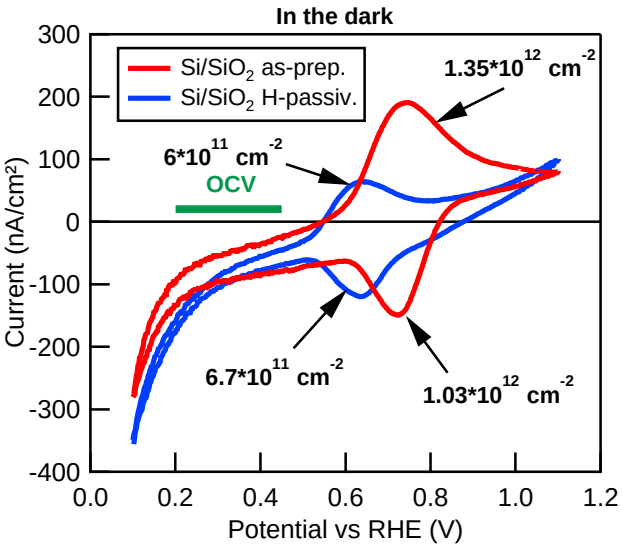

Figure 11.7: Cyclic voltametry results realized in the dark at 100 mV/sec with a passivated (blue) and non-passivated (red) sample.

When passivated, the measured density of charges would be equivalent, in average, to about 1 charge every 10-20 nm on the surface. This is a rather low value if the feature is related to an electrochemical absorption process. Moreover, peak-to-peak distances of the oxidation wave and reduction wave for each sample is about 8 to 14 mV. Typical electrochemical reaction would provide at the minimum the theoretical peak-to-peak distance separating the anodic to the cathodic reaction, which is 57 mV [233]. This value is only valid for a reversible one electron charge transfer and in the case there is no ohmic drop in the electrolyte [233], so, in reality, this value should be even larger. Thus, very likely, the feature we observe on the left plot of Figure 11.7 can be associated to a fast charge exchange between a defect level at the interface region and the silicon. The OCV measurements in the dark provide values situated to the left of the observed feature (Figure 11.7). It can be assumed that, in a normal state, the defect level is filled (reduced state).

Therefore, the feature observed during the CV measurements (Figure 11.7) can be likely related to defect levels located at the Si/SiO_2 interface, which can be ionized following the reaction: $D \rightarrow D^+ + e^-$ or $D^- \rightarrow D + e^-$ during the forward sweep in Figure 11.7. The reverse process would occur during the backward sweep and can be related to a reduction reaction (Figure 11.7).

In Chapter 12, the in-situ XPS measurements realized on passivated Si/SiO_2 surfaces show that a strong positive electric field is formed through the SiO_2 layer. This electric field has been associated to the ionization of the donor states, which results, in the presence of positive charges at the Si/SiO_2 interface, facing negative charges in the outer SiO_2 layer. This explanation would match better the ionization of interface states following the reaction $D \rightarrow D^+ + e^-$, which results in the separation of positive fixed charges and negative mobile charges.

Effectiveness of surface passivation

When cyclic voltametry is performed under light, a larger current density is obtained when the Si/SiO_2 sample is passivated (Figure 11.8, left). Having evidenced the presence of a defect state in the dark, for which the density is reduced after passivation, the larger current density measured under light could be explained by a reduced electron-hole pair recombination at the Si/SiO_2 interface. This result indicates that the hydrogen plasma passivation is beneficial for the interface quality as it would reduce electronic trap states.

Finally, when OCV measurements are carried out either in the dark or under light (Figure 11.8, right), the non-passivated sample shows a charging behaviour: the potential constantly decreases with time whereas the passivated sample is extremely stable. Moreover, the OCV of the non-passivated sample under light shows a higher potential value than in the dark, which is opposite to what is expected. The OCV experiments indicates that the non-passivated Si/SiO_2 sample is continuously charging. The OCV might be determined by charges accumulating at the interface. On the contrary, the OCV of the passivated Si/SiO_2 sample decreases under illumination. The measurements are much more stable with no evidence of charging phenomena (Figure 11.8, right). Therefore, as for the cyclic voltametry experiments (Figure 11.8, left), the OCV experiments highlight a better response of the hydrogen passivated Si/SiO_2 sample in the dark and under light excitation.

Band-diagram at the Si/SiO_2/electrolyte interface

Taking an electron vacuum energy equal to -4.5 eV [135] against the normal hydrogen electrode (pH=0) and an ionization coefficient of -0.06 eV/pH [135], at pH=13 the electron vacuum energy would be situated at -3.72 eV from the reference hydrogen electrode. Therefore the electrochemical feature at 0.6-0.8

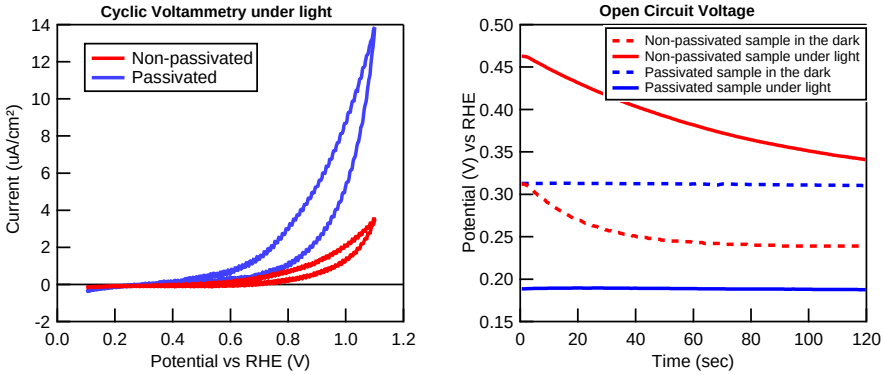

Figure 11.8: Left: Cyclic voltametry results realized under light at 20 mV/sec with a passivated (blue) and non-passivated (red) sample. Right: OCV experiments realized on non-passivated (red) and passivated sample (blue). Dashed line are experiments realized in the dark and full line under light. Experiments under light are always realized before the measurements in the dark.

V vs RHE in Figure 11.7 is at around 4.3-4.5 eV from the electron vacuum energy. The workfunction of our n-type silicon has been determined as being at 4.32 eV from the electron vacuum energy. Comparing the position of the electrochemical feature position with the n-type silicon workfunction, it can be said that the electrochemical feature is situated under the Fermi energy as represented in Figure 11.9. A filled donor state condition can be supported by the fact that before the cyclic voltammetry, the OCV is about 0.25 to 0.45 V vs RHE (Figure 11.8) which is at lower potential than the electrochemical feature observed in Figure 11.7.

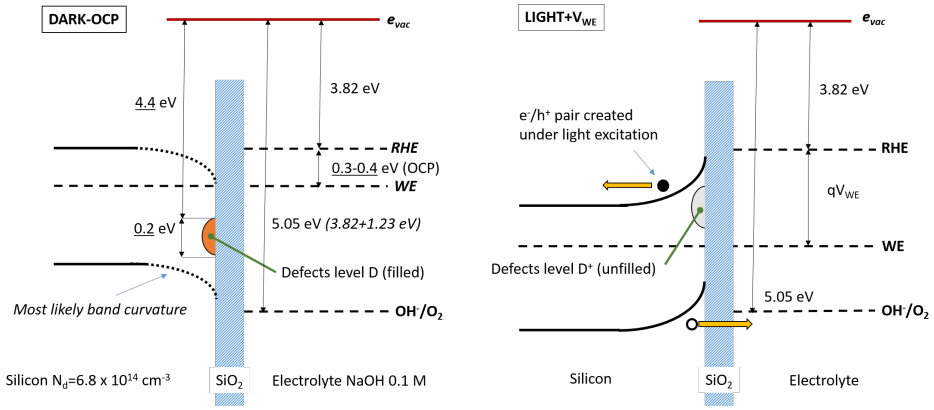

Figure 11.9: Band-diagram when the Si/SiO_2 sample is immersed in a 0.1 M NaOH solution. Left: in the dark in equilibrium. Right: Under light excitation during potential polarization of the working electrode($+V_{WE}$), which induces an ionization of the defect states at the Si/SiO_2 interface and an upwards band-bending in the silicon. All values are given against the electron vacuum energy. The underlined values were determined from the electrochemical measurements while the others are calculated from literature. The electron vacuum energy in the electrolyte is taken as reference.

11.5 Conclusion

SiO_2 layer on top of n-type silicon is obtained by thermal cycle in a furnace at 1000 °C, in dry nitrogen and without annealing step. The resulting SiO_2 layer is about 2.5 nm and is expected to be tunnel-compatible.

Surface cleaning and surface passivation of the Si/SiO_2 sample is performed by exposing the surface of the sample to an hydrogen plasma source according to the procedure detailed in Section 3.2.4. This surface treatment ensures the conditioning of the Si/SiO_2 surfaces for the reproducibility of the experiments.

In addition, the electrochemical measurements proved the effectiveness of the hydrogen passivation process, especially when exposed to a source of light. This can also be put in perspective with the change in the electronic structure of the UPS spectra between non-passivated and passivated Si/SiO_2 surface when exposed to an electron source.

Finally, the electrochemical characterization of the Si/SiO_2 samples could indicate the presence of a donor state in the silicon bandgap at the Si/SiO_2 interface. In order to match the in-situ XPS study of Chapter 12, the reaction of the ionization of the donor state has been assumed to be $D \rightarrow D^+ + e^-$.

CHAPTER 12

Resolving the potential profile through the MIS interfaces

Tunnelling hydrogen passivated n-Si/SiO_2 interfaces were characterized by in-situ XPS measurements under bias assisted electron exposure and during interface experiments with platinum and nickel oxide. The experiments suggest the presence of an interface state which pins the Fermi energy in the silicon ($\sim$ 0.3-0.4 eV) during bias assisted electron exposure or when platinum is deposited and would be responsible to the built-up of a strong electric field ($\sim$ 500 MV/m) throughout the SiO_2 layer which leads to a potential drop of about 1.2 V. The pinning of the Fermi energy is not observed when nickel oxide is deposited even though the same strong electric field is measured by in-situ XPS. The reason has been ascribed to the partial ionization of a donor state at the Si/SiO_2 interface for bias assisted electron exposure experiments or when platinum is deposited while nickel oxide totally ionizes the donor state. The density of the donor state has been evaluated to be about 10^{20} cm^{-3}, is at about 0.4 eV under the Fermi energy of the silicon and is located within the two first nanometer of the silicon from the Si/SiO_2 interface.

12.1 Introduction

The work presented in this chapter originates from the observation that the parameters used to quantify the peaks in the Si 2p region are subjected to some trends when XPS measurements are realized e.g.: during interface experiments with NiO or Pt. Complemented by bias-assisted electron exposure experiments, it turned out that the potential profile along passivated Si/SiO_2 interface could be assessed in assuming the presence of a strong underlying electric field.

12.2 Experimental

The Si/SiO_2 samples are prepared in a furnace at UCL as described in Section 3.2.3. The thickness of the SiO_2 layer is about 2.5 nm, thin enough to be compatible with tunnelling charge transfer and so no charging effect is expected during the electron photo-emission process. The Si/SiO_2 surfaces are cleaned and passivated by surface exposure to a hydrogen plasma source (see Section 3.2.4) in the DAISY-MAT system before being studied in-situ by XPS (for experimental setup of the DAISY-MAT system, see Chapter 11). In-situ XP spectra of the Si 2p. Peak position and full widths at half maximum (FWHM) in the Si 2p region were extracted with a home-made Matlab program filtering noises in the data. Thus, width of the elemental silicon (Si^0) and of the silicon dioxide (Si^{IV}) are determined following a normal routine, the peak position of the Si^0 is determined according to the maximum of the peak and the peak position of the Si^{IV} is determined according to the position of the median at FWHM.

In order to study the band-bending in the silicon, two experimental setups were employed. The first setup used a continuous potential bias on the substrate holder in the XPS chamber while the sample was continuously exposed to an electron flux generated by an electron gun (neutralizer) at 24 mA and 20% of maximum power (Figure 12.1, left). It is believed that a positive bias attracts more electrons from the neutraliser to the sample surface and helps to tune the band-bending in the silicon. Eventually, the XPS results show, after potential bias correction, that it is possible to force the formation of a depleted region in the silicon when a positive DC bias is applied (Figure 12.2). The bias potential is swept from 0 V to 5.5 V. This setup will be referred to as bias-assisted electron exposure in the rest of this chapter. Although this setup is not common, such setup configuration has been described elsewhere [228] and can be used in complement of standard electrical measurements as it enables direct observation of electronic structure in pseudo-operando condition [234]. Eventually, the second setup was a classical interface experiment where the XP spectra were recorded for increasing thickness of deposited materials (Figure 12.1, right). The materials which have been deposited are the platinum (Pt) and the nickel oxide (NiO). The conditions of deposition for the platinum is described in Section 3.1.3 and the nickel oxide has been deposited following the metal layer oxidation (MLO) method described in Chapter 14. NiO is

prepared by MLO at room temperature (RT) and at high temperature (> 100°C, HT).

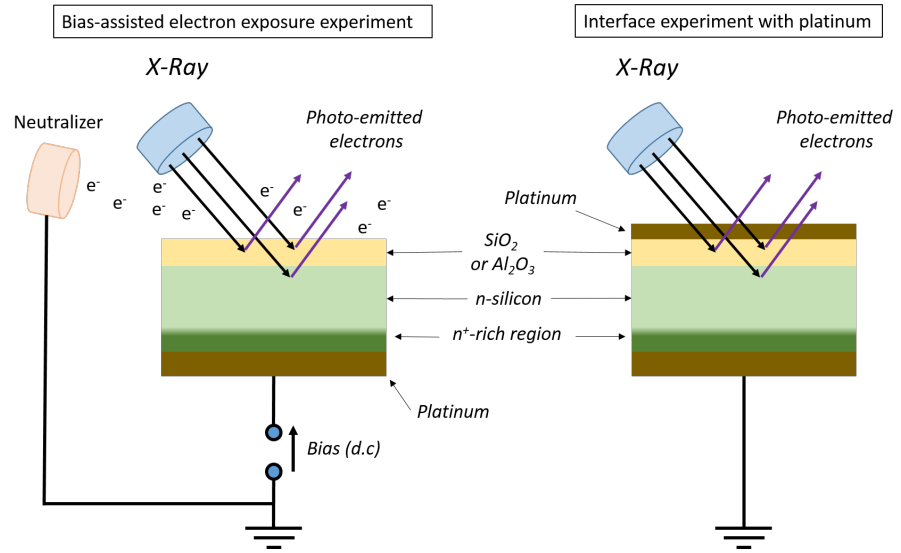

Figure 12.1: Schematic of the experimental setups adopted in this study for in-situ XPS characterization of the hydrogen passivated Si/SiO_2 samples. Left: The schematic represents the in-situ XPS measurements in combination with electron exposure and sample potential bias which is denoted bias-assisted electron exposure in this chapter. Right: Representation of a typical interface experiment with platinum realized on the two studied structures. The platinum or nickel oxide layer (< 1 nm) is sequentially increased and the X-ray photoemission spectra is recorded.

12.3 Results

12.3.1 Bias assisted electron exposure experiments

The bias-assisted electron exposure experiment enabled to create an upward band-bending in the silicon (Figure 12.2). Even more, as it will be detailed later, the experimental setup with the neutraliser provide data, e.g.: during the built-up of the charge depleted region, which are not accessible when Pt or NiO are deposited.

After bias correction, Figure 12.2 shows that for the Si^0 peak, similar binding energy to the calculated flat-band condition are attained with the help of a positive bias. If the bias is close to 0 V, the Si^0 is located to the left of the calculated flat-band position and for higher bias, the Si^0 peak is found to the right of the calculated flat-band position. At this stage, it worth to mention that it can be observed a reduction of the ΔSi 2p peak distance, a reduction of

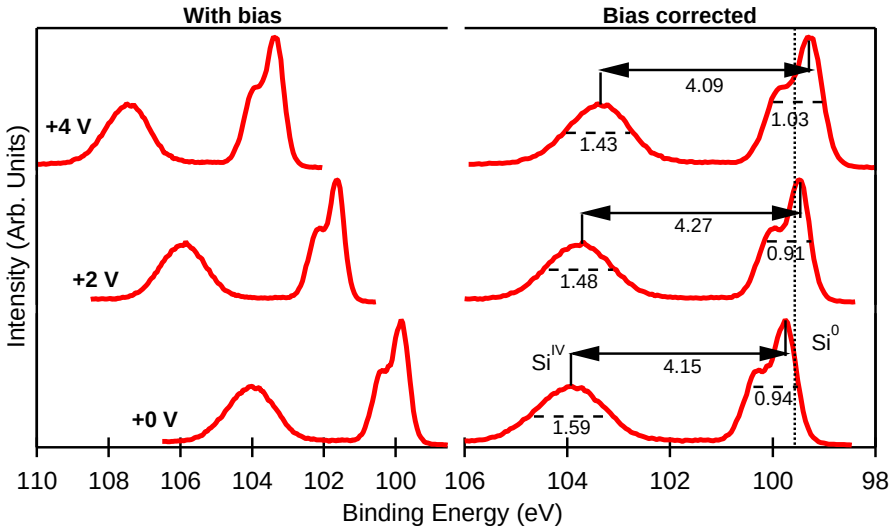

Figure 12.2: Typical in-situ XP spectra recorded from a Si/SiO_2 sample with bias assisted electron exposure measurements. The spectra on the left side are the raw spectra obtained under bias while the spectra on the right side are the bias corrected spectra. After bias correction a shift of the spectra to the right can be noticed which can be interpreted as the built-up of a charge depleted region in the silicon. The vertical line represents the calculated Si^0 peak position in flat-band condition.

the Si^{IV} FWHM and a broadening of the Si^0 peak when the bias potential is equal to +4 V in comparison to the lowest bias.

12.3.2 Interface experiments with Platinum and Nickel Oxide

As seen in Figure 12.3, and similarly to the bias-assisted electron exposure experiments, the depositions of Pt by DC sputtering and NiO with the MLO method on hydrogen passivated Si/SiO_2 surface lead to a shift of the Si^0 peak to the right of the calculated flat-band position. This shift can be interpreted as a consequence of the built-up of a charge depleted region in the silicon. A broadening of the Si^0 peak and the Si^{IV} peak can be observed when Pt or NiO are deposited, while the peak distance ΔSi 2p between the Si^{IV} and the Si^0 peak is substantially reduced in comparison to what is observed during the bias-assisted electron exposure experiments (Figure 12.2).

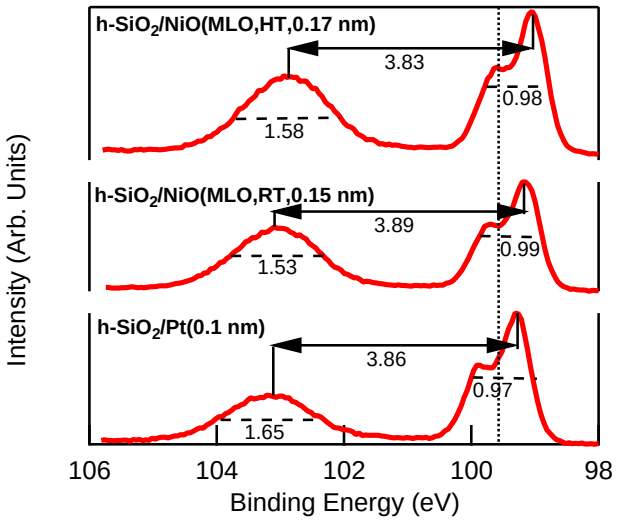

Figure 12.3: Final XP spectra of the Si 2p region after interface experiments with Pt and NiO prepared by the MLO methods at room temperature (RT) and high temperature (HT). The vertical line represents the calculated Si^0 peak position in flat-band condition.

12.3.3 Overall view of the Si^0 and the Si^{IV} peaks

Compilation of the position and width of the elemental silicon Si^0 peak and the silicon in the silicon dioxide layer Si^{IV} in the Si 2p region measured by XPS is displayed in Figure 12.4. This compilation includes the results obtained with as prepared hydrogen passivated Si/SiO_2 samples, then during bias-assisted electron exposure experiments, interface experiments with platinum and interface experiments with nickel oxide.

It can be seen that as-prepared hydrogen passivated Si/SiO_2 surfaces provide a Si^0 peak positioned to the left of the calculated flat-band position (Figure 12.4, left). It indicates that negative charges accumulate on the silicon side. The negative charges could migrate to the surface to compensate positive charges trapped in the vicinity of the Si/SiO_2 interface.

When bias-assisted electron exposure experiments are carried out and also after interface experiment with Pt or NiO, the width of the Si^0 peak increases. This is particularly obvious during bias-assisted electron exposure experiments, for a bias potential comprised between 0 V and 4.5 V. Thus we observe when the Si^0 peak shifts to lower binding energy the width of the Si^0 peak increases from 0.9 to 1 eV. Interestingly, the final Si^0 peak position is about 99.25 eV for both bias-assisted electron exposure experiments and for interface experiments with platinum. On the contrary, the final peak position is about 99.2 eV and 99 eV for the interface experiments with NiO prepared by MLO at RT and HT, respectively. The width of the Si^0 peak obtained when the h-Si/SiO_2 samples are interfaced either with Pt or NiO are dispersed around 0.97 eV.

The right plot of Figure 12.4 shows the evolution of the width of the Si^{IV} peak according to the distance ΔSi 2p between the Si^{IV} and the elemental silicon peak Si^0. The experimental results highlight two regimes of evolution, the first regime is made of datapoint for which the peak distance ΔSi 2p varies between 4.1 and 4.3 eV, while the second regime includes datapoint for which the peak distance ΔSi 2p varies from 3.4 and 4.0 eV. The first regime is characterized by a decrease of the width of the Si^{IV} peak at relatively constant ΔSi 2p peak distance. This regime is exclusively made of data obtained during the bias assisted electron exposure experiments for bias value comprised between 0 and 4.5 V. The evolution in the second regime is characterized by a increase of the Si^{IV} peak width for decreasing distance ΔSi 2p (Figure 12.4).

It is worth mentioning that the lowest Si^{IV} FWHM are obtained with the measurements during the bias-assisted electron exposure experiments. Thus, as for the Si^0 peak (Figure 12.4), the bias-assisted electron exposure experiments can be used to explore inaccessible regions in comparison to standard interface experiments with, for instance in our case, platinum.

Looking at the data obtained during the bias assisted electron exposure experiments for bias potential comprised exclusively between 0 V and 4.5

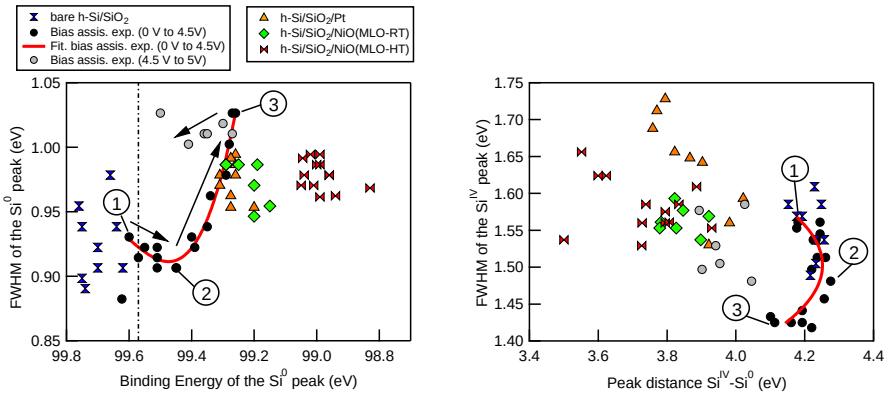

Figure 12.4: Left: Width of the Si^0 peak according to the Si^0 position. As prepared hydrogen passivated Si/SiO_2 are located to the left of the calculated Si^0 position in the flat-band condition (vertical dotted line). It can be observed a broadening of the Si^0 peak during the built-up of the charge depleted region in the silicon for the bias-assisted electron exposure experiments or during the interface experiments. The arrows indicate the sense of increasing bias potential during the bias assisted electron exposure experiments. Right: FWHM of the Si^{IV} peak according to $\Delta Si\,2p$. The interface experiments and the for bias above 4.5 V, the peak distance is substantially reduced and the width of the Si^{IV} is relatively broader than for as prepared sample. The number in circle represents the data extracted from the same XP spectra during the bias assisted electron exposure experiment.

V, three remarkable feature have to be highlighted. These features are labelled 1, 2 and 3 in Figure 12.4. The label 1 is characterized by a high Si^{IV} width ($\sim$ 1.55 eV) and a relatively low Si^0 ($\sim$ 0.93 eV). The width of the Si^{IV} is noticeably reduced with increasing bias potential while the Si^0 is increased. Thus the width of the Si^{IV} is 1.50 eV and 1.45 eV for label 2 and 3, respectively. In the meantime, the width of the Si^0 passes by its minimum at around 0.9 eV (label 2) and it increases up to $\sim$ 1.0 eV when the width of the Si^{IV} peak reaches its minimum (label 3).

12.4 Modelling XPS spectra distortion under an electric field

12.4.1 Motivation

In-situ XPS measurements of the Si/SiO_2 surfaces were performed during both bias-assisted electron exposure and interface experiments with platinum and nickel oxide. Compiling the peak positions, the widths of the Si^0 peak and the widths of the Si^{IV} peaks in the Si 2p region (Figure 12.4) it can be observed a broadening (distortion) of the Si^0 and the Si^{IV} peaks and a decrease of the peak distance ΔSi 2p when the Si^0 shifts to the right. To explain the experimental

phenomena, it has been assumed that an underlying electric field in the vicinity of the Si/SiO_2 interface might arise during the experiments. The electric field would shift accordingly the kinetic energy of the photo-emitted electron. Thus the photo-emitted electrons would gain or loss kinetic energy depending on the value of the local potential. and this would results on distorted XP spectra.

Therefore, as first approximation, simulations of the peak distortion in the presence of an electric field have been realized for a constant electric field throughout the SiO_2 layer and for an electric field screening the top 2 nm of silicon at the Si/SiO_2 interface.

12.4.2 General approach

To investigate the binding energy shifts and broadening of the peaks measured in the Si 2p region, we simulated the Si 2p XP spectra when photo-emitted electrons are ejected from regions with different electrostatic potential. The method relies on the idea that the peak shape $I_{meas}(E)$, where E stands for the binding energy, is nothing else than a superposition of ideal XP spectra $I_{id}(E)$ shifted by the potential $V(x)$ and attenuated by the distance to the surface x, where the material is characterized by an inelastic mean free path (IMFP) factor λ [235]:

$$I_{meas}(E) = \int_0^\infty I_{id}(E - qV(x)) \exp(-x/\lambda)\, dx \tag{12.1}$$

In this study, XPS peak shapes have been simulated for constant electric fields in the $\sim 10^8$ V/m range.

12.4.3 The elemental silicon Si^0 peak

The simulation regarding the distortion of the Si^0 peak has been carried out for an electric field screening the top 2 nm of the silicon side. The ideal XPS profile for elemental silicon Si^0 has been determined by deconvoluting experimental XPS data obtained on a H-terminated oxide-free silicon surface where the Si^0 peak position was found close to the calculated flat-band position (Figure 11.4, right). Thus the ideal Si^0 peak is composed of two Voigt functions separated of 0.56 eV for which the Gaussian/Lorentzian (G/L) ratio is 0.5 and the FWHM are, for the main and satellite peak respectively, 0.467 eV and 0.585 eV.

Simulation of the distortion of the Si^0 peak has been evaluated for an electric field in the 100 MV/m to 400 MV/m range penetrating the top 2 nm of the silicon. These parameters have been fixed after a trial and error adjustment of the penetration thickness and the electric field values.

As seen on Figure 12.5, the simulation carried out on the Si^0 peak shows that the presence of a strong electric field in the vicinity of the silicon surface can distort the Si^0 final shape. Thus, for an electric field of $\pm$ 150 MV/m

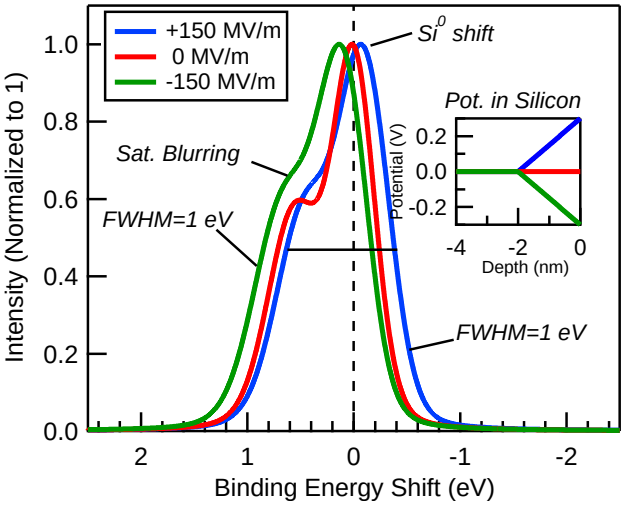

Figure 12.5: Simulated distortion of the Si^0 XPS peak in the presence of an electric field affecting the top 2 nm of the silicon.

penetrating the top 2 nm of the silicon the resulting Si^0 peak is shifted of ± 0.1 eV accordingly to the sign of the electric field. In the meantime the width of the Si^0 peak increases from 0.92 eV to 1 eV. In addition, the depth of the valley between the Si 2p(3/2) and the spin orbit feature Si 2p(1/2) tends to disappear.

12.4.4 The silicon dioxide Si^{IV} peak

Although this is in reality made out of two electronic states, only one Voigt function was used to simulate the Si^{IV} peak, as it gives reasonably good fit with the experimental results. The ideal Si^{IV} XP spectra are then defined by one Voigt function for which the G/L ratio and the FWHM are respectively set to 0.5 and 1.38 eV. Finally, ΔSi 2p, the value of the distance between the Si^0 and Si^{IV} peak, is fixed to 4.22 eV. This value is measured at a minimum FWHM (see Figure 12.4, right). It can therefore be assumed to correspond to a situation for which no electric field is present in the silicon dioxide layer.

As represented in Figure 12.6, the results of the simulation provide a flatter and wider Si^{IV} peak when an electric field is present in the silicon dioxide layer, which can be accompanied to e.g. a reduction of ΔSi 2p. The width of the Si^{IV} and the ΔSi 2p peak distance from simulation have been extracted for various electric field (Figure 12.7). The ΔSi 2p distance was determined according to the median point of the Si^{IV} peak width, which does not necessarily match with the position of the maximum of the Si^{IV} peak, and the maximum of the ideal Si^0 peak position which implies that an electric field in silicon is neglected at this stage.

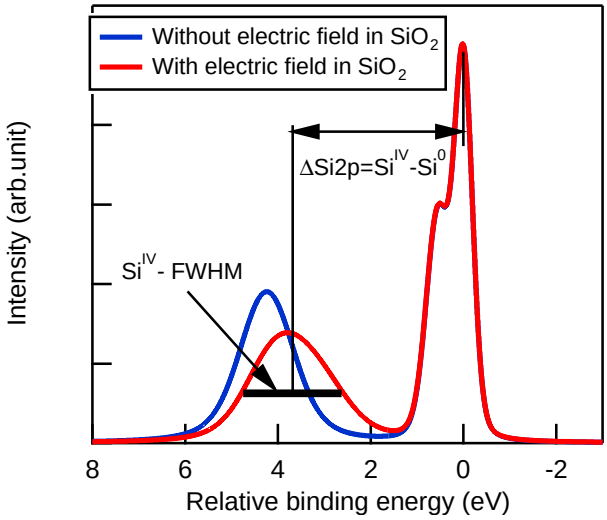

Figure 12.6: Original Si 2p spectra (blue) and distorded Si 2p spectra (red) in the presence of an electric field of +700 MV/m going through the silicon dioxide layer.

The simulation consisted in varying the value of a constant electric field in the silicon dioxide. Figure 12.7 details the approach used to assess the electric field. First of all, a boundary condition needs to be specified when the simulations are ran. Indeed, the simulation is based on the binding energy shift of the XP spectra at a certain depth induced by the potential at this depth. The boundary condition defines the position in the silicon dioxide for which the potential is the same as in the silicon. The boundary condition has been varied from the silicon side to the vacuum side (Figure 12.7, right). As represented in the schematic d) in Figure 12.7, the results of the simulation evidence that the width of the Si^{IV} peak is likely correlated to the value of the electric field whatever the boundary position, while the ΔSi 2p distance depends on the average potential in the silicon dioxide. In consequence, as it is experimentally observed that the distance ΔSi 2p is mostly smaller than 4.2 eV (Figure 12.4), it can be assumed that the potential in the silicon dioxide, in average, is higher than the potential on the silicon side. Therefore, only the non shaded part of Figure 12.6 has to be considered.

12.5 Discussion

In the following part, the trends observed in the Si 2p region by in-situ XPS will be discussed in term of the presence of an underlying electric fields either in the silicon or in the silicon dioxide. The electric field E can originate from the presence of charged species, free charge carriers or trapped charges, following

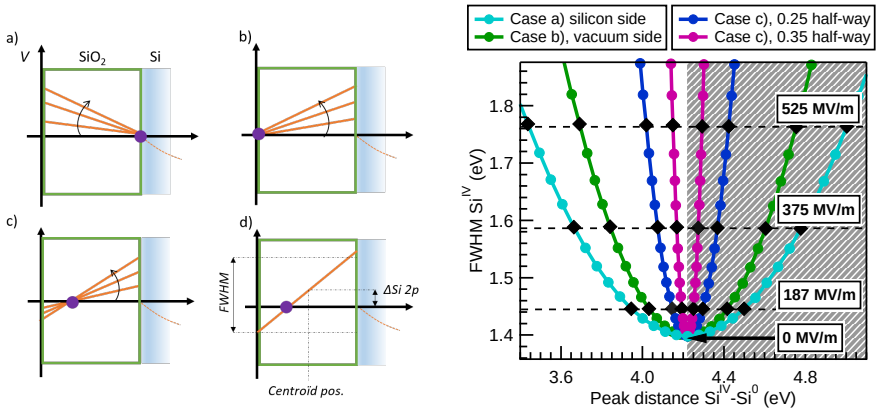

Figure 12.7: Left: Potential profile in the silicon dioxide layer used for the simulations in the Si 2p region. The purple dot defines the position of the boundary condition. Regarding the boundary condition, three cases have been considered: pinning on the silicon side (a), the vacuum side (b) or in the silicon dioxide layer (c). The electric field is increased in the direction where the average potential is higher than the potential on the silicon side. The schematic (d) highlights that the average potential in the silicon dioxide defines the shift $\Delta Si\,2p$ and the potential drop through the silicon layer, the broadening of the Si^{IV} spectra. Right: Typical results obtained with the simulation to assess the effect of the Si^{IV} peak distortion in the presence of a strong electric field. The width of the Si^{IV} peak is represented against the Si^{0} to Si^{IV} peak distance. The shaded grey part is the part which corresponds to increasing peak distance with the electric field, as the contrary has been observed this part can be ignored. Iso-electric field are represented by horizontal dashed lines (187, 375 and 525 MV/m).

the Poisson's law in 1-D:

$$\frac{d\,E}{dx} = -\frac{\rho}{\varepsilon\varepsilon_0} \tag{12.2}$$

with ρ the quantity of charges per volume, ε_0 the vacuum permittivity, ε the relative permittivity of the considered material. With the conditions that at any point of space the electric field respect continuity rules:

$$\varepsilon(x+dx)\varepsilon_0\,E(x+dx) = \varepsilon(x)\varepsilon_0\,E(x) + \rho\,dx \tag{12.3}$$

12.5.1 Electric field in the silicon

The Si^0 peak broadening during the built-up of the space charge region observed in Figure 12.5 (left) can not be explained by the formation of an electric field due to band-bending. Indeed, solving the Poisson equation for n-doped silicon, it is expected to obtain an electric field value at the maximum of 10^5 V/m in the case of a strong built-in voltage (V_{bi}=0.9 V - 1 V). As the XPS thickness sensitivity is in the nanometre range, the potential drop through the probed silicon layer would then be only $\sim 10^{-4}$ V. This is

obviously not enough to broaden the Si^0 peak.

The in-situ XPS measurements indicate that the Si^0 peak shifts of about 0.3 eV and is accompanied by broadening of the width of the peak. The broadening can be explained by the presence of a negative or positive electric field in the top 2 nm. According to the sign of the electric field, the Si^0 can be shifted to lower or higher binding energy (± 0.1 eV) as depicted in Figure 12.5. Thus, the Si^0 peak deviation arises from the contribution of the built-in voltage V_{bi} and the shift due to the screening of the electric field in the vicinity of the silicon sub-surface ΔE_{Screen}. It can be written that:

$$\Delta Si^0 = q\,V_{bi} + \Delta E_{Screen} \tag{12.4}$$

According to the interpretation of the results obtained with the Si^0 peak, the final peak position is pinned $\sim$ 0.3 eV to the right of the calculated flat-band position and this position is made of the contribution of the built-in voltage V_{bi} and the shift of the Si^0 because of the presence of an electric field (—E— $\sim$ 150 MV/m) penetrating the top 2 nm of the silicon. Assuming that such electric field arise from the presence of charges in the top 2 nm of the silicon, according to Equation 12.2 the quantity of charges can be estimated as being:

$$\rho = -\frac{\varepsilon_{Si}\varepsilon_0\,E}{d_E} \tag{12.5}$$

with d_E the thickness of the silicon subjected to the electric field. The calculation gives a charge density ρ = sign(E) × 4.5 × 10^{19} charges/cm^3 which gives a charge surface density of sign(E) × 9 × 10^{12} charges/cm^2. With the function sign() being the sign of the electric field.

Considering that the electric field in the top 2 nm of the silicon originates from the ionization of defective states. It is more logical that the ionization lead to positive charges as defective state at the Si/SiO_2 would be elevated above the Fermi level during the built-up of the depleted region in the n-type silicon. In such a case, the ionization of the defective states D, as in Chapter 11, follows the reaction $D \rightarrow D^+ + e^-$.

12.5.2 Electric field in the silicon dioxide

Thus positive charges in the top 2 nm of the silicon interact then with negative charges at the SiO_2/Pt interface. This results in the formation of an electric field where the system can be considered as a double plate capacitor with the silicon dioxide layer playing the role of insulating layer:

$$C_{SiO_2} = \frac{\varepsilon_{SiO_2}\varepsilon_0}{d_{SiO_2}} \tag{12.6}$$

for a 2.5 nm SiO_2 layer, the equivalent capacitance is estimated to be 1.3 × 10^{-6} F/cm^2.

The width of the Si^{IV} peak is about 1.65-1.7 eV at its maximum when

platinum or nickel oxide is interfaced while, in the meantime, the ΔSi 2p distance is reduced (Figure 12.4). The width of the Si^{IV} can reach up to 1.77 eV, which would correspond, according to the simulation of Figure 12.7, to an electric field of about 500 MV/m and would lead to a potential drop of about 1.2 V through the 2.5 nm silicon dioxide.

The potential drop through the silicon dioxide layer, as determined by in-situ XPS, is about 1.2 V. Therefore, the quantity of charges accumulating at the pole of the capacitor is about $1.2 \times 1.3 \times 10^{-6}$ C/cm^2 $= 1 \times 10^{13}$ charges/cm^2. Considering the approximations taken to evaluate the electric field from the in-situ XPS results, this is an extremely close value to the number of positive charges in the top 2 nm of the silicon in the vicinity of the Si/SiO_2 interface.

12.5.3 Insight on the bias experiment electron exposure experiment

In the previous part, when nickel oxide or platinum is interfaced on passivated Si/SiO_2 surfaces, it is assumed that the ionization of a donor state in the top 2 nm of the silicon during the formation of the space charge region in the silicon can explain the broadening of the Si^0. Indeed, the ionization of this donor state ($D \rightarrow D^+ + e^-$) results in a positively charged layer of about 9×10^{12} charges/cm^2 in the top 2 nm of the silicon in the vicinity of the Si/SiO_2 interface. In the meantime, the Si^{IV} peak is subjected to a broadening of the peak and calculation shows this can result from an accumulation of charges density of about 1×10^{13} charges/cm^2 at the interfaces of the silicon dioxide layer.

The continuity of the electric field at the interface postulate that the slope of the electric field is of the same sign on the silicon and the silicon dioxide side at the Si/SiO_2 transition. Therefore, at first approximation, according to Equation 12.2, the slope of the electric field is negative in both the silicon and the silicon dioxide.

Now let's look back at the datapoints obtained during the bias assisted electron exposure experiments of Figure 12.4. The label 3 indicated a configuration where the Si^0 width is at its maximum whereas the width of the Si^{IV} is at its minimum. On the contrary for label 1 and 2 the Si^0 width reaches a minimum but the width of the Si^{IV} peak is above its minimum.

It can be assumed that for the position indicated by the label 3, a compensating electric field in the silicon attenuate the electric field in the silicon emerging because of the presence of positive charges in the silicon. Such a case can occurs if negative charges compensate the positive charges. These negative charges would be located in the silicon dioxide layer at the Si/SiO_2 transition and can take the form of deep trapped states, negatively charged. Their existence is not absolutely clear and additional work must be carried out.

The position indicated by the label 2 might indicate a situation where there is no ionized positive charges in the silicon, but the remaining negatively trapped charges can interact with positive charges on the SiO_2/vacuum interface. Thus, an electric field arise in the silicon dioxide and is estimated to be about 250 MV/m (taken for a Si^{IV} width of 1.5 eV). In consequence, a potential drop of about 0.6 V arises through the silicon dioxide and could be equivalent to a negatively trapped species density of 5×10^{12} charges/cm^2.

For the label 1, the width of the Si^{IV} peak is larger with about 1.55 eV. The reason could be that for such situation the bias potential does not provide sufficient electron to compensate positive charges on the SiO_2/vacuum side. Thus more positive charges are presents which need to be compensated by negative charges. The trapped negative charges in the silicon dioxide near the Si/SiO_2 transition being limited, the extra negative charges might be brought by mobile charges in the silicon, this results in a downward band-bending. The potential drop in the silicon dioxide is estimated to be about 0.8 V.

Finally for bias between 4.5 eV and 5.5 eV, the reduction of the Si^0 peak could suggest that charges are flowing through the charge depleted region resulting in a lowering of the barrier height. The bias threshold could corresponds to a tunnelling process through the conduction band of the silicon dioxide.

12.5.4 Potential profile when NiO or Pt is interfaced

Even though the electric field would apply a force on the electrons towards the positive charges, the electrons cannot reach the positively ionized state as their energy level (defined by the Fermi level) is lower than of the positively charged states (situated above the Fermi energy) at the Si/SiO_2 interface. Eventually, this donor state pins the bands as long as it is not totally ionized (e.g. when platinum is interfaced) but the built-in voltage can reach higher value only if this donor state is totally ionized (e.g. when nickel oxide is interfaced).

Finally, according to the interpretation made of the experimental results, potential diagrams are proposed for the different MIS structures studied in this chapter. The potential diagram of the Si/SiO_2/Pt structure is drawn in Figure 12.8. On the silicon side, a potential drop of about $\sim$ 0.3 V has been estimated due to the screening of the top 2 nm by an intense electric field ($\sim$ -150 MV/m). In the silicon dioxide the potential drop reaches up to 1.2 V and this electric field builds up because of the ionization ($D \rightarrow D^+ + e^-$) of the donor state at the Si/SiO_2 interface. As determined by the comparison of the experimental data and the simulated curves (Figure 12.5), the potential is pinned in the silicon dioxide in the vicinity of the Si/SiO_2 interface, this was estimated , maybe wrongly, because of the uncertainty on the exact position of the Si^0 peak, as corresponding with the Fermi energy at the Si/SiO_2 interface.

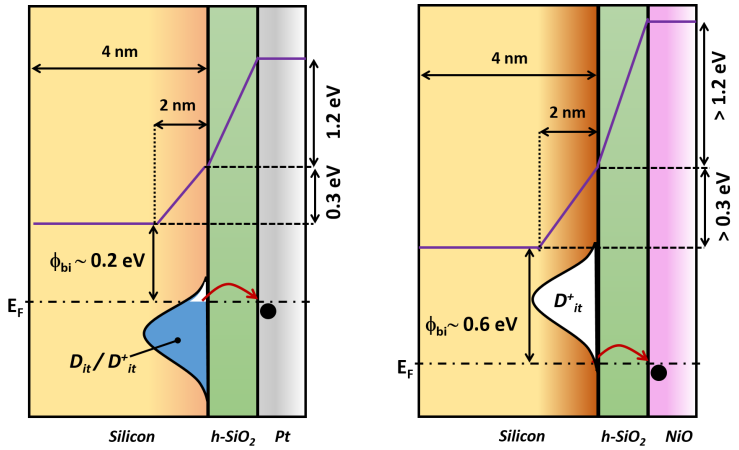

Figure 12.8: Proposed energy band-diagram for the $Si/SiO_2/Pt$ structure (left) and for the $Si/SiO_2/NiO$(MLO, HT) structure (right). Fermi level pinning is determined by the energy level of a donor state for which the ionized charges migrate to the platinum side. The interaction between the ionized states and the platinum entails the formation of a strong electric field through the silicon layer where the potential drop attains about 1.2 V. Additionally, a potential drop of 0.3 V might arise in the silicon sub-surface. The band-bending due to the built-in voltage in the silicon is not represented.

As represented in Figure 12.8, it is assumed that the deposition of platinum only partially ionized the donor state leading to the so called Fermi pinning of the band position. The potential drop through the silicon dioxide, in a first approximation is estimated to be about 1.2 V and in the top 2 nm of the silicon about 0.3 V. On the contrary if NiO is deposited by the MLO method, the band deviation is higher in comparison to case when platinum is interfaced. Thus band-bending reaches at least 0.6 eV and as the interface states is totally ionized, the potential drop through the silicon dioxide layer and the potential drop through the top 2 nm of the silicon is assumed to be higher than what has been estimated as first approximation when platinum is deposited.

12.6 Conclusion

Finally, in-situ XPS measurements obtained during bias-assisted electron exposure experiments and during interface experiments with platinum on passivated Si/SiO_2 interface have been realized. Complemented by rough simulation, the experimental results suggest that a strong electric field can arise in the silicon dioxide layer which would lead to an equivalent potential drop in the 1-1.2 V range and the presence of an electric field within the top 2 nm of the silicon which leads to a 0.3 V potential drop. The resulting potential profile is associated to the ionization of a donor state located at the Si/SiO_2 interface. The deposition of platinum produces only a partial ionization of the donor state, while the deposition of nickel oxide by metal layer oxidation would totally ionize the donor state leading to an apparent Fermi level de-pinning.

CHAPTER 13

Electrical characterizations of the MIS structures

In this chapter, different n-Si/SiO_2/Pt tunnelling MIS Schottky junctions, fabricated in the DAISY-MAT system, are electrically characterized by DC and RF measurements. Platinum has been deposited at room temperature on ex-situ (non treated), h-cleaned and hydrogen passivated Si/SiO_2 surfaces. Also, the temperature of deposition of platinum has been varied from room temperature (RT) to 475 °C for platinum deposited exclusively on hydrogen passivated Si/SiO_2 surfaces.

IV curves and Mott-Schottky plots have been realized from DC and RF measurements, respectively, for which, in particular, the built-in potential (V_{bi}) and the flat-band potential (V_{fb}) have been determined. The results suggest that for any surface preparation the built-in voltage is constant and is in average 0.4 V, while the flat-band potential can vary substantially between -0.3 to 0.4 V according to the conditions of preparation. The difference between the V_{bi} and V_{fb} has been attributed to the presence of the donor state evidenced in the Chapter 12 which delays the emergence of a Mott-Schottky plot behaviour in the space-charge region of the silicon with increasing backward potential. The donor state density has been estimated to be about 5.6×10^{12} charges/cm^2 from the electrical measurements.

In addition, the results of this chapter enable to refine the comprehension of the electrical properties of tunnelling Si/SiO_2 based MIS Schottky junctions.

13.1 Introduction

In order to elaborate a photo-water splitting device, electrical characterization of tunnelling Si/SiO_2 based MIS Schottky junction has been performed beforehand in order to obtain a deeper understanding of the junction and the electrical properties of the Si/SiO_2 interface. Indeed, solid/liquid interfaces are subjected to ionic interaction with the interface, which can give rise to the so-called Helmholtz layer (see Section 2.4), and the in-depth understanding of such structure can become complex. Therefore, solid state $Si/SiO_2/Pt$ junctions have been fabricated in the DAISY-MAT, where the silicon dioxide layer has been grown previously in UCL, and have been studied electrically by RF and DC measurements. The measurements enable to determine the electrical properties of such junction and to evaluate what can be the performance of a photo-water splitting on sole electrical considerations.

13.2 Experimental

n^+-rich region on one side of a n-type silicon wafer was implemented by phosphor diffusion for ohmic back-contacting (see Section 3.2.2). After the phosphor diffusion step, an intensive chemical surface cleaning is performed (see Section 3.2.1) in order to obtain an oxide-free sample surface, and consisted into removing in particular the poly-silicon glass layer on the n^+ side and the thick sacrificial SiO_2 layer on the less doped side. The oxide-free sample is immediately inserted in a furnace to thermally grow a thin SiO_2 layer (< 2.5 nm) in nitrogen at 1000 °C without annealing period (see Section 3.2.2).

Platinum deposition has been performed by DC sputtering in the DAISY-MAT system in order to realize a tunnelling MIS Schottky junction on the n-Si/SiO_2 front side. Then metallic back-contacting is finalized by depositing platinum on the n^+-Si/psg-SiO_2 side which has been hydrogen passivated beforehand. The back-contact is supposed to be ohmic. The platinum deposition conditions are detailed in Section 3.1.3.

Different samples have been prepared in order to evaluate the effect of the Si/SiO_2 passivation and the effect of the temperature of deposition of the platinum on the electrical properties of the MIS Schottky junction. Thus, platinum has been deposited at room temperature (RT) on ex-situ (with carbon contamination), hydrogen cleaned and hydrogen passivated Si/SiO_2 samples. Also platinum has been deposited from RT to 425 ° C on hydrogen passivated Si/SiO_2 samples.

IV and impedance spectroscopy measurements have been performed to electrically characterize the MIS junctions (for details see Section 3.4.4). Impedance spectroscopy is realized by RF signals for a bias potential (V_g) in the -1 V to 0.6 V range. The results obtained by impedance spectroscopy are

analysed in using Nyquist representation and are quantified in using simple equivalent electrical circuit (see Figure 2.20 in Section 2.4.2). IV measurements are realized by DC signals as described in Section 3.4.4. The contact resistance R_c is estimated by impedance spectroscopy and was later used for iR_c post-correction of the bias potential V_g as following: $V_g corr. = V_g - I\,R_c$. The current being in the mA cm^2 range in reverse bias and $R_c \sim 1.2\ \Omega\,\mathrm{cm}^{-2}$, the bias iR_c correction is not significant in this bias domain.

13.3 RF measurements

13.3.1 Impedance spectroscopy

As seen on Figure 13.1, the measured impedance spectra evidence the presence of semi-circles at any bias, typical of resistive and capacitive elements connected in parallel (R//C). At reverse bias, the Nyquist plot displays one semi-circle which can be easily fitted with a R_c+R_{meas}//C_{meas} electrical equivalent circuit where R_c is the contact resistance and *meas* stands for measured. As it will be seen later, the properties of R_{meas} and C_{meas} suggests that they are made of multiple resistive and capacitive elements which are connected in such a way that it provides only one semi-circle on the Nyquist plot. At intermediate forward bias, as shown in Figure 13.1, the Nyquist plot can be made of two semi-circles, for which one semi-circle steadily disappears, assigned to the R_{meas}//C_{meas} system, whereas the second semi-circle, still visible at large forward bias, has been associated to the equivalent electrical circuit is R_{ox}//C_{ox}, where *ox* stands for the silicon dioxide layer of the MIS Schottky junction. Indeed, for large forward potential, the space charge region is in accumulation regime, no significant capacitive element can be induced in the silicon and only the silicon dioxide layer itself can provide the structure for creating a capacitive element.

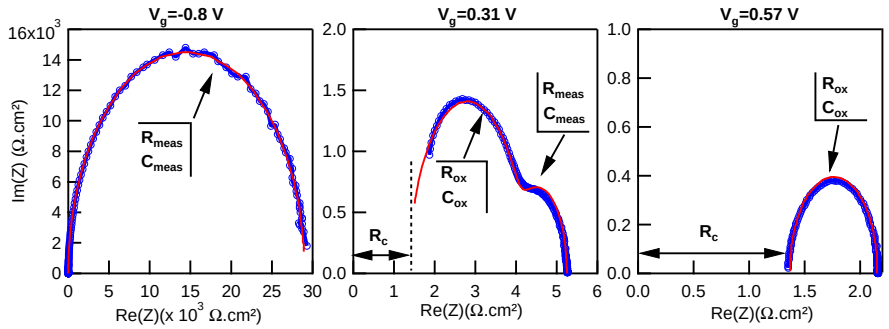

Figure 13.1: Experimental results (blue circle) of impedance spectroscopy of a n^+-Si/n-Si/SiO_2/Pt junction for three different bias potentials. The red line represents the fit of the experimental data with an electrical equivalent circuit made of R+[R//C]$_n$ elements where n is equal to the number of semi-circle.

It has to be mentioned that the presence of a double semi-circle feature

at intermediate forward bias is not always encountered for this batch of sample. The reason has been associated to a situation where the space-charge region capacitive element C_{scr} and the oxide C_{ox} are in the same of order of magnitude and so can be distinguished by impedance spectroscopy. The data were analysed with an electric equivalent circuit including two R//C system: R_c+R_{ox}//C_{ox}+R_{meas}//C_{meas}.

For bias smaller than 0.2 V, when taking a Nyquist representation of the results obtained by impedance spectroscopy, as seen in Figure 13.2 only one semi-circle is obtained. Interestingly, as the space-charge region thickness is reduced with increasing potential, the equivalent impedance of the junction is decreased. This is visually observed on the Nyquist plot of Figure 13.2 by a decrease of the size of the semi-circle. In such bias potential range, the semi-circles were quantified by fitting the experimental data with a simple R_c+R_{meas}//C_{meas} electrical circuit equivalent.

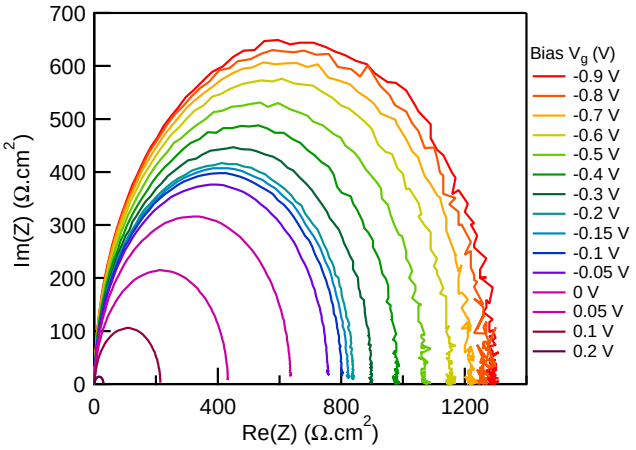

Figure 13.2: Nyquist representation of the impedance measurements realized on the Si/h-SiO_2/Pt-(325 °C) for reverse bias and small forward bias (V_g < 0.2 V). For these potential range, the Nyquist plot only displays one semi-circle which is treated by a simple R_c+R_{meas}//C_{meas} electrical equivalent.

13.3.2 Properties of the MIS equivalent resistance

The following part is dedicated at understanding the properties with bias potential of the resistance R_{meas} determined by impedance spectroscopy.

In considering the tunnelling probability (τ_n) to be constant, the equation 2.19 in Section 2.3.4 becomes for small RF signal:

$$dI = A * T^2 \exp\left(-\frac{\Phi_B}{k_B T}\right) \tau_n * \exp\left(-\frac{qV_g}{k_B T}\right) * \frac{-q}{k_B T} dV_g \qquad (13.1)$$

All the terms have been defined in Section 2.3.4. This equation can be simplified into :

$$\frac{dI}{dV_g} = \frac{1}{R_{scr}} = \frac{-q\, j_0}{k_B T} * \exp\left(-\frac{qV_g}{k_B T}\right) \tag{13.2}$$

Where R_{scr} stands for the equivalent resistance of the space charge region and j_0 is:

$$j_0 = A * T^2 \exp\left(-\frac{\Phi_B}{k_B T}\right) \tau_n \tag{13.3}$$

If the measured resistance R_{meas} is due to the sole contribution of the space-charge region resistance R_{scr}, plotting $\log(1/R_{meas})$ versus the bias potential V_g, one should obtain a linear trend having a slope $\Delta = \frac{1}{\ln(10)} \frac{-q}{k_b T} \sim \frac{-0.43\, q}{k_b T}$ (or $\Delta = \frac{-0.43\, q}{\eta k_b T}$ if non ideal).

However, experimentally, when determined by impedance spectroscopy, the plots of $\log(1/R_{meas})$ vs Vg (Figure 13.3) for the different MIS junctions presented in this chapter, do not show a strict linear trends over the potential range used for the measurements. Instead, as seen in Figure 13.3, when V_g $\rightarrow$ - 1 V, $\log(1/R_{meas})$ saturates to a certain value while for small forward potential, a linear behaviour appears, which could be associated to the R_{scr} behaviour described in equation 13.2.

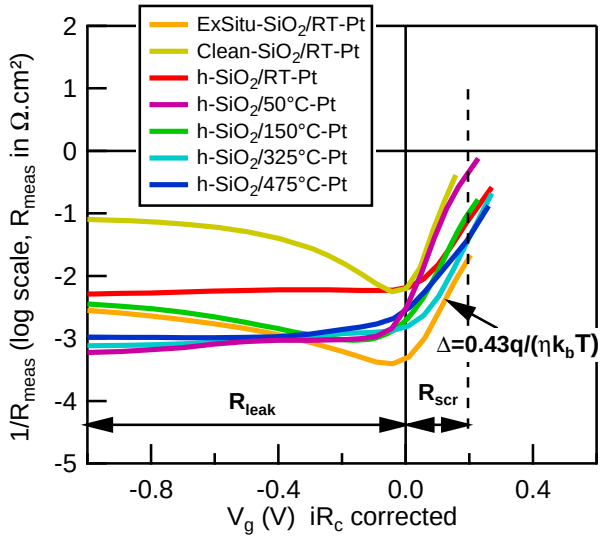

Figure 13.3: Log(1/R_{meas}) vs V_g determined from fitting of the impedance spectra (see Figure 13.1) for the different Si/SiO_2/Pt based junctions studied in this chapter.

To explain the curves when $\log(1/R_{meas})$ is plotted against the bias potential (V_g), it is suggested that the measured R_{meas} resistance, for bias $<$ 0.2 V, is

made of two resistances in parallel, in such a way that:

$$\frac{1}{R_{meas}} = \frac{1}{R_{scr}} + \frac{1}{R_{leak}} \tag{13.4}$$

where R_{leak} is constant and is associated to a leaking current originating from current flowing from non-thermionic displacements (e.g.: current flowing from the sample edges, pin-holes, through defects...), R_{scr} is the resistance related to the MIS diode regime as detailed in equation 13.2. Thus, for large reverse bias (e.g.: V_g= -1 V), $R_{scr} >> R_{leak}$ and $R_{meas} \sim R_{leak}$, on the contrary for small forward bias ($0 < V_g < 0.2$ V), the $R_{scr} << R_{leak}$ and $R_{meas} \sim R_{scr}$.

For $V_g > 0.2$ V, the space-charge region in the silicon accumulates negative charges. Only the oxide of the front contact can hinder the transfer of charges from the silicon to the platinum. Eventually, the resistance for $V_g > 0.2$ V is dominated by the oxide resistance R_{ox} (not represented in Figure 13.3 as the plot focuses only on the properties of R_{meas}).

Interestingly, at the exception of the h-SiO_2/150°C-Pt, the hydrogen passivated Si/SiO_2 samples display a constant R_{meas} at reverse bias. As seen before, for such bias potential, the measured resistance is due to the contribution of the leaking resistance R_{leak} only. It means, for these samples, that the leakage resistance is constant after hydrogen passivation in reverse bias. For the ExSitu-SiO_2/RT-Pt and the Clean-SiO_2/RT-Pt, R_{leak} is decreased with decreasing bias potential. This observation could indicate that trap assisted charge-transfer occurs for non-passivated sample in reverse bias and this can be enhanced with increasing bias potential.

13.3.3 Properties of the MIS equivalent capacitance

For bias potential $V_g < 0.2$ V, capacitive elements can arise at the front contact of the MIS junction from the space-charge region C_{scr}, the silicon dioxide layer C_{ox} and also from an equivalent capacitive element due to interface trapped charges C_{it}.

It is assumed that the measured capacitive element C_{meas} is an equivalent of the contribution of these three capacitive elements. As seen in Chapter 2 equation 2.22, the space charge region can be treated as a double plate capacitor:

$$C_{scr} = \frac{\varepsilon_{Si}\varepsilon_0}{d_{scr}} \tag{13.5}$$

similarly the capacitance of the silicon dioxide layer is:

$$C_{ox} = \frac{\varepsilon_{SiO_2}\varepsilon_0}{d_{ox}} \tag{13.6}$$

The thickness of the space charge region d_{scr} can be evaluated from equation 2.23.

As the silicon dioxide layer is on top of the silicon, the capacitive element C_{scr} is necessarily found in series with the capacitive element C_{ox}. Thus, considering only these two capacitive elements in series it can be written that:

$$\frac{1}{C_{eq}} = \frac{1}{C_{ox}} + \frac{1}{C_{scr}} \tag{13.7}$$

Moreover, as estimated by IV measurements hereafter, taking a barrier height $V_{bi} = 0.2$ V, the space-charge region thickness rapidly reaches value in the 1000 nm range in reverse bias. It definitely overpasses the thickness of the oxide which is about 2.5 nm. Therefore, it can be asserted that $d_{scr} >> d_{ox}$ and so if C_{scr} and C_{ox} are connected in series, as it is assumed to be, the oxide capacitance can be considered negligible in front of the space charge region equivalent capacitance.

However, for a 2.5 nm thick SiO_2 layer, it is therefore expected that the positive charges at the Si/SiO_2 interface interact primarily with negative charges on the SiO_2/Pt interface. The induced potential through the silicon dioxide layer can be estimated to be:

$$V_{ox} = \frac{Q_{trap}}{C_{ox}} \tag{13.8}$$

with Q_{trap} the quantity of ionized interface trapped states and C_{ox} the capacitive element of a 2.5 nm SiO_2 layer. Considering a standard double plate capacitor model, the latter is in theory equal to 1.3×10^{-6} F/cm^2.

13.3.4 Equivalent electrical circuit for the impedance spectroscopy measurements

For bias potential V_g lower than 0.2 V, the impedance spectra display a single semi-circle in the Nyquist representation (Figure 13.2). The semi-circles can be interpreted in term of electrical equivalent in the form of R_c+$R_{meas}//C_{meas}$. In the previous parts, it has been shown that the measured resistance R_{meas} is made of a space charge region resistance R_{scr} connected in series with a leakage resistance R_{leak}. However, the measured capacitive element cannot be directly associated to the space-charge region and should be manipulated with care. Therefore, the notation C_{meas} is preferred at this stage. As represented in Figure 13.4, two electrical circuits equivalent for $V_g < 0$ V and $V_g > 0$ V can be proposed to to interpret impedance spectroscopy measurements.

13.3.5 Flat-band potential and built-in potential

In electronics, when RF measurements are performed, this is common to deal with the flat-band potential (V_{fb}) instead of the built-in voltage. The flat-band potential, is a strange notation. Indeed, the condition for flat-band is not reached for flat-band potential but the measured capacitance C_{meas} reaches a maximum as indicated by the following equation:

$$\frac{1}{C_{meas}^2} = \frac{2}{q\, N_d \varepsilon_{Si} \varepsilon_0 A^2} \times (V_{fb} - V_g) \tag{13.9}$$

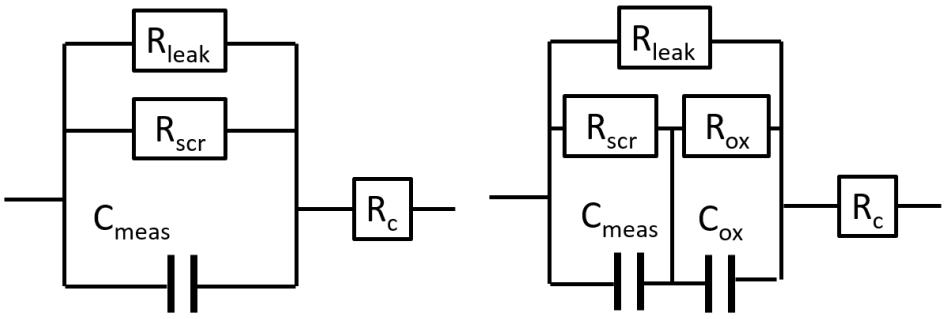

Figure 13.4: Equivalent electrical circuit suggested to correspond to the electrical impedance measurements, for $V_g < 0$ V (left) and for $V_g > 0$ V . The electrical circuit is composed of a leakage resistance R_{leak}, space charge region resistance R_{scr}, space charge region capacitance R_{scr}, the oxide capacitance C_{ox}.

Where the parameters are the same as the Mott-Schottky relationship described in equation 2.24 of Section 2.3.4.

In such a case, the flat-band potential is defined as:

$$V_{fb} = V_{bi} - V_{ox} = V_{bi} - \frac{Q_{def}}{C_{ox}} \tag{13.10}$$

where V_{bi} stands for the built-in potential in the silicon side, Q_{def} and C_{ox} are respectively the equivalent charges and the capacitance associated to the silicon dioxide layer MIS interface.

At the interface, the defects Q_{def} can originate from fixed trapped charges Q_f and interface trapped charges Q_{it} (see Section 2.3.3).

The Mott-Schottky representation of the experimental data obtained by RF measurements is given in Figure 13.5. A straight linear dependence of $1/C^2_{meas}$ with in reverse bias V_g can be identified as modelled in Equation 13.9. The intersection of the linear trend with the horizontal axis gives an estimation of the flat-band potential V_{fb}.

In Figure 13.5, it can be seen discrepancy according to the Si/SiO_2 surface preparation and the temperature of deposition of platinum. Thus, apart for the sample prepared at 475 °C, all the hydrogen passivated Si/SiO_2 surfaces provided similar results with a V_{fb} located to the left of the plot. The ex-situ, the hydrogen cleaned surface and the h-Si/SiO_2/475°C-Pt samples are more located to the right, likely because of the presence of defects which are present on non-passivated surfaces or by the introduction of defects by the reaction of platinum with the silicon dioxide at high temperature.

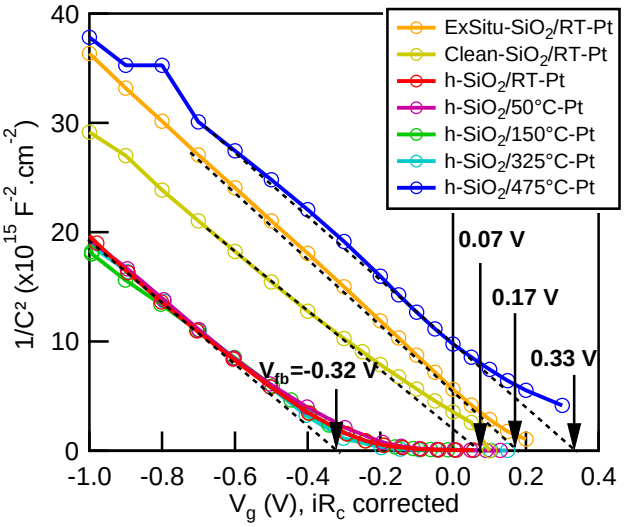

Figure 13.5: Mott-Schottky representation of the C_{meas} determined by impedance spectroscopy following equation 13.9. The intersection of the linear part of the plot in reverse bias with the horizontal axis gives the flat-band potential V_{fb}.

13.4 DC measurements

13.4.1 Understanding the shape of the IV curves

Taking into account the contact resistance R_c and the leaking resistance R_{leak}, evidenced in the previous part, the equation 2.19 describing the IV curves of tunnelling MIS Schottky junction established for thermionic emission over the barrier height in silicon becomes:

$$J_n = \frac{A\tau_n T^2}{1+\frac{\nu_R}{\nu_D}} exp\left(\frac{-\Phi_B}{k_b T}\right) * \left(\exp\left(\frac{q(V_g - J_n R_c)}{k_b T}\right) - 1\right) + \frac{V_g}{R_c + R_{leak}} \quad (13.11)$$

In Figure 13.6 (left), an experimental iR_c corrected plot ($R_c \sim 1.2\ \Omega\,cm^2$) have been plotted along the IV curve calculated for a leaking resistance R_{leak}=1300 $\Omega\,cm^2$. The difference of the two curves is supposed to provide an R_{leak} corrected plot of the experimental data. After this last correction of the experimental plot, changes can be observed changes at low current densities: the IV curve in log scale in reverse bias in flattened and for small forward bias the slope of the IV curve in log scale becomes steeper (Figure 13.6, right). Thus, the diode ideality factor η=1.86 becomes η^*=1.65 after R_{leak} correction. Similarly, the exchange current is I_0=40 $\mu A\,cm^{-2}$, before R_{leak} correction, and becomes I_0^*=20 $\mu A\,cm^{-2}$ after.

Deviation from the ideal curve can be observed at reverse potential and low forward potential due to the excess of current going through the leaking resistance (R_{leak}) overcoming thermionic current. As reported by the

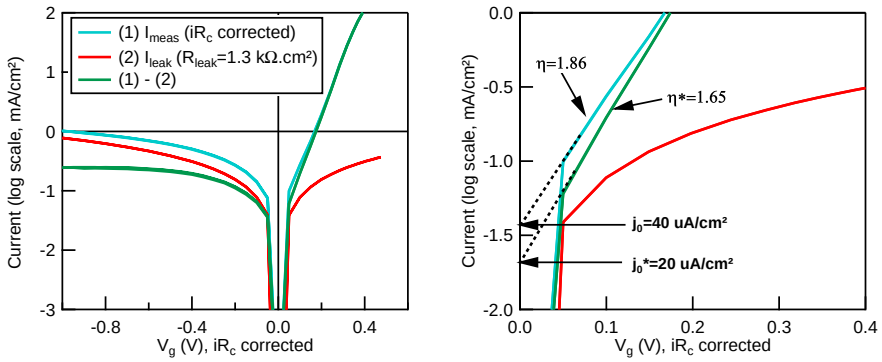

Figure 13.6: Typical IV curve for the Si/SiO_2 based MIS Schottky junction studied in this chapter. The results plotted above were obtained with the h-SiO_2/325 °C-Pt sample.

literature, IV curves in log scale can display a slope discontinuity in the forward potential region [132, 236]. As found in this thesis for $Si/SiO_2/Al_2O_3/Pt$ MIS Schottky junction, in forward bias, the IV curve in log scale can be made up of to three slopes which can be typical of high R_{leak} value ($\sim$ 10000 $\Omega\,cm^2$) (see Appendix A.4). According to literature, lower slope at low forward potential would originate from a non-thermionic excess current, which overcomes the thermionic current, generally observed for large barrier height junctions [236].

It comes out that the diode regime is only observed in a narrow region between 0 and 0.2 V. The features arising from the introduction of the resistance R_{leak} can be easily transposed to the experimental data (Figure 13.6, right). The understanding of the IV curves enabled to refine the value of the exchange current (j_0) from IV curves as displayed in Figure 13.9.

13.4.2 Determination of the DC built-in voltage

For semiconductor metal junction, as described in equation 2.18, the determination of the exchange current j_0 can lead to an estimation of the built-in voltage V_{bi}. However, a tunnelling probability τ_n as to be taken into account in the case of tunnelling MIS Schottky junction and the determination of the built-in voltage from IV measurements becomes:

$$V_{bi} = -\frac{k_B T}{q}\left(\ln\left(\frac{j_0}{A^* T^2}\right) - \ln\left(\tau_n\right)\right) - \frac{1}{q}(E_F - E_{cb}) \tag{13.12}$$

with τ_n comprised between 0 and 1, a low tunnelling probability ($\tau_n \to 0$) can modify the calculated V_{bi} value. In worth case the V_{bi} can be over-estimated. However, it can be assumed that the deviation due to the tunnelling probability can be neglected if:

$$\frac{\ln\left(\frac{j_0}{A^* T^2}\right)}{\ln\left(\tau_n\right)} >> 10 \tag{13.13}$$

For $j_0^* \sim 10\ \mu A/cm^2$, it turns out that in order to respect the condition given in equation 13.13, τ_n must be higher than 0.062 which can be estimated to be a fulfilled condition with a 2.5 nm SiO_2 layer. Therefore, in this chapter, the built-in voltage V_{bi} is calculated from IV measurements in neglecting the term $\ln(\tau_n)$ in equation 13.12.

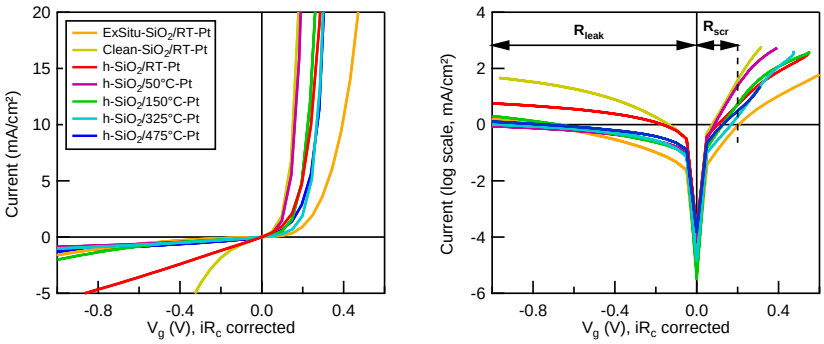

Figure 13.7: IV curves in linear scale (left) and log scale (right) obtained with the different samples prepared in this chapter.

In Figure 13.7 are presented in linear and log scale the IV curves obtained with the samples prepared in this chapter. Regions are defined according to the dominant resistance (R_{leak} or R_{scr}) on the log scale plot. The region where the space-charge region dominates is defined for bias potential comprised between 0 and 0.2 V. The Table 13.1 gives a summary of the values extracted from the plots in Figure 13.7 following the method represented in Figure 13.6. Thus the exchange current j_0, the R_{leak} corrected exchange current j_0^*, the diode ideality factor η_{IV} and the R_{leak} corrected diode ideality factor η_{IV}^* have been determined. In addition, the diode ideality factor $\eta_{R_{meas}}$ determined by reading the slope of $\log(1/R_{meas})$ measured from the RF measurements as shown in Figure 13.3 is provided for comparison with η_{IV}.

	j_0 ($\mu A\,cm^{-2}$)	η_{IV}	$\eta_{R_{meas}}$	j_0^* ($\mu A\,cm^{-2}$)	η_{IV}^*
ExSitu-SiO_2/RT-Pt	12	1.7	1.81	4.3	1.38
Clean-SiO_2/RT-Pt	120	1.4	1.08	36	1.1
h-SiO_2/RT-Pt	169	2.3	2.21	18	1.38
h-SiO_2/50°C-Pt	64	1.3	1.3	51	1.21
h-SiO_2/150°C-Pt	46	1.6	1.74	26	1.45
h-SiO_2/325°C-Pt	40	1.85	1.67	20	1.65
h-SiO_2/475°C-Pt	89	2.08	2.53	47	1.79

Table 13.1: Exchange current j_0, j_0^* and diode ideality factor η_{IV}, η_{IV}^* determined from IV curves in log scale (see Figure 13.6). The star * stands for the data extracted from R_{leak} corrected IV curves.

Looking at the Table 13.1 no particular correlation between the surface

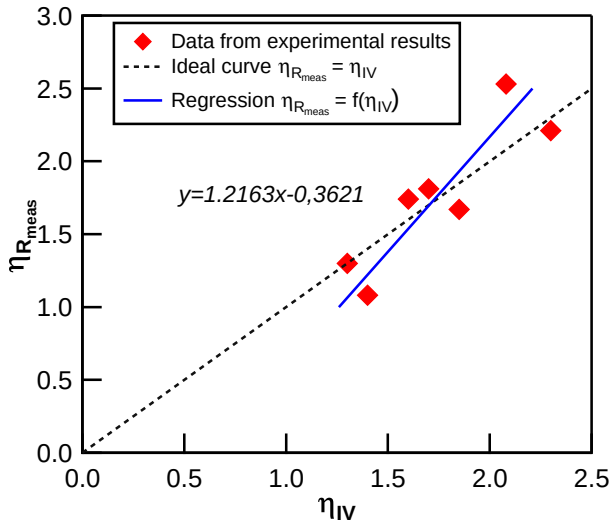

Figure 13.8: Comparison of the value of the diode ideality factor either determined by R_{meas} value $\eta_{R_{meas}}$ or determined from the IV curves in log scale η_{IV}.

preparation with j_0^* and η_{IV}^* can be envisaged. The results suggest that similar j_0^* range is obtained and the reason could be that, whatever the surface preparation, as suggested by in-situ XPS in Chapter 12, the built-in voltage in silicon is the same when platinum is deposited on Si/SiO_2 surfaces. However, the diode ideality factor η_{IV}^* could be degraded with increasing temperature of deposition of platinum. Interestingly, as shown in Figure 13.8, the diode ideality factor η_{IV} and $\eta_{R_{meas}}$ presents correlation which means that the description of the $\log(1/R_{meas})$ plot in Figure 13.6 is relatively correct.

13.5 Built-in voltages and flat-band potential

By compiling the results with the batch of samples presented in this chapter, it is observed that the flat-band voltage V_{fb} determined from the Mott-Schottky plot do not correlate with the built-in voltage determined from the IV curves (Figure 13.9). The values of V_{bi} are in average equal to 0.4 V with not much variation around this value. It means that the deposition of platinum lead to similar built-in voltage V_{bi} for any surface preparation. On the contrary, the flat-band potential V_{fb} spreads from -0.4 V to 0.4 V. Regarding the value obtained by the Mott-Schottky method, it should be mentioned that negative flat-band potentials are found essentially for hydrogen passivated $Si/SiO_2/Pt$ junctions where the temperature of deposition of the platinum is comprised between RT and 325 °C. When the temperature of deposition of the platinum is 475 °C, the flat-band potential is 0.33 V close to the V_{bi} value. This might mean that the temperature of deposition introduce defects, likely because of a reaction between platinum and the SiO_2 layer, which compensate the charges at the Si/SiO_2 interface.

The deviation between the flat-band potential and the built-in voltage is not new and can be attributed to the presence of interface states [237] or to a non-ideal device, especially if the back contact is not ohmic [238]. Thus, many so-called "anomalous" or "abnormal" situations regarding characterization of MIS interfaces have been encountered in numerous type of devices [239] but can be explained taking Q_{def} into consideration. As the back-contact is supposed to be ohmic, it is assumed that the deviation between V_{bi} and V_{fb} originate only from defective electronic states and more particularly from interface states at the $Si/SiO_2/Pt$ junction.

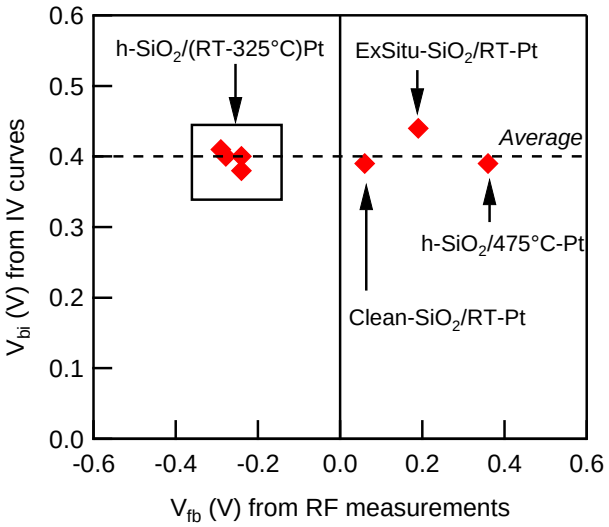

Figure 13.9: Assessment of the built-in voltage (V_{bi}) determined from j_0^* for the various MIS junctions studied in this chapter. For each sample the flat-band voltage (V_{fb}) is determined by Mott-Schottky plots (X-axis) and the built-in voltage V_{bi} from IV curves (Y-axis).

13.6 Interface trapped charges

Experimentally for any samples, when $1/C_{meas}$ is plotted against the bias potential V_g, what is observed matches more to a translation of the theoretical curve to the left depending on interface preparation (Figure 13.10, left). Moreover, for potential lower then the flat-band potential determined in Figure 13.5, the inverse of the capacitive element follow perfectly the shape of a space-charge region capacitive element C_{scr}. At high forward bias, it can be seen that C_{meas} increases asymptotically (as for a theoretical C_{scr}) and even a second capacitive element arises. The second capacitive element is relatively constant ($\sim 10^{-5}$ F/cm^2)on the potential range when it can be detected. It has been associated to the capacitive element related to the 2.5 nm silicon dioxide layer. In theory the value of C_{ox} is 1.3×10^{-6} F/cm^2. It is assumed

that the measured C_{ox} has higher value than the theoretical C_{ox} value because of tunnelling effects for such thin layer.

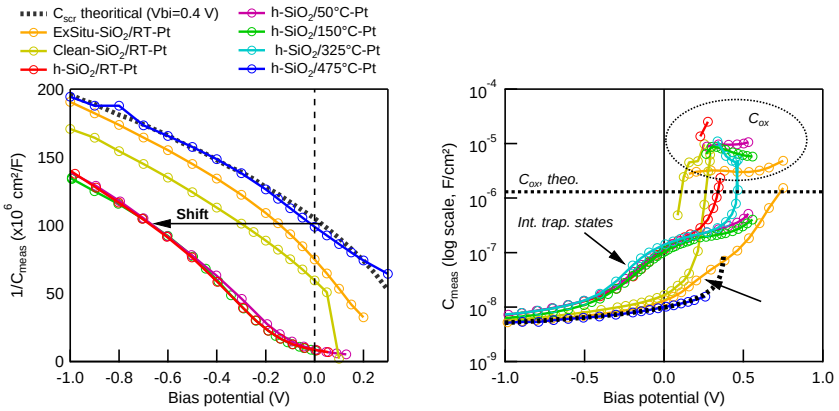

Figure 13.10: Left: Inverse of the measured capacitance C_{meas} versus the bias potential for bias < 0.3 V. This representation enables to evidence the space-charge regime of the curve where the theoritical plot can be easily shifted. Right: C_{meas} plot. For high forward potential, the space-charge region being very small, the capacitive element associated to the silicon dioxide layer can be detected (data in the dotted circle). When platinum is deposited between RT and 350 °C on passivated Si/SiO_2 a bump like behaviour can be observed for bias between -0.5 V and 0.3 V (indicated by the arrows). This has been associated to the ionization of interface trapped state delaying the polarization of the space-charge region.

Between -0.5 V and 0.3 V, a small bump can be clearly observed in the C_{meas} plot (Figure 13.10, right) when platinum is deposited between RT and 350°C on passivated Si/SiO_2 and when platinum is deposited at room temperature on ex-situ sample. In Chapter 12, an interface trapped state is detected by in-situ XPS measurement on passivated Si/SiO_2 interface which pins the Fermi level. It has been assumed that if platinum is deposited on top, this interface trapped state is partially ionized (left schematic, Figure 13.11) but if NiO is deposited with the metal layer oxidation (MLO) technique (see Chapter 14) it is likely totally ionized. Moreover, it has been assumed that the positive charges resulting from the ionization of the interface trapped charges interact with negative charges located at the SiO_2/Pt (or NiO) side. Therefore, it means the more the states are ionized the more charges interact on each side of the silicon dioxide layer. It should result into an increase of the potential drop through the silicon dioxide layer.

During the polarization of the MIS Schottky junction the region between -0.5 V and 0.3 V, the bias potential very likely falls completely through the silicon dioxide layer following this mechanism: for each potential increment ΔV_g, a certain quantity of donors ΔQ_{def} are ionized in such a way that the potential drop through the silicon dioxide layer is ΔV_g and thus $\Delta V_g = \Delta Q_{def}/C_{ox}$ (middle schematic of Figure 13.11). It means that the potential variation at

the pole of the space-charge region is limited. It can be assumed that the polarization of the space-charge region ΔV_{def}, in the potential range where the interface state is ionized, depends on the distribution of the energy state and so:

$$Q_{def} = [D(E)]_{V_1}^{V_2} \tag{13.14}$$

where D(E) is the energy distribution of the donor state density, the brackets '[ ]' the integral of D(E) and V_2-V_1=ΔV_{def}.

For large reverse bias, the donor state is totally ionized and an increment of bias potential ΔV_g falls completely into the silicon space charge region (right plot in Figure 13.11). It is then followed by a Mott-Schottky like behaviour of the measured C_{meas} by impedance spectroscopy.

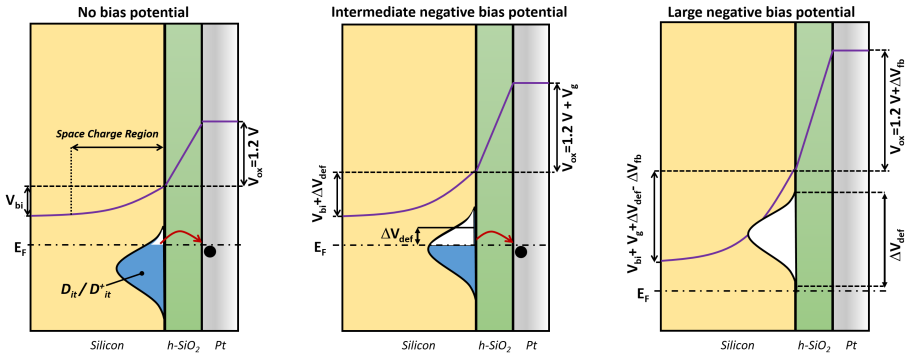

Figure 13.11: Left: Band position for an as-prepared hydrogen passivated $Si/SiO_2/Pt$(RT-350 °C) where the band-bending in the silicon is determined by the position of the donor state at the Si/SiO_2 interface. Middle: Band position when a reverse bias potential V_g is applied. All the bias falls through the silicon dioxide due to the polarisation of the donor state. Right: case representing the a situation where the donor state is totally ionized. In such a case, the bias potential polarize the space charge region of the silicon.

The reason why the h-Si/SiO_2/Pt(475 °C), the hClean-Si/SiO_2/Pt(RT) and the hClean-Si/SiO_2/Pt(RT) provide higher flat band potential V_{fb} is assumed to be related to the fact that for such structures either additional charges (probably fixed charges) ionize the donor states or that as with the NiO deposited by MLO in Chapter 12, the SiO_2/Pt interface have somewhat a higher workfunction. Thus, less polarization is required to ionize the donor state.

Finally, the quantity of donor state can be estimated as being:

$$Q_{def} = C_{ox}\,(V_{bi} - V_{fb}) = 5.6 \times 10^{12}\text{charges/cm}^2 \tag{13.15}$$

13.7 Conclusion

In this chapter, DC and RF electrical measurements of tunnelling $Si/SiO_2/Pt$ MIS Schottky junctions have been carried out. The interpretation of the results enabled to identify the presence of leakage resistance in reverse bias, to refine electrical circuit equivalent for the electrical impedance spectroscopy measurements, to extract the barrier height from IV measurements and to evidence an interface trapped state at the Si/SiO_2 junction. The interface trapped state is assumed to be a donor state which interact with negatives charges located at the SiO_2/Pt interface. If the donor state is not completely ionized for an as-prepared junction, the bias potential will fall first through the SiO_2 layer, then when completely ionized, the bias potential falls in the space-charge region.

CHAPTER 14

Deposition of nickel oxide by DC-Sputtering

Summary

Along this chapter, we study different sputtering based deposition methods of nickel oxide (NiO) on passivated Si/SiO_2 where the SiO_2 layer is about 2.5 nm (tunnel-compatible). Results highlight that the presence of oxygen in the deposition chamber during reactive sputtering drastically deteriorates the Si/SiO_2 interface. The smoothest method for the preparation of NiO is the sputtering of metallic nickel in oxygen-free atmosphere followed by a post-oxidation of the deposited layer in an oxygen rich atmosphere without plasma exposition. We introduce this method as Metal Layer Oxidation (MLO). Using this technique, the barrier height on n-type silicon increases from $\sim$ 0.4 eV for reactively sputtered NiO to more than 0.6 eV for the MLO method. In-situ photo-electron spectroscopy evidences the formation of an extra electronic state when NiO is reactively sputtered, which is assigned to the intense oxygen ion bombardment of the Si/SiO_2 surface during the process. This extra-electronic state pins the silicon energy bands in an undesirable position. The MLO process could be implemented to create high interface quality, for example: in silicon based solar cell and water splitting applications.

The scientific material of this Chapter served to compose the article:

R. Poulain J. Proost and A. Klein. **Sputter Deposition of Transition Metal Oxides on Silicon: Evidencing the Role of Oxygen Bombardment for Fermi-Level Pinning**. *physica status solidi (a)*, 2019.

In open access online: `https://doi.org/10.1002/pssa.201900730`

14.1 Introduction

Transition Metal Oxides (TMO) provide a wide set of materials properties with varying work functions and band gaps. Recently, the interest in interfacing TMOs with silicon has substantially increased. Silicon/TMO structures can be encountered in water-splitting devices where the TMO layer is a catalytic layer [20, 240], but also in solid-state junctions where the TMO layer could be implemented for creating a charge selective contact [23, 25, 240–245]. For instance, n-type materials as TiO_2 and ZnO could be implemented to create electron selective contacts on silicon [241, 242] while p-type materials or high work function materials, such as MoO_3, WO_3, V_2O_5 and NiO, could be implemented to create hole selective contacts [240, 243, 244]. The literature on TMO deposition suggests that soft deposition methods, such as atomic layer deposition, thermal evaporation, pulse laser deposition or solution-based deposition would be the most adequate for depositing a TMO layer on a photo-active material [24, 26, 27, 242]. On the contrary, sputtering or e-beam evaporation deposition might damage the silicon surface and reduce the interface quality [23, 29, 240, 246, 247].

Regarding the sputtering technique, Ellmer *et al.* have shown that negative ion bombardment (e.g. by oxygen ions) in the chamber of deposition can have significant consequences [223]. Contrary to other particles having kinetic energy in the 1-20 eV range, the negative ions can escape the plasma at extremely high energy. For instance, having a cathode potential of 400 V, a negative oxygen ion can acquire a kinetic energy of 400 eV, which corresponds to a particle speed of $\sim$ 70 km/s in vacuum. Several issues can arise from negative ion bombardment: etching of the substrate or implantation of ions in the sub-surface of the deposited layer. The latter, because of the introduction of interstitial oxygen, has been presented as being one reason of the decrease in conductivity in n-type TCO [248]. In order to reduce negative ion bombardment, a list of solutions has been proposed: the increase of the pressure, the reduction of the cathode potential, the increase of the distance between the target and the sample or to adopt an off-axis deposition [223].

Thus, the direct deposition of TMO on silicon by reactive sputtering might not be appropriate. It could produce a high number of defects, which can potentially pin the Fermi level and act as recombination centers for electron/hole pairs, created in the silicon under illumination [102, 249].

Also, to minimize the quantity of defects at the silicon/TMO interface, the insertion of a thin passivating silicon dioxide layer (2-3 nm [103]) might be beneficial to reduce the interface state density, particularly after hydrogen passivation [103, 104]. Thus, charge carrier lifetimes of 500 μs have been reported for bare Si/SiO_2 interfaces after hydrogen passivation [122]. Also, the addition of alumina on top of the silicon dioxide layer could help to further improve the performance of the device [120, 125, 126]. We therefore studied TMO deposition on top of both hydrogen passivated n-Si/SiO_2 and

n-Si/SiO_2/Al_2O_3 substrates using photoelectron spectroscopy (XPS). XPS provides simultaneous information on the chemical nature of the surfaces and of the electronic structure [9]. It has the advantage that single interfaces can be studied, without the requirement of optimizing a device structure, in which many layers and patterns for e.g.: electrical characterization are necessary.

Along this chapter, we will see that during reactive sputtering of a TMO on silicon, the negatively charged oxygen ions deteriorate the interface. This is indicated by the formation of defect states in the SiO_2 layer, which induce a Fermi level pinning and limit the band bending in the Si substrate. Defect formation and Fermi level pinning can be avoided by growing the TMO sequentially using repeated sputtering and oxidation of a very thin metallic layer. We introduce this method as Metal Layer Oxidation (MLO). We take, as practical example, the deposition of p-type NiO on n-Si/SiO_2 and n-Si/SiO_2/Al_2O_3 substrates, as NiO could be implemented in numerous applications including silicon based MIS structure [23, 25] and photoelectrochemical water splitting devices [20].

14.2 Experimental

Experiments are realized with n-type float zone silicon single crystal (100) wafers. The sheet resistivity has been determined by the van der Pauw method and is 10.1 Ω cm. Therefore, the doping concentration is estimated to be 4.4 $\times$ 10^{14} /cm^3 and so the Fermi level position to the valence band maximum is calculated to be 0.83 eV.

Silicon chemical cleaning and silicon dioxide thermal growth are detailed in Section 3.2. Si/SiO_2 surface passivation by atomic hydrogen is explained in Section 3.2.4 and all surface measurements are carried out in the DAISY-MAT system (Section 3.3.1).

Atomic Layer Deposition (ALD)-alumina (Section 3.2.5) is realized at low temperature in order to avoid any SiO_2 de-passivation reaction. Overall, ten ALD cycles are realized. After the ALD deposition another hydrogen cleaning and hydrogen passivation step is processed as previously described.

The deposition of nickel oxide on the Si/SiO_2 substrates has been realized by DC and RF reactive sputtering in 5% O_2 and a target-to-substrate distance of 13 cm. The pressure is set to 6 Pa and 1 Pa for DC and RF sputtering, respectively. The Metallic Layer Oxidation (MLO) process has been realized in similar condition except that the nickel layer is DC sputtered in oxygen-free atmosphere, which is then followed by an in-situ post-oxidation step without plasma exposure. The oxidation of the metallic nickel in UHV works relatively well for thickness of less than 1 nm. Oxidation was tested for gas pressures between 1-6 Pa from 10% to 100% oxygen content and various temperatures from RT to 200 °C. All conditions provided a fully oxidized nickel layer as confirmed by XPS.

All XPS measurements are realized with a 1486.6 eV Al-K_α monochromatic X-ray and 45° take-off angle to the sample. Fermi level in the XPS chamber is measured beforehand against a clean silver surface used as reference for post-data correction.

14.3 Results and Discussion

The in-situ XPS measurements of the Si 2p region display the typical two emission structures, which can be associated to the silicon and the silicon dioxide layer, respectively. As seen in Figure 14.1, the elemental silicon peak is at lower binding energies. The peak is composed of a double feature: a main peak Si^0 and a satellite peak, which are actually the photoemission of the spin-orbit split Si $2p_{3/2}$ and Si $2p_{1/2}$ components, respectively. At higher binding energies, the photoemission from the silicon in the SiO_2 layer is observed. This is labelled as Si^{IV} in Figure 14.1.

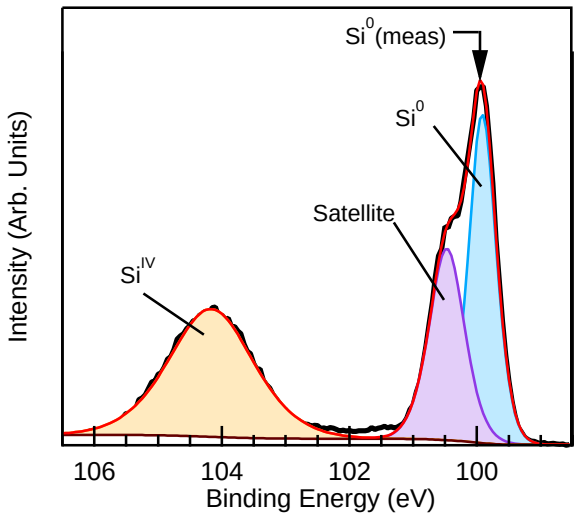

Figure 14.1: Typical XP spectra of the Si 2p region. Two main features can be indentified: the photoemission from the silicon dioxide layer on the surface (Si^{IV}) and the photoemission from the elemental silicon substrate. The elemental silicon is composed of a main peak Si^0 and a satellite peak, which are associated to the spin-orbit split Si $2p_{3/2}$ and Si $2p_{1/2}$ components, respectively. The Si^0(meas) arrow indicates the Si^0 peak position.

14.3.1 Chemical interface properties

As observed in Fig. 14.2, after the deposition by sputtering of nickel in oxygen free atmosphere and before oxidation, the XP spectra of the Ni 2p region

displays a sharp peak at binding energy $\sim$ 854 eV which can be associated to elemental nickel Ni^0, and, after exposition of the metallic layer to an oxygen rich atmosphere, the peak is broadened and shifted to higher binding energy as a results of the oxidation of nickel to nickel oxide. No obvious trace of metallic nickel is visible after oxidation. This result indicates that the metallic nickel layer is totally converted into nickel oxide after oxidation and so that the MLO method is able to produce a metal oxide layer.

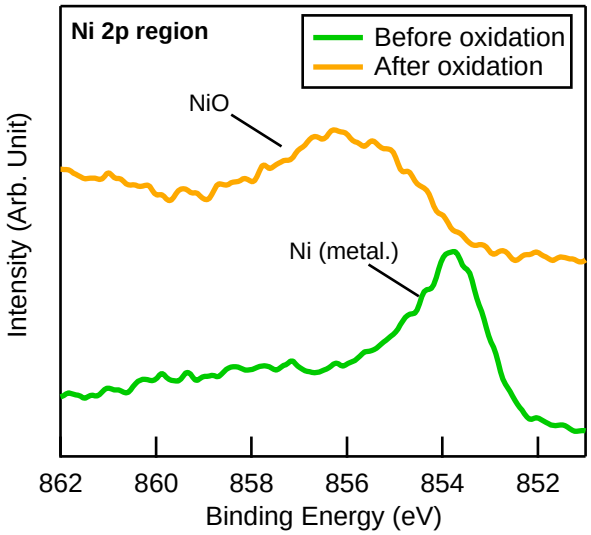

Figure 14.2: XP spectra of the Ni $2p_{3/2}$ region before and after exposition of a metallic nickel layer to an oxygen rich atmosphere. The thickness of the final nickel oxide layer is about 0.3 Å.

The evolution of the Ni $2p_{3/2}$ emission in dependence on NiO film thickness is shown in Fig. 14.3. The spectra are recorded during NiO growth using the metal layer oxidation process. The spectra of the thickest layer shows the typical features of NiO with a main emission line near 854 eV and a characteristic satellite emission at 1.5 - 2 eV higher binding energies [86, 250]. A more detailed description of the Ni 2p spectra is provided in Chapter 4. Identical spectra are obtained for magnetron sputtered films. At lower film thickness, the spectra are broadened and have higher binding energies. Such a behaviour is frequently observed in dependence on film thickness [250] and can be associated to the change in the local structure of the NiO layer [251]. The Si substrate intensity is attenuated exponentially in dependence on NiO film thickness, indicating a layer-by-layer growth and a conformal coverage of the NiO layer.

Si 2p photoelectron spectra recorded during stepwise growth of NiO onto Si/SiO_2 are shown in Fig. 14.4. Three different experiments with NiO

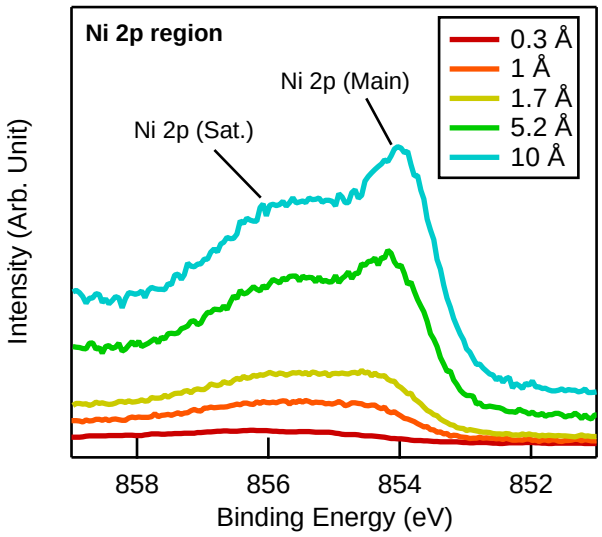

Figure 14.3: XP spectra of the Ni $2p_{3/2}$ region after exposure to oxygen of a thin metallic nickel layer deposited by sputtering in argon. The spectra are recorded for successive NiO layers.

grown by metal-layer-oxidation, reactive DC and reactive RF sputtering are compared. The spectra are normalized to the Si^0 intensity for better comparison.

The spectra in Fig. 14.4 clearly show that a new emission arises between the Si^0 and the Si^{IV} peaks when NiO is deposited by reactive DC or RF magnetron sputtering. According to literature, such intermediate emissions, which are labeled as Si^{def} in Fig. 14.4, can be associated to the presence of non-completely coordinated Si with intermediate oxidation states (Si^{I-III}) [123, 227, 252, 253]. Contrary to reactive sputtering, no Si^{def} emission is observed if the NiO is grown by the MLO method. The results indicate that Si^{def} only appears when oxygen is present during sputtering. This suggests that the Si^{def} emissions are related to the bombardment of the substrate with negatively charged oxygen species formed in the plasma during deposition. For the reactively sputtered NiO films, the Si^{def} emissions increase with NiO film thickness, indicating that its intensity is proportional to the exposure time of the surface to the plasma.

The maximum of the Si^{def} emission occurs at 58% of the distance between the Si^0 and the Si^{IV} peaks. Therefore, the Si^{def} state might correspond to the Si in the oxidation state +III, which has been reported to occur at 62% of the distance between the Si^0 and the Si^{IV} peaks [123].

The Si^{def} emissions may have a different origin: i) they can result from an uncomplete reaction, of the incoming oxygen ions with the underneath

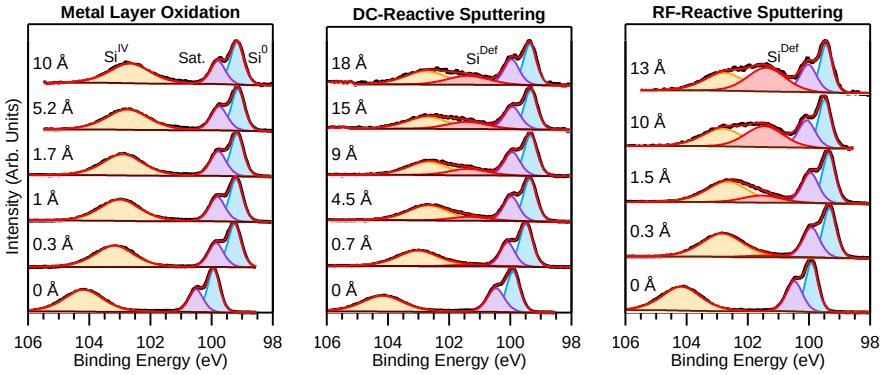

Figure 14.4: Si 2p spectra measured by XPS during the interface experiments with NiO on Si/SiO_2 substrates. Three deposition methods have been evaluated: Metal Layer Oxidation (MLO), DC reactive sputtering and RF reactive sputtering. The spectra are normalized to the Si^0 intensity for better comparison of the evolution of the peak shapes.

silicon, after diffusion through the SiO_2 layer; ii) they could be related to surface etching of the silicon dioxide layer; or finally iii) they could be the fingerprint of the presence of interstitial oxygens in the SiO_2 layer. The latter case (iii) could eventually result in the formation of Si^{III} states under X-ray irradiation [111].

Regarding case i), it has to be mentioned that we also observed a comparable Si^{def} emission next to the Si^{IV} peak (Appendix A.7) in the course of deposition of Barium Strontium Titanate (BST: (Ba,Sr)TiO_3 on thick SiO_2 by RF sputtering in an Ar:O_2 (99:1) atmosphere. In this case, the oxygen source could be the target itself. This result suggests that Si^{def} states appear even when no metallic Si^0 is present in the substrate, indicating that the Si^{def} state is not related to the reaction of the elemental silicon Si^0 with the incoming oxygen ions. Therefore, case i) is rather unlikely.

Cases ii) and iii) can be differentiated by comparing the intensity of the oxide emission in comparison to the intensity of the elemental silicon Si^0. For case ii) (etching of SiO_2), a reduction of the SiO_2 thickness has to be expected. Therefore, the intensity of the elemental silicon should increase in comparison to the Si^{IV} peak. On the contrary, at first sight, no substantial change of that intensity ratio is expected for case iii) (interstitial oxygens). To compare the relative area intensity, the ratio R_A between the area of the oxide (A_{oxide}), which includes the Si^{IV} and the Si^{def} states, and the elemental silicon ($A_{silicon}$) is introduced:

$$R_A = \frac{A_{\text{oxide}}}{A_{\text{silicon}}} \tag{14.1}$$

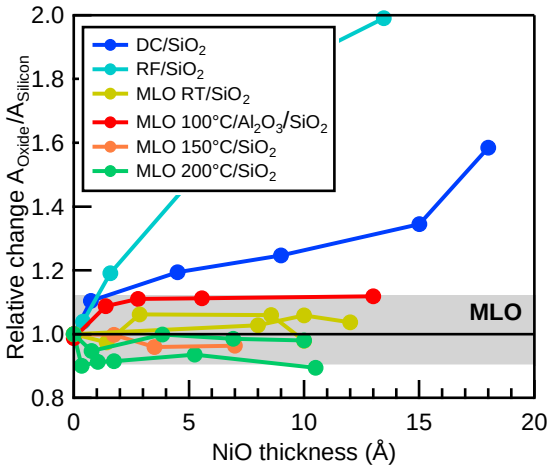

Figure 14.5: Evolution of the ratio of the oxide area (Si^{IV} and Si^{def}) over the elemental silicon area Si^0 for the different NiO deposition methods. Values are normalized against the value obtained before NiO deposition.

The evolution of the ratio R_A with NiO thickness is displayed for the different deposition methods in Fig. 14.5. The result clearly indicates that the ratio R_A increases with NiO thickness for both reactive sputtering methods. This trend discards etching of SiO_2 as origin of the Si^{def} states. This is consistent with the relatively high pressure used for the DC and RF sputtering, which favors thin film deposition in the Keller-Simmon regime, where no etching of the surface is expected [223].

The data in Fig. 14.5 also show that the ratio R_A does not significantly change when NiO is prepared by the MLO method, contrary to what can be obtained with reactive sputtering. This indicates that the MLO method preserves the Si/SiO_2 interface integrity relatively well.

Although a more complicated situation might also account for the Si^{def} states, our analysis suggests that these states are related to the presence of oxygen interstitial in the silicon dioxide layer (case iii). This proposition is supported by the work of Chen *et al.* [111], who showed using DFT calculations that oxygen interstitials in SiO_2 are the origin of numerous defective structures, which can be stabilized along the oxygen bridging bonded (OBB) structure:

$$\equiv Si - \overset{\overset{O_i}{|}}{O} - Si \equiv \tag{14.2}$$

The OBB structure might convert into a Peroxy Radical (POR) structure where the bond between the silicon and the oxygen (Si-O) is broken when exposed to irradiation (e.g. X-Rays) [111]. In the POR structure, the silicon atom would be bonded by three covalent pairs only to the silicon dioxide structure. Therefore,

the Si^{def} state observed in this work may be associated to a POR structure, which should exhibit a binding energy corresponding to Si^{III} in XPS.

14.3.2 Electronic interface properties

Interface experiments such as those shown in Fig. 14.4 aim at determining the built-in voltage (V_{bi}) in the silicon substrate of the $Si/SiO_2/NiO$ interface. However, the observed binding energy shifts of the Si 2p emission do not necessarily correspond to the built-in voltage. The observed shift can be smaller, as a photovoltage U_{ph} can be induced by the electron-hole pairs generated by the X-ray irradiation [254]. The binding energy of the elemental Si relative to the calculated flat-band position ($\Delta E_b(Si^0)$), then corresponds to:

$$\Delta E_b(Si^0) = E_{fb}(Si^0) - E_b(Si^0) = q\,(V_{bi} - U_{ph}) \tag{14.3}$$

where q is the charge of the electron. Following the calculations described by Schafranek *et al.* [255], which describe measurements in the same setup used in this work, the photovoltage in silicon can be estimated for a built-in voltage V_{bi} varying from 0 V to 0.9 V. In Fig. 14.6 the relationship between the measured peak deviation $\Delta E_b(Si^0)$ in dependence on built-in voltage is shown. It shows two different regimes: a linear dependence of $\Delta E_b(Si^0)$ on V_{bi} for $V_{bi} < 0.6$ V and a saturation regime where $\Delta E_b(Si^0) \approx 0.62$ eV for $V_{bi} > 0.6$ V. The development of the photovoltage causes a saturation of the observable binding energy shifts. Consequently, $\Delta E_b(Si^0)$ measured by XPS is only directly correlated to the built-in voltage if the value is smaller than ~ 0.6 V. Larger built-in voltages can not be identified any more. Therefore, if the observed binding energy of the Si^0 emission is 0.6 eV higher than that of the flat band position, it can only be said that the built-in voltage is 0.6 V or higher.

The binding energies of the Si^0 emission of hydrogen passivated Si/SiO_2 substrates are shown in dependence on NiO film thickness in Fig. 14.7. After hydrogen passivation, the binding energy of the Si peak $E_b(Si^0)$ is close to 99.6 - 99.7 eV (Figure 14.7). The flat-band position ($E_{fb}(Si^0)$), where no charge accumulation (negative or positive) occurs at the silicon surface, is calculated to be 99.57 ± 0.05 eV when the bulk Fermi level and the binding energy of the Si^0 emission with respect to the valence band maximum are taken as 0.83 eV (see section 14.2) and 98.74 eV [230], respectively. Therefore, as discussed in Chapter 11, the measurements suggest that passivated Si/SiO_2 samples are slightly accumulating negative charges at the silicon surface (Figure 14.7). This would imply that not all trapped charges are suppressed after hydrogen passivation. However, the hydrogen passivation step was found to remove contaminants and to reduce substantially the accumulation of charges at the Si/SiO_2 interface (See Chapter 11). The accumulation of negative charge after the hydrogen passivation step can arise because of the presence of positive trapped charges at the Si/SiO_2 interface [106, 110, 112] or in the SiO_2 layer [108, 109, 111].

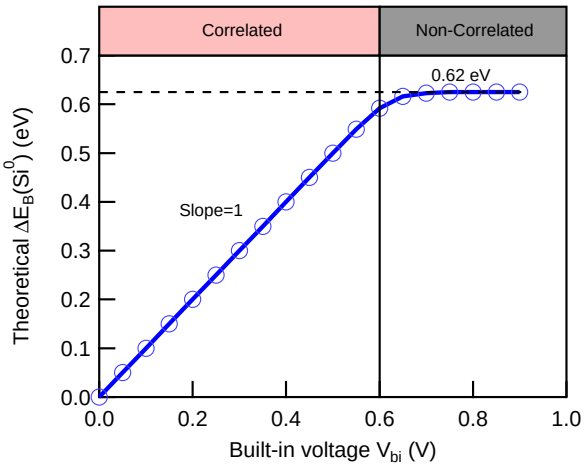

Figure 14.6: Calculated peak deviation $\Delta E_b(\mathrm{Si}^0)$ (see Eq. 14.3). For built-in voltages $V_{bi} > 0.6$ eV, the peak deviation saturates due to the development of a photovoltage induced by the X-ray source.

Figure 14.7 shows that the position of the Si^0 peak shifts to lower binding energy for any deposition method, indicating that the deposition of NiO leads to the formation of a depletion layer in the silicon with a built-in voltage $V_{bi} > 0$. The binding energies at the interfaces with RF and DC sputtered NiO saturate at ~ 99.2 eV, corresponding to a built-in potential of 0.4 V. This value is in line with what has been reported in literature [20]. In contrast, the binding energies obtained when NiO is deposited by MLO at $T > 100°C$ saturate at $\sim$ 99.0 eV, which is 0.6 eV lower than expected for flat band condition. As discussed above (see Fig. 14.6), it can then only be said that the built-in voltage V_{bi} in the silicon is at least 0.6 eV.

The interface experiments highlight that a larger Si^0 peak deviation is obtained with the MLO method if sufficient temperature is brought to the substrate during the oxidation step (Figure 14.7). A lower peak deviation, comparable to that for reactively sputtered NiO, is observed when NiO is deposited by MLO with the oxidation step carried out at room temperature. This lower V_{bi} could be due to an incomplete surface reaction of the metallic nickel with oxygen during the oxidation step, or due to the formation of a non-homogeneous material. It is mentioned that $\Delta E_b(\mathrm{Si}^0)$ is also $\sim$ 0.6 eV, when a thin ALD Al_2O_3 layer is inserted between the silicon dioxide and the nickel oxide layer. This can be particularly interesting as it has been reported that tunneling SiO_2/Al_2O_3 structures on top of silicon might provide better device performance [120, 125, 126]. Also, it could be assumed that the alumina layer may be used as a diffusion blocking layer to avoid degradation over time, by the reaction of hydrogen from the hydrogen passivated SiO_2 layer and the reduction of the NiO layer.

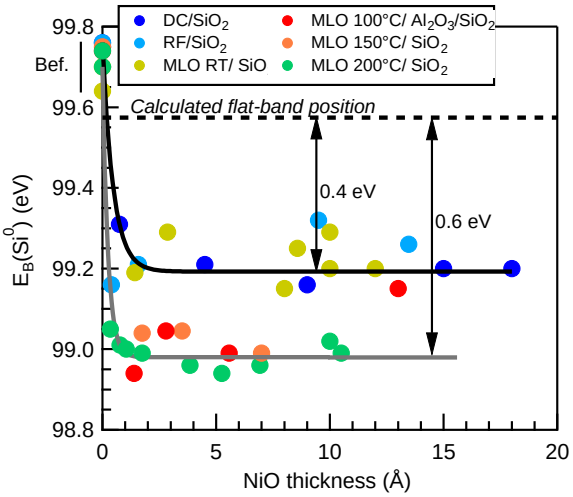

Figure 14.7: Binding energy of the Si^0 peak during interface formation of n-Si/SiO_2 substrates with differently deposited NiO in dependence on NiO film thickness. The label Bef. stands for before and indicates the position of the Si^0 before the deposition of NiO. The Si^0 binding energies of the uncovered, hydrogen passivated samples are slightly above the calculated flat-band position. It suggests that negative charges accumulate at the interface.

Finally, as depicted in Figure 14.8, the limited Si^0 deviation when NiO is deposited by reactive sputtering could be associated to the presence of oxygen interstitials in the silicon dioxide layer, resulting from the intense bombardment of the surface by energetic ionized oxygen particles during deposition. In comparison to the results obtained by MLO, the defects produced during NiO deposition by reactive sputtering would pin the Fermi energy in a non-desired position. Therefore, in order to produce a high quality interface of a transition metal oxide by sputtering on Si/SiO_2 substrates, the results presented in this chapter suggest that it is preferable to start from a metallic target, to sputter, without oxygen, a thin metallic layer (< 1 nm) and to oxidize by exposing the metallic layer to oxygen without the plasma. For practical use, this method can be referred to as Metallic Layer Oxidation (MLO).

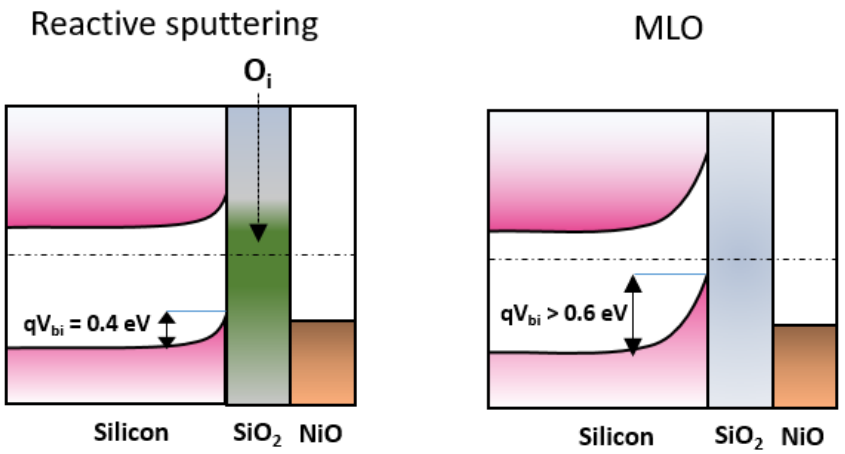

Figure 14.8: Band-diagram representing the $Si/SiO_2/NiO$ junction when NiO is deposited by reactive sputtering (left) or by metal-layer-oxidation (right). The silicon band-bending is pinned at 0.4 eV for reactively sputtered NiO due to the presence of oxygen interstitial (O_i), while it might exceed 0.6 eV if NiO is prepared by the MLO method.

14.4 Conclusion

Along this chapter, an alternative to reactive sputtering has been presented to interface thin TMO layers (< 5 nm) with Si/SiO_2. The deposition consisted of the growth of thin metallic (nickel) layers (< 1 nm) in oxygen free atmosphere followed by a subsequent oxidization step in oxygen without plasma, where the addition of thermal energy during the oxidation process might increase the TMO layer quality. Named Metallic Layer Oxidation (MLO), the method has the advantage to avoid direct surface exposition to negative oxygen ion bombardment as for DC and RF reactive sputtering.

Thus, the band deviation in silicon has been estimated to be at least 0.6 eV when passivated Si/SiO_2 substrates are interfaced with nickel oxide by the MLO method. On the contrary, DC and RF reactive sputtering processes provide a more limited band-bending ($\sim$ 0.4 eV). The results suggest that reactive sputtering pin the bands in an undesired position as a consequence of the intense bombardment by negative oxygen ions of the Si/SiO_2 interface which might implant oxygen interstitials into the SiO_2 layer.

CHAPTER 15

The integrated device

15.1 Introduction

After three years of research on nickel oxide with the final objective being to assemble a functional device for silicon based water-splitting, a pretty clear picture of structure and the method to mount the device could be defined.

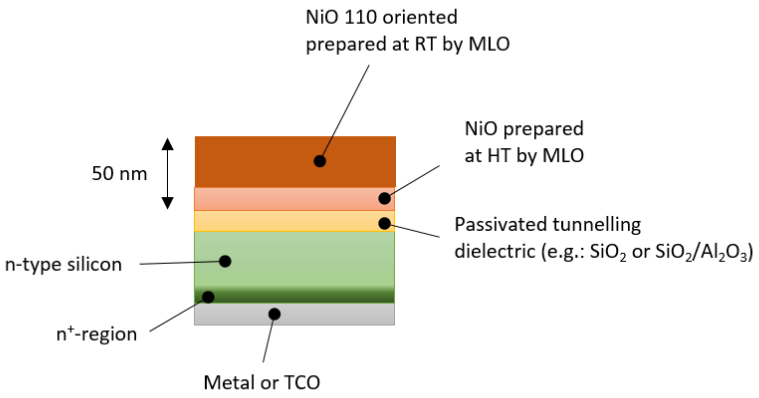

Figure 15.1: Schematic of the ideal photo-anode for water-splitting based on n-type silicon and nickel oxide according to the results obtained along this thesis. The electrolyte is on the nickel oxide side.

Thus, as drawn in Figure 15.1 the ideal device would be n^+ back-contacted by phosphor diffusion (see Section 3.2.2) and where, for the front contact, a tunnelling SiO_2 layer (2-3 nm) is thermally grown (see Chapter 11). The front contact would be then hydrogen cleaned and passivated by surface exposure to a hydrogen plasma source (see Chapter 11). Although not proved, an ALD alumina layer could be deposited in addition on top of the passivated Si/SiO_2 structure to improve the interface quality (see Section 3.2.5). The nickel oxide has to be deposited by the metal layer oxidation (MLO) method detailed in Chapter 14 to avoid introduction of oxygen interstitials in the silicon dioxide layer in the case of direct exposure of the front contact to negatively ionized oxygen particle bombardment as for reactive sputtering. Ideally, the MLO

layer has to be prepared at high temperature. However, as demonstrated in Chapter 10, the NiO prepared at high temperature has poor catalytic performance towards the OER. Therefore, an additional NiO layer prepared at room temperature on top of the NiO prepared at high temperature should be deposited by MLO again. Eventually, if possible the condition of deposition of the nickel oxide thin film should be selected in order to favour the growth of the (110) orientation at room temperature. Indeed, the (110) orientation might produce a more stable and catalytically active hydroxide structure according to Chapter 9.

Front side illumination (through the electrolyte) has been preferred to back side illumination (through air). Indeed, front side illumination allows to sputter a metal on the back-contact whereas a back side illumination would require the deposition of a transparent conductive material (e.g.: indium tin oxide), which would inevitably produce an intense oxygen bombardment of the back-contact and might potentially deteriorate the back-contact interface quality.

15.2 Experimental

Two water-splitting prototypes have been fabricated and characterized. Because of lack of time, the prototypes did not resemble the ideal structure proposed in Figure 15.1 and no deep characterization of the devices could be realized.

Both structure were n^+ back-contacted (Section 3.2.2) and a tunnelling SiO_2 layer was thermally grown to form the front contact (Section 3.2.3), which was subsequently passivated by atomic hydrogen generated in a plasma source (Section 3.2.4).

The first structure consisted in depositing nickel oxide ($\sim$ 1 nm) by MLO (Chapter 14) at room temperature on passivated Si/SiO_2 junction. Room temperature oxidation was preferred to avoid any risk of surface de-passivation by the reaction of hydrogen atoms from the silicon dioxide layer by direct contact with the oxygen diffusing through the metallic layer during the oxidation step of the MLO process. Hydrogen depassivation has not been effectively proven to happen but because of lack of time the least risky approach has been chosen.

The second structure consisted in oxidizing the metallic nickel layer at (100) °C where an hydrogen passivated ALD alumina layer (10 cycles, $\sim$ 1 nm) is deposited on top of the Si/SiO_2 layer at 50 °C (Section 3.2.5). The alumina layer is also hydrogen cleaned and passivated. The thickness of the alumina layer is supposed to be thin enough to allow charge tunnelling. The effect of the alumina layer has not really been well identified at this stage although it could improve substantially the interface passivation (Section 2.3.3). Also the insertion of the alumina between the passivated silicon dioxide and the

nickel oxide could provide a chemical barrier hindering a possible reaction of the hydrogen from the silicon dioxide layer and the oxygen from the nickel oxide layer. It has been assumed that the alumina layer helps to reduce any depassivation process of the Si/SiO_2 interface and so such interface could be more compatible with higher oxidation temperatures during the MLO process. Thus NiO is deposited by the MLO process ($\sim$ 1 nm) at (100) °C on the passivated $Si/SiO_2/Al_2O_3$ structure.

Before the electrochemical experiments, the shift of the band position has been evaluated in DAISY-MAT (Section 3.3.1) after surface exposure of the $Si/SiO_2/Al_2O_3/NiO$ (MLO-100 °C) structure to water (water exposure experiments, Chapter 8). Because of lack of time, the experiment has only been carried out on one structure.

Electrochemical experiments were performed in a 0.1 M NaOH solution at room temperature at TU-Darmstadt with PECC-2 (Zahner PEC-Cell) and a solar simulator where the distance between the light source and the sample was set such that the received surface energy density on the sample surface is equal to 1 sun (See Section 3.3.2). Because of lack of time no in-depth study of the two designs has been carried out. Thus, the electrochemical experiments simply consisted in 10 cyclic voltammetry at 50 mV/sec. The last cycle is the one represented in Figure 15.3

15.3 Band-alignment

Water exposure experiments evidence that the band-bending in the silicon is reduced of about 100 meV when the sample surface is exposed to water in vacuum (Figure 15.2).

It should mentioned that the peak associated to elemental silicon is at about 0.45 eV lower binding energy than the calculated flat-band position. This value is above the value obtained for the case of Fermi level pinning when platinum is interfaced (Section 12), which was about 0.2-0.3 eV. It means that the shift to higher binding energy of the Si^0 peak can not be due to the pinning of the Fermi energy.

Thus, even though the reason is not absolutely clear, it is assumed that similar to what was observed for oriented NiO thin films in Chapter 8, the Nickel oxide deposited by the MLO process favours the adsorption of negatively charged hydroxide species (OH^-), leaving behind a positive layer of hydrogen in the layer of water in interaction with the NiO surface.

The in-situ XPS measurements in Figure 15.2 indicates that the band-bending in the silicon is lower when the $Si/SiO_2/Al_2O_3/NiO$(MLO-100 °C) surface is exposed to water than on bare structure. This result highlights that the band-bending in the silicon is not fixed and can evolve depending on the chemical species present on the NiO surface. This can be a major issue for the

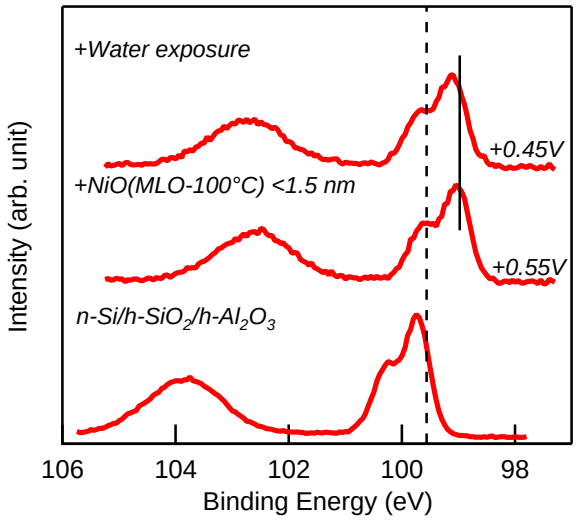

Figure 15.2: XP spectra of the Si 2p region of the as-prepared $Si/SiO_2/Al_2O_3$ layer after deposition of the NiO layer by the MLO method at (100) °C and after water exposure of the surface of the $Si/SiO_2/Al_2O_3/NiO$(MLO-100 °C) structure. The experiments are realized in-situ in the DAISY-MAT system.

water-splitting devices studied in this chapter especially when the interface is plunged into an electrolyte.

15.4 Electrochemical measurements

Figure 15.3 displays the result of the electrochemical measurement in the dark and under light.

In the dark, the current density is very limited, even for large forward potential where the oxygen evolution reaction should be triggered (Figure 15.3, left). The variation of current of the $Si/SiO_2/Al_2O_3/NiO$(MLO-100 °C) structure is particularly restricted, on the contrary $Si/SiO_2/NiO$(MLO-RT) provides a broader cyclic voltammogram. The reason being that in the potential window adopted for the electrochemical experiments, the junctions works as photo-detector (the junction is in reversely biased), and so in the dark the absence of photo-generated minority charge carriers prevent any conduction. It results to the situation where no electrical charge can be transferred from the silicon to the electrolyte.

Under illumination, the electrochemical measurements display a substantial increase of the current density in the 1.2-2 V potential range, typical of the OER, for both samples (Figure 15.3, right). The current arises because of photo-generated minority charge carriers in the valence band of the silicon

after electron-hole pair are formed under photo-excitation. However, in comparison to what could be obtained on poly-crystalline NiO thin films (Section 10), the current density is relatively low. For instance, on poly-crystalline thin films prepared at room temperature the current density exceeds 40 mA/cm^2 at 1.6 V vs RHE in 1 M KOH whereas in Figure 15.3, the current does not exceed 5 mA/cm^2 in 0.1 M NaOH. Although the solution is less concentrated, the lower current density for the devices can not be directly associated to the difference in concentration of the electrolyte. Indeed, a lower electrolyte concentration would provide a saturating current plateau. Thus from this comparison it is concluded that a thin NiO layer in the 1 nm range and grown by MLO is not providing an efficient catalytic material for the OER.

However, it is observed that current density is higher for the $Si/SiO_2/NiO$(MLO-RT) structure than for the $Si/SiO_2/Al_2O_3/NiO$(MLO-100 °C) structure (Figure 15.3, right). The reason is not absolutely clear as deeper investigations need to be carried out in order to clarify the origin of this difference, but two reasons could be raised: first the catalytic properties of the NiO prepared by MLO at (100) °C is worse than the NiO prepared by MLO at room temperature, second, the insertion of the alumina layer might hinder charge transfer more than expected from the silicon to the NiO.

Interestingly, no saturation of the current is observed in the cyclic voltametry obtained under light (Figure 15.3, right) contrary to what was reported by Tengeler *et al.* when NiO is reactively DC sputtered onto Si or Si/SiO_2 [20]. Although the condition of the measurements differ in this study, the saturation of the current reported by Tengeler *et al.* is indicated by a dashed horizontal line on the right picture of Figure 15.3. This indicates that the MLO method can provide an improvement in the preparation of photo water-splitting devices based on Si/SiO_2 structure.

15.5 Conclusion

The main results obtained along this thesis in order to fabricate a functional water-splitting device have been implemented in two types of structures. The results obtained did not provide clear evidence of that a functional water-splitting device has been built, but instead raised additional questions, which would need to be answered through an in-depth characterization and structure optimization.

However, it has been shown by in-situ XPS measurement that the band-bending at the silicon interface is reduced in contact to water. It implies that the silicon band position is not fixed but might evolve according to the adsorbate anchoring on the NiO surface. The electrochemical results of the two devices suggest that additional optimization must be carried out, which could be, for instance, to render MLO deposited NiO thin films catalytically active towards the OER or to improve the charge transfer from the silicon to the catalytic site at the interface, if an alumina layer is inserted.

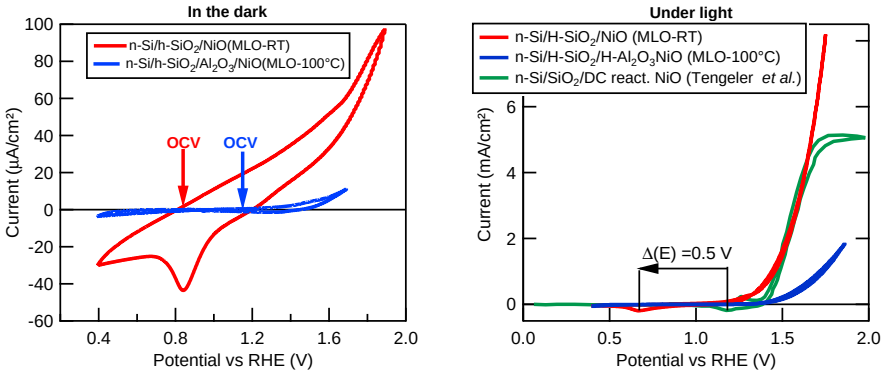

Figure 15.3: Cyclic voltametry of the two experimented devices for photo water-splitting, in the dark (left) and under light (right). The green curve represents the saturation of the current when NiO is DC sputtered on Si or Si/SiO_2, as reported by Tengeler et al. [20]. However, the comparison should be taken with care as the conditions of measurement in the paper of Tengeler et al. are not exactly the same as those used in this chapter.

CHAPTER 16

Conclusion and outlook for future works

Everything comes to a end, even a PhD program. The research carried out during the three years was focused on the study of nickel oxide and its use in the anodic part of a photo water-splitting device where n-type silicon is used as photo-active material. The work was distributed between UCL and TU-Darmstadt, and the realization of the project can be basically split into three parts: the study of the NiO surface properties by in-situ XPS/UPS, the study of the NiO/electrolyte interface and the study of the silicon/SiO_2/NiO interface.

Regarding nickel oxide, as detailed in Chapter 4, it has been found that the conditions of preparation during reactive sputtering (temperature, oxygen concentration) can substantially tune the nickel oxide thin film surface properties. Thus, at high temperature and at intermediate oxygen concentration the Fermi energy can reach up to 1.1 eV above the valence band maximum and the work function can be as low as 4.5 eV. At room temperature, the Fermi energy is decreased by 0.5 eV and reaches 0.6 eV for any oxygen concentration, while the workfunction increases to 5.2 eV. The variation can be related to the creation of defects acting like dopants in the NiO thin film crystallographic structure, which are compensated by holes (valence band doping) for low defect density in the thin film as obtained in high temperature condition. However, for a high quantity of dopants, the Fermi energy is pinned at 0.6 eV and the charge compensation of dopants is guaranteed by the formation of positive charges on the oxygen atoms and the nickel atoms. It has been concluded that, at high temperature, the dopants are primarily nickel vacancies, while at room temperature the dopant could be both nickel vacancies and oxygen interstitial.

The work on the origin of the conductivity of NiO thin films prepared at room temperature (Chapter 5) (RT) has been carried out in collaboration with the EMAT team of the University of Antwerp. ACOM images shown that NiO thin films are polycrystalline. In complement, a TEM/EELS study evidenced the presence of a secondary oxygen-rich phase accumulating first at the grain boundaries before appearing in the bulk of the grain with increasing oxygen concentration during the sample preparation. This secondary phase is unstable with temperature. It disappears if the thin film prepared at room temperature is heated above 200 °C. This instability has been claimed to be the origin of electrical ageing reported in literature, where the conductivity of the RT-thin films decreases over time when exposed to air. Eventually, the secondary phase provides electrical paths with higher mobility, which might be responsible of the high conductivity and low electrical activation energy reported in RT-NiO

thin films. These defects can necessary to obtain catalytically active NiO based material. Indeed, as seen in Chapter 10, the highly defective NiO thin films obtained at room temperature displayed a high electro-catalytic activity towards the OER in comparison to the sample prepared at higher temperature.

The NiO/electrolyte interface has been studied with respect to its performance towards adsorption reactions on the surface and towards the oxygen evolution reaction. The experiments evidence that best catalytic performance is obtained when the thin films are prepared at room temperature, while temperature during the thin film fabrication reduces substantially the catalytic activity of the thin film (Chapter 10). In addition, adsorption studies have been carried out on oriented samples in-situ (water exposure in vacuum) and in an electrolyte in the stability window of water (Chapter 8). Before experiments, UPS measurements on as-prepared oriented NiO thin films revealed distinct electronic features in the valence band region according to the dominant orientation. Eventually, adsorption experiments suggested that the (100) oriented films provide adsorption sites for both hydrogen and hydroxides while the (110) and (111) oriented films provide only adsorption sites for hydroxides.

Regarding the electrochemical study of oriented NiO thin films towards the oxygen evolution reaction (Chapter 9), it has been found that the (110) oriented films provide better electrochemical activity than the (111) and the (100) oriented films. The (100) oriented films are the least active surface towards the OER. This has been ascribed to the formation of the β-$Ni(OH)_2$ phase on the (110) oriented films, while the (111) and (100) oriented surfaces prefer the formation of the α-$Ni(OH)_2$ phase. The β-$Ni(OH)_2$ is electrochemically more active than the α-$Ni(OH)_2$ phase. To explain the lower catalytic activity of the (100) oriented films in comparison to the (111) oriented films, it has been assumed, according to the experiments, that the α-$Ni(OH)_2$ layer growing on top of the (100) oriented films is thinner and less homogeneous than the hydroxide layer growing on top of the (111) oriented films.

Nickel oxide has been deposited on Si/SiO_2 interfaces. Improvement in the preparation of the silicon/NiO interface has been achieved. In Chapter 14, it has been shown that a better interface quality can be obtained when the NiO layer is grown by the deposition of a metallic layer by sputtering in argon and a subsequent oxidation in an oxygen rich atmosphere without plasma. The method is called metal layer oxidation (MLO). It avoids any direct exposition of the silicon to negatively charged oxygen ions, which would implant oxygen interstitials in the silicon dioxide layer, as it is the case for reactive sputter deposition. Also, in-depth studies of the Si/SiO_2 interface by in-situ XPS highlighted the presence of a donor state in the silicon bandgap at the Si/SiO_2 interface which pins the Fermi energy and limits the built-in voltage of the space-charge region (Chapter 12). The presence of a donor state at the Si/SiO_2 has been charged of the Fermi level pinning observed particularly when platinum is deposited. Because of the ionization of the

donor states during the space-charge region built-up, an intense electric field in the 100 MV/m range in the top 2 nm of the silicon is created and an electric field in the 500 MV/m range is formed through the silicon dioxide. It has been assumed that the donor state is partially ionized when platinum is deposited but totally ionized for nickel oxide prepared by MLO on top of the Si/SiO_2 interface. Therefore, larger band deviation can be attained with nickel dioxide MLO deposited. The results enabled to refine the comprehension of the electrical behaviour of a $Si/SiO_2/Pt$ metal insulator semi-conductor (MIS) Schottky junction (Chapter 13) where it is proposed that large fraction of the bias potential falls through the silicon dioxide layer in reverse bias as long the donor state is not fully ionized which accounts for bias potential V_g comprised between the built-in potential V_{bi} (determined by DC electrical measurements) and the flat-band potential V_{fb} (determined by RF electrical measurements). Once the donor states are totally ionized ($V_g < V_{fb}$), the measured capacitance follows a standard Mott-Schottky behaviour due to the polarization of the space-charge region in the silicon by the bias potential (once all donors are ionized, the bias potential is linearly correlated to the polarization of the space charge region).

Finally, as shown in Chapter 15, the implementation of the finding summarized above in a functional photo water-splitting device has not been absolutely successful and the optimization required additional time, which was not available. However, it can be said that the device provided a positive response to photo-illumination and that there was likely no current limitation due to charge recombination at the interface, but it might be assumed that charge transfer from the silicon to the catalytic site and the catalytic properties towards the OER of the NiO layer should be optimized to improve further the performance of a full photo-water splitting device.

From the author's perspective, the thesis could open further work especially regarding the NiO/electrolyte interface and the fabrication of TMO based electronic devices.

To what concerns the NiO/electrolyte interface, it could be valuable to try to grow a thick hydroxide layer (electrochemically or by sputtering) on top of oriented NiO thin films. The idea being to verify, by XRD, which hydroxide crystallographic structure is adopted in function of the orientation of the NiO underlayer orientation. Thus, it could be shown what kind of hydroxide phase develop on each NiO orientation, in particular that the β-$Ni(OH)_2$ develops on (110) oriented NiO surfaces and the α-$Ni(OH)_2$ on the (111) and the (100) surfaces. Moreover, efforts should be carried out to produce a single crystal NiO thin film, free of any grain boundaries, on top of a conductive substrate. Thus, it could be possible to further support the work presented in Chapter 8 on the adsorption of water in vacuum and the study of the electrochemical adsorption processes in an electrolyte. Indeed, the studied oriented thin films presented irregularities and the surfaces were not completely flat. Such irregularities could weaken partially the conclusions, which were drawn in

Refinement of the potential profile through a multi-layered Si/SiO_2 based structure and deeper study of the understanding of the operating condition of the Si/SiO_2 interface has to be carried out. Such study could unveil and resolve uncertainty and approximation taken when interpretation of the electrical measurements are carried out on a functional device.

Regarding the fabrication of TMO based electronic devices, the metal layer oxidation (MLO) method presented in Chapter 14 could open the road in developing more efficient electronic structures, especially the development of electron/hole selective contacts could be promising. However, if n-type silicon is used as photo-active material, the presence of the donor state in the silicon bandgap has to be taken into consideration and, if detrimental on the device performances, some measures should be taken to avoid the pinning of the Fermi level. It would be interesting to fabricate a full solar device, which could be electrically characterized where the critical parts, based on oxide, are prepared by the MLO method.

Finally, the fabrication of a functional silicon based photo water-splitting device, as detailed in Chapter 15, needs optimization to be carried out. According to the results presented in Chapter 15, the optimization should focus on the improvement of the charge transfer between the silicon and electrolyte by tuning both the properties of the catalytic layer and the properties of the tunnelling dielectric layer.

APPENDIX A

Appendix

A.1 TLM on n-Si/metal and n^+-Si/metal structures

Transmission Line Measurements (TLM) have been carried in order to assess the effect of Phosphor diffusion on the contact resistance of the superficial silicon layer. The method for the TLM is described in the Section 3.4.4. Superficial n^+-Si layer on top of n-Si is obtained in Phosphor furnace at 950 °C. Diffusion time has been assessed for 5 mins, 10 mins and 45 mins. TLM measurements are mainly carried out on the n-Si/n^+-Si samples for diffusion time of 10 and 45 mins. The reason is that, furnace calibration started with longer time and went shorter. As the ohmic back-contacting could be easily obtained with a diffusion time of 10 and 45 mins, and that the RF measurements on the 5 mins diffusion time provided features indicating an ohmic back contact it has been assumed that what we learn with the 10 and 45 mins diffusion is still valid with the 5 mins one.

As displayed in Figure A.1, the direct deposition of a metal on silicon provide a rectifying junction whereas the diffusion of phosphor on top suppress this rectifying behaviour. The measured current is planar, it means that most of the condution path is likely supported by the n^+-Si layer. However, the diffusion of Phosphor is supposed to inject a very high quantity of electron in the silicon conduction band. It turns out that the conduction band is located at the Fermi level and it can be assumed that no built-in potential arises in the bulk of the n-type silicon.

The TLM measurements have been realized in order to estimate the contact resistance between metals and the silicon for Phosphor diffusion time of 10 and 45 mins. A post-annealing step has been also performed. The results are displayed in Figure A.2. It can be observed that the longer the diffusion time, the lower the contact resistance R_c and that the post annealing step does not substantially change its value which denotes a certain stability of the junction. In addition, whatever the material of the metallic stripe, the contact resistance is similar on n-Si/n^+-Si surfaces. Finally, in order to avoid Phosphor contamination of the furnace used to growth thermally the silicon dioxide layer (see Chapter 11) because of a too heavily superficially doped n-Si/n^+-Si by Phosphor, it has been decided to reduce the diffusion time to of Phosphore to 5 mins. The RF measurements provided results confirming that ohmic back-contact is also obtained for such short time. Although the contact

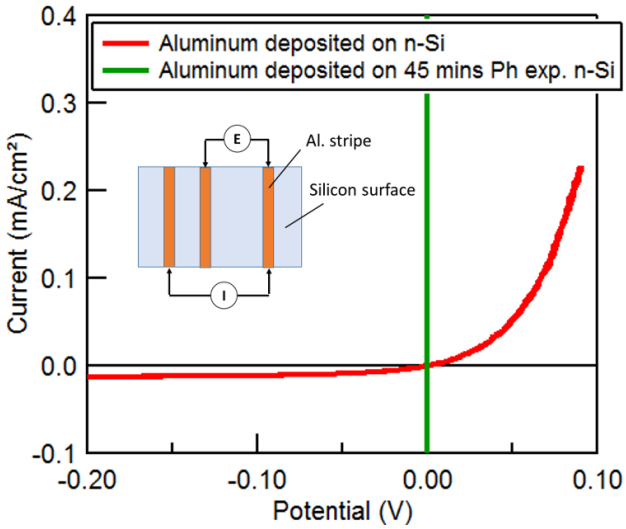

Figure A.1: IV curves of n-Si/Al and n-Si/n^+-Si/Al contact. The n^+ layer is obtained by phosphor diffusion at 950 °C for 45 mins. The n-Si/Al contact displays a rectifying behaviour whereas the n-Si/n^+-Si/Al contact is ohmic. For the latter junction, the overall resistance is so low that it provides like a straight vertical line on the plot. Electrical measurements set-up is described in the inset.

resistance is likely higher than what can be obtained with 10 and 45 mins it can be assumed that for a 5 mins diffusion time, as for the 10 and 45 mins, the surface is stable with heat and that it will provide an ohmic contact whatever the nature of the metal deposited on top of the n-Si/n^+-Si structure.

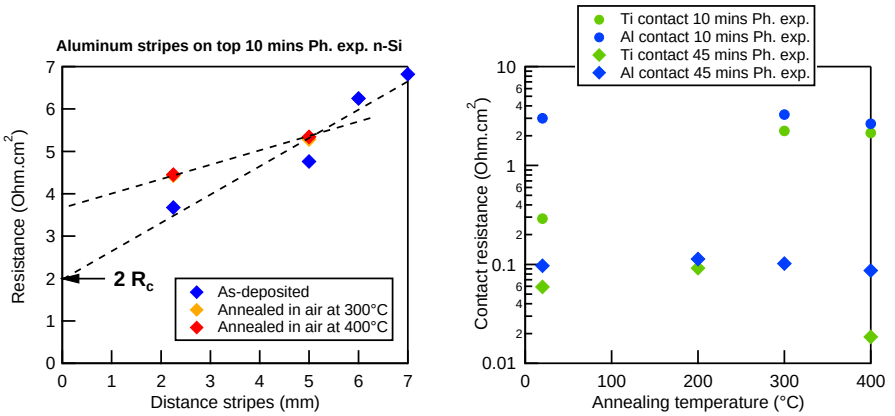

Figure A.2: Left: Extraction of the contact resistance with the TLM method of n-Si/n^+-Si/Al structure for different post-annealing temperature. The n^+ rich region is obtained by phosphor diffusion at 950 °C for 10 mins. Right: extracted contact resistance (R_c) for different structure and different post-annealing time.

A.2 Structure of the Silicon/NiO transition

TEM/EELS measurements reveals the presence of an SiO_x layer formed on top of a Ni^0 rich region (Figure A.3). This can be due to cationic inter-diffusion at the interface as the cations are smaller in diameter than the oxygens. This results is particularly interesting concerning the attempt to create Transition Metal Oxide (TMO) based selective contacts directly on silicon by PVD [23, 29, 240, 246] and show that the interface of a Si/TMO junction is likely a more complicated structure at atomic level than expected.

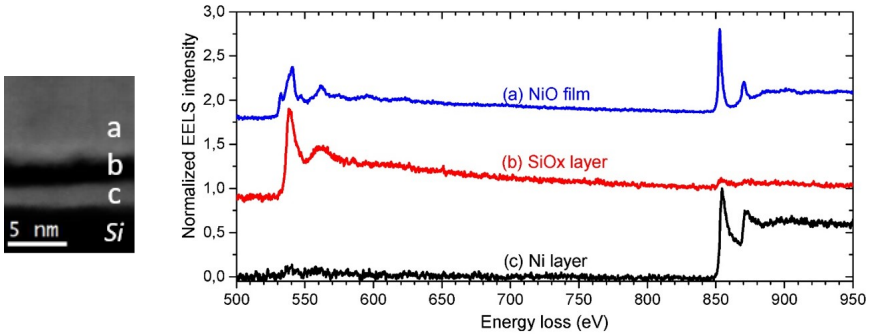

Figure A.3: EELS spectra taken at point a), b) and c) (left picture). The spectra of point c) shows typical fingerprint of metallic nickel while point b) would suggest the presence of a SiO_x layer. Finally point a) shows typical spectra of NiO where peaks of oxygen and nickel are found. The measurements have been realized on a NiO thin film prepared on silicon with 2.5 % of oxygen at room temperature at UCL.

A.3 ALD deposition of an alumina layer

It has been reported that the addition of alumina on top of a SiO_2 layer could help to improve the performance of a Si/SiO_2 based MIS device [120, 125, 126]. Therefore, the effect of a thin tunnelling alumina layer deposited by Atomic Layer Deposition (ALD) on top of the Si/SiO_2 structure has been assessed. Beforehand, as for the SiO_2 layer, the right condition of deposition (temperature and thickness) and surface conditioning (surface cleaning and passivation) of the alumina layer were studied.

A low deposition temperature (RT-200°C) of the alumina layer on hydrogen passivated Si/SiO_2 sample was preferred in order to avoid a possible reaction with the SiO_2 layer but also to limit the risk of depassivation of the SiO_2 by the removal of atomic hydrogen. After ALD deposition of the alumina layer, carbon originating from the TMA reaction with water is left on the surface as can be seen in the XPS survey (Figure A.4, left). The detrimental effect of the presence of carbon in the alumina layer is not known but as it might arise from an incomplete ALD reaction, the presence of the carbon was considered as undesired in this work. Therefore, the surface has been exposed to a hydrogen plasma as described in Section 3.2.4. Following the cleaning procedure, the carbon peak can be effectively suppressed. After the cleaning step, another exposure to the plasma source was performed on the cleaned $Si/SiO_2/Al_2O_3$ sample. For the second step, exposure time and temperature were similar to what was chosen for the passivation procedure of the Si/SiO_2 sample. Although it cannot be concluded that the second step passivates the alumina layer (suppress defects), as the conditions were the same as for a standard Si/SiO_2 passivation, the processed samples are referred to as

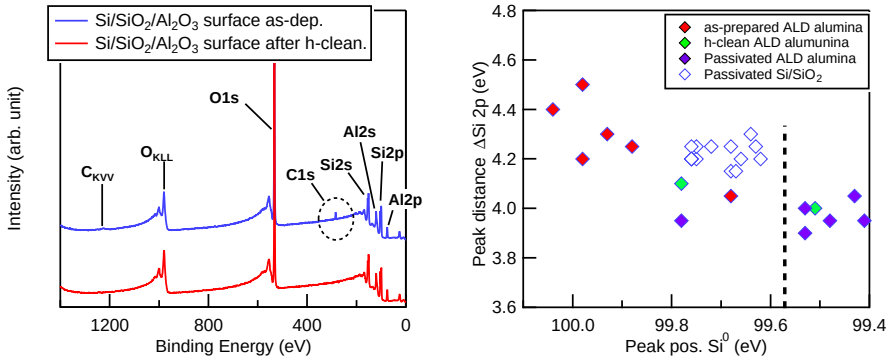

Figure A.4: Left: Cleaning of the ALD-Al_2O_3 layer by surface exposure to the hydrogen plasma. The carbon peak in the XPS survey is removed by the cleaning. Right: Compilation of the $\Delta Si\,2p$ peak distance according to the Si^0 peak position for different $Si/SiO_2/Al_2O_3$ sample preparation. The vertical dashed line represents the calculated flat-band position of the Si^0 main peak.

passivated $Si/SiO_2/Al_2O_3$ samples.

Similar to what was observed with contaminated Si/SiO_2 sample, the Si^0 peak positions of as-prepared $Si/SiO_2/Al_2O_3$ samples are found at higher binding energy than the calculated flat-band position (Figure A.4, right). The peak deviation, which is accompanied by larger ΔSi 2p, indicates an accumulation of negative charges in the silicon near the Si/SiO_2 interface.

Then, after the passivation steps, the Si^0 peak deviates to the right of the theoretical flat-band position. This indicates the built-up of a charge depleted region in the silicon at the Si/SiO_2 interface (Figure A.4). It could originate from the presence of negatively fixed charges in the alumina layer as it has been reported in the literature [126] or because of a formation of a dipole at the SiO_2/Al_2O_3 interface with the negative end pointing towards the silicon [128–131]. Thus, the negative fixed charges would repel mobile charges in the silicon (n-type) and would lead to the formation of an electron depleted region in the silicon.

A.4 IV curves of n-Si/SiO_2/Al_2O_3/Pt MIS Schottky junction

In Figure A.5 (left), equation 13.11 has been plotted for a typical value $R_c \sim 1\ \Omega\,cm^2$, $R_{leak} \sim 10000\ \Omega\,cm^2$, τ_n=1 and built-in voltage V_{bi}=0.2 V. Deviation from the ideal curve can be observed at reverse potential and low forward potential due to the excess of current going through the leaking resistance (R_{leak}) overcoming thermionic current.

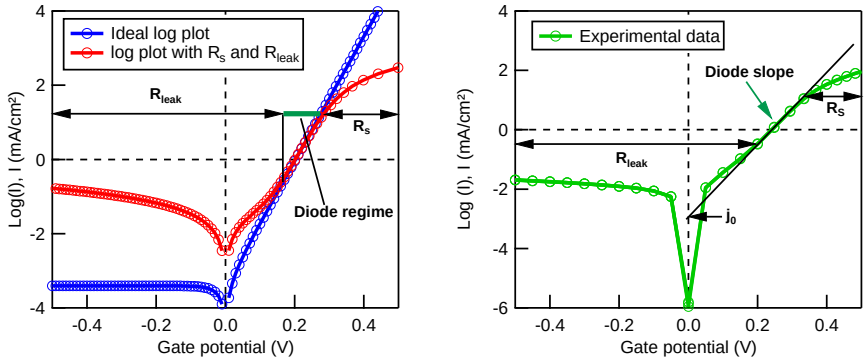

Figure A.5: Left plot: Simulated IV curve with (red) and without (blue) the introduction of the contact resistance R_c and the leaking resistance R_{leak}. Right plot: experimental data obtained with a n^+-Si/n-Si/SiO_2/Al_2O_3/Pt structure where are transposed the features reported on the left plot .

A.5 Electrochemical activation for the adsorption experiments

In the Chapter 8, in order to study the NiO surfaces towards the electrochemical adsorption reaction, an electrochemical activation has been carried out. It basically consisted in sweeping at 100 mV/sec for at least 20 cycles. If the cyclic voltamograms are similar between the first and the last cycles, it can be assumed that the surface is in steady-state condition. For each sample, the experiments are first performed in the oxygen poor electrolyte and then in the oxygen rich electrolyte which are obtained in bubbling wet N_2 and wet O_2, respectively, in an 0.1 NaOH solution.

Figure A.6 shows the cyclic voltamograms obtained during the 2^{nd} cycle and the 20^{th} cycle for the different studied NiO surfaces (see Chapter 7). The 2^{nd} cycle is preferred to the 1^{st} cycle as the 2^{nd} is a complete cycle and the 1^{st} starts only from the open circuit potential. The curves show that the surfaces are extremely stable in an oxygen poor electrolyte. On the contrary in oxygen rich electrolyte the higher cathodic current can be measured in the lower potential range. This can be attributed to the oxygen reduction reaction (ORR). The drift between the 2^{nd} and the 20^{th} cycle in the oxygen rich electrolyte can be due to a reduction of the oxygen concentration at the NiO/electrolyte interface.

Interestingly, when the NiO thin films are prepared at higher oxygen concentration, the current intensity becomes broader and can denote an higher electrochemical activities towards the adsorption processes. The comparison of the electrochemical results in the oxygen rich and the oxygen poor could highlight specific feature for the adsorption of the oxygen for a certain orientation of the nickel oxide thin film. However, this has not been realized.

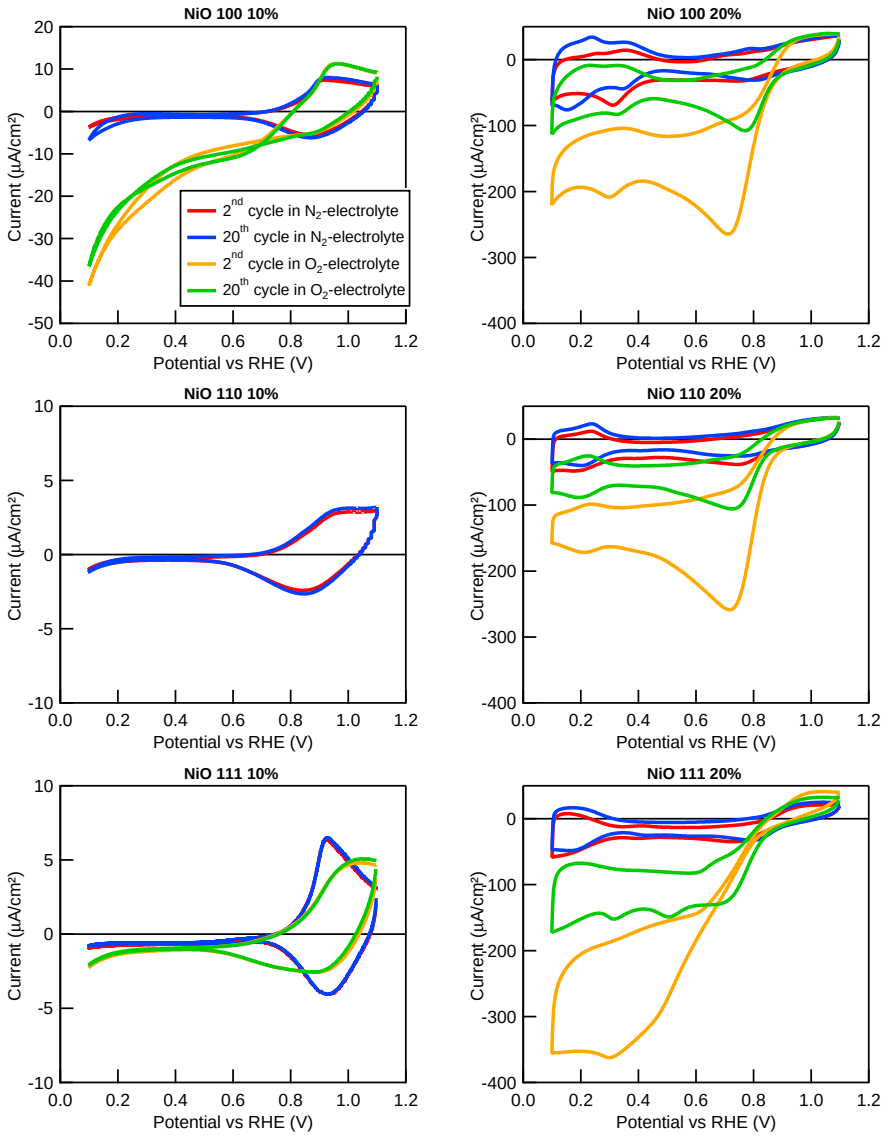

Figure A.6: Cyclic voltametry realized at 100 mV/sec for conditioning the NiO surfaces with the electrolyte before the electrochemical characterization of the adsorption processes. Two type of electrolyte are used: an oxygen poor one and an oxygen rich one which are simply referenced as N_2-electrolyte and O_2-electrolyte, respectively. The experiments in an oxygen rich electrolyte on the NiO 110 10% sample failed and this is not represented here.

A.6 Electrochemical impedance spectra of the adsorption experiments

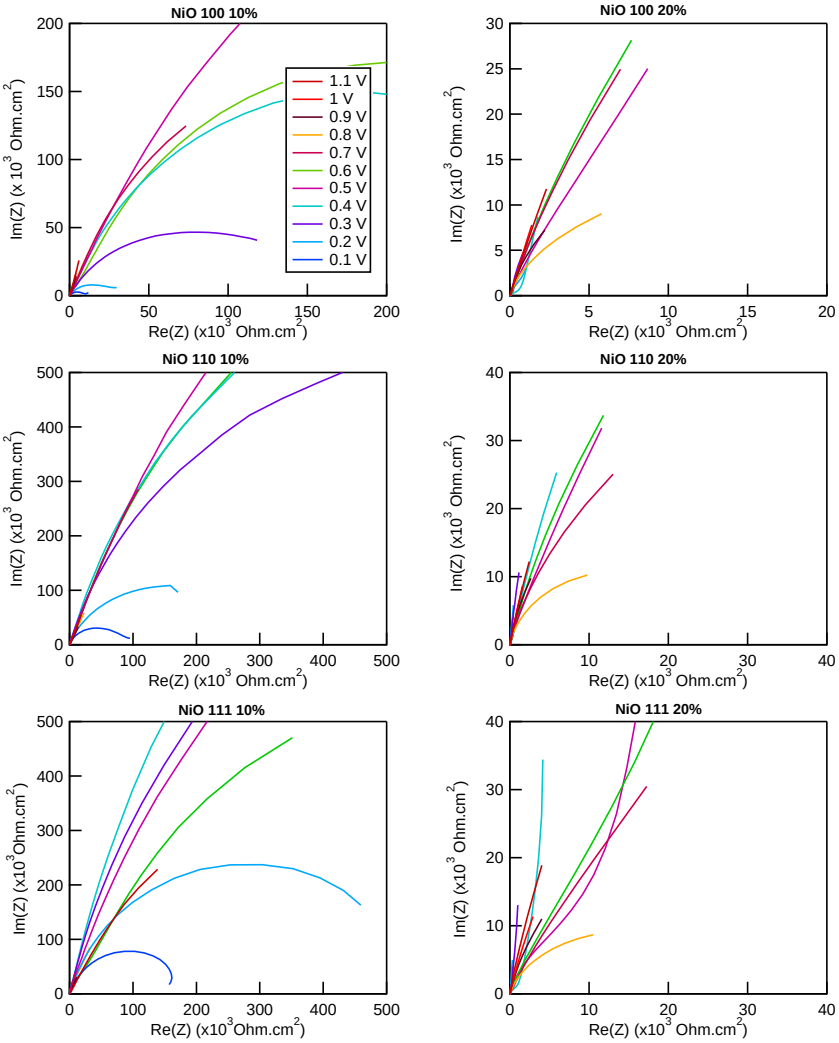

Figure A.7: Nyquist representation of the data obtained by electrochemical impedance spectroscopy on the NiO thin films used for the adsorption experiments in Chapter 8. The NiO thin films morphologies are provided in Chapter 7

A.7 Reactive sputtering on a thick SiO_2 layer

A similar electronic feature in the Si 2p region as reported in the article, and associated to defective electronic state, has been observed for sputtered Barium Strontium Titanate (BST-(Ba,Sr)TiO_3) onto Si(100)/SiO_2/TiO_2/Pt(111) where the signal of elemental Si^0 is not detected (no signal from the Si/SiO_2 interface). The silicon dioxide layer is thicker than in the article and is about 5 nm. The BST was RF-sputtered in Ar:O_2 atmosphere (ratio 99:1) at 650 °C as detailed by Schafranek *et al.* [256]. Although the photo-emitted electron are from bulk SiO_2, the in-situ XPS spectra (Figure A.8) evidence, during interface experiments, the built-up of an additional electronic state in the Si 2p region as for reactive DC sputtering of NiO (labelled $Si^{Def.}$ on Figure A.8). Therefore, similarly, the experimental results might suggest the oxygen from the BST target or from the sputtering atmosphere are ionized and accelerated towards the sample, which would diffuse through the TiO_2/Pt layers, until it reaches the SiO_2 layer where the ionized oxygen atoms are implanted. The experiment suggests that the defective electronic state is formed in the bulk of the SiO_2 layer.

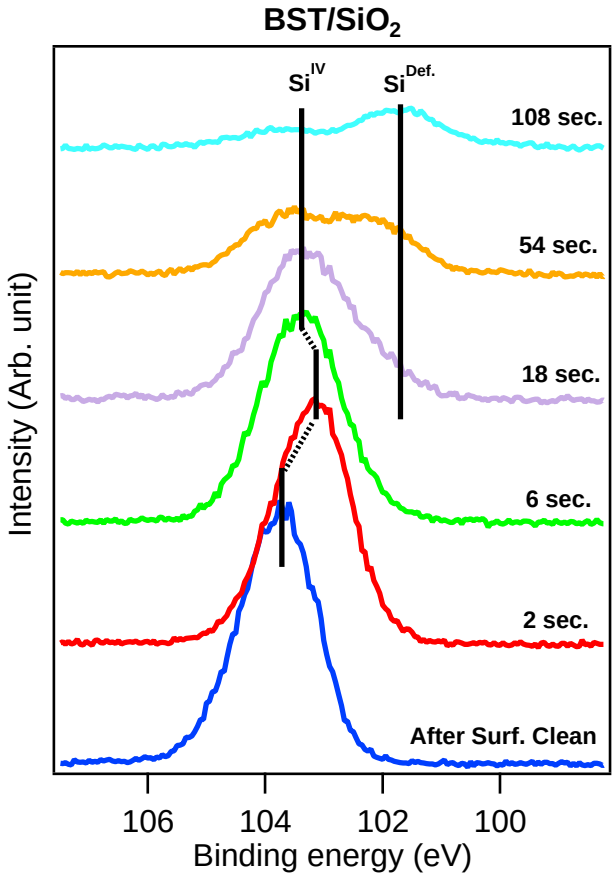

Figure A.8: Si 2p region measured by in-situ XPS during BST interfacing on a thick SiO_2 layer. The sputtering of BST onto SiO_2 results onto similar electronic feature as observed in the article. Data were obtained in the work of Schafranek et al. [256].

A.8 TEM images of NiO deposited on MgO single crystal

High Resolution Transmission Electron Microscope (HR-TEM) have been realized by the EMAT team of the University of Antwerp for two NiO thin films grown, at 400 °C and with 12.5 % oxygen, on MgO(100) and MgO(111) substrates. The pictures in Figure A.9 demonstrate that the NiO thin films adopt the orientation of the MgO substrates. The thin film grown on MgO(100) provides square like pattern while when grown on the MgO(111) substrate, the NiO thin film displays lines parallel to the substrate surface. The square like pattern and the parallel lines can be easily assigned to the NiO 100 and NiO 111 orientation along the direction of growth on the MgO 100 and MgO 111,

respectively. Larger picture of the thin films did not highlighted the presence of cracks or grain boundaries. This could suggest the NiO thin films to be single crystals.

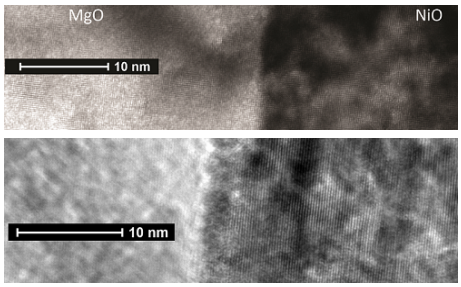

Figure A.9: HR-TEM pictures of the MgO(100)/NiO(100) (top) and MgO(111)/NiO(111) (bottom) interfaces. The deposited NiO thin films adopt perfectly the preferential orientation provided by the MgO substrates without any trace of apparent dislocation or defects. The thin films have been deposited at 400 °C and with 12.5 % oxygen.

A.9 Raman measurements

Raman measurements have been carried out on oriented NiO(100) and NiO(111) thin films grown at 400°C on oriented MgO(100) and MgO(111), respectively. The NiO thin films thickness was about 100-150 nm. The thin films are supposed to adopts a regular oriented structure as seen in Figure A.10. The Raman spectra has been realized at the UCL with a 532 nm laser source for which power is set to 10 mW. Figure A.10 shows that the 100 oriented NiO thin films provides more peaks, which are more defined, than the Raman spectra obtained on the 111 oriented thin films. Two peaks are remarkables at 1100 cm^{-1} and 1500 and cm^{-1}. According to Mironova-Ulmane *et al.* [257], they stand for the two phonon (2P) and the two magnon (2M) bands, respectively.

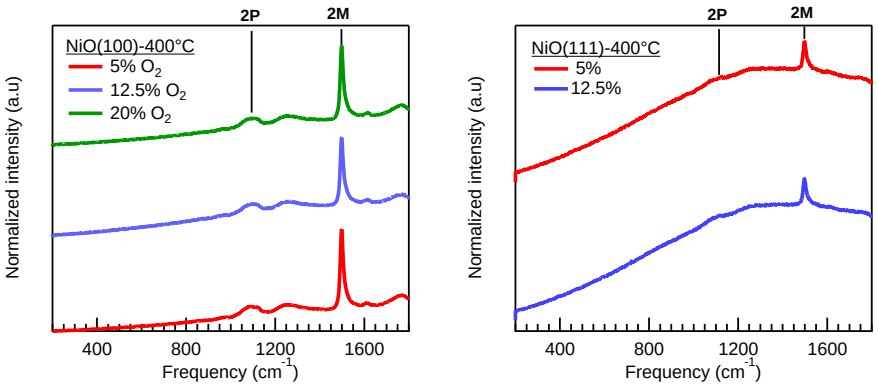

Figure A.10: Raman spectroscopy of the NiO 100 thin films grown on MgO(100) substrates (Left) and NiO 111 thin films grown on MgO (111) (Right).

Bibliography

[1] "Global Energy and CO_2 Status Report 2018," report, International Energy Agency, 2019.

[2] M. S. Prévot and K. Sivula, "Photoelectrochemical Tandem Cells for Solar Water Splitting," *The Journal of Physical Chemistry C*, vol. 117, no. 35, pp. 17879–17893, 2013.

[3] L. M. Peter and K. G. Upul Wijayantha, "Photoelectrochemical water splitting at semiconductor electrodes: fundamental problems and new perspectives," *Chemphyschem*, vol. 15, no. 10, pp. 1983–95, 2014.

[4] M. R. Nellist, F. A. Laskowski, F. Lin, T. J. Mills, and S. W. Boettcher, "Semiconductor-Electrocatalyst Interfaces: Theory, Experiment, and Applications in Photoelectrochemical Water Splitting," *Acc Chem Res*, vol. 49, no. 4, pp. 733–40, 2016.

[5] M. G. Walter, E. L. Warren, J. R. McKone, S. W. Boettcher, Q. X. Mi, E. A. Santori, and N. S. Lewis, "Solar Water Splitting Cells," *Chemical Reviews*, vol. 110, no. 11, pp. 6446–6473, 2010.

[6] N. S. Lewis and D. G. Nocera, "Powering the planet: chemical challenges in solar energy utilization," *Proc Natl Acad Sci U S A*, vol. 103, no. 43, pp. 15729–35, 2006.

[7] R. van de Krol and M. Grätzel, *Photoelectrochemical Hydrogen Production*. Electronic Materials: Science & Technology, 2012.

[8] K. Sun, S. Shen, Y. Liang, P. E. Burrows, S. S. Mao, and D. Wang, "Enabling silicon for solar-fuel production," *Chem Rev*, vol. 114, no. 17, pp. 8662–719, 2014.

[9] A. Klein, "Interface Properties of Dielectric Oxides," *Journal of the American Ceramic Society*, vol. 99, no. 2, pp. 369–387, 2016.

[10] H. F. Wardenga, M. V. Frischbier, M. Morales-Masis, and A. Klein, "In Situ Hall Effect Monitoring of Vacuum Annealing of In_2O_3:H Thin Films," *Materials (Basel)*, vol. 8, no. 2, pp. 561–574, 2015.

[11] M. V. Hohmann, A. Wachau, and A. Klein, "In situ Hall effect and conductivity measurements of ITO thin films," *Solid State Ionics*, vol. 262, pp. 636–639, 2014.

[12] W. Sheng, M. Myint, J. G. Chen, and Y. Yan, "Correlating the hydrogen evolution reaction activity in alkaline electrolytes with the hydrogen binding energy on monometallic surfaces," *Energy Environ. Sci.*, vol. 6, pp. 1509–1512, 2013.

[13] K. T. Møller, T. R. Jensen, E. Akiba, and H.-W. Li, "Hydrogen - A sustainable energy carrier," *Progress in Natural Science: Materials International*, vol. 27, no. 1, pp. 34–40, 2017.

[14] E. Verlage, S. Hu, R. Liu, R. J. R. Jones, K. Sun, C. X. Xiang, N. S. Lewis, and H. A. Atwater, "A monolithically integrated, intrinsically safe, 10% efficient, solar-driven water-splitting system based on active, stable earth-abundant electrocatalysts in conjunction with tandem III-V light absorbers protected by amorphous TiO_2 films," *Energy & Environmental Science*, vol. 8, no. 11, pp. 3166–3172, 2015.

[15] T. J. Jacobsson, V. Fjallstrom, M. Edoff, and T. Edvinsson, "CIGS based devices for solar hydrogen production spanning from PEC-cells to PV-electrolyzers: A comparison of efficiency, stability and device topology," *Solar Energy Materials and Solar Cells*, vol. 134, pp. 185–193, 2015.

[16] F. Urbain, V. Smirnov, J. P. Becker, U. Rau, J. Ziegler, B. Kaiser, W. Jaegermann, and F. Finger, "Application and modeling of an integrated amorphous silicon tandem based device for solar water splitting," *Solar Energy Materials and Solar Cells*, vol. 140, pp. 275–280, 2015.

[17] T. J. Jacobsson, C. Platzer-Björkman, M. Edoff, and T. Edvinsson, "$CuIn_xGa_{1-x}Se_2$ as an efficient photocathode for solar hydrogen generation," *International Journal of Hydrogen Energy*, vol. 38, no. 35, pp. 15027–15035, 2013.

[18] D. G. Nocera, "The artificial leaf," *Acc Chem Res*, vol. 45, no. 5, pp. 767–76, 2012.

[19] A. C. Nielander, M. R. Shaner, K. M. Papadantonakis, S. A. Francis, and N. S. Lewis, "A taxonomy for solar fuels generators," *Energy & Environmental Science*, vol. 8, no. 1, pp. 16–25, 2015.

[20] S. Tengeler, M. Fingerle, W. Calvet, C. Steinert, B. Kaiser, T. Mayer, and W. Jaegermann, "The Impact of Different Si Surface Terminations in the (001) n-Si/NiO_x Heterojunction on the Oxygen Evolution Reaction (OER) by XPS and Electrochemical Methods," *Journal of The Electrochemical Society*, vol. 165, no. 4, pp. H3122–H3130, 2018.

[21] S. M. Sze, "Citation Classic - Physics of Semiconductor-Devices," *Current Contents/Engineering Technology & Applied Sciences*, no. 27, pp. 28–28, 1982.

[22] H. W. Park, J. H. Bang, K. N. Hui, P. K. Song, W. S. Cheong, and B. S. Kang, "Characteristics of NiO–AZO thin films deposited by magnetron co-sputtering in an O_2 atmosphere," *Materials Letters*, vol. 74, pp. 30–32, 2012.

[23] R. Islam, P. Ramesh, J. H. Nam, and K. C. Saraswat, "Nickel Oxide Carrier Selective Contacts for Silicon Solar Cells," in *42nd Photovoltaic Specialist Conference (PVSC)* (IEEE, ed.), 2015.

[24] L. D'Amario, G. Boschloo, A. Hagfeldt, and L. Hammarstrom, "Tuning of Conductivity and Density of States of NiO Mesoporous Films Used in p-Type DSSCs," *Journal of Physical Chemistry C*, vol. 118, no. 34, pp. 19556–19564, 2014.

[25] R. Islam, G. Shine, and K. C. Saraswat, "Schottky barrier height reduction for holes by Fermi level depinning using metal/nickel oxide/silicon contacts," *Applied Physics Letters*, vol. 105, no. 18, 2014.

[26] K. X. Steirer, J. P. Chesin, N. E. Widjonarko, J. J. Berry, A. Miedaner, D. S. Ginley, and D. C. Olson, "Solution deposited NiO thin-films as hole transport layers in organic photovoltaics," *Organic Electronics*, vol. 11, no. 8, pp. 1414–1418, 2010.

[27] M. D. Irwin, J. D. Servaites, D. B. Buchholz, B. J. Leever, J. Liu, J. D. Emery, M. Zhang, J. H. Song, M. F. Durstock, A. J. Freeman, M. J. Bedzyk, M. C. Hersam, R. P. H. Chang, M. A. Ratner, and T. J. Marks, "Structural and Electrical Functionality of NiO Interfacial Films in Bulk Heterojunction Organic Solar Cells," *Chemistry of Materials*, vol. 23, no. 8, pp. 2218–2226, 2011.

[28] M. D. Irwin, D. B. Buchholz, A. W. Hains, R. P. H. Chang, and T. J. Marks, "p-Type semiconducting nickel oxide as an efficiency-enhancing anode interfacial layer in polymer bulk-heterojunction solar cells," *Proceedings of the National Academy of Sciences*, vol. 105, no. 8, pp. 2783–2787, 2008.

[29] S. Y. Liu, R. Liu, Y. Chen, S. H. Ho, J. H. Kim, and F. So, "Nickel Oxide Hole Injection/Transport Layers for Efficient Solution-Processed Organic Light-Emitting Diodes," *Chemistry of Materials*, vol. 26, no. 15, pp. 4528–4534, 2014.

[30] J. You, L. Meng, T. B. Song, T. F. Guo, Y. M. Yang, W. H. Chang, Z. Hong, H. Chen, H. Zhou, Q. Chen, Y. Liu, N. De Marco, and Y. Yang, "Improved air stability of perovskite solar cells via solution-processed metal oxide transport layers," *Nat Nanotechnol*, vol. 11, no. 1, pp. 75–81, 2016.

[31] K. Sun, F. H. Saadi, M. F. Lichterman, W. G. Hale, H. P. Wang, X. Zhou, N. T. Plymale, S. T. Omelchenko, J. H. He, K. M. Papadantonakis, B. S. Brunschwig, and N. S. Lewis, "Stable solar-driven oxidation of water by semiconducting photoanodes protected by transparent catalytic nickel oxide films," *Proc Natl Acad Sci U S A*, vol. 112, no. 12, pp. 3612–7, 2015.

[32] R. D. Smith, M. S. Prevot, R. D. Fagan, Z. Zhang, P. A. Sedach, M. K. Siu, S. Trudel, and C. P. Berlinguette, "Photochemical route for accessing amorphous metal oxide materials for water oxidation catalysis," *Science*, vol. 340, no. 6128, pp. 60–3, 2013.

[33] L. J. Enman, M. S. Burke, A. S. Batchellor, and S. W. Boettcher, "Effects of Intentionally Incorporated Metal Cations on the Oxygen Evolution Electrocatalytic Activity of Nickel (Oxy)hydroxide in Alkaline Media," *Acs Catalysis*, vol. 6, no. 4, pp. 2416–2423, 2016.

[34] S. Klaus, M. W. Louie, L. Trotochaud, and A. T. Bell, "Role of Catalyst Preparation on the Electrocatalytic Activity of $Ni_{1-x}Fe_xOOH$ for the Oxygen Evolution Reaction," *The Journal of Physical Chemistry C*, vol. 119, no. 32, pp. 18303–18316, 2015.

[35] V. Butera and M. Caspary Toroker, "Electronic Properties of Pure and Fe-Doped β-$Ni(OH)_2$: New Insights Using Density Functional Theory with a Cluster Approach," *The Journal of Physical Chemistry C*, vol. 120, no. 23, pp. 12344–12350, 2016.

[36] M. P. Browne, "Electrochromic Nickel Oxide Films for Smart Window Applications," *International Journal of Electrochemical Science*, pp. 6636–6647, 2016.

[37] E. Turgut, O. Coban, S. Saritas, S. Tuzemen, M. Yildirim, and E. Gur, "Oxygen partial pressure effects on the RF sputtered p-type NiO hydrogen gas sensors," *Applied Surface Science*, vol. 435, pp. 880–885, 2018.

[38] C. Park, S. H. Jeon, S. C. Chae, S. Han, B. H. Park, S. Seo, and D. W. Kim, "Role of structural defects in the unipolar resistive switching characteristics of Pt/NiO/Pt structures," *Applied Physics Letters*, vol. 93, no. 4, 2008.

[39] D. Choi and C. S. Kim, "Coexistence of unipolar and bipolar resistive switching in Pt/NiO/Pt," *Applied Physics Letters*, vol. 104, no. 19, 2014.

[40] C. Guedj, G. Auvert, and E. Martinez, "Electrical 1D tomography of nanofilaments using in-operando electrical characterization of Pt/NiO/Pt resistive memory cells during FIB milling," *Microelectronic Engineering*, vol. 156, pp. 78–81, 2016.

[41] H. Y. Peng, Y. F. Li, W. N. Lin, Y. Z. Wang, X. Y. Gao, and T. Wu, "Deterministic conversion between memory and threshold resistive switching via tuning the strong electron correlation," *Sci Rep*, vol. 2, p. 442, 2012.

[42] J. Y. Son and Y. H. Shin, "Direct observation of conducting filaments on resistive switching of NiO thin films," *Applied Physics Letters*, vol. 92, no. 22, 2008.

[43] W. Shin and N. Murayama, "High performance p-type thermoelectric oxide based on NiO," *Materials Letters*, vol. 45, no. 6, pp. 302–306, 2000.

[44] D. Su, M. Ford, and G. Wang, "Mesoporous NiO crystals with dominantly exposed (110) reactive facets for ultrafast lithium storage," *Sci Rep*, vol. 2, p. 924, 2012.

[45] S. K. Meher, P. Justin, and G. R. Rao, "Microwave-mediated synthesis for improved morphology and pseudocapacitance performance of nickel oxide," *ACS Appl Mater Interfaces*, vol. 3, no. 6, pp. 2063–73, 2011.

[46] G. Hu, C. Li, and H. Gong, "Capacitance decay of nanoporous nickel hydroxide," *Journal of Power Sources*, vol. 195, no. 19, pp. 6977–6981, 2010.

[47] X. Ma, Y. Li, Z. Wen, F. Gao, C. Liang, and R. Che, "Ultrathin β-$Ni(OH)_2$ nanoplates vertically grown on nickel-coated carbon nanotubes as high-performance pseudocapacitor electrode materials," *ACS Appl Mater Interfaces*, vol. 7, no. 1, pp. 974–9, 2015.

[48] T. Moriyama, K. Oda, T. Ohkochi, M. Kimata, and T. Ono, "Spin torque control of antiferromagnetic moments in NiO," *Sci Rep*, vol. 8, no. 1, p. 14167, 2018.

[49] A. Klein, C. Korber, A. Wachau, F. Sauberlich, Y. Gassenbauer, S. P. Harvey, D. E. Proffit, and T. O. Mason, "Transparent Conducting Oxides for Photovoltaics: Manipulation of Fermi Level, Work Function and Energy Band Alignment," *Materials (Basel)*, vol. 3, no. 11, pp. 4892–4914, 2010.

[50] D. Adler and J. Feinleib, "Electrical and Optical Properties of Narrow-Band Materials," *Physical Review B*, vol. 2, no. 8, pp. 3112–3134, 1970.

[51] P. W. Tasker and D. M. Duffy, "The Structure and Properties of the Stepped Surfaces of MgO and NiO," *Surface Science*, vol. 137, no. 1, pp. 91–102, 1984.

[52] J. Goniakowski, F. Finocchi, and C. Noguera, "Polarity of oxide surfaces and nanostructures," *Reports on Progress in Physics*, vol. 71, no. 1, 2008.

[53] B. Warot, E. Snoeck, P. Baulès, J. Ousset, M. Casanove, S. Dubourg, and J. Bobo, "Original surface morphology of epitaxial NiO layers grown on MgO(1 1 0)," *Journal of Crystal Growth*, no. 224, p. 7, 2001.

[54] B. Warot, E. Snoeck, J. C. Ousset, M. J. Casanove, S. Dubourg, and J. F. Bobo, "Surface morphology of NiO layers on MgO(0 0 1), MgO(1 1 0) and MgO(1 1 1)," *Applied Surface Science*, vol. 188, no. 1-2, pp. 151–155, 2002.

[55] B. Warot, E. Snoeck, P. Baulès, J. C. Ousset, M. J. Casanove, S. Dubourg, and J. F. Bobo, "Epitaxial growth of NiO layers on MgO(0 0 1) and MgO(1 1 0)," *Applied Surface Science*, vol. 177, no. 4, pp. 287–291, 2001.

[56] B. Warot, E. Snoeck, P. Baules, J. Ousset, M. Casanove, S. Dubourg, and J. Bobo, "Formation of tetrahedral islands in epitaxial NiO layers deposited on MgO(1 1 1)," *Journal of Crystal Growth*, no. 234, p. 7, 2002.

[57] A. Barbier, C. Mocuta, H. Kuhlenbeck, K. F. Peters, B. Richter, and G. Renaud, "Atomic structure of the polar NiO(111)- p(2×2) surface," *Phys Rev Lett*, vol. 84, no. 13, pp. 2897–900, 2000.

[58] W. Zhao, M. Bajdich, S. Carey, A. Vojvodic, J. K. Norskov, and C. T. Campbell, "Water Dissociative Adsorption on NiO(111): Energetics and Structure of the Hydroxylated Surface," *Acs Catalysis*, vol. 6, no. 11, pp. 7377–7384, 2016.

[59] W. B. Zhang and B. Y. Tang, "Stability of the polar NiO(111) surface," *J Chem Phys*, vol. 128, no. 12, p. 124703, 2008.

[60] M. A. Langell and M. H. Nassir, "Stabilization of Nio(111) Thin-Films by Surface Hydroxyls," *Journal of Physical Chemistry*, vol. 99, no. 12, pp. 4162–4169, 1995.

[61] N. Kitakatsu, V. Maurice, C. Hinnen, and P. Marcus, "Surface hydroxylation and local structure of NiO thin films formed on Ni(111)," *Surface Science*, vol. 407, no. 1-3, pp. 36–58, 1998.

[62] P. M. Olivert, S. C. Parkerf, and W. C. Mackrodtt, "Computer simulation of the crystal morphology of NiO," 1993.

[63] D. Cappus, C. Xu, D. Ehrlich, B. Dillmann, C. A. Ventrice, K. Alshamery, H. Kuhlenbeck, and H. J. Freund, "Hydroxyl-Groups on Oxide Surfaces - NiO(100), NiO(111) and Cr_2O_3(111)," *Chemical Physics*, vol. 177, no. 2, pp. 533–546, 1993.

[64] L. Liu, S. Wang, S. Liu, Q. Guo, and J. Guo, "Interaction of water with faceted NiO(111) surface tuned by films thickness," *Surface Science*, vol. 667, pp. 8–12, 2018.

[65] J. M. Blaisdell and A. B. Kunz, "Theoretical-Study of O-Chemisorption on NiO - Perfect Surfaces and Cation Vacancies," *Physical Review B*, vol. 29, no. 2, pp. 988–995, 1984.

[66] J. J. Varghese and S. H. Mushrif, "Insights into the C–H Bond Activation on NiO Surfaces: The Role of Nickel and Oxygen Vacancies and of Low Valent Dopants on the Reactivity and Energetics," *The Journal of Physical Chemistry C*, vol. 121, no. 33, pp. 17969–17981, 2017.

[67] G. T. Surratt and A. B. Kunz, "Theoretical Study of H Chemisorption on NiO Surface," *Physical Review Letters*, vol. 40, no. 5, pp. 347–350, 1978.

[68] J. M. McKay and V. E. Henrich, "Surface electronic structure of NiO: Defect states, O_2 and H_2O interactions," *Physical Review B*, vol. 32, no. 10, pp. 6764–6772, 1985.

[69] A. Zangwill, *Physics at Surfaces*. CAMBRIDGE UNIVERSITY PRESS, 1988.

[70] S. Hufner, "Electronic-Structure of NiO and Related 3d-Transition-Metal Compounds," *Advances in Physics*, vol. 43, no. 2, pp. 183–356, 1994.

[71] G. A. Sawatzky and J. W. Allen, "Magnitude and Origin of the Band-Gap in Nio," *Physical Review Letters*, vol. 53, no. 24, pp. 2339–2342, 1984.

[72] J. Feinleib and D. Adler, "Band Structure and Electrical Conductivity of NiO," *Physical Review Letters*, vol. 21, no. 14, pp. 1010–1013, 1968.

[73] P. Lunkenheimer, A. Loidl, C. R. Ottermann, and K. Bange, "Correlated barrier hopping in NiO films," *Phys Rev B Condens Matter*, vol. 44, no. 11, pp. 5927–5930, 1991.

[74] O. Bengone, M. Alouani, P. Blöchl, and J. Hugel, "Implementation of the projector augmented-wave LDA+U method: Application to the electronic structure of NiO," *Physical Review B*, vol. 62, no. 24, pp. 16392–16401, 2000.

[75] J. Zaanen, G. A. Sawatzky, and J. W. Allen, "Band gaps and electronic structure of transition-metal compounds," *Phys Rev Lett*, vol. 55, no. 4, pp. 418–421, 1985.

[76] C. Y. Kuo, T. Haupricht, J. Weinen, H. Wu, K. D. Tsuei, M. W. Haverkort, A. Tanaka, and L. H. Tjeng, "Challenges from experiment: electronic structure of NiO," *European Physical Journal-Special Topics*, vol. 226, no. 11, pp. 2445–2456, 2017.

[77] S. Lany, "Semiconducting transition metal oxides," *J Phys Condens Matter*, vol. 27, no. 28, p. 283203, 2015.

[78] P. S. Bagus, R. Broer, C. de Graaf, and W. C. Nieuwpoort, "The electronic structure of NiO for Ni 3s-hole states including full orbital relaxation and localization," *Journal of Electron Spectroscopy and Related Phenomena*, vol. 98, pp. 303–319, 1999.

[79] M. R. Castell, S. L. Dudarev, P. L. Wincott, N. G. Condon, C. Muggelberg, G. Thornton, D. Nguyen Manh, A. P. Sutton, and G. A. D. Briggs, "Atomic Resolution STM of the NiO (001) Surface Structure and Defect Sites:. c(2×2) Patterning and Effects of Covalent Bonding," *Surface Review and Letters*, vol. 04, no. 05, pp. 1003–1008, 1997.

[80] R. J. Powell and W. E. Spicer, "Optical Properties of NiO and CoO," *Physical Review B*, vol. 2, no. 6, pp. 2182–2193, 1970.

[81] M. Taguchi, M. Matsunami, Y. Ishida, R. Eguchi, A. Chainani, Y. Takata, M. Yabashi, K. Tamasaku, Y. Nishino, T. Ishikawa, Y. Senba, H. Ohashi, and S. Shin, "Revisiting the valence-band and core-level photoemission spectra of NiO," *Phys Rev Lett*, vol. 100, no. 20, p. 206401, 2008.

[82] S. Lany, J. Osorio-Guillen, and A. Zunger, "Origins of the doping asymmetry in oxides: Hole doping in NiO versus electron doping in ZnO," *Physical Review B*, vol. 75, no. 24, pp. 241203–241207, 2007.

[83] D. Y. Cho, S. J. Song, U. K. Kim, K. M. Kim, H. K. Lee, and C. S. Hwang, "Spectroscopic investigation of the hole states in Ni-deficient NiO films," *Journal of Materials Chemistry C*, vol. 1, no. 28, pp. 4334–4338, 2013.

[84] P. Kuiper, G. Kruizinga, J. Ghijsen, G. A. Sawatzky, and H. Verweij, "Character of holes in LixNi1-xO and their magnetic behavior," *Phys Rev Lett*, vol. 62, no. 2, pp. 221–224, 1989.

[85] J. van Elp, H. Eskes, P. Kuiper, and G. A. Sawatzky, "Electronic structure of Li-doped NiO," *Phys Rev B Condens Matter*, vol. 45, no. 4, pp. 1612–1622, 1992.

[86] J. Y. Zhang, W. W. Li, R. L. Z. Hoye, J. L. MacManus-Driscoll, M. Budde, O. Bierwagen, L. Wang, Y. Du, M. J. Wahila, L. F. J. Piper, T. L. Lee, H. J. Edwards, V. R. Dhanak, and K. H. L. Zhang, "Electronic and transport properties of Li-doped NiO epitaxial thin films," *Journal of Materials Chemistry C*, vol. 6, no. 9, pp. 2275–2282, 2018.

[87] R. J. Mossanek, G. Dominguez-Canizares, A. Gutierrez, M. Abbate, D. Diaz-Fernandez, and L. Soriano, "Effects of Ni vacancies and crystallite size on the O 1s and Ni 2p x-ray absorption spectra of nanocrystalline NiO," *J Phys Condens Matter*, vol. 25, no. 49, p. 495506, 2013.

[88] N. Palina, L. Wang, S. Dash, X. Yu, M. B. H. Breese, J. Wang, and A. Rusydi, "Investigation of the metal-insulator transition in NdNiO3 films by site-selective X-ray absorption spectroscopy," *Nanoscale*, vol. 9, no. 18, pp. 6094–6102, 2017.

[89] A. M. Reddy, A. S. Reddy, K. S. Lee, and P. S. Reddy, "Growth and characterization of NiO thin films prepared by dc reactive magnetron sputtering," *Solid State Sciences*, vol. 13, no. 2, pp. 314–320, 2011.

[90] A. Venter and J. R. Botha, "Optical and electrical properties of NiO for possible dielectric applications," *South African Journal of Science*, vol. 107, no. 1/2, 2011.

[91] S. D. Singh, A. Das, R. S. Ajimsha, M. N. Singh, A. Upadhyay, R. Kamparath, C. Mukherjee, P. Misra, S. K. Rai, A. K. Sinha, and T. Ganguli, "Studies on structural and optical properties of pulsed laser deposited NiO thin films under varying deposition parameters," *Materials Science in Semiconductor Processing*, vol. 66, pp. 186–190, 2017.

[92] C. H. Ho, Y. M. Kuo, C. H. Chan, and Y. R. Ma, "Optical Characterization of Strong UV Luminescence Emitted from the Excitonic Edge of Nickel Oxide Nanotowers," *Sci Rep*, vol. 5, p. 15856, 2015.

[93] A. C. Gandhi and S. Y. Wu, "Strong Deep-Level-Emission Photoluminescence in NiO Nanoparticles," *Nanomaterials (Basel)*, vol. 7, no. 8, pp. 231–243, 2017.

[94] H. P. Parkhomenko, M. N. Solovan, A. I. Mostovoi, I. G. Orletskii, O. A. Parfenyuk, and P. D. Maryanchuk, "Optical and Electrical Properties of Thin NiO Films Deposited by Reactive Magnetron Sputtering and Spray Pyrolysis," *Optics and Spectroscopy*, vol. 122, no. 6, pp. 944–948, 2017.

[95] H. Sato, T. Minami, S. Takata, and T. Yamada, "Transparent Conducting P-Type Nio Thin-Films Prepared by Magnetron Sputtering," *Thin Solid Films*, vol. 236, no. 1-2, pp. 27–31, 1993.

[96] A. Karpinski, N. Ouldhamadouche, A. Ferrec, L. Cattin, M. Richard-Plouet, L. Brohan, M. A. Djouadi, and P. Y. Jouan, "Optical characterization of transparent nickel oxide films deposited by DC current reactive sputtering," *Thin Solid Films*, vol. 519, no. 17, pp. 5767–5770, 2011.

[97] S. Mildner, J. Hoffmann, P. E. Blöchl, S. Techert, and C. Jooss, "Temperature-and doping-dependent optical absorption in the small-polaron system $Pr_{1-x}Ca_xMnO_3$," *Physical Review B*, vol. 92, no. 3, 2015.

[98] A. J. Rettie, W. D. Chemelewski, D. Emin, and C. B. Mullins, "Unravelling Small-Polaron Transport in Metal Oxide Photoelectrodes," *J Phys Chem Lett*, vol. 7, no. 3, pp. 471–9, 2016.

[99] I. G. Austin and N. F. Mott, "Polarons in crystalline and non-crystalline materials," *Advances in Physics*, vol. 18, no. 71, pp. 41–102, 1969.

[100] A. Klein, "Energy band alignment at interfaces of semiconducting oxides: A review of experimental determination using photoelectron spectroscopy and comparison with theoretical predictions by the electron affinity rule, charge neutrality levels, and the common anion rule," *Thin Solid Films*, vol. 520, no. 10, pp. 3721–3728, 2012.

[101] A. J. Bard, A. B. Bocarsly, F. R. F. Fan, E. G. Walton, and M. S. Wrighton, "The Concept of Fermi Level Pinning at Semiconductor-Liquid Junctions - Consequences for Energy-Conversion Efficiency and Selection of Useful Solution Redox Couples in Solar Devices," *Journal of the American Chemical Society*, vol. 102, no. 11, pp. 3671–3677, 1980.

[102] M. Hermle, *Passivated Contacts*, book section 3.6, p. 125. Wiley, 2016.

[103] J. Robertson, "High dielectric constant oxides," *The European Physical Journal Applied Physics*, vol. 28, no. 3, pp. 265–291, 2004.

[104] A. G. Aberle, "Surface passivation of crystalline silicon solar cells: A review," *Progress in Photovoltaics*, vol. 8, no. 5, pp. 473–487, 2000.

[105] A. W. Stephens, A. G. Aberle, and M. A. Green, "Surface recombination velocity measurements at the silicon-silicon dioxide interface by microwave-detected photoconductance decay," *Journal of Applied Physics*, vol. 76, no. 1, pp. 363–370, 1994.

[106] S. H. Lee, M. F. Bhopal, D. W. Lee, and S. H. Lee, "Review of advanced hydrogen passivation for high efficient crystalline silicon solar cells," *Materials Science in Semiconductor Processing*, vol. 79, pp. 66–73, 2018.

[107] A. Pasquarello, M. S. Hybertsen, and R. Car, "Interface structure between silicon and its oxide by first-principles molecular dynamics," *Nature*, vol. 396, no. 6706, pp. 58–60, 1998.

[108] C. J. Nicklaw, Z. Y. Lu, D. M. Fleetwood, R. D. Schrimpf, and S. T. Pantelides, "The structure, properties, and dynamics of oxygen vacancies in amorphous SiO_2," *IEEE Transactions on Nuclear Science*, vol. 49, no. 6, pp. 2667–2673, 2002.

[109] K. Kajihara, L. Skuja, and H. Hosono, "Diffusion and Reactions of Photoinduced Interstitial Oxygen Atoms in Amorphous SiO2 Impregnated with 18O-Labeled Interstitial Oxygen Molecules," *The Journal of Physical Chemistry C*, vol. 118, no. 8, pp. 4282–4286, 2014.

[110] D. J. Chadi, "Intrinsic and H-induced defects at Si/SiO_2 interfaces," *Physical Review B*, vol. 64, no. 19, 2001.

[111] Z. H. Chen, J. W. Wang, Y. Song, and X. Zuo, "First-principles investigation of oxygen-excess defects in amorphous silica," *Aip Advances*, vol. 7, no. 10, 2017.

[112] C. Herring, N. M. Johnson, and C. G. Van de Walle, "Energy levels of isolated interstitial hydrogen in silicon," *Physical Review B*, vol. 64, no. 12, 2001.

[113] W. Fussel, M. Schmidt, H. Angermann, G. Mende, and H. Flietner, "Defects at the Si/SiO_2 interface: Their nature and behaviour in technological processes and stress," *Nuclear Instruments & Methods in Physics Research Section a-Accelerators Spectrometers Detectors and Associated Equipment*, vol. 377, no. 2-3, pp. 177–183, 1996.

[114] V. Schmidt, S. Senz, and U. Gösele, "Influence of the Si/SiO2 interface on the charge carrier density of Si nanowires," *Applied Physics A*, vol. 86, no. 2, pp. 187–191, 2006.

[115] A. Stirling, A. Pasquarello, J. Charlier, and R. Car, "Dangling bond defects at Si-SiO2 interfaces: atomic structure of the P(b1) center," *Phys Rev Lett*, vol. 85, no. 13, pp. 2773–6, 2000.

[116] D. A. Muller, T. Sorsch, S. Moccio, F. H. Baumann, K. Evans-Lutterodt, and G. Timp, "The electronic structure at the atomic scale of ultrathin gate oxides," *Nature*, vol. 399, no. 6738, pp. 758–761, 1999.

[117] F. J. Himpsel, F. R. McFeely, A. Taleb-Ibrahimi, J. A. Yarmoff, and G. Hollinger, "Microscopic structure of the SiO_2/Si interface," *Phys Rev B Condens Matter*, vol. 38, no. 9, pp. 6084–6096, 1988.

[118] J. H. Zhao, A. H. Wang, P. P. Altermatt, S. R. Wenham, and M. A. Green, "24efficient PERL silicon solar cell: Recent improvements in high efficiency silicon cell research," *Solar Energy Materials and Solar Cells*, vol. 41-2, pp. 87–99, 1996.

[119] F. Feldmann, M. Simon, M. Bivour, C. Reichel, M. Hermle, and S. W. Glunz, "Carrier-selective contacts for Si solar cells," *Applied Physics Letters*, vol. 104, no. 18, 2014.

[120] R. Kotipalli, R. Delamare, O. Poncelet, X. Tang, L. A. Francis, and D. Flandre, "Passivation effects of atomic-layer-deposited aluminum oxide," *EPJ Photovoltaics*, vol. 4, 2013.

[121] D. K. Zhong, S. Choi, and D. R. Gamelin, "Near-complete suppression of surface recombination in solar photoelectrolysis by "Co-Pi" catalyst-modified W:BiVO4," *J Am Chem Soc*, vol. 133, no. 45, pp. 18370–7, 2011.

[122] G. Bourret-Sicotte, P. Hamer, R. S. Bonilla, K. Collett, and P. R. Wilshaw, "Shielded hydrogen passivation – a novel method for introducing hydrogen into silicon," *Energy Procedia*, vol. 124, pp. 267–274, 2017.

[123] B. Stegemann, A. Schoepke, D. Sixtensson, B. Gorka, T. Lussky, and M. Schmidt, "Hydrogen passivation of interfacial gap state defects at UHV-prepared ultrathin SiO2 layers on Si(111), Si(110), and Si(100)," *Physica E: Low-dimensional Systems and Nanostructures*, vol. 41, no. 6, pp. 1019–1024, 2009.

[124] M. Mews, T. F. Schulze, N. Mingirulli, and L. Korte, "Hydrogen plasma treatments for passivation of amorphous-crystalline silicon-heterojunctions on surfaces promoting epitaxy," *Applied Physics Letters*, vol. 102, no. 12, p. 122106, 2013.

[125] I. A. Digdaya, G. W. P. Adhyaksa, B. J. Trzesniewski, E. C. Garnett, and W. A. Smith, "Interfacial engineering of metal-insulator-semiconductor junctions for efficient and stable photoelectrochemical water oxidation," *Nat Commun*, vol. 8, p. 15968, 2017.

[126] G. Dingemans, F. Einsele, W. Beyer, M. C. M. van de Sanden, and W. M. M. Kessels, "Influence of annealing and Al_2O_3 properties on the hydrogen-induced passivation of the Si/SiO_2 interface," *Journal of Applied Physics*, vol. 111, no. 9, 2012.

[127] G. Dingemans and W. M. M. Kessels, "Recent progress in the development and understanding of the silicon surface passivation by aluminium oxide for photovoltaic," *25th european photovoltaic solar*

energy conference and exhibition/ 5th world conference on photovoltaic energy conversion, p. 8, 2010.

[128] Y. Hotta, I. Kawayama, S. Miyake, I. Saiki, S. Nishi, K. Yamahara, K. Arafune, H. Yoshida, S. Satoh, N. Sawamoto, A. Ogura, A. Ito, H. Nakanishi, M. Tonouchi, and H. Tabata, "Control of dipole properties in high-k and SiO_2 stacks on Si substrates with tricolor superstructure," *Applied Physics Letters*, vol. 113, no. 1, 2018.

[129] H. Kamata and K. Kita, "Design of Al_2O_3/SiO_2 laminated stacks with multiple interface dipole layers to achieve large flatband voltage shifts of MOS capacitors," *Applied Physics Letters*, vol. 110, no. 10, 2017.

[130] P. D. Kirsch, P. Sivasubramani, J. Huang, C. D. Young, M. A. Quevedo-Lopez, H. C. Wen, H. Alshareef, K. Choi, C. S. Park, K. Freeman, M. M. Hussain, G. Bersuker, H. R. Harris, P. Majhi, R. Choi, P. Lysaght, B. H. Lee, H. H. Tseng, R. Jammy, T. S. Böscke, D. J. Lichtenwalner, J. S. Jur, and A. I. Kingon, "Dipole model explaining high-k/metal gate field effect transistor threshold voltage tuning," *Applied Physics Letters*, vol. 92, no. 9, 2008.

[131] K. Shimura, R. Kunugi, A. Ogura, S. Satoh, J. Fei, K. Kita, and T. Watanabe, "Positive and negative dipole layer formation at high-k/SiO_2 interfaces simulated by classical molecular dynamics," *Japanese Journal of Applied Physics*, vol. 55, no. 4S, 2016.

[132] D. K. Schroder, *Semiconductor Material and Device Characterization*. John Wiley & Sons, third edition ed., 2005.

[133] S. B. G. and B. S., *Solid State Electronic Devices*. Upper Saddle River: Prentice-Hall, 6th edition ed., 2006.

[134] P. L. Hanselaer, R. L. Vanmeirhaeghe, W. H. Laflere, and F. Cardon, "Large Barrier Tunnel Metal-Insulator - Semiconductor Structures," *Semiconductor Science and Technology*, vol. 2, no. 2, pp. 94–101, 1987.

[135] S. R. Morrison, *Electrochemistry at Semiconductor and Oxidized Metal Electrodes*. New York: Plenum Press, second edition ed., 1980.

[136] M. A. Henderson, "The interaction of water with solid surfaces: fundamental aspects revisited," *Surface Science Reports*, vol. 46, no. 1-8, pp. 1–308, 2002.

[137] H. Kuhlenbeck, G. Odörfer, R. Jaeger, G. Illing, M. Menges, T. Mull, H. J. Freund, M. Pöhlchen, V. Staemmler, S. Witzel, C. Scharfschwerdt, K. Wennemann, T. Liedtke, and M. Neumann, "Molecular adsorption on oxide surfaces: Electronic structure and orientation of NO on NiO(100)/Ni(100) and on NiO(100) as determined from electron spectroscopies andab initiocluster calculations," *Physical Review B*, vol. 43, no. 3, pp. 1969–1986, 1991.

[138] B. Hammer and J. Nørskov, "Theoretical Surface Science and Catalysis—Calculations and Concepts," *Advances in Catalysis*, vol. 45, p. 58, 2000.

[139] Z. Shen, R. S. List, D. S. Dessau, B. O. Wells, O. Jepsen, A. J. Arko, R. Barttlet, C. K. Shih, F. Parmigiani, J. C. Huang, and P. A. Lindberg, "Electronic structure of NiO: Correlation and band effects," *Phys Rev B Condens Matter*, vol. 44, no. 8, pp. 3604–3626, 1991.

[140] H. Xin and S. Linic, "Communications: Exceptions to the d-band model of chemisorption on metal surfaces: The dominant role of repulsion between adsorbate states and metal d-states," *J Chem Phys*, vol. 132, no. 22, p. 221101, 2010.

[141] I. Mora-Sero, G. A. Garcia-Belmonte, P. P. Boix, M. A. Vazquez, and J. Bisquert, "Impedance spectroscopy characterisation of highly efficient silicon solar cells under different light illumination intensities," *Energy& Environmental Science*, vol. 2, no. 6, pp. 678–686, 2009.

[142] I. Mora-Sero, Y. Luo, G. Garcia-Belmonte, J. Bisquert, D. Munoz, C. Voz, J. Puigdollers, and R. Alcubilla, "Recombination rates in heterojunction silicon solar cells analyzed by impedance spectroscopy at forward bias and under illumination," *Solar Energy Materials and Solar Cells*, vol. 92, no. 4, pp. 505–509, 2008.

[143] B. Klahr, S. Gimenez, F. Fabregat-Santiago, J. Bisquert, and T. W. Hamann, "Photoelectrochemical and impedance spectroscopic investigation of water oxidation with "Co-Pi"-coated hematite electrodes," *J Am Chem Soc*, vol. 134, no. 40, pp. 16693–700, 2012.

[144] G. Garcia-Belmonte, A. Guerrero, and J. Bisquert, "Elucidating Operating Modes of Bulk-Heterojunction Solar Cells from Impedance Spectroscopy Analysis," *J Phys Chem Lett*, vol. 4, no. 6, pp. 877–86, 2013.

[145] J. Bisquert, L. Bertoluzzi, I. Mora-Sero, and G. Garcia-Belmonte, "Theory of Impedance and Capacitance Spectroscopy of Solar Cells with Dielectric Relaxation, Drift-Diffusion Transport, and Recombination," *Journal of Physical Chemistry C*, vol. 118, no. 33, pp. 18983–18991, 2014.

[146] B. Hirschorn, M. E. Orazem, B. Tribollet, V. Vivier, I. Frateur, and M. Musiani, "Determination of effective capacitance and film thickness from constant-phase-element parameters," *Electrochimica Acta*, vol. 55, no. 21, pp. 6218–6227, 2010.

[147] P. Zoltowski, "On the electrical capacitance of interfaces exhibiting constant phase element behaviour," *Journal of Electroanalytical Chemistry*, vol. 443, no. 1, pp. 149–154, 1998.

[148] D. Depla, S. Heirwegh, S. Mahieu, J. Haemers, and R. De Gryse, "Understanding the discharge voltage behavior during reactive sputtering

of oxides," *Journal of Applied Physics*, vol. 101, no. 1, pp. 013301–013310, 2007.

[149] D. Depla, X. Y. Li, S. Mahieu, and R. De Gryse, "Determination of the effective electron emission yields of compound materials," *Journal of Physics D-Applied Physics*, vol. 41, no. 20, pp. 202003–202007, 2008.

[150] J. Keraudy, J. G. Molleja, A. Ferrec, B. Corraze, M. Richard-Plouet, A. Goullet, and P. Y. Jouan, "Structural, morphological and electrical properties of nickel oxide thin films deposited by reactive sputtering," *Applied Surface Science*, vol. 357, pp. 838–844, 2015.

[151] K. Rachut, T. J. M. Bayer, J. O. Wolff, B. Kmet, A. Benčan, and A. Klein, "Off-Stoichiometry of Magnetron Sputtered $Ba_{1-x}Sr_xTiO_3$ Thin Films," *physica status solidi (b)*, vol. 256, no. 10, p. 1900148, 2019.

[152] H. Angermann, O. Gref, and B. Stegemann, "Effect of wet-chemical substrate smoothing on passivation of ultrathin-SiO_2/n-Si(111) interfaces prepared with atomic oxygen at thermal impact energies," *Central European Journal of Physics*, vol. 9, no. 6, pp. 1472–1481, 2011.

[153] B. Stegemann, D. Sixtensson, T. Lussky, U. Bloeck, and M. Schmidt, "Ultrahigh vacuum preparation and passivation of abrupt SiO2/Si(111) interfaces," *Chimia*, vol. 61, no. 12, pp. 826–830, 2007.

[154] T. J. M. Bayer, A. Wachau, A. Fuchs, J. Deuermeier, and A. Klein, "Atomic Layer Deposition of Al_2O_3 onto Sn-Doped In_2O_3: Absence of Self-Limited Adsorption during Initial Growth by Oxygen Diffusion from the Substrate and Band Offset Modification by Fermi Level Pinning in Al_2O_3," *Chemistry of Materials*, vol. 24, no. 23, pp. 4503–4510, 2012.

[155] Hüfner, S., *Photoelectron Spectroscopy.* Springer Series in Solid-State Sciences, 1996.

[156] Powell, C. J. and A, Jablonski., *NIST Electron Inelastic-Mean-Free-Path Database.* Gaithersburg: National Institute of Standard and Technology, Version 1.2, SRT71 ed., 2010.

[157] J. Proost, F. Henry, R. Tuyaerts, and S. Michotte, "Effect of internal stress on the electro-optical behaviour of Al-doped ZnO transparent conductive thin films," *Journal of Applied Physics*, vol. 120, no. 7, 2016.

[158] T. Scharf, J. Faupel, K. Sturm, and H. U. Krebs, "Intrinsic stress evolution in laser deposited thin films," *Journal of Applied Physics*, vol. 94, no. 7, pp. 4273–4278, 2003.

[159] B. W. Sheldon, A. Ditkowski, R. Beresford, E. Chason, and J. Rankin, "Intrinsic compressive stress in polycrystalline films with negligible grain boundary diffusion," *Journal of Applied Physics*, vol. 94, no. 2, pp. 948–957, 2003.

[160] S. C. Seel and C. V. Thompson, "Tensile stress generation during island coalescence for variable island-substrate contact angle," *Journal of Applied Physics*, vol. 93, no. 11, pp. 9038–9042, 2003.

[161] A. S. Hassanien and A. A. Akl, "Effect of Se addition on optical and electrical properties of chalcogenide CdSSe thin films," *Superlattices and Microstructures*, vol. 89, pp. 153–169, 2016.

[162] V. P. Patil, S. Pawar, M. Chougule, P. Godse, R. Sakhare, S. Sen, and P. Joshi, "Effect of Annealing on Structural, Morphological, Electrical and Optical Studies of Nickel Oxide Thin Films," *Journal of Surface Engineered Materials and Advanced Technology*, vol. 01, no. 02, pp. 35–41, 2011.

[163] H.-L. Chen, Y.-M. Lu, and W.-S. Hwang, "Characterization of sputtered NiO thin films," *Surface and Coatings Technology*, vol. 198, no. 1-3, pp. 138–142, 2005.

[164] S. Park, H.-S. Ahn, C.-K. Lee, H. Kim, H. Jin, H.-S. Lee, S. Seo, J. Yu, and S. Han, "Interaction and ordering of vacancy defects in NiO," *Physical Review B*, vol. 77, no. 13, 2008.

[165] J. Zhang, D. Zeng, Q. Zhu, J. Wu, Q. Huang, and C. Xie, "Effect of Nickel Vacancies on the Room-Temperature NO_2 Sensing Properties of Mesoporous NiO Nanosheets," *The Journal of Physical Chemistry C*, vol. 120, no. 7, pp. 3936–3945, 2016.

[166] J.-C. Dupin, D. Gonbeau, P. Vinatier, and A. Levasseur, "Systematic XPS studies of metal oxides, hydroxides and peroxides," *Physical Chemistry Chemical Physics*, vol. 2, no. 6, pp. 1319–1324, 2000.

[167] M. T. Greiner, L. Chai, M. G. Helander, W. M. Tang, and Z. H. Lu, "Transition Metal Oxide Work Functions: The Influence of Cation Oxidation State and Oxygen Vacancies," *Advanced Functional Materials*, vol. 22, no. 21, pp. 4557–4568, 2012.

[168] A. Klein, "Transparent Conducting Oxides: Electronic Structure-Property Relationship from Photoelectron Spectroscopy within situSample Preparation," *Journal of the American Ceramic Society*, 2012.

[169] O. Diaz-Morales, D. Ferrus-Suspedra, and M. T. M. Koper, "The importance of nickel oxyhydroxide deprotonation on its activity towards electrochemical water oxidation," *Chem Sci*, vol. 7, no. 4, pp. 2639–2645, 2016.

[170] A. Van der Ven, D. Morgan, Y. S. Meng, and G. Ceder, "Phase stability of nickel hydroxides and oxyhydroxides," *Journal of The Electrochemical Society*, vol. 153, no. 2, p. 5, 2006.

[171] D. S. Hall, D. J. Lockwood, C. Bock, and B. R. MacDougall, "Nickel hydroxides and related materials: a review of their structures, synthesis and properties," *Proc Math Phys Eng Sci*, vol. 471, no. 2174, p. 20140792, 2015.

[172] K. N. S. Schuldt, *Electronic characterization of thin film Sr-doped $LaFeO_3$*. Thesis, 2018.

[173] M. C. Biesinger, B. P. Payne, L. W. M. Lau, A. Gerson, and R. S. C. Smart, "X-ray photoelectron spectroscopic chemical state quantification of mixed nickel metal, oxide and hydroxide systems," *Surface and Interface Analysis*, vol. 41, no. 4, pp. 324–332, 2009.

[174] X. Xu, L. Li, J. Huang, H. Jin, X. Fang, W. Liu, N. Zhang, H. Wang, and X. Wang, "Engineering Ni^{3+} Cations in NiO Lattice at the Atomic Level by Li^{+} Doping: The Roles of Ni^{3+} and Oxygen Species for CO Oxidation," *ACS Catalysis*, vol. 8, no. 9, pp. 8033–8045, 2018.

[175] A. Hakim, J. Hossain, and K. A. Khan, "Temperature effect on the electrical properties of undoped NiO thin films," *Renewable Energy*, vol. 34, no. 12, pp. 2625–2629, 2009.

[176] R. Egerton, *Electron Energy-Loss Spectroscopy in the Electron Microscope*. Springer US, 2011.

[177] G. Lumbeeck, H. Idrissi, B. Amin-Ahmadi, A. Favache, R. Delmelle, V. Samaee, J. Proost, T. Pardoen, and D. Schryvers, "Effect of hydriding induced defects on the small-scale plasticity mechanisms in nanocrystalline palladium thin films," *Journal of Applied Physics*, vol. 124, no. 22, 2018.

[178] I. Valyukh, S. Green, H. Arwin, G. A. Niklasson, E. Wackelgard, and C. G. Granqvist, "Spectroscopic ellipsometry characterization of electrochromic tungsten oxide and nickel oxide thin films made by sputter deposition," *Solar Energy Materials and Solar Cells*, vol. 94, no. 5, pp. 724–732, 2010.

[179] N. Gauquelin, E. Benckiser, M. K. Kinyanjui, M. Wu, Y. Lu, G. Christiani, G. Logvenov, H. U. Habermeier, U. Kaiser, B. Keimer, and G. A. Botton, "Atomically resolved EELS mapping of the interfacial structure of epitaxially strained $LaNiO_3/LaAlO_3$ superlattices," *Physical Review B*, vol. 90, no. 19, 2014.

[180] A. Atkinson and R. I. Taylor, "The diffusion of 63-Ni along grain boundaries in nickel oxide," *Philosophical Magazine A*, vol. 43, no. 4, pp. 979–998, 1981.

[181] J. Deuermeier, H. F. Wardenga, J. Morasch, S. Siol, S. Nandy, T. Calmeiro, R. Martins, A. Klein, and E. Fortunato, "Highly conductive grain boundaries in copper oxide thin films," *Journal of Applied Physics*, vol. 119, no. 23, pp. 235303–235311, 2016.

[182] G. D. Canizares, *Nanostructured Nickel Oxide thin films grown by Reactive RF Magnetron Sputtering.* Thesis, 2014.

[183] W. L. Jang, Y. M. Lu, W. S. Hwang, T. L. Hsiung, and H. P. Wang, "Effect of substrate temperature on the electrically conductive stability of sputtered NiO films," *Surface & Coatings Technology*, vol. 202, no. 22-23, pp. 5444–5447, 2008.

[184] W.-L. Jang, Y.-M. Lu, and W.-S. Hwang, "Effect of different atmospheres on the electrical stabilization of NiO films," *Vacuum*, vol. 83, no. 3, pp. 596–598, 2008.

[185] W.-L. Jang, Y.-M. Lu, and W.-S. Hwang, "Effect of different atmospheres on the electrical stabilization of NiO films," *Vacuum*, vol. 83, no. 3, pp. 596–598, 2008.

[186] A. Freitag, V. Staemmler, D. Cappus, C. A. Ventrice, K. A. Shamery, H. Kuhlenbeck, and H. J. Freund, "Electronic Surface-States of NiO (100)," *Chemical Physics Letters*, vol. 210, no. 1-3, pp. 10–14, 1993.

[187] Y. Kakehi, S. Nakao, K. Satoh, and T. Kusaka, "Room-temperature epitaxial growth of NiO(111) thin films by pulsed laser deposition," *Journal of Crystal Growth*, p. 5, 2002.

[188] K. Uchida, K. Yoshida, D. Zhang, A. Koizumi, and S. Nozaki, "High-quality single crystalline NiO with twin phases grown on sapphire substrate by metalorganic vapor phase epitaxy," *Aip Advances*, vol. 2, no. 4, 2012.

[189] J. H. Lee, Y. H. Kwon, B. H. Kong, J. Y. Lee, and H. K. Cho, "Biepitaxial Growth of High-Quality Semiconducting NiO Thin Films on (0001) Al_2O_3 Substrates: Microstructural Characterization and Electrical Properties," *Crystal Growth& Design*, vol. 12, no. 5, pp. 2495–2500, 2012.

[190] R. Yamauchi, Y. Hamasaki, T. Shibuya, A. Saito, N. Tsuchimine, K. Koyama, A. Matsuda, and M. Yoshimoto, "Layer matching epitaxy of NiO thin films on atomically stepped sapphire (0001) substrates," *Sci Rep*, vol. 5, p. 14385, 2015.

[191] C. Hagendorf, R. Shantyr, H. Neddermeyer, and W. Widdra, "Pressure-dependent Ni-O phase transitions and Ni oxide formation on Pt(111): an in situ STM study at elevated temperatures," *Phys Chem Chem Phys*, vol. 8, no. 13, pp. 1575–83, 2006.

[192] K. Marre and H. Neddermeyer, "Growth of Ordered Thin-Films of NiO on Ag(100) and Au(111)," *Surface Science*, vol. 287, no. 287/288, pp. 995–999, 1993.

[193] L. Gragnaniello, F. Allegretti, R. R. Zhan, E. Vesselli, A. Baraldi, G. Comelli, S. Surnev, and F. P. Netzer, "Surface structure of nickel

oxide layers on a Rh(111) surface," *Surface Science*, vol. 611, pp. 86–93, 2013.

[194] S. Wang, S. M. Liu, J. D. Guo, K. H. Wu, and Q. L. Guo, "Surface electronic structure of polar NiO(111) films," *Surface Science*, vol. 606, no. 3-4, pp. 378–382, 2012.

[195] E. Lindahl, J. Lu, M. Ottosson, and J. O. Carlsson, "Epitaxial NiO (100) and NiO (111) films grown by atomic layer deposition," *Journal of Crystal Growth*, vol. 311, no. 16, pp. 4082–4088, 2009.

[196] Q. Guo, C. Xu, and D. W. Goodman, "Ultrathin films of NiO on MgO(100): Studies of the oxide-oxide interface," *Langmuir*, vol. 14, no. 6, pp. 1371–1374, 1998.

[197] J.Wollschlager, D.Erdos, H.Goldbach, R.Hopken, and K.M.Schroder, "Growth of NiO and MgO Films on Ag(100)," *Thin Solid Films*, vol. 400, p. 8, 2001.

[198] K. L. Kostov, S. Polzin, S. K. Saha, O. Brovko, V. Stepanyuk, and W. Widdra, "Surface-phonon dispersion of a NiO(100) thin film," *Physical Review B*, vol. 87, no. 23, 2013.

[199] M. Portalupi, L. Duò, G. Isella, R. Bertacco, M. Marcon, and F. Ciccacci, "Electronic structure of epitaxial thin NiO(100) films grown on Ag(100): Towards a firm experimental basis," *Physical Review B*, vol. 64, no. 16, 2001.

[200] R. Reissner and M. Schulze, "Multilayer adsorption of water on NiO(100) at 120 and 143 K," *Surface Science*, vol. 454, pp. 183–190, 2000.

[201] M. Kawai, K. Ito, and Y. Shimakawa, "Resistance switching in a single-crystalline NiO thin film grown on a $Pt_{0.8}Ir_{0.2}$ electrode," *Applied Physics Letters*, vol. 95, no. 1, 2009.

[202] H. W. Ryu, G. P. Choi, G. J. Hong, and J. S. Park, "Growth and surface morphology of textured NiO thin films deposited by off-axis RF magnetron sputtering," *Japanese Journal of Applied Physics Part 1-Regular Papers Brief Communications & Review Papers*, vol. 43, no. 8a, pp. 5524–5525, 2004.

[203] R. Stumpf and M. Scheffler, "Ab initio calculations of energies and self-diffusion on flat and stepped surfaces of Al and their implications on crystal growth," *Phys Rev B Condens Matter*, vol. 53, no. 8, pp. 4958–4973, 1996.

[204] C. A. Cadigan, A. R. Corpuz, F. Lin, C. M. Caskey, K. B. H. Finch, X. Wang, and R. M. Richards, "Nanoscale (111) faceted rock-salt metal oxides in catalysis," *Catalysis Science & Technology*, vol. 3, no. 4, pp. 900–911, 2013.

[205] H. J. Freund, "Metal Oxide Surfaces: Electronic Structure and Molecular Adsorption," *physica status solidi (b)*, vol. 192, no. 2, pp. 407–440, 1995.

[206] M. Fingerle, S. Tengeler, W. Calvet, T. Mayer, and W. Jaegermann, "Water Interaction with Sputter-Deposited Nickel Oxide on n-Si Photoanode: Cryo Photoelectron Spectroscopy on Adsorbed Water in the Frozen Electrolyte Approach," *Journal of the Electrochemical Society*, vol. 165, no. 4, pp. H3148–H3153, 2018.

[207] P. A. Thiel and T. E. Madey, "The interaction of water with solid surfaces: Fundamental aspects," *Surface Science Reports*, vol. 7, no. 6-8, pp. 211–385, 1987.

[208] Y. Joseph, C. Kuhrs, W. Ranke, and W. Weiss, "Adsorption of water on Fe_3O_4(111) studied by photoelectron and thermal desorption spectroscopy," *Surface Science*, vol. 433-435, pp. 114–118, 1999.

[209] D. T. Payne, Y. Zhang, C. L. Pang, H. H. Fielding, and G. Thornton, "Creating Excess Electrons at the Anatase TiO_2(101) Surface," *Topics in Catalysis*, vol. 60, no. 6-7, pp. 392–400, 2016.

[210] R. Poulain, A. Klein, and J. Proost, "Electrocatalytic Properties of (100)-, (110)-, and (111)-Oriented NiO Thin Films toward the Oxygen Evolution Reaction," *The Journal of Physical Chemistry C*, vol. 122, no. 39, pp. 22252–22263, 2018.

[211] K. A. Stoerzinger, L. Qiao, M. D. Biegalski, and Y. Shao-Horn, "Orientation-Dependent Oxygen Evolution Activities of Rutile IrO_2 and RuO_2," *J Phys Chem Lett*, vol. 5, no. 10, pp. 1636–41, 2014.

[212] R. Reissner, U. Radke, M. Schulze, and E. Umbach, "Water coadsorbed with oxygen and potassium on thin NiO(100) films," *Surface Science*, vol. 402, no. 1-3, pp. 71–75, 1998.

[213] Y. F. Li and A. Selloni, "Mechanism and Activity of Water Oxidation on Selected Surfaces of Pure and Fe-Doped NiO_x," *Acs Catalysis*, vol. 4, no. 4, pp. 1148–1153, 2014.

[214] A. J. Tkalych, K. Yu, and E. A. Carter, "Structural and Electronic Features of β-$Ni(OH)_2$ and β-NiOOH from First Principles," *The Journal of Physical Chemistry C*, vol. 119, no. 43, pp. 24315–24322, 2015.

[215] S. Klaus, Y. Cai, M. W. Louie, L. Trotochaud, and A. T. Bell, "Effects of Fe Electrolyte Impurities on $Ni(OH)_2$/NiOOH Structure and Oxygen Evolution Activity," *Journal of Physical Chemistry C*, vol. 119, no. 13, pp. 7243–7254, 2015.

[216] L. Trotochaud, S. L. Young, J. K. Ranney, and S. W. Boettcher, "Nickel-iron oxyhydroxide oxygen-evolution electrocatalysts: the role of intentional and incidental iron incorporation," *J Am Chem Soc*, vol. 136, no. 18, pp. 6744–53, 2014.

[217] M. E. G. Lyons and M. P. Brandon, "The Oxygen Evolution Reaction on Passive Oxide Covered Transition Metal Electrodes in Aqueous Alkaline Solution. Part 1-Nickel," *International Journal of Electrochemical Science*, vol. 3, no. 12, pp. 1386–1424, 2008.

[218] E. L. Miller and R. E. Rocheleau, "Electrochemical and electrochromic behavior of reactively sputtered nickel oxide," *Journal of the Electrochemical Society*, vol. 144, no. 6, pp. 1995–2003, 1997.

[219] B. S. Yeo and A. T. Bell, "In Situ Raman Study of Nickel Oxide and Gold-Supported Nickel Oxide Catalysts for the Electrochemical Evolution of Oxygen," *Journal of Physical Chemistry C*, vol. 116, no. 15, pp. 8394–8400, 2012.

[220] S. Machill and D. Rahner, "In situ electrochemical characterization of lithium-alloying materials for rechargeable anodes in lithium batteries," *Journal of Power Sources*, vol. 54, no. 2, pp. 428 – 432, 1995. Proceedings of the Seventh International Meeting on Lithium Batteries.

[221] J. C. B. Nadesan and A. C. C. Tseung, "Oxygen Evolution on Nickel-Oxide Electrodes," *Journal of the Electrochemical Society*, vol. 132, no. 12, pp. 2957–2959, 1985.

[222] M. E. G. Lyons and R. L. Doyle, "Oxygen Evolution at Oxidised Iron Electrodes: A Tale of Two Slopes," *International Journal of Electrochemical Science*, vol. 7, no. 10, pp. 9488–9501, 2012.

[223] K. Ellmer and T. Welzel, "Reactive magnetron sputtering of transparent conductive oxide thin films: Role of energetic particle (ion) bombardment," *Journal of Materials Research*, vol. 27, no. 5, pp. 765–779, 2012.

[224] S. J. Xie, Y. Zhao, and Y. J. Jiang, "Laser-induced hydrophobicity on single crystal zinc oxide surface," *Applied Surface Science*, vol. 263, pp. 405–409, 2012.

[225] R. P. Vasquez and F. J. Grunthaner, "Intensity analysis of XPS spectra to determine oxide uniformity: Application to SiO_2/Si interfaces," *Surface Science*, vol. 99, no. 3, pp. 681–688, 1980.

[226] J. Hill, D. Royce, C. Fadley, L. Wagner, and F. Grunthaner, "Properties of oxidized silicon as determined by angular-dependent x-ray photoelectron spectroscopy," *Chemical Physics Letters*, vol. 44, no. 2, pp. 225 – 231, 1976.

[227] F. J. Grunthaner, P. J. Grunthaner, R. P. Vasquez, B. F. Lewis, J. Maserjian, and A. Madhukar, "Local Atomic and Electronic-Structure of Oxide-Gaas and SiO_2-Si Interfaces Using High-Resolution XPS," *Journal of Vacuum Science & Technology*, vol. 16, no. 5, pp. 1443–1453, 1979.

[228] B. Ulgut and S. Suzer, "XPS studies of SiO_2/Si system under external bias," *Journal of Physical Chemistry B*, vol. 107, no. 13, pp. 2939–2943, 2003.

[229] H. Kobayashi, T. Kubota, H. Kawa, Y. Nakato, and M. Nishiyama, "Oxide thickness dependence of energy shifts in the Si 2p levels for the SiO2/Si structure, and its elimination by a palladium overlayer," *Applied Physics Letters*, vol. 73, no. 7, pp. 933–935, 1998.

[230] R. Fritsche, E. Wisotzki, A. B. M. O. Islam, A. Thissen, A. Klein, W. Jaegermann, R. Rudolph, D. Tonti, and C. Pettenkofer, "Electronic passivation of Si(111) by Ga–Se half-sheet termination," *Applied Physics Letters*, vol. 80, no. 8, pp. 1388–1390, 2002.

[231] Y. Gassenbauer, R. Schafranek, A. Klein, S. Zafeiratos, M. Hävecker, A. Knop-Gericke, and R. Schlögl, "Surface states, surface potentials, and segregation at surfaces of tin-doped In_2O_3," *Physical Review B*, vol. 73, no. 24, 2006.

[232] Y. J. Chabal, G. S. Higashi, K. Raghavachari, and V. A. Burrows, "Infrared spectroscopy of Si(111) and Si(100) surfaces after HF treatment: Hydrogen termination and surface morphology," *Journal of Vacuum Science & Technology A: Vacuum, Surfaces, and Films*, vol. 7, no. 3, pp. 2104–2109, 1989.

[233] N. Elgrishi, K. J. Rountree, B. D. McCarthy, E. S. Rountree, T. T. Eisenhart, and J. L. Dempsey, "A Practical Beginner's Guide to Cyclic Voltammetry," *Journal of Chemical Education*, vol. 95, no. 2, pp. 197–206, 2017.

[234] M. Copuroglu, D. Caliskan, H. Sezen, E. Ozbay, and S. Suzer, "Location and Visualization of Working p-n and/or n-p Junctions by XPS," *Sci Rep*, vol. 6, p. 32482, 2016.

[235] A. F. Zurhelle, X. Tong, A. Klein, D. S. Mebane, and R. A. De Souza, "A Space-Charge Treatment of the Increased Concentration of Reactive Species at the Surface of a Ceria Solid Solution," *Angew Chem Int Ed Engl*, vol. 56, no. 46, pp. 14516–14520, 2017.

[236] F. Chekir, G. N. Lu, and C. Barret, "Anomalies in Schottky diode I−V characteristics," *Solid-State Electronics*, vol. 29, no. 5, pp. 519–522, 1986.

[237] S. Ashok, J. M. Borrego, and R. J. Gutmann, "Electrical Characteristics of Gaas Mis Schottky Diodes," *Solid-State Electronics*, vol. 22, no. 7, pp. 621–631, 1979.

[238] K. Mallik, R. J. Falster, and P. R. Wilshaw, "Schottky diode back contacts for high frequency capacitance studies on semiconductors," *Solid-State Electronics*, vol. 48, no. 2, pp. 231–238, 2004.

[239] M. Ershov, H. C. Liu, L. Li, M. Buchanan, Z. R. Wasilewski, and A. K. Jonscher, "Negative capacitance effect in semiconductor devices," *Ieee Transactions on Electron Devices*, vol. 45, no. 10, pp. 2196–2206, 1998.

[240] L. G. Gerling, S. Mahato, A. Morales-Vilches, G. Masmitja, P. Ortega, C. Voz, R. Alcubilla, and J. Puigdollers, "Transition metal oxides as hole-selective contacts in silicon heterojunctions solar cells," *Solar Energy Materials and Solar Cells*, vol. 145, pp. 109–115, 2016.

[241] X. Yang, Q. Bi, H. Ali, K. Davis, W. V. Schoenfeld, and K. Weber, "High-Performance TiO_2-Based Electron-Selective Contacts for Crystalline Silicon Solar Cells," *Adv Mater*, vol. 28, no. 28, pp. 5891–7, 2016.

[242] R. Pietruszka, B. S. Witkowski, S. Gieraltowska, P. Caban, L. Wachnicki, E. Zielony, K. Gwozdz, P. Bieganski, E. Placzek-Popko, and M. Godlewski, "New efficient solar cell structures based on zinc oxide nanorods," *Solar Energy Materials and Solar Cells*, vol. 143, pp. 99–104, 2015.

[243] C. Battaglia, S. M. de Nicolas, S. De Wolf, X. T. Yin, M. Zheng, C. Ballif, and A. Javey, "Silicon heterojunction solar cell with passivated hole selective MoO_x contact," *Applied Physics Letters*, vol. 104, no. 11, p. 5, 2014.

[244] M. Bivour, C. Messmer, L. Neusel, F. Zähringer, J. Schön, S. W. Glunz, and M. Hermle, "Principles of Carrier-Selective Contacts Based on Induced Junctions," in *33rd European PV Solar Energy Conference and Exhibition*.

[245] W. Lin, W. Wu, Q. Xie, Z. Liu, K. Qiu, L. Cai, Z. Yao, L. Meng, B. Ai, Z. Liang, and H. Shen, "Conductive Cuprous Iodide Hole-Selective Contacts with Thermal and Ambient Stability for Silicon Solar Cells," *ACS Appl Mater Interfaces*, vol. 10, no. 50, pp. 43699–43706, 2018.

[246] H. Sarı, H. Sakakura, D. Kawade, M. Itagaki, and M. Sugiyama, "Quantification of sputtering damage during NiO film deposition on a Si/SiO_2 substrate using electrochemical impedance spectroscopy," *Thin Solid Films*, vol. 592, pp. 150–154, 2015.

[247] H. Kanda, A. Uzum, A. K. Baranwal, T. A. N. Peiris, T. Umeyama, H. Imahori, H. Segawa, T. Miyasaka, and S. Ito, "Analysis of Sputtering Damage on I–V Curves for Perovskite Solar Cells and Simulation with Reversed Diode Model," *The Journal of Physical Chemistry C*, vol. 120, no. 50, pp. 28441–28447, 2016.

[248] D. Mergel, W. Stass, G. Ehl, and D. Barthel, "Oxygen incorporation in thin films of In_2O_3:Sn prepared by rf-sputtering," *J. Appl. Phys.*, vol. 88, pp. 2437–2442, 2000.

[249] Y. C. Yeo, P. Ranade, T. J. King, and C. M. Hu, "Effects of high-kappa gate dielectric materials on metal and silicon gate workfunctions," *Ieee Electron Device Letters*, vol. 23, no. 6, pp. 342–344, 2002.

[250] D. M. Long, A. Klein, and E. C. Dickey, "Barrier formation at $BaTiO_3$ interfaces with Ni and NiO," *Appl. Surf. Sci.*, vol. 466, pp. 472–476, 2019.

[251] D. Alders, F. C. Voogt, T. Hibma, and G. A. Sawatzky, "Nonlocal screening effects in 2p x-ray photoemission spectroscopy of NiO (100)," *Phys Rev B Condens Matter*, vol. 54, no. 11, pp. 7716–7719, 1996.

[252] F. Rochet, C. Poncey, G. Dufour, H. Roulet, C. Guillot, and F. Sirotti, "Suboxides at the Si/SiO_2 interface: a Si2p core level study with synchrotron radiation," *Journal of Non-Crystalline Solids*, 1997.

[253] P. J. Grunthaner, M. H. Hecht, F. J. Grunthaner, and N. M. Johnson, "The localization and crystallographic dependence of Si suboxide species at the SiO_2/Si interface," *Journal of Applied Physics*, vol. 61, no. 2, pp. 629–638, 1987.

[254] M. Alonso, R. Cimino, and K. Horn, "Surface photovoltage effects in photoemission from metal-GaP(110) interfaces: Importance for band bending evaluation," *Phys. Rev. Lett.*, vol. 64, pp. 1947–1950, 1990.

[255] R. Schafranek, S. Payan, M. Maglione, and A. Klein, "Barrier height at(Ba,Sr)TiO_3/Ptinterfaces studied by photoemission," *Physical Review B*, vol. 77, no. 19, 2008.

[256] R. Schafranek, A. Giere, A. G. Balogh, T. Enz, Y. Zheng, P. Scheele, R. Jakoby, and A. Klein, "Influence of sputter deposition parameters on the properties of tunable barium strontium titanate thin films for microwave applications," *Journal of the European Ceramic Society*, vol. 29, no. 8, pp. 1433–1442, 2009.

[257] N. Mironova-Ulmane, A. Kuzmin, I. Sildos, and M. Pars, "Polarisation dependent Raman study of single-crystal nickel oxide," *Central European Journal of Physics*, vol. 9, no. 4, pp. 1096–1099, 2011.